ISBN 978-82-326-4806-1 (printed ver.)
ISBN 978-82-326-4807-8 (electronic ver.)
ISSN 1503-8181

Jonas Kristoffer Sunde

Doctoral thesis

Doctoral theses at NTNU, 2020:229

Jonas Kristoffer Sunde

The Effect of Elevated Temperatures on Precipitation in Aluminium Alloys

An Advanced Transmission Electron Microscopy Study

NTNU
Norwegian University of Science and Technology

Doctoral theses at NTNU, 2020:229

NTNU
Norwegian University of Science and Technology
Thesis for the Degree of
Philosophiae Doctor
Faculty of Natural Sciences
Department of Physics

NTNU
Norwegian University of Science and Technology

Jonas Kristoffer Sunde

The Effect of Elevated Temperatures on Precipitation in Aluminium Alloys

An Advanced Transmission Electron Microscopy Study

Thesis for the Degree of Philosophiae Doctor

Trondheim, August 2020

Norwegian University of Science and Technology
Faculty of Natural Sciences
Department of Physics

NTNU
Norwegian University of
Science and Technology

NTNU
Norwegian University of Science and Technology

Thesis for the Degree of Philosophiae Doctor

Faculty of Natural Sciences
Department of Physics

ISBN 978-82-326-4806-1 (printed ver.)
ISBN 978-82-326-4807-8 (electronic ver.)
ISSN 1503-8181

Doctoral theses at NTNU, 2020:229

Printed by NTNU Grafisk senter

Abstract

Aluminium (Al) alloys comprise a large and important group of engineering materials that find widespread use due to a favourable combination of material properties, including: high strength-to-weight and conductivity-to-weight ratios, ease of forming, good corrosion resistance, and excellent recyclability. Recently, driven by stricter regulations and demands to cut carbon dioxide emissions in the transporation sector, Al has become one of the fastest growing materials for automotive applications. Put simply, if you have a lighter car, you need less energy to move it forward. This leads to improvements in fuel economy and reduced emissions, or one can travel further per battery charge. The development entails gradually introducing lighter material substitutes for components traditionally made of steel. Challenges emerge when Al alloys are used in components that might see elevated temperatures ($\gtrapprox 70\,^{\circ}\mathrm{C}$) under in-service conditions, e.g. automotive components located in the engine room, heat exchangers, and subsea/offshore electrical cables. If given sufficient amounts of time, the microstructure – and hence properties – of an Al alloy will change if exposed to elevated temperatures. Therefore, a fundamental understanding of the behaviour of Al alloys after prolonged exposure to elevated temperatures is needed, which has been a major part of the motivation for this work.

The main groups of Al alloys used in structural applications are age-hardenable, meaning that they primarily obtain their strength due to high densities of nano-sized precipitate phases that form during thermal treatments. The principal scientific instrument used in this thesis is the transmission electron microscope (TEM), which is an excellent tool for studying the different types of precipitate phases, their sizes, and their distribution in the Al alloy microstructure. An operational mode called high-angle annular dark-field scanning TEM (HAADF-STEM) combined with aberration corrected lenses provides spatial resolution all the way down to the atomic scale. This mode is also capable of distinguishing atomic columns with different average atomic numbers (Z). Additions of Cu ($Z = 29$) in Al-Mg-Si alloys ($Z = 13, 12, 14$) are a common way of improving alloy strength and thermal

stability. In this work, HAADF-STEM has been used to carefully assess the effect of low Cu additions on precipitate crystal structures after prolonged thermal ageing. It was found that even very low additions of Cu (0.01 atomic $\%$) may change the Al-Mg-Si system precipitation, particularly after long temperature exposure. This has important implications for alloy recycling, where inclusions of trace elements are practically unavoidable. In addition, three key building blocks for Cu-containing precipitate phases in the Al-Mg-Si(-Cu) system have been identified. The same materials were also subjected to detailed mechanical testing and modelling of material strength.

Another powerful capability of the TEM is the option to switch between imaging and diffraction mode. Electron diffraction patterns hold rich information about the atomic arrangements of the studied material. Electron diffraction – more specifically, an advanced technique called scanning precession electron diffraction (SPED) – has been a key technique used throughout this thesis. By changing alloy compositions and thermomechanical processing routes, there are possibilities for large variations in the distribution of forming precipitate phases, with important consequences for material properties. Therefore, techniques and methodologies for obtaining improved precipitate statistics from large areas of the specimen in an objective manner are needed. It is shown how the SPED technique combined with advanced data analysis may provide such information. In addition, direct observations of precipitate transformations during thermal ageing have been achieved using *in situ* heating TEM, which was combined with SPED. In the study of an Al-Mg-Si-Cu alloy, it was shown that the fragmented L phase exhibits a significantly improved thermal stability as compared to the main age-hardening precipitate phase β''.

The works presented in this thesis provide several examples of how recent advancements in TEM techniques, instrumentation, and related data analysis offer powerful new ways of acquiring and analysing data from nano-sized crystalline phases. Most results are obtained on precipitate phases of the 6xxx series Al-Mg-Si(-Cu) system, but a study of a 2xxx series (Al-Cu) alloy is also included. Finally, it is emphasised that the methodologies applied have potential for broad applications within multi-phase materials, such as other metallic systems, semiconductors, and minerals.

Preface

This thesis is submitted to the Norwegian University of Science and Technology (NTNU) as part of the application for the degree of Philosophiae Doctor (PhD). The work was done over the course of four years, starting in August 2016 and ending in June 2020, and was mainly conducted at the Department of Physics (IFY), NTNU. One out of four years was dedicated to assistance in teaching undergraduate physics courses at IFY, which mainly entailed laboratory supervision.

During the spring of 2017 the candidate spent three weeks at the University of Cambridge, discussing and working together with Prof. Paul A. Midgley's group on topics that formed the background for Papers **I**, **II**, and **III**. In 2018 the candidate went on a research stay in Japan, first working one month for the materials company Kobe Steel Ltd., and subsequently staying over a month as a junior research fellow at Tokyo Institute of Technology. This was enabled through the Norwegian-Japanese Aluminium Alloy Research Collaboration (INTPART project), which is a collaboration between NTNU, SINTEF, Hydro, and the Japanese universities Tokyo Institute of Technology and Toyama University.

The PhD position has been part of the AMPERE project – *Aluminium Alloys with Mechanical Properties and Electrical Conductivity at Elevated Temperatures* – which started in 2015 and is scheduled to finish by the end of 2020. AMPERE is a knowledge-building project for industry (KPN), co-financed by the Research Council of Norway (NFR), and the industrial partners Hydro, Gränges, Neuman Aluminium Raufoss (Raufoss Technology), and Nexans.

The research was primarily conducted at the TEM Gemini Centre in Trondheim, which involves scientific staff from IFY and the Department of Materials Science and Engineering (IMA) at NTNU, as well as scientists from SINTEF Industry. The centre is a part of the Norwegian Centre for Transmission Electron Microscopy (NORTEM), a nationally coordinated initiative by the two leading Norwegian TEM groups in Trondheim (NTNU and SINTEF) and Oslo (UiO and SINTEF) within the physical sciences. The research was carried out under the main

supervision of Prof. Randi Holmestad from IFY, NTNU, and co-supervision from Dr. Calin Daniel Marioara from SINTEF Industry.

This thesis consists of three main parts. The first part is a general introduction to the research topics of this PhD work, the material system studied, and the experimental techniques applied. This in turn should enable the reader to appreciate the key findings of the research papers produced. The second part summarises the main findings of each paper produced, followed by a discussion of the research conducted and the outlook of the topics covered. The third and final part is a collection of seven research papers that represent the main scientific achievements in the PhD project. At the time of submitting this thesis, the status of each paper is as follows: Papers **I**-**V** – accepted and published, Paper **VI** – to be submitted, and Paper **VII** – in preparation for submission. As Paper **VI** has not yet been published, the supplementary information planned to follow this paper is also provided here. Paper **VII** is a draft that has not yet been reviewed in detail by the co-authors. The plan is to have it finalised and submitted around the time of the PhD defense.

Papers Included in the Thesis

I

Precipitate statistics in an Al-Mg-Si-Cu alloy from scanning precession electron diffraction data

J. K. Sunde, Ø. Paulsen, S. Wenner, R. Holmestad.

Journal of Physics: Conference Series **902** (2017) 012022.

II

The evolution of precipitate crystal structures in an Al-Mg-Si(-Cu) alloy studied by a combined HAADF-STEM and SPED approach

J. K. Sunde, C. D. Marioara, A. T. J. van Helvoort, R. Holmestad.

Materials Characterization **142** (2018) 458–469.

III

Crystallographic relationships of T-/S-phase aggregates in an Al–Cu–Mg–Ag alloy

J. K. Sunde, D. N. Johnstone, S. Wenner, A. T. J. van Helvoort, P. A. Midgley, R. Holmestad.

Acta Materialia **166** (2019) 587–596.

IV

In situ heating TEM observations of evolving nanoscale Al-Mg-Si-Cu precipitates

J. K. Sunde, S. Wenner, R. Holmestad.

Journal of Microscopy (2019) doi: 10.1111/jmi.12845.

V

The effect of low Cu additions on precipitate crystal structures in overaged Al-Mg-Si(-Cu) alloys

J. K. Sunde, C. D. Marioara, R. Holmestad.

Materials Characterization **160** (2020) 110087.

VI

Linking mechanical properties to precipitate microstructure in three high strength Al-Mg-Si(-Cu) alloys

J. K. Sunde, F. Lu, C. D. Marioara, B. Holmedal, R. Holmestad.

To be submitted.

VII

On the microstructural origins of improvements in conductivity by heavy deformation and ageing of Al-Mg-Si alloy 6101

J. K. Sunde, C. D. Marioara, R. Holmestad.

Manuscript in preparation.

Statement of Author Contributions

Paper **I**

The experiment and idea were designed by J. K. Sunde. JKS acquired all SPED data, developed and conducted the subsequent data analysis, and was in main charge of writing the manuscript. Heat treatment and specimen preparation were done by Ø. Paulsen. ØP also calculated precipitate statistics by conventional TEM methodologies, assisted in preparation of paper figures, and in discussing results. S. Wenner acquired presented HAADF-STEM images. The manuscript was discussed by all co-authors and finalised by JKS.

Paper **II**

The experiment and idea were conceived by J. K. Sunde. JKS heat treated and prepared all TEM specimens. All experimental data was obtained by JKS, including (S)TEM images and SPED data, and the data analysis routines were developed and performed by JKS. C. D. Marioara assisted in interpretation of HAADF-STEM images and SPED data. A. T. J. van Helvoort contributed to discussions regarding the SPED data and analysis. JKS wrote the manuscript with comments from all co-authors. All authors contributed in discussions regarding the results and

interpretations.

Paper **III**

The experiment and idea were designed by J. K. Sunde and D. N. Johnstone. Heat treatment, specimen preparation, and TEM work was mainly performed by JKS, with some STEM experiments conducted by S. Wenner. Analysis of SPED data was mainly conducted by JKS with assistance by DNJ. All authors contributed to discussions and interpretation of the results. JKS prepared all figures for the manuscript and was in main charge of writing the manuscript with comments and input from all co-authors.

Paper **IV**

J. K. Sunde, S. Wenner, and R. Holmestad conceived the idea and experiment. JKS heat treated the material, and SW prepared the TEM heating chip lamella by focused ion-beam (FIB) and scanning electron microscopy combined with electron backscatter diffraction (SEM-EBSD). JKS performed all TEM heating experiments and analysed the data. All authors contributed to discussions and interpretations of the results. JKS prepared all figures for the manuscript and wrote the manuscript with comments from all co-authors.

Paper **V**

The experiment and idea were designed by J. K. Sunde, C. D. Marioara and R. Holmestad. JKS heat treated specimens in collaboration with Feng Lu (NTNU, not author). DSC experiments were conducted during JKS' industry internship at Kobe Steel Ltd. in Moka, Japan. TEM and SPED data were obtained by JKS, with some assistance on TEM image acquisition by CDM. All authors discussed and interpreted the results. JKS made all figures and wrote the manuscript with comments and input from all co-authors.

Paper **VI**

The experiments and ideas were planned by all authors. J. K. Sunde and F. Lu collaborated in all material heat treatments and specimen preparations. TEM experiments and analysis were mainly done by JKS, with some assistance from C. D. Marioara and FL. Material hardness and conductivity were mainly measured by FL, with some assistance by JKS. FL performed tensile testing of the materials and analysed the mechanical results together with B. Holmedal. Precipitate statistics were calculated by JKS. Modelling work was done by FL and BH with some input from JKS. All authors discussed and interpreted the results. JKS was in main charge of writing the manuscript with comments and input from all co-authors.

Paper **VII**

The experiment and idea were designed by J. K. Sunde, C. D. Marioara, and R. Holmestad. Material testing and sample preparation were done by JKS in collaboration with Birgitte Karlsen (SINTEF Industry, not author). JKS and CDM collaborated on performing TEM experiments, and atom probe tomography (APT) experiments were done by JKS. CDM calculated precipitate statistics from TEM data. JKS made all figures and was in main charge of writing the manuscript.

Other Scientific Contributions

Publications

- "Scanning precession electron diffraction study of hybrid precipitates in a 6xxx series aluminium alloy" – **J. K. Sunde**, D. N. Johnstone, C. D. Marioara, A. T. J. van Helvoort, P. A. Midgley, R. Holmestad. *Microscopy and Microanalysis*, **23** S1 (2017) 114–115.

- "Effect of thermomechanical processing on microstructure and mechanical properties in an Al-Cu-Mg-Si alloy" – M. Gazizov, **J. K. Sunde**, S. Wenner, R. Holmestad, R. Kaibyshev. *Proceedings of the 16th International Aluminum Alloys Conference (ICAA16) 2018*, Chapter: Thermomechanical Processing (2018) 400441.

- "Scanning precession electron diffraction to aid aluminum alloy development" – **J. K. Sunde**, E. Christiansen, E. Thronsen, S. Wenner, C. D. Marioara, A. T. J. van Helvoort, R. Holmestad. *Microscopy and Microanalysis*, **25** S2 (2019) 1920–1921.

- "The effect of heavy deformation on the precipitation in an Al-1.3Cu-1.0Mg-0.4Si wt.% alloy" – E. Thronsen, C. D. Marioara, **J. K. Sunde**, K. Minakuchi, T. Katsumi, I. Erga, S. J. Andersen, J. Friis, K. Marthinsen, K. Matsuda, R. Holmestad. *Materials & Design*, **186** (2020) 108203.

Selected scientific presentations (presenter underlined)

- "Phase mapping of 2xxx-series aluminium alloys by scanning precession electron diffraction" – **J. K. Sunde**, S. Wenner, A. T. J. van Helvoort, D. N. Johnstone, P. A. Midgley, R. Holmestad. *EMC2016*, Lyon France, 28th August –2nd September, 2016. [Poster]

- "Precipitate statistics in an Al-Mg-Si-Cu alloy from scanning precession electron diffraction data" – **J. K. Sunde**, Ø. Paulsen, S. Wenner, A. T. J. van Helvoort, R. Holmestad. *EMAG2017*, Manchester UK, 3rd–6th July, 2017. [Talk]

- "Scanning Precession Electron Diffraction Study of Hybrid Precipitates in a 6xxx Series Aluminium Alloy" – **J. K. Sunde**, D. N. Johnstone, C. D. Marioara, A. T. J. van Helvoort, P. A. Midgley, R. Holmestad. *Microscopy and Microanalysis 2017*, St. Louis USA, 7th–10th August, 2017. [Talk]

- "Studying the effect of low Cu additions in 6082 alloys" – **J. K. Sunde**, C. D. Marioara, A. T. J. van Helvoort, R. Holmestad. *Third INTPART Workshop between NTNU, University of Toyama, and Tokyo Institute of Technology*, Tokyo Japan, 7th–8th May 2018. [Talk]

- "The effect of low Cu additions in overaged Al-Mg-Si alloys studied by advanced transmission electron microscopy techniques" – **J. K. Sunde**, C. D. Marioara, R. Holmestad. *16th International Conference on Aluminium Alloys (ICAA16)*, Montréal Canada, 17th – 21st June, 2018. [Talk]

- "Quantitative analysis of precipitate crystal structure evolution in Al-Mg-Si-Cu alloys using scanning precession electron diffraction" – **J. K. Sunde**, C. D. Marioara, A. T. J. van Helvoort, R. Holmestad. *19th International Microscopy Congress (IMC19)*, Sydney Australia, 9th–14th September, 2018. [Talk]

- "Scanning electron diffraction as a versatile tool for studying the microstructure of Al alloys" – **J. K. Sunde**, S. Wenner, C. D. Marioara, A. T. J. van Helvoort, R. Holmestad. *EMAG2019*, Manchester UK, 1st–4th July, 2019. [Talk]

- "Tracking the growth and transformation of Al-Mg-Si-Cu precipitates by in situ heating TEM" – **J. K. Sunde**, C. D. Marioara, R. Holmestad. *17th International Conference on Aluminium Alloys (ICAA17)*, Grenoble France, 14th – 18th June, 2020 (postponed). [Accepted Talk]

Acknowledgements

My four years as a PhD candidate at IFY, NTNU, is approaching the end, and in that context there are several people whose help and support along the way I would like to acknowledge. The thesis you are now reading is the product of many hours of effort. Many of those hours, both at daytime and nighttime, have been spent sitting in a mostly dark room, with a large microscope at its centre. There have been times of exciting discoveries and enjoyment of science, but also times of great frustration. Fortunately, the former has greatly outweighed the latter.

One of the key persons in my pursuit of science is Prof. Randi Holmestad from IFY, NTNU. Randi was the supervisor of my Master's thesis back in 2015-2016, and for the last four years she has also been the main supervisor of my PhD work. Randi has always been very supportive of my ideas, and has exhibited great enthusiasm and interest in my work. I would especially like to thank her for giving me great freedom in the choices I have made for my work, which I believe has been absolutely crucial for my overall enjoyment of science. She has been a great role model, and has shown that academic life can be combined with a normal family life. Your laid-back attitude and openness have been refreshing, even though it often means that the topics of our meetings may drift far apart from actual science. A huge *thank you* for your positive spirit, optimism, understanding, and lastly, for giving me the opportunity to pursue a PhD.

A big thanks is also in order for my great co-supervisor Dr. Calin Daniel Marioara from SINTEF Industry. *Thank you*, Calin, for your great insight and your never-ending passion for Al alloys and science in general. We have had many great discussions, first and foremost on topics related to science, but also topics bordering on the more philosophical, or related to travelling or other joys in life. His advice and suggestions on microscopy, papers, and other scientific topics have been invaluable. We have worked very well together, and we share a passion for scientific rigorousness and good microscopy. Your excitement is truly contagious, and it has always left me with increased motivation and enjoyment of what I do.

Science cannot progress without dedicated funding, and the Research Council of Norway (NFR) is greatly acknowledged for funding my PhD through the AMPERE project, and for the funding of the NORTEM infrastructure, providing me with access to the TEMs I have used in my work. The AMPERE project was co-financed by the industry partners in the project: Hydro, Gränges, Neuman Aluminium Raufoss (Raufoss Technology), and Nexans. The industry partners of AMPERE are also acknowledged for their contribution and participation in the project. The interest they have shown towards my research has been very important, and has motivated me to push forward.

I have been very fortunate to be part of a large and truly enjoyable research group at IFY. There are too many people to mention all by name, but a big thank you is in order for all of you. Thanks to Dr. Per Erik Vullum at SINTEF Industry for microscopy training and discussions, which have included many random topics, such as food, sports, and interesting people. Thanks to our excellent engineers Bjørn Gunnar Soleim and Dr. Ragnhild Sæterli for keeping the microscopes in proper condition in a very efficient manner, and for answering the phone at all hours of the day. Thanks to Prof. Antonius van Helvoort for his great enthusiasm and for encouraging everyone to perform their best. In particular, I want to thank Emil, Julie, Aleksander, Adrian, Jonas (#2), Tina, Håkon, and Elisabeth for fun and valuable conversations regarding everything from TEM to the struggles and frustration that might arise in the PhD life. The kind, positive, and fun social atmosphere of this research group have helped a great deal, and I wish you all the best.

I also want to thank all the co-authors of my papers that have not been mentioned up to this point: Dr. Duncan N. Johnstone, Prof. Paul A. Midgley, Prof. Bjørn Holmedal, Feng Lu, Øyvind Paulsen, and Dr. Sigurd Wenner, for collaborating on my research papers, and for fruitful and engaging discussions on a wide variety of topics.

Finally, I wish to thank the most important people outside of my work life, which is appropriate to do in Norwegian. Ein stor takk til familien min for å ha støtta meg gjennom heile livet, og for alltid å stå bak meg i mine vegval. Takk til mamma for framleis å dulle med meg som ein gutunge når du er på besøk, og til pappa for dei jamnlege samtalane våre og interessa du har vist for studia mine. Takk til mine kjære lillesøstre, Silje og Emilie. Det er alltid like kjekt når vi samlast heime i feriar, eller når vi reiser på turar saman. Det er den beste måten for å lade opp att batteria, noko som har komt godt med når ein er tilbake på jobb og forskinga skal takast vidare. Eg vil takke nære venar heimefrå: Knut, Elisabeth, Håvard & Håvard. Det har vert stor stas at så kjekke venar òg har tilbrakt mange år i studiebyen Trondheim. Våre venskap går langt tilbake i tid, og eg håpar at

vi alltid held kontakta, uansett kor vi endar opp. I tillegg vil eg takke venar frå studietida, spesielt Håkon, Anders, Ola, Kristoffer & Maria. Til sist ein stor takk til min kjære sambuar Aurora. Takk for støtta du har vist for vala mine. Utan deg hadde eg nok grodd fast i kontoret og labben. Takk for din utømmelege energi, di flotte personlegheit og for kjærleiken du har vist.

Trondheim, June 2020

Jonas Kristoffer Sunde

List of Acronyms

AA Artificial Ageing

APT Atom Probe Tomography

DED/DDD Direct Electron Detection/Direct Detection Device

fcc face-centred cubic

GB Grain Boundary

(HA)ADF (High-Angle) Annular Dark-Field

IACS International Annealed Copper Standard

NA Natural Ageing

NMF Non-negative Matrix Factorisation

OR Orientation Relationship

PCA Principal Component Analysis

SHT Solution Heat Treatment

(S)PED (Scanning) Precession Electron Diffraction

SSSS Supersaturated Solid Solution

(S)TEM (Scanning) Transmission Electron Microscopy

TMP Thermomechanical Processing

UA/OA Underaged/Overaged

(V)BF/(V)DF (Virtual) Bright-field/(Virtual) Dark-field

ZA Zone Axis

Contents

PART I

BACKGROUND

Chapter 1

Introduction

1.1 Motivation

From the Stone Age to the present, the mastering and development of novel materials have historically had a tremendous impact on both technology and human culture. Our modern society is no exception, which is reflected in our extensive utilisation of semiconductors and metals. These materials form the cornerstone of our technological progress and can be found in many aspects of our everyday lives. Metals are found in applications ranging from beverage cans and zippers on clothing, to building frameworks and space-crafts. The demand is still growing due to an increasing world population and rapid economic growth. Aluminium (Al) is the most abundant metal in the earth's crust, where it comprises about 8% of the total weight (wt.%) [1]. Being a highly reactive metal, Al is rarely found in its pure metallic state, but rather exists as a constituent of numerous minerals, the chief ore being bauxite. The process of obtaining pure Al from its various ores is very energy demanding, and higher than most other engineering materials [2]. The two main processes involved in the production of Al are the refinement of bauxite to produce alumina (Al_2O_3), and subsequently the smelting and reduction of alumina to produce pure Al. In the production of pure Al, the world average energy consumptions are 11.4 kWh/t alumina [3] and 14.2 kWh/t Al from alumina [4]. As two tonnes of alumina are required to produce one tonne Al, this gives a total estimate of 133.2 MJ/t Al – to be compared with about 19.8 MJ/t steel [5]. There are additional considerations that could be taken into account when calculating these numbers, but most estimates show that the primary production of Al is somewhere between 6-10 times more energy demanding than steel – so *why* do we need this metal?

The world production of Al has shown an overall increasing trend since 2000 [6], and will likely continue to increase in the future, for several good reasons. Al alloys can be tailored to exhibit a favourable combination of material properties, including: high strength, lightness, good formability, good corrosion resistance, excellent recyclability, as well as high conductivity. Recycling of Al alloys is becoming increasingly important, largely due to the facts that continued recycling does not deteriorate material properties, and that the energy used for recycling is only 5-7% of that required in primary production [7]. It is estimated that some 75% of all Al ever produced is still in use. This is crucial in order to offset the high energy cost required in production, and a key property that enables Al to be an important metal in a circular economy. This will be important in reaching the United Nation's 12th sustainable development goal: *Ensuring sustainable consumption and production patterns* [8].

The main groups of high strength, age-hardening (heat treatable) Al alloys are the 2xxx (Al-Cu), 6xxx (Al-Mg-Si) and 7xxx (Al-Zn-Mg) series, which are strengthened by high densities of nano-sized precipitate phases formed during thermal treatments. Of particular interest to transportation and building applications are the Al–Mg–Si alloys [9], exhibiting medium strengthening potential and good formability. These alloys are also increasingly found and sought for in many applications at elevated temperatures ($\gtrapprox 70\,^{\circ}\mathrm{C}$), one of the most important being automotive applications [9, 10]. In the car industry, small reductions in weight lead to large reductions in emissions, or may extend the range of electrical vehicles significantly. This is achieved by introducing lighter Al ($\sim 2.7\ \mathrm{g\,cm^{-3}}$) substitutes for components made of steel ($\sim 8\ \mathrm{g\,cm^{-3}}$). However, this must not come at the cost of e.g. reduced crashworthiness or thermal stability of key components. New challenges emerge when Al alloys are introduced in components that are exposed to in-service conditions of elevated temperatures, e.g. automotive components located in or near the engine room, heat exchangers, or electric wires in cars. In addition, Al alloys that are commonly found in high voltage power transmission and distribution, are under serious consideration for replacing copper (Cu) in subsea/offshore electrical cables due to their high conductivity-to-weight ratio and lower cost ($\approx$ 80% cheaper than Cu) [11]. However, these applications require increasingly demanding combinations of high strength and high conductivity without degrading other properties such as creep and fatigue resistance. The solution to the aforementioned challenges lies in improving the understanding of the effect of alloy composition and processing on microstructure-property relationships. A fundamental understanding of the behaviour of Al alloys as an effect of prolonged exposure to elevated temperatures is needed, which has been the main motivation behind this PhD project.

1.2 Objectives

The overall objective of the AMPERE project – *Aluminium Alloys with Mechanical Properties and Electrical Conductivity at Elevated Temperatures* – was to establish a scientific basis that enables the design of alloys and processing schedules to yield optimum combination of various mechanical properties and electrical conductivity at elevated temperatures [11]. This was to be achieved through enhanced fundamental understanding of the correlation between material microstructure, mechanical properties and electrical conductivity, and the influence of elevated temperature and time. In reaching this overall goal, the secondary objectives of direct relevance to this PhD work were:

- Conduct detailed and quantitative characterisation by TEM and atom probe tomography (APT) of selected alloys with focus on the microstructure evolution during thermomechanical processing and exposure to elevated temperatures.
- Measure associated changes in relevant material properties like strength and conductivity.
- Provide input for microstructure evolution models and models that can predict changes in relevant mechanical properties and electrical conductivity during thermal treatments.

The improved understanding, knowledge, and models built in the project are expected to instigate innovation in alloy, processing, and product development at the industrial partners. This is turn should lead to an increased use of Al in different applications where the use thus far has been limited.

In reading through this thesis, it becomes clear that it revolves heavily around the use of scanning precession electron diffraction (SPED) and related developments for studying the metastable precipitate phases formed in Al-Mg-Si(-Cu) alloys. This focus naturally arose in an attempt to fulfill the two main overall goals of the PhD project: (i) to push TEM techniques and related data analysis in order to build new competence at the TEM research group, and (ii) to study materials and topics of interest to the AMPERE project. For the main part, the two objectives have been combined in the research papers produced. Paper **II** and Papers **IV**-**VII** combine the two-fold focus to a large extent, by applying new TEM methodologies and by studying materials selected in the AMPERE project. Papers **I** and **III** are focused with SPED developments, and studies materials outside the AMPERE project. Paper **III** was written together with collaborating researchers at the University of Cambridge; a group which has been leading in (S)PED developments

and related data processing. This thesis provides several good examples that illustrate the rich information obtained, and the future potential in acquiring relatively large, multi-dimensional electron diffraction datasets combined with recent developments in data analysis. In addition, other powerful TEM capabilities such as *in situ* heating to study the precipitate phases directly are demonstrated.

Chapter 2

The Al Alloy Material System

Al is first and foremost used as a structural material, meaning that high demands are put on the material's mechanical properties. Pure Al is a relatively soft metal with a yield strength of about $7 - 11\ \mathrm{MPa}$. In comparison, the range of yield strengths exhibited by steels vary between $200 - 2000\ \mathrm{MPa}$. However, by alloying Al with various elements and applying heat treatments (ageing) the properties can be improved tremendously [1, 12]. The age-hardening Al-Cu, Al-Mg-Si, and Al-Zn-Mg systems exhibit yield strengths in the range $200 - 700\ \mathrm{MPa}$, hence greatly improving the strength as compared to pure Al. As the alloying additions are typically only a few atomic % (at.%), the density of the alloy does not change considerably as compared to pure Al, which has a density of $2.7\ \mathrm{g\,cm^{-3}}$. This means that steels at about $8\ \mathrm{g\,cm^{-3}}$ density are comparable to Al alloys in terms of strength-to-weight ratio, also known as specific strength. Al alloys have specific strengths in the range $75-260\ \mathrm{N\,m\,g^{-1}}$, and steels vary between $25-250\ \mathrm{N\,m\,g^{-1}}$.

Furthermore, it is not only material strength that can be improved by alloying Al. Alloying may also improve many additional properties such as formability, weldability, ductility, corrosion resistance, and surface properties. Several material properties are interlinked. For example, high strength usually implies lower ductility, and a high conductivity normally corresponds with medium or low strength. It is the optimisation of various properties that has given rise to the many different alloying systems and alloy labels, each tailored to its specific application.

In the following, the microstructural origins of Al alloys' interesting properties are elaborated. The presentation uses the Al-Mg-Si(-Cu) system as the main example, due to its high relevance to the research topics and papers in this thesis.

2.1 Precipitation - From solute atoms to precipitate phases

The main underlying cause of the great strengthening potential of age-hardening Al alloys is the high density of nano-sized precipitate phases which forms after thermal ageing. The mechanism behind their strengthening contribution will become clear later in this chapter, but for now their formation and subsequent phase transformation will be treated.

It was first in 1906 that the positive effect of applying heat treatments to Al alloys was discovered by Alfred Wilm, and the observations were published a few years later [13]. His alloys, containing Mg and Cu as alloying elements (solutes), had exhibited improvements in hardness after being kept for a longer time at room temperature, which was due to the formation of atomic clusters [14]. After the discovery of this effect, the general age-hardening phenomenon was later explained based on the formation of microscopic precipitate phases [15]. Since its discovery over 100 years ago, the effect of thermal ageing and mechanical processing of Al alloys – together denoted as thermomechanical processing (TMP) – has become well-understood and widely applied in large-scale industries. As an example, Figure 2.1 shows a generic industrial TMP route for an extruded 6xxx alloy. The microstructure of the material will change in all processing steps, with consequences for final material properties.

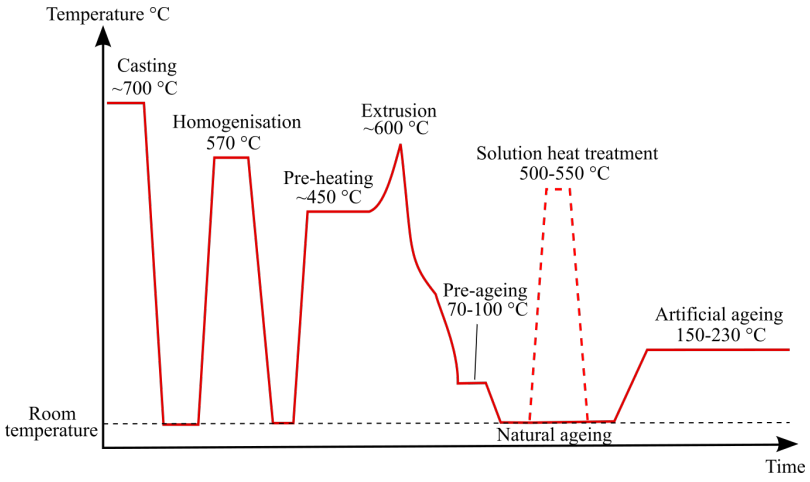

Figure 2.1. An example of a thermomechanical process applied to an extruded 6xxx alloy. For alloys with scientific purposes, a solution heat treatment step with a strictly controlled temperature is usually added after extrusion (dashed).

Whereas the first few TMP steps indicated in Figure 2.1 are mainly used to form and shape the material, the final two, solution heat treatment (SHT) and artificial

ageing (AA), are particularly crucial for the formation of precipitate phases. The precipitates form by substitutional diffusion through solid-solid phase transformations, which start with nucleation and growth mechanisms. The treatment of these classical topics are fundamental in physical metallurgy, and described in books such as [12, 16, 17]. The solubility of alloying elements in Al is limited, and varies for different elements. When the concentration of an alloying element is higher than its solubility, stable secondary phases form in order to minimise the total energy of the system. In the SHT step, the temperature is set above the solvus temperature, but below the solidus temperature of Al. This dissolves any structures rich in solutes, and distributes these uniformly in the face-centred cubic (fcc) Al matrix. The process occurs rather fast, as dissolution and diffusion are accelerated by an increased concentration of *vacancies* – point defects where atoms are missing from fcc lattice sites in the Al matrix, see Figure 2.2. Vacancies occur naturally in all crystalline materials. At any given temperature, up to the melting point of the material, there is an equilibrium concentration, i.e. a ratio of vacant lattice sites to those containing atoms. The temperature dependence is usually expressed as [16]

$$N_{\mathrm{v}} = N \cdot e^{-\Delta G_{\mathrm{v}}/\mathrm{k_b}T}, \tag{2.1}$$

where N_{v} is the vacancy concentration, ΔG_{v} is the energy required for vacancy formation, $\mathrm{k_b}$ is the Boltzmann constant, T is the absolute temperature, and N is the concentration of atomic sites. Near the melting point of some metals, the vacancy concentration can be as high as 1:1000, i.e. that 1 in 1000 lattice sites are unoccupied [18].

In the subsequent step the alloy is usually rapidly cooled (quenched), and in this process a high concentration of vacancies is said to be *quenched-in*. At this point, the solutes are in a state of non-equilibrium referred to as a supersaturated solid solution (SSSS) [16]. The solutes in the SSSS diffuse via the presence of the quenched-in vacancies by substitutional diffusion, and may be enhanced through effects such as the vacancy pump mechanism [19]. Eventually, solute enriched regions or atomic clusters are formed (nucleated). The growth of clusters occurs by statistical fluctuations towards a critical size of nucleation, or they dissolve, again reduced to individual atoms [17]. The nucleation is driven by a negative free energy change, and the subsequent growth is determined by the balance of two opposing forces [16, 17]: (i) volume free energy and (ii) precipitate-matrix interfacial energy. Assuming that the nuclei are spherical, this is expressed through the classical equation

$$\Delta G_{\text{total}} = -\frac{4}{3}\pi r^3 \Delta G_{\text{b}} + 4\pi r^2 \gamma. \tag{2.2}$$

Here, ΔG_{total} is the total change in free energy, ΔG_{b} is the bulk free energy of the secondary phase, r is the radius of the spherical nucleus, and γ is the interfacial energy. It is seen that the bulk free energy term causes a reduction in the energy of the system, whereas the interfacial energy term leads to an increase in energy.

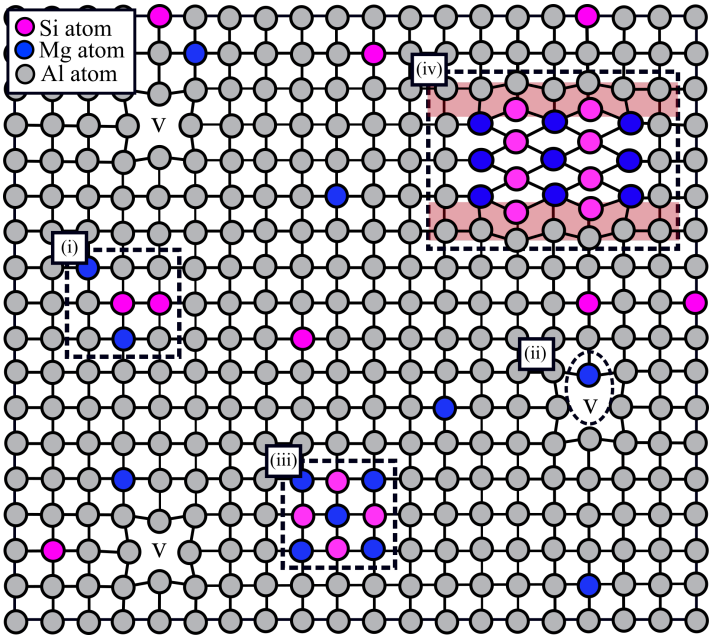

Figure 2.2. Schematic of the fcc Al matrix as seen from the $[001]_{\text{Al}}$ zone axis (ZA) showing vacancies (v), randomly distributed solutes, an atomic cluster (i), a solute-vacancy pair (ii), a precipitate phase with a fully coherent interface (iii), and a precipitate phase with a semi-coherent interface (iv). Red regions indicate significant strain at the precipitate-matrix interface. The precipitate structures are arbitrarily chosen.

Precipitation is the formation of a phase that differs in composition and crystal structure from the surrounding (Al) matrix. It forms due to long-range diffusion of solute atoms, through nucleation and growth. Equilibrium phases, as given by the alloy's equilibrium phase diagram, do not form directly. Instead, it has been found that precipitates form in a sequence, with several metastable precipitate phases forming sequentially towards the equilibrium crystal structure. The main explanation for this sequential nature is due to the precipitate-matrix interfacial energy term in Eq. 2.2: $4\pi r^2\gamma$. Equilibrium phases usually have high interface energies because they form *incoherent* interfaces. All precipitates start out small, which

implies a high ratio of interface area to volume, making interface energy the dominant term. This represents a large energy barrier. Therefore, in order to make progress towards the final stable structure, a series of metastable, (semi-)coherent precipitate phases form instead, see Figure 2.2. The (semi-)coherent interfaces have lower interface energies, as generally fewer atomic bonds are broken with respect to the surrounding Al matrix. Therefore, the energy barrier can more easily be overcome. The most coherent precipitates may induce a relatively high strain in the matrix [20], but have a low enough interface energy to still be most beneficial at early stages of precipitation, as they also represent a relatively high bulk energy. After the precipitate has grown large, the balance shifts and coherency loses importance. This favours a transition to phases of lower bulk energy but which have poorer coherencies with the matrix.

At intermediate temperatures ($150 - 230\,^{\circ}\mathrm{C}$), as applied in the AA step, the precipitation is enhanced because the atomic diffusivity increases. Hence, the precipitates grow and equilibrium phases form eventually when the bulk free energy is large enough to stabilise them. The diffusivity depends on the alloying elements. For example, in the fcc Al matrix, the diffusivity, D, for Si, Mg, and Cu are ordered as: $D_{\mathrm{Si}} > D_{\mathrm{Mg}} > D_{\mathrm{Cu}}$ [21, 22].

2.1.1 The precipitation sequence of Al-Mg-Si alloys

In wrought 6xxx series Al alloys the total addition of precipitate forming elements Mg and Si is typically <2 at.%. The Al–Mg–Si alloy system has a number of possible precipitate phases. The types of precipitates that form, their physical dimensions, and their dispersion in the Al matrix depend on alloy composition (e.g. Si:Mg ratio) and TMP parameters, including: natural ageing (NA) under storage, ageing time/temperature, heating/cooling rates, and deformation. All precipitates in this alloy system grow and keep the alignment along $\langle 100 \rangle_{\mathrm{Al}}$, which is the main growth and coherency direction. As a consequence, the precipitates have needle/lath/rod morphologies extending along $\langle 100 \rangle_{\mathrm{Al}}$ directions, see Figure 2.3. The established precipitation sequence is given as [23, 24]

$$\begin{aligned} \mathrm{SSSS} &\rightarrow \text{solute clusters} \rightarrow \text{GP-zones} \\ &\rightarrow \beta'' \rightarrow \beta', \mathrm{U1}, \mathrm{U2}, \mathrm{B}' \rightarrow \beta, \mathrm{Si}. \end{aligned} \tag{2.3}$$

An overview of the compositions, crystal structures, and orientation relationships (ORs) for the different main precipitate phases of the Al-Mg-Si system is given in Table 2.1. Figure 2.3a shows the typical microstructure of an Al–Mg–Si alloy at peak strength. Most precipitates observed are of β'' type, and they are seen forming

a high density of short precipitates with characteristic strain contrast (dark lines) running parallel to the main growth directions. The β'' phase is the most important precipitate for strengthening in 6xxx alloys as it has an excellent coherency with the Al matrix. Its secondary coherency directions are along $\langle 310 \rangle_{\mathrm{Al}}$ and $\langle 320 \rangle_{\mathrm{Al}}$ which together with $\langle 100 \rangle_{\mathrm{Al}}$ usually define the precipitate–matrix interfaces, see Figure 2.4a.

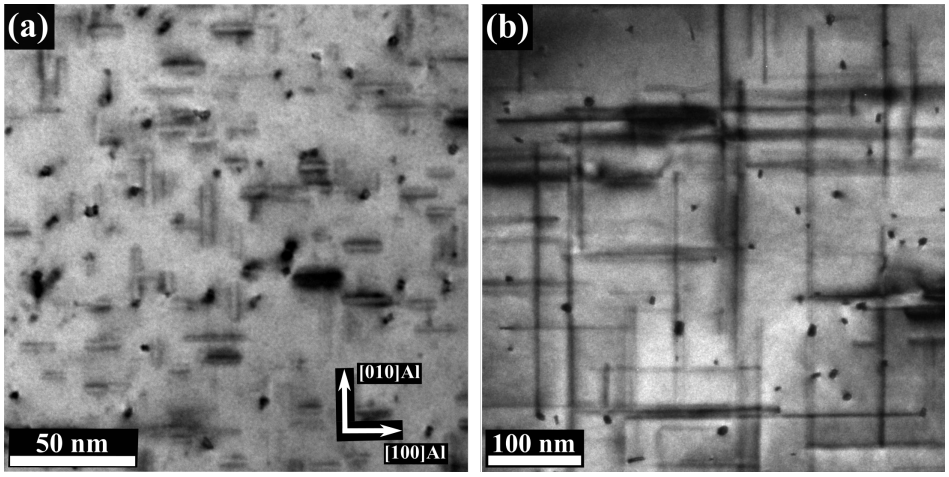

Figure 2.3. Bright-field TEM images of the microstructure of a 6082 alloy at (a) peak strength and (b) a significantly overaged condition.

Upon further ageing, there occurs a loss in strength as one reaches overaged conditions of the material. Here, precipitates continue to grow and coarsen, and new phases, often referred to as post-β'' phases, are formed. The density of precipitates usually drops quite significantly, as larger precipitates grow at the expense of smaller ones, see Figure 2.3b. The most common of post-β'' phases is the hexagonal β' phase. It forms as longer, thicker, and less coherent rods than the β'' phase, and usually has a rounded cross-sectional shape, see Figure 2.4c.

The details of how overaged precipitate phases form from a microstructure mainly consisting of β'' or other phases existing at peak strength are still not known. What *is* known, however, is that the transition to overaged precipitate structures entails the establishment of an ordered, ($[001]_{\mathrm{Al}}$ projected) hexagonal Si network, that permeates all post-β'' precipitate structures [25, 26]. Regarding the transformation of phases there are two main possibilities: (i) internal transformations, which require coordinated and collective shifts of many atoms, and (ii) external nucleation of a new phase on the interface of an existing precipitate. It seems most plausible that a combination of the two is occurring, starting with case (ii). β'' precipitates normally become rounder upon overageing, and start to include fragments

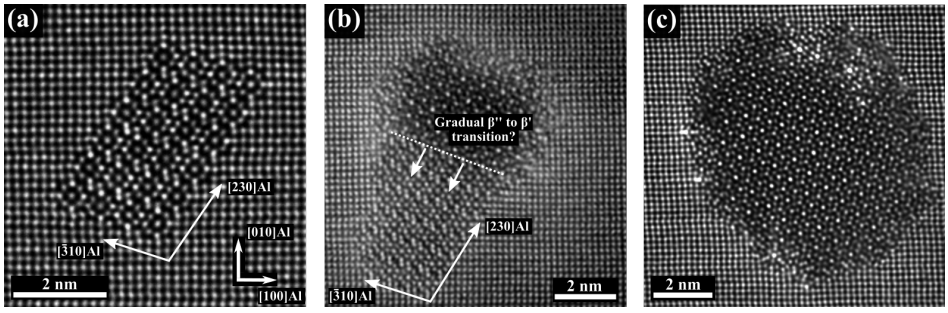

Figure 2.4. HAADF-STEM lattice images of the most common precipitate phases in Al-Mg-Si alloys. (a) A pure β'' phase precipitate, (b) a precipitate with near 50/50 mix between β'' and β' phases, and (c) a relatively pure β' phase precipitate. It is still not known how the β'' to β' phase structural transition occurs.

and sub-structures of post-β'' phases hosting the Si network, which are predominantly found at the precipitate-matrix interface. Subsequently, the transformation of the remaining parts of the β'' structure may progress by structural changes occurring locally, which slowly takes over the full precipitate structure, see Figure 2.4b. There are many structural similarities between the different Al-Mg-Si phases, which are discussed in the provided references of Table 2.1. From an energy point of view, this is important for the plausibility of case (i) phase transitions.

2.1.2 Additions of Cu to Al-Mg-Si alloys

Cu additions in Al-Mg-Si alloys are frequently used to increase the age-hardening response, and to form a higher number density of smaller precipitates with improved thermal stability [27–31]. The introduction of Cu ($\gtrapprox 0.4$ at.%) leads to a more complex precipitation sequence (cf. precipitation sequence 2.3), that can be stated as [27, 32–35]

$$\begin{aligned} \text{SSSS} &\rightarrow \text{solute clusters} \rightarrow \text{GP-zones} \\ &\rightarrow \beta'', \text{L} \rightarrow \beta'_{\text{Cu}}, \text{S}, \text{Q}', \text{C} \rightarrow \text{Q}, \text{Si}. \end{aligned} \tag{2.4}$$

Figure 2.5 presents HAADF-STEM lattice images of the main Cu-containing phases, and Table 2.2 presents an overview of the compositions, crystal structures, and ORs for the different precipitate phases in the Al-Mg-Si-Cu system. Despite the increased complexity, the precipitates still form an ordered Si network on overageing. In fact, all metastable precipitate phases in the Al-Mg-Si(-Cu) system are structurally related due to this common network of Si atomic columns along the precipitate lengths [32]. In $\langle 100 \rangle_{\text{Al}}$ projection, this network exhibits a near

hexagonal symmetry with $a = b \approx 4\,\text{Å}$. For the β'' phase, the network is partly fragmented due to a high coherency with the Al matrix [36]. The different types of precipitates are distinguished based on how their Al, Mg, and Cu atomic columns are positioned with respect to the Si network columns. Al and Mg are always positioned in-between the Si network columns, and Cu is positioned in-between (Q′ phase and C phase), or replacing parts of the Si network columns (β'_{Cu} phase) [37]. The β'_{Cu} phase is somewhat special in the sense that this phase is very rarely observed forming full crystal unit cells. However, sub-units of the β'_{Cu} phase are common at precipitate-matrix interfaces, see e.g. Figure 2.5d. Precipitate atomic columns can also exhibit variations in atomic modulation and/or mixed element occupancy. In the precipitation sequence 2.4, the frequently used notations QP and QC seen in the literature are not included, being instead interpreted as fragments of Al-Mg-Si(-Cu) phases on the Si network and the β'_{Cu} phase, respectively. The details of this discussion are presented in the reviews conducted by Saito *et al.* [25] and Andersen *et al.* [26]. In this PhD work, the effect of low Cu additions in Al-Mg-Si alloys has been the topic of several papers, including Paper **II**, and Papers **IV-VI**.

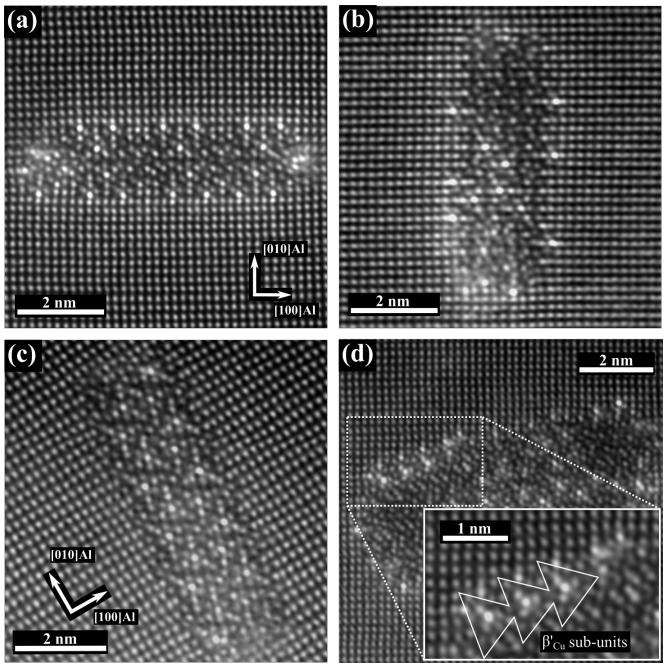

Figure 2.5. HAADF-STEM lattice images of the main Al-Mg-Si-Cu precipitate phases. (a) C phase, (b) L phase, (c) Q′ phase, and (d) fragmented Q′ phase precipitate with sub-units of β'_{Cu} phase at the matrix-precipitate interface, highlighted in the insert.

Table 2.1. Crystal structure data for Al-Mg-Si precipitate phases. The notation $\mathbf{a}_{\mathrm{A}}$, $\mathbf{b}_{\mathrm{A}}$, and $\mathbf{c}_{\mathrm{A}}$ for a given phase A denotes the main crystallographic vectors defining the unit cell of phase A.

Phase	Alternative labelling	Composition	Space group	Unit cell parameters [Å]	Unit cell OR	Reference(s)
β''	-	$Al_2Mg_5Si_4$	C2/m	$a = 15.16$, $b = 4.05$, $\beta = 105.3°$, $c = 6.74$	$\langle 230\rangle_{\mathrm{Al}} \parallel \mathbf{a}_{\beta''}$, $\langle 001\rangle_{\mathrm{Al}} \parallel \mathbf{b}_{\beta''}$, $\langle 130\rangle_{\mathrm{Al}} \parallel \mathbf{c}_{\beta''}$	[38, 39]
β'	-	$Mg_6Si_{3.33}$	$P6_3$	$a = b = 7.15$, $c = 4.05$, $\gamma = 120°$	$\langle 130\rangle_{\mathrm{Al}} \parallel \mathbf{a}_{\beta'}$, $\langle 001\rangle_{\mathrm{Al}} \parallel \mathbf{c}_{\beta'}$	[40]
β	-	Mg_2Si	$Fm\bar{3}m$	$a = 6.35$	Incoherent	[41]
U1	Type A	Al_2MgSi_2	$P\bar{3}1m$	$a = b = 4.05$, $c = 6.74$	$\langle 001\rangle_{\mathrm{Al}} \parallel \mathbf{a}_{\mathrm{U1}}$, $\langle 3\bar{1}0\rangle_{\mathrm{Al}} \parallel \mathbf{c}_{\mathrm{U1}}$	[42, 43]
U2	Type B	AlMgSi	Pnma	$a = 6.75$, $b = 4.05$, $c = 7.94$	$\langle 130\rangle_{\mathrm{Al}} \parallel \mathbf{a}_{\mathrm{U2}}$, $\langle 001\rangle_{\mathrm{Al}} \parallel \mathbf{b}_{\mathrm{U2}}$	[43, 44]
B′	Type C	$Al_3Mg_9Si_7$	$P\bar{6}$	$a = b = 10.40$, $c = 4.05$, $\gamma = 120°$	$\langle 150\rangle_{\mathrm{Al}} \parallel \mathbf{a}_{\mathrm{B}'}$, $\langle 001\rangle_{\mathrm{Al}} \parallel \mathbf{c}_{\mathrm{B}'}$	[43, 45, 46]
Si network	QP	Varies with phase(s)	Hexagonal	$a = b = 3.93$, $c = 4.05$	Varies with phase(s)	[32, 35]

Table 2.2. Crystal structure data for Al-Mg-Si-Cu precipitate phases. The notation $\mathbf{a}_\mathrm{A}$, $\mathbf{b}_\mathrm{A}$, and $\mathbf{c}_\mathrm{A}$ for a given phase A denotes the main crystallographic vectors defining the unit cell of phase A.

Phase	Alternative labelling	Composition	Space group	Unit cell parameters [Å]	Unit cell OR	Reference(s)
β'_Cu	QC	$Al_3Mg_3Si_2Cu$	$P\bar{6}2m$	$a = b = 6.90$, $c = 4.05$, $\gamma = 120°$	$\langle 130\rangle_\mathrm{Al} \parallel \mathbf{a}_{\beta'_\mathrm{Cu}}$, $\langle 001\rangle_\mathrm{Al} \parallel \mathbf{b}_{\beta'_\mathrm{Cu}}$	[32, 47][a]
Q′	-	$Al_xMg_{12-x}Si_7Cu_2$[b]	$P\bar{6}$	$a = b = 10.32$, $c = 4.05$, $\gamma = 120°$	$\langle 150\rangle_\mathrm{Al} \parallel \mathbf{a}_{Q'}$, $\langle 001\rangle_\mathrm{Al} \parallel \mathbf{c}_{Q'}$	[39, 48]
Q	-	$Al_xMg_{12-x}Si_7Cu_2$[b]	$P\bar{6}$	$a = b = 10.39$, $c = 4.05$, $\gamma = 120°$	Incoherent	[39, 48, 49]
S	QP1	Varies with phase(s)	-	-	Varies with phase(s)	[35, 50]
C	-	$AlMg_4Si_3Cu$	$P2_1$	$a = 10.32$, $b = 4.05$, $\beta = 100.9°$, $c = 8.10$	$\langle 010\rangle_\mathrm{Al} \parallel \mathbf{c}_\mathrm{C}$ $\langle 001\rangle_\mathrm{Al} \parallel \mathbf{b}_\mathrm{C}$	[51]
L	QP2	Varies with phase(s)	-	Contains fragments of Q′ phase and C phase	At least one interface coh. with $\langle 100\rangle_\mathrm{Al}$	[50, 52]

[a] One of the cited papers studies the isostructural Ag-containing variant of this phase.
[b] $x = 6$ applies for the Q′ phase and $x = 3$ corresponds to the Q phase. For the Q phase some of the Al sites in the Q′ structure are replaced by Mg.

2.2 Strengthening of Al alloys

There exist several different measures for the mechanical strength of a material. The most common ones used are inferred from material tensile tests and the resulting stress-strain curves, as shown schematically in Figure 2.6. Tensile tests are conducted by stretching a material at a defined speed while recording the value of the tensile stress (force per area) and the corresponding strain (relative elongation of the sample). The maximum stress that the material can withstand while being stretched before it eventually fractures is called the ultimate tensile strength (UTS). A more useful measure is the yield strength (YS), σ_y, which is the stress that defines the transition from the material's elastic to the plastic deformation regime. When the material has experienced a stress above the yield point, the material is permanently deformed, and will not relax back to zero strain when relieved of this stress. The integrated area under the stress-strain curve is an indication of the material's energy absorption capacity, also referred to as material toughness.

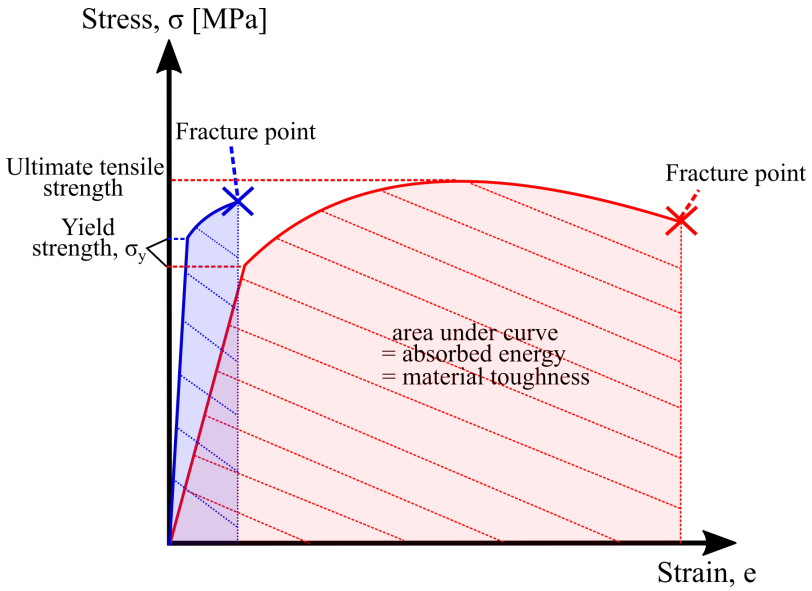

Figure 2.6. Typical engineering stress–strain curves of a brittle (blue) and ductile (red) material.

2.2.1 Dislocations

Intuitively, one might envision plastic deformation and material fracture occurring due to the breaking of many atomic bonds at some atomic plane in the material. This does not occur, however, as the chemical bonds between atoms in a material are very strong. Plastic flow in crystals occurs by propagation of very small dis-

placements, which are due to imperfections existing in the crystal lattice, causing relatively abrupt changes in the local arrangement of atoms. These imperfections are known as *dislocations*. The crystal structure restricts both the magnitude and direction of the displacements, and the planes on which they propagate. The movement of dislocations causes atoms to slide over each other, referred to as glide or slip. Lines separating slipped and non-slipped regions are called dislocation lines, the displacements are called Burgers vectors, and the planes of propagation are called glide planes. A dislocation is defined by its line vector, $\vec{t}$, which may vary along its length, and its Burgers vector, $\vec{b}$, which must be constant along its length. When $\vec{t} \perp \vec{b}$, the dislocation is called an edge dislocation. Crystallographically, the edge dislocation is equivalent to inserting or removing a half-plane of atoms in the crystal, see Figure 2.7. Therefore, $\vec{b}$ is given by the crystal structure, and propagation of this quantised displacement on crystallographic glide planes causes plastic flow of the crystal. For the fcc crystal structure of Al, the dislocations normally have Burgers vectors $\vec{b} = \frac{1}{2}\langle 110 \rangle_{\mathrm{Al}}$, which propagate on close-packed $\{111\}_{\mathrm{Al}}$ planes [53–56]. Due to the symmetry of the fcc crystal structure, there are 12 combinations of such vectors and planes, and therefore in total 12 different slip systems. Plastic deformation is therefore generally achieved by a combination of these 12 slip systems.

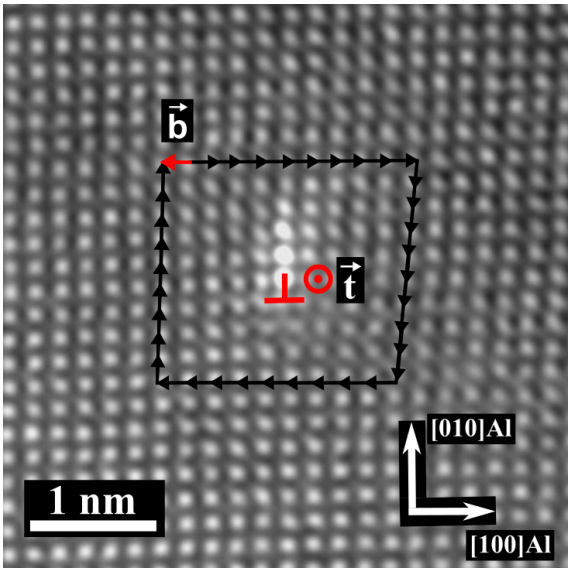

Figure 2.7. HAADF-STEM lattice image of an edge dislocation observed in a 6082 Al-Mg-Si(-Cu) alloy. The Burgers vector, $\vec{b}$, is defined through the Burgers loop around the dislocation line, $\vec{t}$. The atomic columns near the edge dislocation are brighter than the other corresponding columns due to partial occupancy of Cu.

Figure 2.7 also shows how the Burgers vector is defined through the Burgers loop around the dislocation line. Other types of dislocations exist as well, e.g. the screw dislocation, which has $\vec{t} \parallel \vec{b}$. The glide plane of a dislocation is defined by $\vec{t} \times \vec{b}$, i.e. the plane that contains both vectors. This implies that edge dislocations are more limited in terms of glide than screw dislocations. In reality, however, dislocations generally curve and bend, as seen in Figure 2.8, which means that they are of mixed character. Dislocations produce surrounding strain fields in the lattice, which affect how they interact with different obstacles in the material microstructure, such as solutes, vacancies, atomic clusters, precipitate phases, or other dislocations.

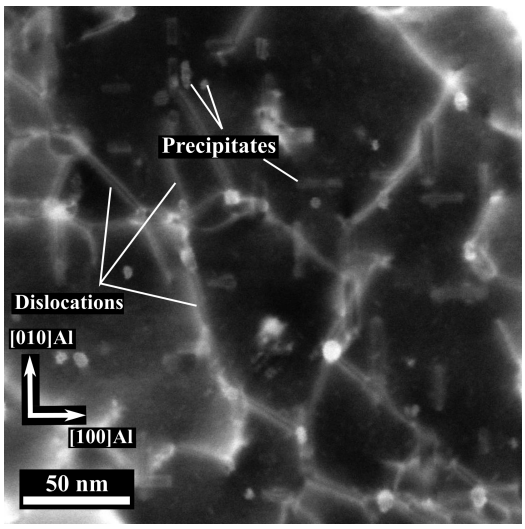

Figure 2.8. ADF-STEM image showing the deformation microstructure of a heavily deformed 6101 Al-Mg-Si alloy. Dislocation strain fields and precipitates are visible (highlighted).

2.2.2 Strengthening contributions

Several strengthening mechanisms are operative at room temperature for Al alloys, with the most important being that due to the precipitates, σ_{p}. In addition, there are contributions from solute solution strengthening, σ_{ss}, grain boundary (GB) strengthening, σ_{GB}, dislocation strengthening, σ_{disloc}, as well as the intrinsic strength of pure Al, σ_{i}. In the following, these different contributions to strengthening will be treated briefly. The contributions are typically added linearly, giving the material yield strength as [57, 58]:

$$\sigma_{\mathrm{y}} = \sigma_{\mathrm{i}} + \sigma_{\mathrm{GB}} + \sigma_{\mathrm{disloc}} + \sigma_{\mathrm{ss}} + \sigma_{\mathrm{p}}. \tag{2.5}$$

Grain boundary strengthening

GBs constitute an insurmountable obstacle for dislocations moving through the crystal lattice. When approaching GBs, they tend to pile up, causing stress build-up in the adjacent grain. Eventually, this stress activates new dislocation sources in the neighbouring grain, causing deformation. The strengthening contribution has been observed to increase with decreasing grain size as expressed by the well-known Hall-Petch empirical relation [12, 56]

$$\sigma_{\mathrm{GB}} = \sigma_0 + \frac{k_{\mathrm{y}}}{\sqrt{d}}. \tag{2.6}$$

Here, σ_0 is a materials constant related to the starting stress for dislocation movement, k_{y} is a strengthening coefficient specific to different materials, and d is the average grain size diameter. With typical grain sizes in extruded Al alloys being on the order of a few $\mu\mathrm{m}$, this usually represents a small contribution. For severely plastically deformed (SPD) materials, however, where grain sizes can be on the order of $100\,\mathrm{nm}$ [59–61], this can be much more significant.

Dislocation strengthening

From the point of view of the deformation microstructure, a typical tensile test involves several different stages. For a fcc single crystal, the initial stage involves slip occurring on a single slip system, i.e. the one with the highest resolved shear stress. Subsequently, slip starts to occur on multiple slip systems, and interactions between moving dislocations lead to a complex, entangled microstructure of increasing dislocation density, see Figure 2.8. Additional stress is then required to force dislocations to pass each other, as the resulting steps on the dislocation lines will not glide as easily. The material is said to *work-harden*. Dislocations can also annihilate in order to reduce the free energy of the system, which is a result of long range elastic interactions between dislocations. All dislocation models qualitatively predict the same contribution to material strength [53, 62]

$$\sigma_{\mathrm{disloc}} = \alpha G |\vec{b}| \sqrt{\rho}. \tag{2.7}$$

Here, α is a constant (≈ 0.3), G is the material shear modulus, and ρ denotes the dislocation density.

Solid solution strengthening

The solutes dispersed throughout the Al matrix will impede dislocation movement and strengthen the material [63, 64]. The stress field around solute atoms exerts a force on dislocations that must be overcome for plastic flow to occur. The force arises from four main interactions [64]: size misfit, modulus misfit, electrostatic interaction, and stacking-fault interaction. Various models exist, but a power law of the solute concentration is most common [63, 64]. If more than one solute species is present in the alloy, the total strengthening contribution is usually calculated as a linear sum of each element [63, 65, 66]

$$\sigma_{\mathrm{ss}} = \sum_i k_i C_i^{\mathrm{r}}, \tag{2.8}$$

where the concentrations of each species, c_{i}, are weighted by drag-coefficients k_{i} [63]. Examples of values used are: 66.3 $\mathrm{MPa/wt.\%}$, 29.0 $\mathrm{MPa/wt.\%}$, and 46.4 $\mathrm{MPa/wt.\%}$, for k_{Si}, k_{Mg}, and k_{Cu}, respectively [57]. As previously noted are total additions usually < 2 wt.%. Assuming a perfect dispersion of 2 wt.% total alloying additions and $r = 2/3$ then gives a range of $46 - 105$ MPa in contribution to alloy strength.

A clear example of the interaction between solute elements and edge dislocations is provided in Figure 2.7. It is here seen that the atomic columns near the edge dislocation appear considerably brighter than the other corresponding columns. From the alloy composition it can be stated with high certainty that this is due to partial occupancy of Cu. Cu atoms have a negative size misfit in the Al matrix, and are here seen located in the compressive stress field of the dislocation. Cu ($Z_{\mathrm{Cu}} = 29$) is observed with a higher contrast than the other elements Mg ($Z_{\mathrm{Mg}} = 12$), Al ($Z_{\mathrm{Al}} = 13$), and Si ($Z_{\mathrm{Si}} = 14$) due to the $Z^{1.7-2.0}$ atom column scattering power at high angles for HAADF-STEM imaging [67–69].

Precipitation strengthening

The main interaction that determines the mechanical properties of age-hardenable Al alloys is that occurring between precipitates and moving dislocations. There are two main types of precipitate-dislocation interactions: (i) the mobile dislocations pass through the precipitate (shearable), or (ii) they bypass the precipitate, e.g. via the Orowan looping process (non-shearable) [65, 70, 71]. Whether a particular precipitate is sheared or bypassed depends on several factors, where interface coherence and precipitate size are the most important. As noted, during ageing the precipitates typically start out as small and coherent phases in the Al matrix, and gradually evolve into larger and coarser phases with reduced coherency. Small

and coherent precipitates are normally shearable, while larger and more incoherent precipitates are usually bypassed. For instance, there exists strong evidence that β'' is generally shearable [72–75]. In overaged conditions, the precipitates are to a larger extent non-shearable, e.g. β' [76], meaning that they remain undeformed while the matrix around them is deformed. Several studies have made attempts to estimate the value of the critical dimension that determines the transition point between shearable and non-shearable precipitates for the various precipitate phases existing in the Al-Mg-Si(-Cu) system, e.g. [74, 76]. The critical dimension, r_{c}, where this transition occurs is important in order to model the strength in these alloys, as the obstacle strength, $F(r)$, is usually separated into a weak (shearable) ($r \leq r_{\mathrm{c}}$) and strong (bypassed) ($r > r_{\mathrm{c}}$) regime.

Despite the complexity of the underlying strengthening mechanisms, many yield strength models developed for Al-Mg-Si-Cu alloys capture the general evolution of material strength with ageing to a reasonable extent. The crudest models assume a single precipitate type approximated as equivalent spherical volumes, whereas more advanced models also take into account the $\langle 100 \rangle_{\mathrm{Al}}$ oriented, rod-/lath-shaped nature of the precipitates and their size distribution [57, 58, 65, 70, 71, 77–82]. Most models build on the assumption by Deschamps and Brechet [78], which states that σ_{p} can be generally expressed as:

$$\sigma_{\mathrm{p}} = \frac{M\bar{F}}{bl} = \frac{M}{bl}\int_0^\infty f(r)F(r)\mathrm{d}r \tag{2.9}$$

$$= \frac{M}{bl}\left(\int_0^{r_{\mathrm{c}}} f(r)F_{\mathrm{weak}}(r)\mathrm{d}r + \int_{r_{\mathrm{c}}}^\infty f(r)F_{\mathrm{strong}}(r)\mathrm{d}r\right). \tag{2.10}$$

Here, M is the Taylor factor, $\bar{F}$ is the mean obstacle strength, and l is the effective mean distance between precipitates along the dislocation line. $f(r)$ and $F(r)$ denote the precipitate size distribution and the obstacle strength for a precipitate of radius r, respectively. The differences between the applied models mainly relate to how the precipitate geometry and distribution are taken into account, as well as the obstacle strength, $F(r)$.

The classic case of precipitation strengthening is shown in Figure 2.9, where a dislocation is pinned by a series of obstacles. Under the influence of an applied shear stress τ, the dislocation curves into an arc. Each of the dislocation segments on either side of an obstacle exerts a force, $\vec{\Gamma}$, that acts along the tangent of the segment, forming an angle, ϕ, between the line tensions. Force balance then requires that the obstacle exerts a force $\vec{F} = \vec{\Gamma}_1 + \vec{\Gamma}_2$ back on the dislocation. The fundamental equation for precipitation strengthening is given as [53, 54, 83]

$$|\vec{F}| = 2|\vec{\Gamma}|\cos(\phi/2)\,, \tag{2.11}$$

which cannot become greater than $2|\vec{\Gamma}| = 2\Gamma$.

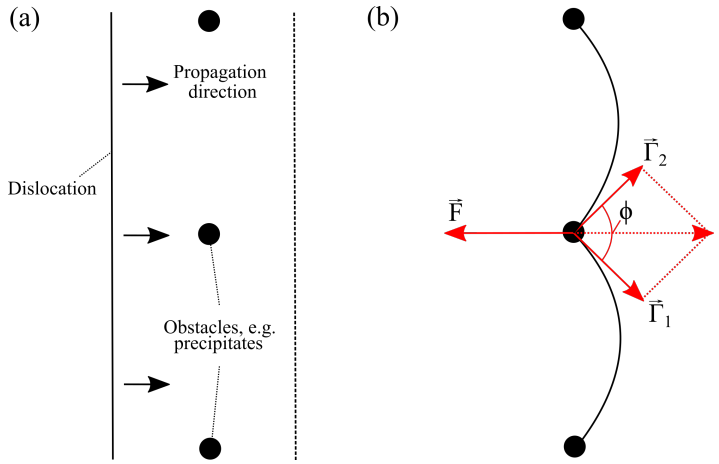

Figure 2.9. Schematic of dislocation pinning and resulting forces acting on an obstructed dislocation (a) before and (b) after pinning.

By using Kocks statistics [70, 71], which are based on numerical line-tension simulations of a dislocation gliding through an array of obstacles, combined with recent line-tension simulations [84, 85], the precipitate contribution to the strength, σ_{p}, can be expressed as [81]

$$\sigma_{\mathrm{p}} = M\tau = 0.9\mu b\sqrt{n}\bar{f}^{\frac{3}{2}}\left(1 - \frac{1}{6}\bar{f}^{5}\right). \tag{2.12}$$

Here, M is the Taylor factor, τ is the critical resolved shear stress, μ is the shear modulus of the Al matrix, and n is the density of obstacles per area slip plane. $\bar{f} = \bar{F}/\mu b^2 = \cos(\phi_{\mathrm{c}}/2)$ is the non-dimensional mean obstacle strength, where $\bar{F}$ is the mean obstacle strength and ϕ_{c} is the obstacle breaking angle of the dislocation. This framework and expression were used in Paper **VI** in this thesis, and was found to be in good agreement with experimental results.

2.3 Electrical properties of Al alloys

A defining characteristic of metals is that they exhibit high conductivity, as there are many available electron energy levels near the Fermi level [86]. The outer shell of electrons freely dissociate from their parent atoms and form a 'sea' of electrons that may travel through the positive ionic lattice under the application of an external electric potential (voltage). Classical treatments of the conductivity of pure metals as first given by the Drude model in 1900 show that it may be expressed as [86, 87]

$$\begin{aligned} \vec{J} &= \sigma \vec{E}, \\ \vec{J} &= \left(\frac{ne^2\tau}{m_{\mathrm{e}}^*} \right) \vec{E}, \end{aligned} \tag{2.13}$$

where $\vec{J}$ is the current density, σ is the electrical conductivity, and $\vec{E}$ is the electrical field. The conductivity may be calculated from: the density of conduction electrons, n, the elementary charge of electrons, e, the mean free time, τ, between collisions with the ionic lattice, and the effective mass of the conduction electrons, m_{e}^*. The Drude model was later supplemented with the results of quantum mechanics in 1933 by Arnold Sommerfeld and Hans Bethe, mainly by taking into account Fermi–Dirac statistics which apply for electrons, and which lead to the Drude–Sommerfeld model [86, 87]. The electrical resistivity, ρ, is given by the reciprocal relationship $\rho = \sigma^{-1}$. The mean free time, τ, can be expressed as

$$\tau = \frac{\lambda}{v_{\mathrm{F}}}, \tag{2.14}$$

where λ is the mean free path of electrons and v_{F} is the Fermi velocity of the conduction electrons. In pure Al, this length is about $\lambda_{\mathrm{Al}} \approx 14\,\mathrm{nm}$ and the mean free time is $\tau \approx 7.2 \cdot 10^{-15}$ s. Electrical resistivity is caused by the scattering of conducting electrons. From λ_{Al} the conducting electrons on average thus travel about 35 interatomic distances in Al between each scattering event. One of the main causes of scattering is due to electron-phonon collisions, i.e. the thermal vibrations of the ionic lattice. This is the main cause of the temperature dependence of resistivity, which is normally approximated by a linear dependence

$$\rho_{\mathrm{T}} = \rho_0[1 + \alpha(T - T_0)]. \tag{2.15}$$

Here, α is the temperature coefficient [K^{-1}], T_0 is a fixed reference temperature (often taken as room temperature), and ρ_0 is the resistivity at T_0. This linear approximation holds well for most metals, particularly at higher temperatures. Table 2.3 lists the electrical properties of selected high conductivity metals. Cu, specifically annealed Cu, is used as an international standard reference due to its high conductivity and established usage. The conductivity of other materials is often expressed as a % of the international annealed copper standard (IACS), at $5.80 \cdot 10^7$ S/m. Pure Al also has a high conductivity at about 65%IACS. High conductivity in conductor applications is crucial for reducing energy losses during power transmission ($\propto I^2R$, I = current and $R = \rho\frac{l}{A}$ resistance of a conductor with cross-section area, A, and length, l).

Table 2.3. Electrical properties of selected high conductivity metals [87, 88].

Metal	Resistivity, ρ [$\Omega \cdot$ m] at 20 °C	Conductivity, σ [S/m] at 20 °C	Temperature coefficient, α [K^{-1}]
Ag	$1.59 \cdot 10^{-8}$	$6.30 \cdot 10^7$	0.00380
Cu	$1.68 \cdot 10^{-8}$	$5.96 \cdot 10^7$	0.00404
Annealed Cu	$1.72 \cdot 10^{-8}$	$5.80 \cdot 10^7$	0.00393
Au	$2.44 \cdot 10^{-8}$	$4.11 \cdot 10^7$	0.00340
Al	$2.65 \cdot 10^{-8}$	$3.77 \cdot 10^7$	0.00390

There are many important conductor applications which also put high demands on mechanical performance. Examples are overhead power lines and subsea/offshore cables. In these applications, the material is subjected to high mechanical stresses, both constant and cyclical. This has consequences for properties such as creep and fatigue, both of which may ultimately cause material failure. In several km long subsea cables – several 10s of km offshore – this would entail a huge economic cost to replace. There exist different approaches for improving on mechanical properties while still achieving high conductivity. In overhead power lines, this is conventionally obtained using pure Al conductors reinforced by steel cores, or by using carbon cores [89]. However, multi-material solutions may have several drawbacks depending on the application, e.g. increased total weight and physical dimensions, or increased susceptibility to corrosion. It may also require increased costs in production. It is therefore of interest to develop alloys that both exhibit high conductivity and strength, without degrading other properties such as creep and fatigue resistance. This can for instance be achieved using lean 6xxx series Al alloys, which can be processed to exhibit medium yield strengths ($\approx 120 - 260\,\mathrm{MPa}$) while maintaining high conductivity ($\approx 54 - 62\%$IACS) [90–92]. Compared to pure metals, alloys have several additional microstructural features that may cause increased scattering of conducting electrons, and hence increased electrical res-

istivity. These include:

- Defects: grain boundaries, vacancies, dislocations
- Impurities, such as alloying elements in solid solution
- Intermetallic particles and precipitate phases

Matthiessen's rule is an empirical relation that expresses the total electrical resistivity of a material, ρ_{tot}, as a linear sum of the individual contributions from different microstructural features in the material, and which often yields good agreement with experimental results [61, 93]. Using Matthiessen's rule, the total electrical resistivity of a 6xxx Al alloy, ρ_{tot}, as a function of temperature, T, and the solute solution concentration of elements, c_{i}^{ss}, may be stated as

$$\rho_{\text{tot}}(T, c_{\text{i}}^{\text{ss}}) = \rho_0(T) + \sum_i \alpha_{\text{i}} c_{\text{i}}^{ss} + \rho_{\text{disloc}} + \sum_j f_{\text{par, j}}\ \rho_{\text{par, j}} + \rho_{\text{GB}}. \qquad (2.16)$$

Here, ρ_0 is the resistivity of pure Al, incorporating the overall temperature dependence. The factor $\rho_{\text{par, j}}$ accounts for the effect of particles such as precipitate phases in the microstructure, each with a volume fraction, $f_{\text{par, j}}$. ρ_{disloc}, ρ_{GB}, and α_{i} are constants accounting for the contribution of respectively dislocations, grain boundaries, and solute elements in the Al matrix of a concentration c_{i}^{ss}. In order to achieve high conductivity, the alloy will normally be used in an overaged condition. As the grain size and interparticle spacing of 6xxx Al alloys in overaged conditions are much larger than the free electron mean free path λ_{Al}, the factors ρ_{GB} and $f_{\text{par, j}}\ \rho_{\text{par, j}}$ usually become negligible. Furthermore, as long as the material has not been processed using e.g. severe plastic deformation [59, 61] or is used directly after cold-drawing, the term ρ_{disloc} is also normally very small. The main contribution to the electrical resistivity is hence due to solute solution contribution $\sum_i \alpha_{\text{i}} c_{\text{i}}^{ss}$. The element-specific coefficients α_{i} at room temperature ($T = 20\,^{\circ}\text{C}$) equal 0.6186 and 0.5745 $\cdot 10^{-8}\Omega$·m/wt.% for Si and Mg, respectively [93, 94]. From Table 2.3, it is seen that these can be on the same order of magnitude as the resistivity of pure Al at room temperature. The key to control the conductivity of Al alloys is therefore to lock as much solute as possible inside precipitate phases, which will also improve the mechanical performance of the material. A trade-off in properties is generally necessary, as too long ageing will lead to a weak material with large, coarsened precipitates which will exhibit high conductivity. The distribution of solute elements and the effect of different TMP routes on resulting material conductivity is the topic of Paper **VII** in this thesis.

Chapter 3

Transmission Electron Microscopy

The works presented in this thesis are mainly experimental, and a number of different techniques for testing of material properties and microstructure characterisation has been applied. The main scientific instrument used, however, is the TEM. The TEM has been the principal instrument used in all papers produced, and this chapter is therefore dedicated to explain general aspects of the TEM and some of its many different techniques. The focus is on the TEM techniques applied in this thesis, and wherever relevant, examples are drawn from the study of Al alloys and precipitates. The final section of this chapter goes into some depth on the analysis of SPED data, which has been an important contribution from this PhD work. Although other scientific instruments have been used, e.g. APT and differential scanning calorimetry (DSC), the application of these techniques have used standard approaches, with limited degree of novelty. Details on the use of these techniques are provided in the relevant papers of this thesis. Increased focus has therefore instead been placed on SPED and associated developments, due to the application of relatively novel approaches, especially as it relates to the studies of age-hardening Al alloys.

A TEM operates through many of the same physical principles as the more familiar optical microscope. An optical microscope uses visible light, i.e. photons, which are focused through curved glass lenses and under ambient atmospheric conditions. A TEM uses electrons which are focused through electromagnetic lenses and kept in a closed system with high- to ultra-high vacuum conditions. Both instruments share the same scientific purpose: to provide clear, magnified images of the specimen under study. Because electrons are elementary particles with a mass and charge, they interact much more strongly with matter than photons, and a beam of electrons can also be manipulated in other ways than what can be achieved with

photons. Figure 3.1 shows a simplified schematic of a TEM column, indicating the main components comprising the electro-optical system. A detailed treatise of the workings and technicalities of present day TEMs is far beyond the scope of this thesis, and for an introduction to these topics the books by Williams and Carter [95], Erni [96], and Zuo and Spence [97] should be consulted. More details can also be found in e.g. Hirsch, Howie, Nicholson, Pashley and Whelan [98], Humphreys [99], Nellist and Pennycook [67], Kirkland [100], and Reimer and Kohl [101].

It follows from the wave-particle duality principle due to De Broglie that the electron exhibits wave-like properties similar to photons [99]. The De Broglie wavelength, λ, for an electron with rest mass, m_0, and momentum, p, is given as

$$\lambda = \frac{\mathrm{h}}{p}, \tag{3.1}$$

where h denotes Planck's constant. The interdependency of wavelength and momentum means that by changing the electron's velocity, its effective wavelength is also altered. The obtained velocity is adjustable by changing its energy, and in the TEM the electrons obtain high energies by being accelerated through a high voltage, usually in the range $80 - 300$ kV. At 100 kV, the electron obtains a speed of 55% the speed of light in vacuum, c. The theory of electron scattering in the TEM therefore needs to take into account relativistic effects, leading to the expression [95]

$$\lambda = \frac{\mathrm{h}}{\sqrt{2m_0eU(1 + eU/2m_0c^2)}}. \tag{3.2}$$

Here, eU denotes the energy obtained when an electron with one negative elemental charge, e, is accelerated through the column potential, U. At 200 kV acceleration voltage the effective electron wavelength is 2.51 pm. This is a minuscule wavelength as compared to the lower end of the visible light spectrum (violet $\approx 380\,\mathrm{nm}$), and thus potentially allows much smaller structures to be observed. In optical microscopes obtained spatial resolutions are on the same order of magnitude as that of applied wavelengths. In TEMs however, obtainable resolutions are much worse than 2.51 pm[1] due to the poor performance of electromagnetic lenses, which is mainly caused by aberrations.

[1] The world record is currently at 0.39 Å $= 39$ pm [102].

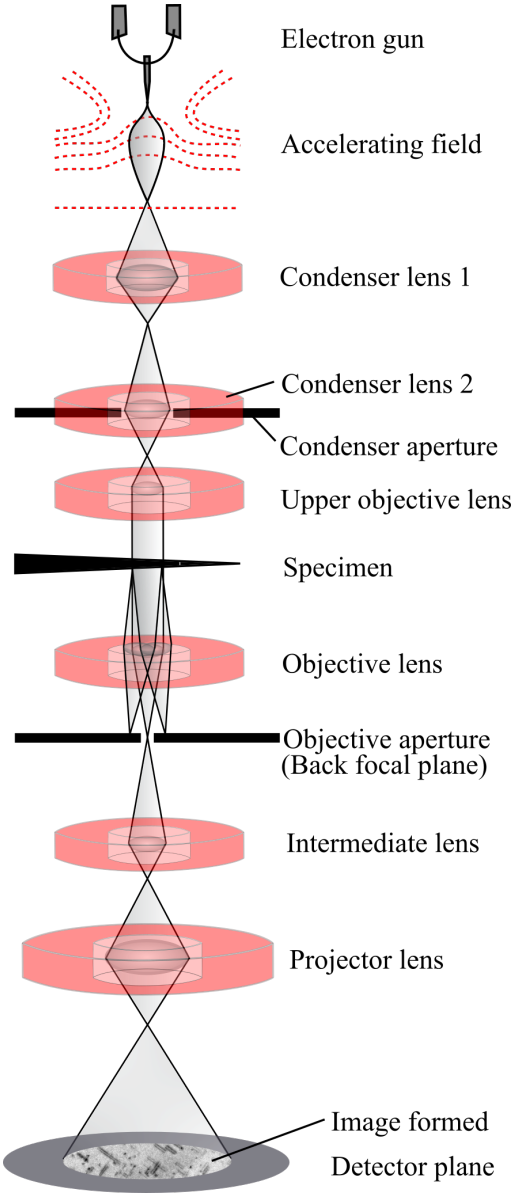

Figure 3.1. A schematic showing the main components of a TEM, from the electron gun to the detector plane. The objective aperture sits here in the back focal plane where it blocks beams scattered to higher angles. This corresponds to the bright-field operation mode. In reality there are many more lenses and several additional components enabling beam control and adjustments than those indicated here.

However, with the advent of aberration corrected lenses[2] in TEMs [103], spatial resolution is not a particularly limiting factor of modern TEMs. In ordered solids, the atomic spacing between two bonded atoms is generally a few ångströms (1 Å $= 0.1\,\mathrm{nm}$). Many conventional TEMs obtain spatial resolutions of about 2 Å, and aberration corrected instruments may routinely achieve resolutions in the range $0.7 - 1.3\,$Å [95]. A TEM can therefore image materials at extraordinary magnifications, providing direct visualisation of the atomic arrangements. Through different, strong electron-specimen interaction mechanisms, a TEM can in addition determine atomic species, ionic states, material bandgaps, as well as electronic and magnetic properties of materials, down to the atomic level. In comparison to other nanoscale characterisation techniques, a great advantage of the TEM is its ability to perform multiple experiments, including imaging, diffraction, and spectroscopy in the same nanoscale area of a specimen at very high spatial resolution.

Some of the major limitations of TEMs include the fact that specimens must be prepared very thin (usually $< 200\,\mathrm{nm}$), studied under high- to ultra high vacuum conditions, and will be subjected to high energy, ionising electron bombardment. This is important as it means that materials usually cannot be studied in their bulk or native states, and in addition one might introduce unwanted beam damage during experiments. All aspects are important to assess carefully before one generalises findings at the atomic and nm-level to explain macroscopic specimen properties and structure. Further emphasising this point, the data recorded are (in most cases) 2D projections of a 3D object, which also needs consideration. Fortunately, there are many recent and ongoing developments that improve upon these issues, such as the development of environmental and *in situ* TEM holders [104, 105], as well as significantly improved detector technologies retaining good signal with much smaller electron doses [106–108].

3.1 Electron diffraction

The fast moving electrons in the TEM interact strongly with materials due to their charge, e, which creates surrounding electromagnetic fields. There are several different electron-specimen interactions which give rise to different scattering, excitation, and absorption mechanisms, and which generate different types of secondary signals, see Figure 3.2. The scattering is termed *elastic* if the electron leaves the state of the specimen atoms unaltered after transmission, i.e. with its initial energy, $E_0 = eU$. *Inelastic* scattering alters the state of the specimen. This can include single electron excitation, or collective excitations, such as in generation of plasmons. Furthermore, one distinguishes *coherent* and *incoherent* interactions

[2] At the time of writing this thesis, the developers Rose, Haider, Urban, and Krivanek were recently acknowledged by receiving the Kavli Prize in Nanoscience in May 2020.

depending on whether phase coherency is preserved or not. The different types of interactions lead to different generated signals and characteristic angular distributions, which are exploited using different spectroscopic, diffraction, and imaging techniques [101].

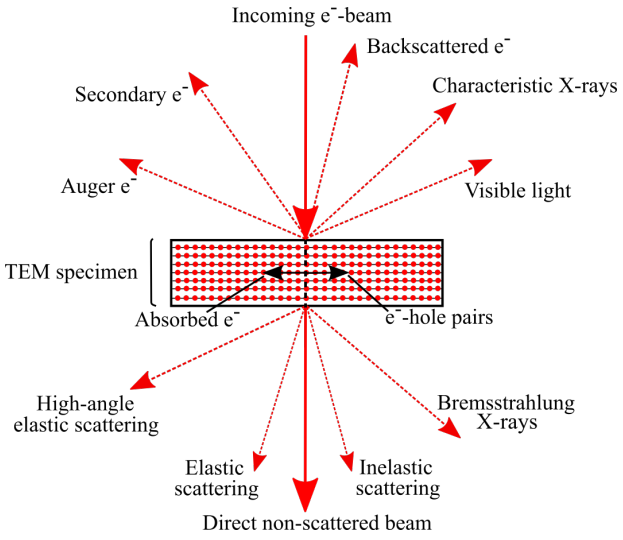

Figure 3.2. Different types of electron-specimen interactions, scattering mechanisms, and secondary signals generated in the TEM. Arrows indicate relative angular distributions, greatly exaggerated for clarity.

When electromagnetic radiation with wavelength comparable to- or smaller than inter-atomic distances is incident upon a crystal lattice, the surrounding electron clouds of each atom may spread the incoming radiation elastically in all directions with equal frequency. The radiation from all atoms in the crystal lattice will interfere, which results in stringent conditions for producing intensity maxima about the crystal, which only occur for a special set of directions. This set of directions in space is described by Bragg's law, the fundamental equation in diffraction theory, which reads

$$2d_{\mathrm{hkl}} \sin(\theta_{\mathrm{hkl}}) = n\lambda. \tag{3.3}$$

Bragg's law relates the the inter-planar distance, d_{hkl}, the scattering angle, θ_{hkl}, and the wavelength, λ. Real space interpretation visualises specularly scattered radiation from atomic planes (hkl), giving constructive interference when the wave path difference equals an integer multiple of wavelengths, $n\lambda$. Its reciprocal space equivalent, the Laue condition, reads

$$\vec{Q} = \vec{k}_{\mathrm{f}} - \vec{k}_{\mathrm{i}} = \vec{g}_{\mathrm{mno}} + \vec{s}. \tag{3.4}$$

Here, $\vec{Q}$ is the total scattering vector, and $\vec{k}_{\mathrm{f}}$ and $\vec{k}_{\mathrm{i}}$ denote the wave vector of the scattered and incoming electron wave, respectively, where $|\vec{k}_{\mathrm{i}}| = 2\pi/\lambda$. The reciprocal lattice vector, $\vec{g}_{\mathrm{mno}}$, describes a point in reciprocal space that corresponds to a set of atomic planes (mno) in real space. Furthermore, small deviations from the Bragg condition are included through the *excitation error*, $\vec{s} = \langle s_{\mathrm{x}}, s_{\mathrm{y}}, s_{\mathrm{z}} \rangle$. Equation 3.4 is visualised through the Ewald-sphere construction, see Figure 3.3. The excitation error connects the point $\vec{g}_{\mathrm{mno}}$ in reciprocal space to the Ewald sphere in the direction parallel to the incident beam direction $\vec{k}_{\mathrm{i}}$.

The construction of *Laue zones* is useful for the indexing and computation of resulting electron diffraction patterns. The product of a translation vector of the crystal lattice, $\vec{R}_{\mathrm{hkl}}$, and a reciprocal lattice vector $\vec{g}_{\mathrm{mno}}$, is given as $\vec{g}_{\mathrm{mno}} \cdot \vec{R}_{\mathrm{hkl}} = mh + nk + ol = N$, where N is an integer. If $N = 0$, all the $\vec{g}_{\mathrm{mno}}$ for a given value of $\vec{R}_{\mathrm{hkl}}$ lie on a plane through the origin of the reciprocal lattice and are normal to the *zone axis* (ZA), $\vec{R}_{\mathrm{hkl}}$, or [hkl]. The system of lattice planes that belongs to these values of $\vec{g}_{\mathrm{mno}}$ forms a bundle of planes that have the ZA as a common line of intersection. The reciprocal lattice plane that contains the corresponding $\vec{g}_{\mathrm{mno}}$ is called the zero order Laue zone (ZOLZ). For $N = 1, 2, ...$ the first- (FOLZ), second-(SOLZ), and higher order (HOLZ) Laue zones are obtained, respectively. These are parallel to the zero order Laue zone, from which it follows that the Laue zones are parallel sections through the reciprocal lattice, see Figure 3.3.

The intensity of a reflection is proportional to the square of the modulus of the *crystal structure factor*, $I \propto |F_{\mathrm{crystal}}(\vec{Q})|^2$. The crystal structure factor is defined as the amplitude of the waves scattered by the crystal at unit distance in the direction $(\vec{k}_{\mathrm{i}} + \vec{Q})$. Assuming the crystal to be parallelepipedal in shape, with edge lengths $L_{\mathrm{i}} = M_{\mathrm{i}} a_{\mathrm{i}}$, i = (1,2,3), parallel to the vectors $\vec{a}_{\mathrm{i}}$ defining the crystal unit cell, the defining equation becomes [101]

$$\begin{aligned} F_{\mathrm{crystal}}(\vec{Q}) &= \sum_{\mathrm{crystal}} f_{\mathrm{j}}(\vec{Q}) \exp\left(-\mathrm{i}(\vec{Q} + \vec{s}) \cdot (\vec{R}_{\mathrm{hkl}} + \vec{r}_{\mathrm{j}})\right) \\ &= \underbrace{\sum_{h=1}^{M_1} \sum_{k=1}^{M_2} \sum_{l=1}^{M_3} \exp\left(-\mathrm{i}(\vec{Q} + \vec{s}) \cdot \vec{R}_{\mathrm{hkl}}\right)}_{\text{Lattice amplitude}} \underbrace{\sum_{j} f_{\mathrm{j}}(\vec{Q}) \exp\left(-\mathrm{i}(\vec{Q} + \vec{s}) \cdot \vec{r}_{\mathrm{j}}\right)}_{\text{Structure amplitude}}. \end{aligned} \tag{3.5}$$

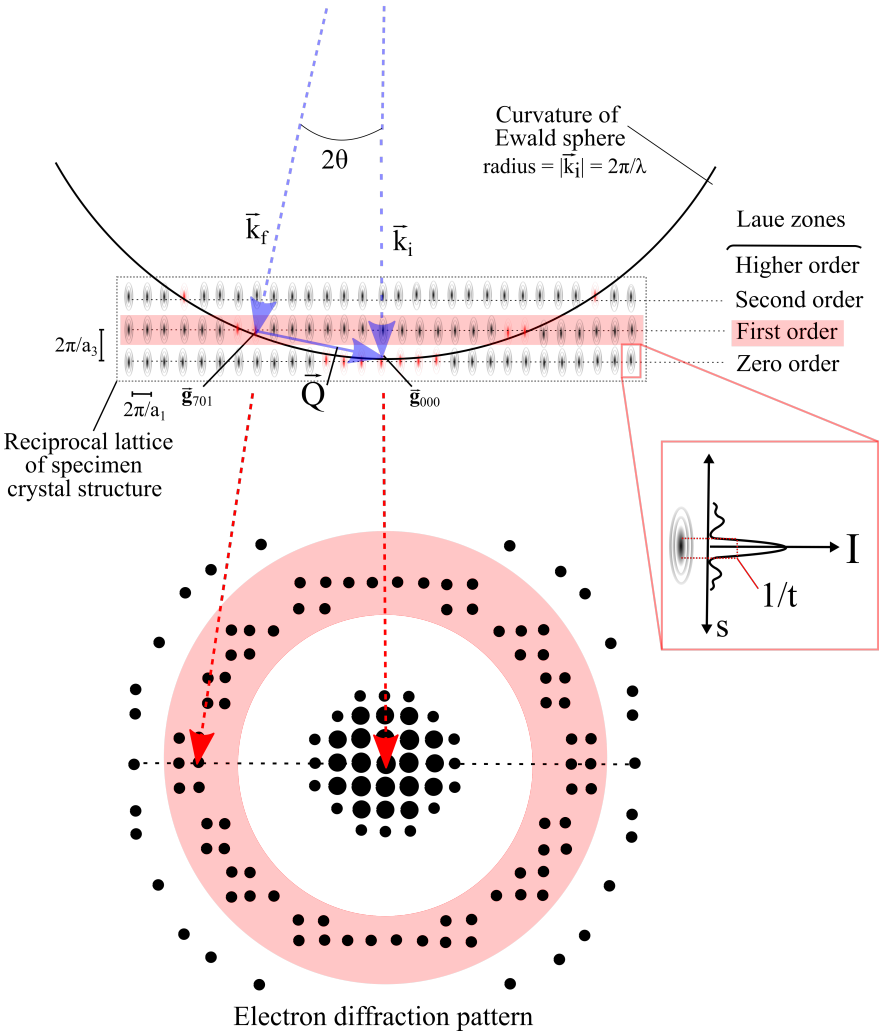

Figure 3.3. The Ewald sphere construction for elastic scattering on a crystalline material in [001] ZA orientation. The reciprocal lattice points are expanded into reciprocal lattice rods (rel-rods) parallel to the surface normal of the thin, plate-shaped specimen. The scattering geometry for a particular reflection ($\vec{g}_{710}$) in the first order Laue zone (highlighted) is shown, as well as a generic electron diffraction pattern exhibiting reflections from multiple Laue zones. The lattice points intersected by the Ewald sphere (red) causes diffraction described by the respective vectors $\vec{g}_{\text{mno}}$. The intensity, I, as a function of the excitation error, s, is indicated for the highlighted reciprocal lattice point, and which has a FWHM of $1/t$, where t is specimen thickness.

The sum runs over all crystal atoms, reached through the vector sum $\vec{R}_{\text{hkl}}+\vec{r}_{\text{j}}$. The lattice amplitude depends on the external shape of the crystal, and the structure amplitude depends on the relative positions and atomic species inside the crystal unit cell. These will be denoted as G and $F_{\text{uc}}(\vec{Q})$ in the following, respectively. $\vec{r}_{\text{j}}$ is the relative position of the j^{th} atom in the basis, whose scattering is described through an *atomic scattering amplitude*, $f_{\text{j}}(\vec{Q})$. The atomic scattering amplitude for electrons in the first Born approximation may be expressed as [99]

$$\begin{aligned} f_{\text{j}}(\vec{Q}) &= -\frac{me^2}{8\pi\epsilon_0 h^2 Q^2}\int_{-\infty}^{\infty}\exp\left(-\text{i}\vec{Q}\cdot\vec{r}\right)[Z\delta(\vec{r})-\rho_{\text{e}}(\vec{r})]\text{d}\vec{r} \\ &= -\frac{me^2}{8\pi\epsilon_0 h^2 Q^2}[Z-f^{\mathbf{X}}(\vec{Q})], \end{aligned} \tag{3.6}$$

where $\rho_{\text{e}}(\vec{r})$ is the atomic electron density, ϵ_0 is the permittivity of vacuum, $f^{\mathbf{X}}(\vec{Q})$ is the scattering factor for X-rays, and Z is the atomic number. Equation 3.6 is the Mott-Bethe formula, which directly relates the electron- and X-ray scattering factors. The first term is due to Rutherford scattering by the nucleus and the second term is due to scattering by the atomic electrons.

Now, substituting Equation 3.4 into the lattice amplitude of Equation 3.5, and using $\vec{g}_{\text{mno}}\cdot\vec{R}_{\text{hkl}}=N$, as well as replacing the sum with an integral gives the expression for the total intensity as [101]

$$\begin{aligned} I(\vec{Q}) &= |F_{\text{uc}}(\vec{Q})|^2|G|^2 \\ &= |F_{\text{uc}}(\vec{Q})|^2\frac{\sin^2(\pi s_{\text{x}}M_1a_1)}{(\pi s_{\text{x}}a_1)^2}\frac{\sin^2(\pi s_{\text{y}}M_2a_2)}{(\pi s_{\text{y}}a_2)^2}\frac{\sin^2(\pi s_{\text{z}}M_3a_3)}{(\pi s_{\text{z}}a_3)^2}. \end{aligned} \tag{3.7}$$

This is a similar result as the diffracted intensity distribution in optics from a grating with M_{i} slits of spacing a_{i}. A typical TEM specimen can be approximated as a thin plate, thickness $t=M_3a_3$, with its lateral dimensions L_1 and L_2 far exceeding t. The *sinc*-terms of equation 3.7 tend to δ-functions for large L_1 and L_2. The total intensity diffracted by a thin plate of thickness, t, follows from Equation 3.7 as

$$I(\vec{Q}) = \frac{|F_{\text{uc}}(\vec{Q})|^2L_1L_2}{V_{\text{uc}}^2}\frac{\sin^2(\pi ts_{\text{z}})}{(\pi s_{\text{z}})^2}\delta(s_{\text{x}})\delta(s_{\text{y}}). \tag{3.8}$$

Here, $V_{\text{uc}}=a_1a_2a_3$, denotes the volume of the unit cell. Equation 3.8 shows that the intensity $I(\vec{Q})$ is spread out in the form of a spike parallel to the surface

normal of the plate-shaped crystal. The full width at half maximum (FWHM) in reciprocal space is approximately t^{-1}. The effect on the Ewald sphere construction is to extend the points to rods of width t^{-1} in the direction parallel to the surface normal of the specimen. The resulting rods are known as reciprocal lattice rods, or *rel-rods* for short, see Figure 3.3. The intensity scattered through 2θ in the g^{th} diffracted beam from a crystal of thickness t in the kinematical theory follows from integrating Equation 3.8, and can be written as [99]

$$I_{\vec{g}}(t) = \left(\frac{\pi}{\xi_{\text{g}}}\right)^2 \left(\frac{\sin(\pi t s)}{\pi s}\right)^2. \tag{3.9}$$

Here, $\xi_{\text{g}} = \pi V_{\text{r}}/\lambda F_{\text{uc}}(\vec{Q})$ denotes the *extinction length* and V_{r} is the volume of the unit cell in reciprocal space. Now, here comes an important warning sign, normally negligible in the theory of X-ray diffraction. $I_{\vec{g}}(t)$ cannot be greater than unity, i.e. the incident beam intensity. At the exact Bragg position, $s = 0$, and $I_{\vec{g}}(t) = \left(\frac{\pi t}{\xi_{\text{g}}}\right)^2$. Hence, an upper limit of the specimen thickness, t_{max}, for which kinematical theory is valid at the Bragg position is $t_{\text{max}} = \xi_{\text{g}}/\pi$. With typical extinction distances in the range of a few hundred Å, $t_{\text{max}} \approx 100$ Å. In fact, this is very much an upper limit, as kinematical theory assumes a single scattering event, and hence assumes that the diffracted beam is much weaker than the incident beam. For larger deviations, s, from the exact Bragg condition, the kinematical theory holds to a somewhat better extent. For typical TEM specimen thicknesses in the range $50-100\,\text{nm}$, it is apparent that in electron diffraction there is need for an extended theory including *dynamical* effects. In multiple scattered waves there are dynamic exchanges of intensity between different Bragg diffracted beams. This alters the intensity distribution in the diffraction plane. Among other important results, some kinematically forbidden reflections can be present in the diffraction pattern. This complicates matters significantly because the intensity of a scattered beam is no longer given by kinematic equations, and depends non-linearly on the thickness, t, of the specimen [98, 99, 101]. In a two-beam condition, i.e. a situation where only a single reciprocal lattice point lies close to the Ewald sphere in addition to the direct beam, the intensities (transmission $T = \psi_0\psi_0^*$, reflection $R = \psi_{\text{g}}\psi_{\text{g}}^*$, ψ = electron wave amplitude) become [101]

$$\begin{aligned} R = \psi_{\text{g}}\psi_{\text{g}}^* = 1 - T &= 1 - \psi_0\psi_0^* \\ &= \frac{1}{1+w^2}\sin^2\left(\pi\sqrt{1+w^2}\frac{t}{\xi_{\text{g}}}\right), \end{aligned} \tag{3.10}$$

where $w = s\xi_g$. For $w \gg 0$ (large tilt out of the Bragg condition, Equation 3.4) this becomes identical with the solution of kinematical theory, Equation 3.9. For $w = 0$, kinematical theory predicts that R increases as t^2 and becomes larger than one, which contradicts conservation of intensity, $T + R = 1$. Equation 3.10, given by the dynamical theory results in $R = 1 - T = \sin^2(\pi t/\xi_g)$ for $w = 0$. This means that, even in the Bragg condition, the electron intensity oscillates between the primary and the Bragg-reflected beam with increasing film thickness (the so-called "pendellösung" of the dynamical theory). This also explains the name *extinction distance* ξ_g; it is the periodicity in depth of this oscillation. At thicknesses $t = (n + 1/2)\xi_g$ the intensity is completely concentrated in the Bragg reflection, and at $t = n\xi_g$, the intensity returns to the incident beam direction. This dynamical transfer of intensity between the direct beam and the scattered beam becomes increasingly difficult to predict for increasing numbers of excited beams (i.e. for more reciprocal lattice points close to the Ewald sphere), as each scattered beam will interact dynamically with all others. The problem therefore becomes impossible to solve analytically, and usually requires application of advanced, large-scale computations instead [95, 98], e.g. based on dynamical Bloch-wave simulations or multi-slice calculations [109, 110].

3.2 Bright-field and dark-field imaging

Imaging techniques based on amplitude contrast are some of the most basic and efficient techniques available in the TEM. Here, the contrast is mainly determined by diffraction and/or mass/thickness effects. Bright-field (BF) and dark-field (DF) imaging are the two main techniques that are used. When applying these techniques, the specimen is illuminated by a nearly parallel beam, and an objective aperture is inserted in the back focal plane of the objective lens. The objective aperture will block out all beams that do not enter the aperture opening. It therefore acts to select beams that are scattered to angles chosen based on the aperture placement in the back focal plane. In BF imaging, the objective aperture is centred on the direct beam, thus removing most or all of the scattered beams, see Figure 3.4a. The contrast in the resulting BF image will be determined by the beam intensity scattered out of the incident beam direction.

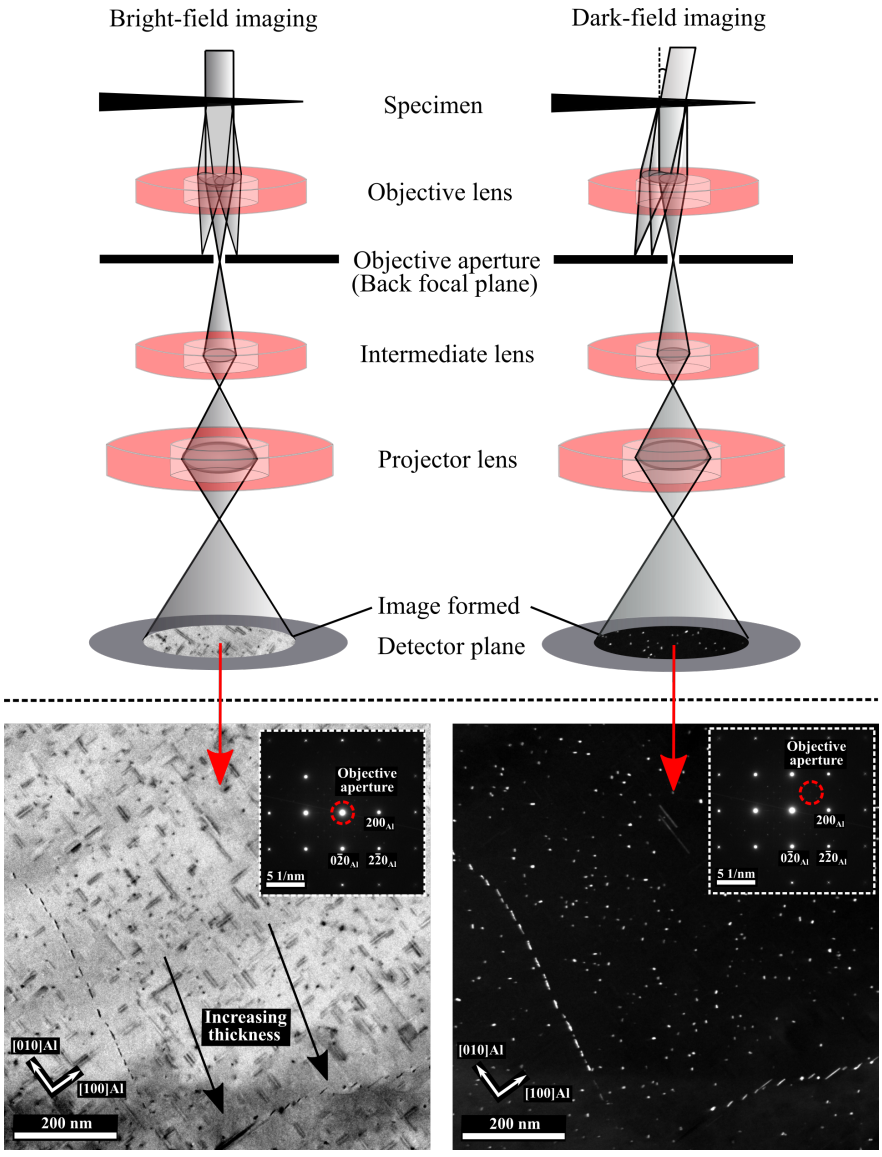

Figure 3.4. Ray diagram schematics for BF and DF TEM imaging modes and examples of images obtained with the two techniques. The images were acquired in the same specimen region in an Al-Mg-Si alloy near the peak strength condition. $\langle 100 \rangle_{\mathrm{Al}}$ oriented precipitate needles/rods are clearly visible in the BF image, and the DF image shows the distribution of precipitate cross-sections. The inserts show objective aperture placements in the electron diffraction patterns, which are formed in the back focal plane of the objective lens. Both diffraction contrast and thickness contrast are visible in the BF image.

DF imaging is achieved by positioning the objective aperture away from the central beam, thus only enabling specific reflections $\vec{g}_{\text{mno}}$ to contribute to the resulting image. These images appear bright where crystalline phases scatter to the corresponding angles, with all other regions appearing dark, see Figure 3.4b. In order to optimise imaging conditions, the objective aperture is not necessarily moved away from the optical axis. Instead, the beam can be tilted so that the sought reflection $\vec{g}_{\text{mno}}$ is aligned with the optical axis. This is done in order to minimise the effect of lens aberrations, which increases with larger lateral distance to the optical axis. Ray diagram schematics and examples of images acquired using both techniques are provided in Figure 3.4, showing images from the same specimen region in an Al-Mg-Si alloy.

Amplitude contrast does also arise due to varying thickness over the field of view. Generally, a crystal scatters more with increasing thickness. However, due to dynamical effects this may not always be the case. When the thickness of the crystal equals an integer number of extinction distances for any reflection (see Equation 3.10), the intensity of these reflections decrease. This gives rise to thickness fringes if the specimen thickness varies over the imaged region. In addition, higher average atomic column Z number will have a similar effect, so that variations in scattered intensity can be both due to an increase in thickness and/or average mass (Z number).

3.3 Scanning transmission electron microscopy

Instead of having a parallel beam illuminating a larger region of the specimen, the beam can also be focused to a small spot and scanned rapidly across the same region in a raster. This forms the basis of scanning transmission electron microscopy (STEM). The electrons scattered to different angular ranges are recorded in each scan pixel, and images of the scanned region can subsequently be reconstructed.

Similar to BF and DF TEM imaging, there exists (annular) bright-field ((A)BF) and annular dark-field (ADF) STEM imaging. In ABF-STEM, the electrons scattered to small angles in an annular geometry about the optical axis are used to form the image. ADF-STEM uses electrons scattered to higher angles than with ABF, and one also distinguishes a high-angle ADF (HAADF) STEM mode. The specific angular ranges of the different modes are not rigorously defined, but some approximate numbers are: ABF 10-$20\,\text{mrad}$, ADF 20-$45\,\text{mrad}$, and HAADF $> 45\,\text{mrad}$. The different angular ranges are associated with different scattering mechanisms, which give rise to differences in image contrast. Figure 3.5 shows a schematic of the STEM setup, in addition to examples of ABF and HAADF-STEM lattice images of an Al-Mg-Si-Cu precipitate (L phase). HAADF-STEM images are very useful because the intensity in each pixel roughly corresponds to the square of the

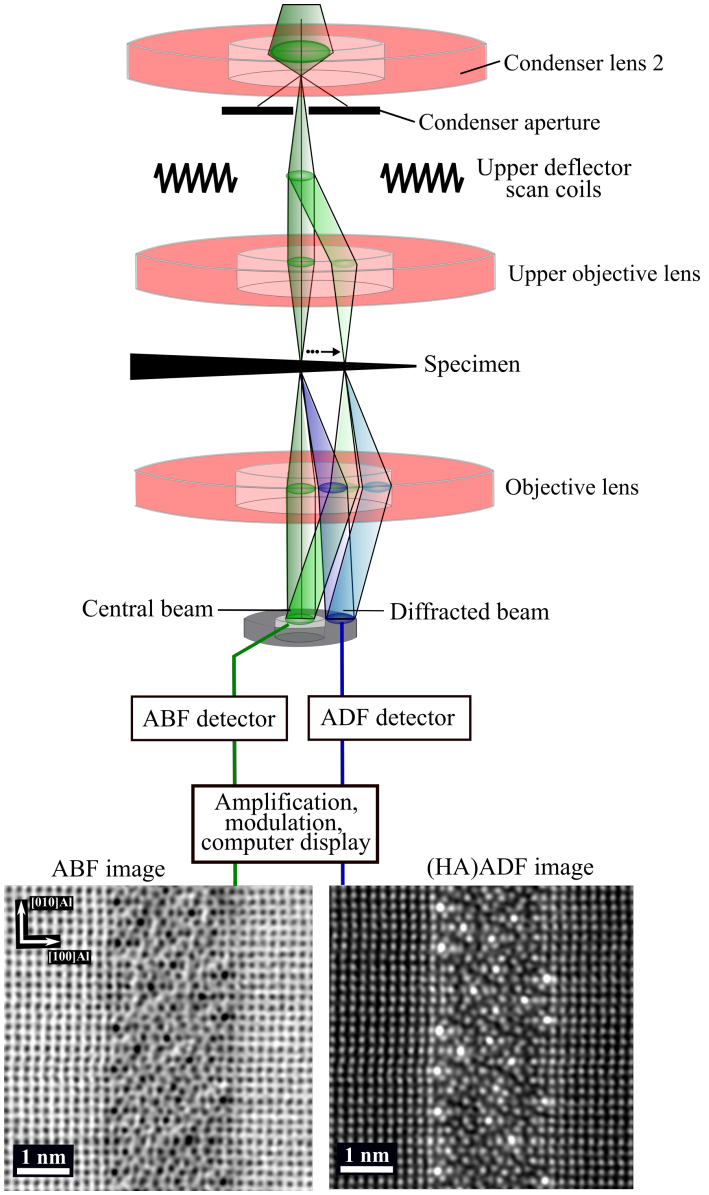

Figure 3.5. Schematic of the ABF and (HA)ADF-STEM modes in the TEM. The direct- and a scattered beam (green and blue, respectively) are shown for two different scan positions. Example images are provided for the two modes, which were obtained on an L phase precipitate. The HAADF-STEM image was obtained using a detector collection angle of 42-178 mrad.

atomic number Z [67, 96, 111], which greatly aids image interpretation. Qualitatively, this follows from Equation 3.6, as it can be shown that

$$I(\theta)_{\theta\to 90^\circ} \propto |f_\mathrm{j}(\theta)|^2_{\theta\to 90^\circ} = \left(\frac{me^2}{8\pi\epsilon_0 h^2 Q^2}\right)^2 Z^2. \tag{3.11}$$

Equation 3.11, the Rutherford scattering equation, describes scattering by the atomic nucleus. It is valid for large scattering angles for which $f^{\mathbf{X}}(\vec{Q})$ is negligibly small. Although $45\,\mathrm{mrad} \approx 2.6^\circ$ is far from 90°, $f_\mathrm{j}(\theta)$ for fast moving electrons is very sharply peaked in the forward direction. It can be shown that the curve of $f_\mathrm{j}(\theta)$ against θ has a semi-half-peak of about $1^\circ \approx 17\,\mathrm{mrad}$ for 100 keV electrons [99]. This means that Rutherford scattering starts to contribute significantly at about 1°. In order to increase the number of electrons detected, the angular range will normally also include other mechanisms than Rutherford scattering, e.g. Bragg scattering, and therefore screening by the atomic electrons will cause the atomic number dependency to be slightly smaller than squared.

A second important effect of recording electrons at high scattering angles is that the atoms become more independent scattering centers, which is a key characteristic of *incoherent* imaging. At high angles, the effective d_hkl spacing, see Equation 3.3, eventually becomes so small that it is comparable to the thermal vibration amplitude of the atoms. Here, phase relationships will vary randomly in time as the atoms vibrate, and every electron will 'see' the atoms with a different spacing, and scatters in different directions. This is an example of incoherent scattering, denoted thermal diffuse scattering (TDS), which is an important contributing factor to HAADF-STEM image intensities. HAADF-STEM images provide an efficient way of observing the crystal structure of Al alloy precipitates directly, see Figure 3.6, without complications arising from phase contrast mechanisms, which is limited in this incoherent imaging mode. Due to the accumulated knowledge on the precipitate phase structures, HAADF-STEM images such as Figure 3.6a can be used to construct atomic overlays as seen from image Figure 3.6b. Note that the brightest columns seen in this HAADF-STEM image are due to Cu occupancy ($Z = 29$). The construction of such overlays exploits both differences in atomic column intensities of HAADF-STEM images as well as discovered rules for atomic connections in this material system [36]. The presented overlay was automatically labelled using an in-house software [112].

Furthermore, other scattering events may be recorded than the high-angle events. With decreasing inner-angle, the resulting image will contain more contributions

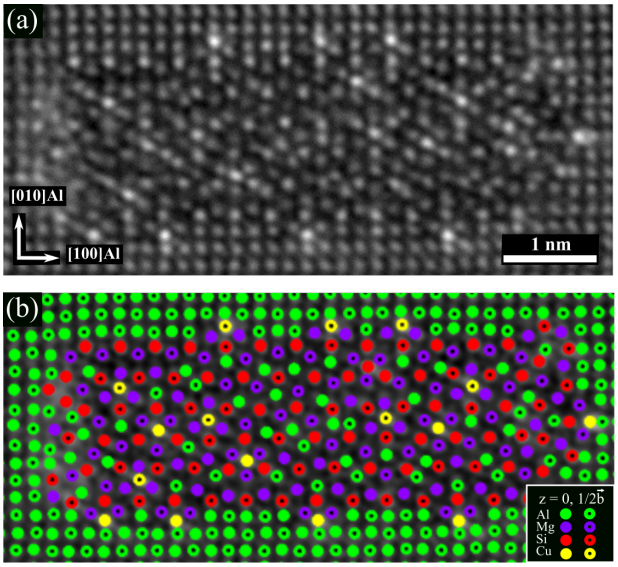

Figure 3.6. (a) HAADF-STEM image obtained on a L phase precipitate in an Al-Mg-Si-Cu alloy. (b) Atomic overlay of the precipitate in (a).

from coherent scattering and phase information. For instance, by acquiring a medium-angle ADF or an ABF signal, strain contrast becomes more important and can be used to observe e.g. dislocations [113]. An example of this was provided in section 2.2.1 of chapter 2, see Figure 2.8.

3.4 (Scanning) Precession electron diffraction

Precession electron diffraction (PED) is a diffraction technique where a focused probe is rocked in a hollow cone above the specimen, while simultaneously being de-rocked below [114], see Figure 3.7. After de-rocking, the intensities are recorded in the geometry of a conventional electron diffraction pattern. The precession effectively integrates the intensities of reflections through a range of incident wave vectors, which can reduce the contribution of non-systematic dynamical perturbations to the diffracted intensities. For Equation 3.10 of section 3.1, expressing the dynamical solution for the diffracted intensity in a two-beam condition, it was pointed out that for $w = s\xi_g \gg 0$ (large tilt out of the Bragg condition) the solution becomes identical to that predicted by kinematical theory (Equation 3.9). This is a qualitative indication that by tilting the beam off exact ZA orientation (by the precession angle, ϕ), and furthermore by integrating the diffraction conditions through one or several full rotations about the optical axis, together may act to suppress dynamical effects. Indeed, by more rigorous analyses it has been demon-

strated that the intensities of PED patterns are 'more kinematic' in nature [115, 116], and an example supporting this will be provided later in this chapter. This is a crucial aspect for ab-initio structure determination, which is what PED was originally intended for. As the specimen is probed using many different incident wave vectors this increases the number of reflections of a typical PED pattern as compared to a conventional (static) diffraction pattern, see Figure 3.8.

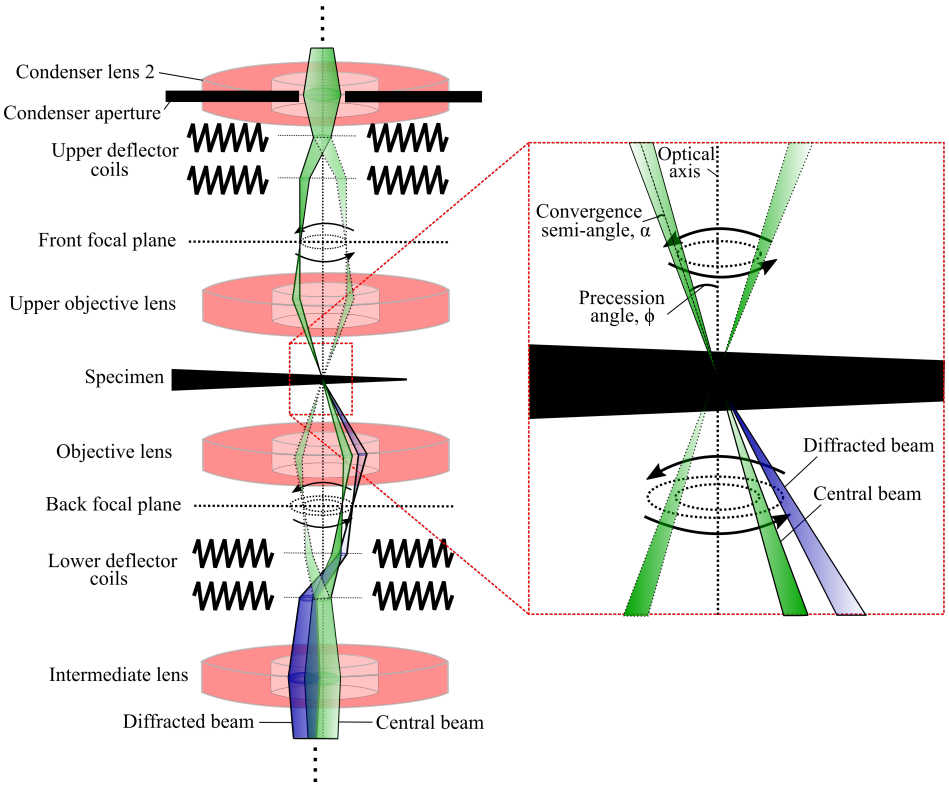

Figure 3.7. Schematic of the PED system. A small, focused probe (convergence semi-angle $\alpha \approx 0.5 - 2\,\mathrm{mrad}$) is tilted off the optical axis by a precession angle ϕ ($\lesssim 2^\circ = 35\,\mathrm{mrad}$), and precessed about the optical axis through an angle θ, with a precession frequency $\dot{\theta}$. Below the specimen, the beam is deflected back (de-rocked) to again run parallel with the optical axis. The central beam (green) is shown on either side of the precession cycle, in addition to a diffracted beam (blue). Without de-rocking, the beam traces a circle as it enters the objective lens with an angle ϕ, and is focused to a spot ϕ degrees out from the optical axis in the back focal plane of the objective lens.

By coupling the PED setup to the microscope's scanning system, scanning PED (SPED) was later developed [117–119]. The scanning frequency, f, and the precession frequency, $\dot{\theta}$, are normally tuned so that $\dot{\theta}/f = 2\pi n$, i.e. the acquired

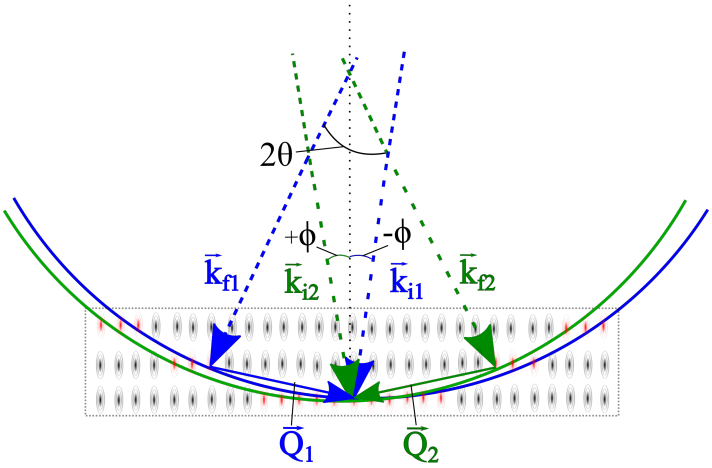

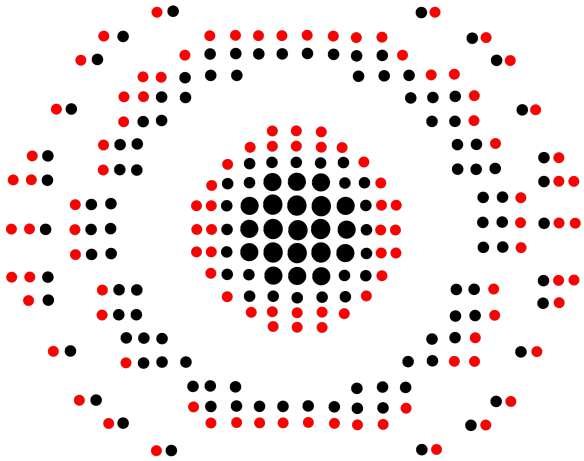

Electron diffraction pattern

Figure 3.8. Schematic of the Ewald sphere construction for PED in a 2D planar section cut through the rotation cycle. Two incident beams (blue and green) are indicated, forming an angle $\pm\phi$ to the optical axis. The curvature of the two Ewald spheres are shown, corresponding to the two incident beam configurations at either side of the precession cycle. The lattice points intersected by the Ewald spheres are shown in red, and cause diffraction described by respective vectors $\vec{g}_{\mathrm{mno}}$. By probing the specimen with different incident beam directions, more reflections (highlighted in red) are excited as compared to a conventional static diffraction pattern (black reflections, cf. Figure 3.3).

PED pattern is integrated over an integer, n, number of full rotations about the optical axis. With SPED, a 4D dataset is obtained comprising 2D PED patterns at each position in a 2D scan region. Combined with subsequent data processing, this constitutes a powerful method for extracting a range of valuable material insights, including: phase mapping and crystallography in multi-phase materials [120, 121], orientation mapping [118, 119], strain mapping [122, 123], and more. The case of orientation mapping illustrates many of the important advantages obtained using precession. For instance, the increased number of reflections obtained with SPED improves indexing results in template-based approaches [118]. The precessing motion also smooths out small variations in orientation, which additionally may aid phase identification [119]. Furthermore, by averaging across a large number of orientations, the structured background visible in many diffraction patterns, e.g. due to Kikuchi diffraction, will effectively be suppressed, which aids peak finding algorithms [124, 125]. It has also been shown that precession may even improve energy dispersive X-ray spectroscopy (EDS) [126] and electron energy loss spectroscopy (EELS) results [127].

3.5 Analysis of SPED data

The 4D datasets obtained with SPED contain rich information about the scanned specimen, and in order to extract this information one usually has to apply different advanced data analysis approaches. Initially, SPED data was mainly analysed in proprietary software, e.g. for the purpose of phase and orientation mapping [118]. Although proprietary software may solve certain problems to a satisfactory extent, they also have several major drawbacks due to their static nature and limited flexibility. Some of the processing and/or analysis steps may also not be completely transparent, which to some extent defeats scientific purposes. In this thesis, SPED data analysis has mostly been done using the Python open-source HyperSpy and pyXem packages [128, 129], in addition to the MTEX MATLAB toolbox [130]. HyperSpy offers an effective as well as intuitive way of inspecting and treating multi-dimensional data, and has its origin from the electron microscopy community. This package has grown rapidly over the last few years, fueled by the independent contributions and developments of many researchers all over the world. The last few years have also seen a surge of powerful software developments for the analysis of big data, machine learning methods, artificial intelligence, and so forth. These developments are being quickly integrated into open-source programs, providing access to state-of-the-art tools for data processing and analysis. This section touches briefly upon some of the tools at one's disposal when processing SPED data, and which have been frequently applied throughout this thesis.

Virtual imaging

The usual starting point of SPED data analysis is visual inspection and then performing *virtual* imaging. The latter is obtained by plotting the intensity within a selected sub-set of diffracting pixels, as a function of probe position, see Figure 3.9. The sub-set of diffracting pixels is chosen by the use of a *virtual aperture*. In the terminology of HyperSpy, a SPED dataset constitutes a 2D *navigation space* (x, y), where each pixel has an associated 2D *signal space* $(k_{\mathrm{x}}, k_{\mathrm{y}})$. Flexibility is provided in the choice of virtual aperture size and geometry in the signal space. If chosen as circular, one may perform virtual bright-field (VBF) and virtual dark-field (VDF) imaging, completely analogous to conventional BF and DF imaging in the TEM, cf. section 3.2. This flexibility gives a huge advantage over conventional BF and DF imaging, as all results are obtained post-facto, away from the microscope. Furthermore, multiple apertures can be placed in signal space and used to form e.g. a summed and enhanced image.

Linear matrix decomposition

Usually, the goal of SPED data analysis is to gather information from each PED pattern, and then combine this information to describe the sample over the full scan region. A common way to extract information from multi-dimensional datasets is through different factorisation or decomposition approaches. A multi-dimensional dataset can be re-written as a signal matrix $\mathbf{X}$ of some dimensionality. Matrix decomposition approaches attempt to decompose the signal matrix $\mathbf{X}$ into a small number, K, of basis components or signals, $\mathbf{S}$, and the corresponding loadings, $\mathbf{L}$, at each sampling position such that [131]

$$\mathbf{X} = \mathbf{LS}. \tag{3.12}$$

This decomposition implies a linear mixing model. A SPED dataset holds n_{nx} and n_{ny} navigation space pixels in the x and y scan directions, respectively. Similarly, each navigation space pixel is associated with n_{sx} and n_{sy} signal space pixels in k_{x} and k_{y} directions in reciprocal space, respectively. In performing matrix decomposition in e.g. HyperSpy, the SPED data is reshaped into a large 2D signal matrix $\mathbf{X}$ ($\in \mathbb{R}^{n_{\mathrm{nx}} \cdot n_{\mathrm{ny}} \times n_{\mathrm{sx}} \cdot n_{\mathrm{sy}}}$), where each column of length $n_{\mathrm{sx}} \cdot n_{\mathrm{sy}}$ contains a measured PED pattern signal, and each row has a length of $n_{\mathrm{nx}} \cdot n_{\mathrm{ny}}$. Each column vector in $\mathbf{S}$ ($\in \mathbb{R}^{n_{\mathrm{sx}} \cdot n_{\mathrm{sy}} \times K}$) contains one of the K basis signals, and each row vector in $\mathbf{L}$ ($\in \mathbb{R}^{K \times n_{\mathrm{nx}} \cdot n_{\mathrm{ny}}}$) describes the spatial intensity distribution of the corresponding basis signal.

The number of unique signals in the SPED dataset $\mathbf{X}$ is usually very small compared to the number of collected PED patterns. In multi-phase materials such as

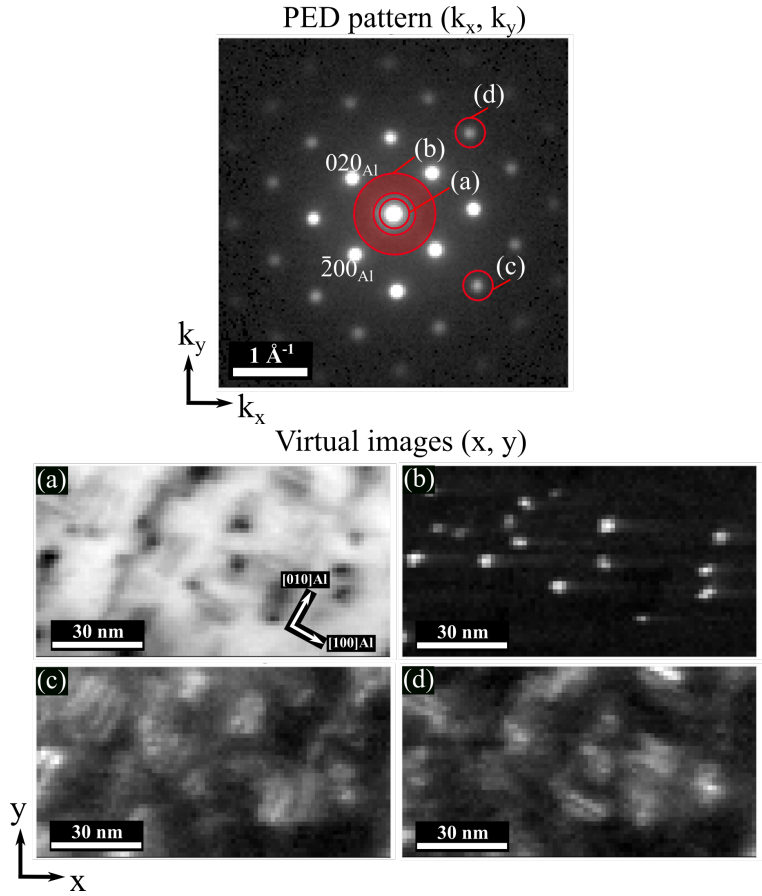

Figure 3.9. Examples of VBF and VDF images formed from a SPED scan of an Al-Mg-Si alloy near peak hardness condition in the $[001]_{\mathrm{Al}}$ ZA. Pure β'' phase precipitates are present in the scan region. Virtual aperture placements (a-d) indicated in the PED pattern formed the respective (a) VBF and (b-d) VDF images below.

age-hardening Al alloys, a reasonable starting point would be to pick K equal to the number of phases present, multiplied with the number of possible ORs allowed. The number might however increase rapidly if the SPED scan is not conducted in ZA orientation, or if there are large specimen tilts over the scan region, significant deformation, non-ideal alignments, and so forth. From a selected number K, a proper decomposition will give a subspace in which $\mathbf{X}$ can be approximately expressed ($\mathbf{X} \approx \mathbf{LS}$). The agreement may be quantified by calculating e.g. the Frobenius norm $||\mathbf{X} - \mathbf{LS}||_{\mathrm{F}}$, and minising this will give a criterion for optimisation. Without any constraints, the matrix decomposition in Equation 3.12 is generally ill-conditioned, meaning that is has many possible solutions. Any unitary

rotation matrix $\mathbf{U} \in \mathbb{R}^{K\times K}$ can be introduced such that

$$\mathbf{X} = \mathbf{LS} = \mathbf{LU}^T\mathbf{US} = \tilde{\mathbf{L}}\tilde{\mathbf{S}}. \tag{3.13}$$

This changes the components obtained, $\mathbf{LS} \rightarrow \tilde{\mathbf{L}}\tilde{\mathbf{S}}$, without affecting the variance captured by the model. Therefore, in order to resolve the ambiguity of the decomposition problem, additional constraints have to be imposed. The different choices for these constraints give different linear matrix decomposition methods, two of which will be described briefly in the following.

Principal components analysis

Principal components analysis (PCA) resolves the ambiguity by requiring the components to be orthogonal and ordered by variance. In geometric terms, it is sought an orthonormal coordinate system that best approximates the data, in as few components as possible. This can be achieved by seeking a vector, $\mathbf{v}$, that maximises the overlap, $\mathbf{o}$, with the signal data matrix, $\mathbf{X}$. For the i^{th} component, the expectancy

$$E(\mathbf{o_i}^2) = E(\mathbf{v_i}^T\mathbf{X}\mathbf{X}^T\mathbf{v_i}) = \mathbf{v_i}^T\mathbf{C}\mathbf{v_i}, \tag{3.14}$$

is maximised. Here, $\mathbf{o_i} = \mathbf{v_i}^T\mathbf{X}$ denotes the overlap of the i^{th} component. Orthonormality is ensured by requiring that $\mathbf{v_i}^T\mathbf{v_i} = |\mathbf{v_i}|^2 = 1$. By using the locally optimal choice at each stage, successive components are found iteratively by subtracting the contributions from the previously computed component, i.e.

$$\mathbf{X} \leftarrow \mathbf{X} - \mathbf{o_i}\mathbf{v_i}. \tag{3.15}$$

This ensures that successively computed components describe variance orthogonal to the already computed space. This is the PCA method [132, 133]. The matrix $\mathbf{C} = \mathbf{X}\mathbf{X}^T$ is the covariance of $\mathbf{X}$. Therefore, all $\mathbf{v}_\text{i}$ can be found via its eigenvalue decomposition. This iterative process hence removes the eigenvector with the highest contribution to variance in each step. The size of the eigenvalues can be used to determine which eigenvectors to keep. The eigenvalue problem can be solved using singular value decomposition (SVD), which gives the eigenvectors at the same time.

It is often useful to estimate the dimensionality of the data by plotting the explained variance against the component index, see e.g. Figure 3.10. This plot is sometimes called a *scree plot*. Ideally, this plot should drop-off quickly, eventually becoming a slowly descending line. The point at which the scree plot becomes linear,

often referred to as the 'elbow', is generally judged to be a good estimate of the dimensionality of the data, or equivalently, the number of basis components K that should be kept. One of the most popular uses of PCA is with data denoising. This is achieved by using a limited set of components to make a model of the original signal, omitting the subsequent components that ideally contain only noise. This is also known as dimensionality reduction.

Non-negative matrix factorisation

Although PCA achieves a unique decomposition by constraining the components to be orthogonal and ordered by variance, this is not a physically meaningful constraint in practice. Non-negative matrix factorisation (NMF) is a method which constrains the factorisation problem in Equation 3.12 by requiring that all components L_{ij} of $\mathbf{L}$ and S_{ij} of $\mathbf{S}$ are non-negative [134]. In the case of SPED, the constraint of positive components is a rational choice in light of the positive nature of PED pattern intensities recorded. Furthermore, non-negativity encourages separation into the distinct parts of the original matrix since they have to be additive. This differs from PCA in that it allows more eigenvectors to be combined to form one part [134], and aids the physical interpretation of components, e.g. [120, 135]. The minimisation of $||\mathbf{X}-\mathbf{LS}||_{\mathrm{F}}$ can be regarded as optimising the set of basis vectors for a linear representation of all data in $\mathbf{X}$. If the correct number of basis signals K is chosen, factorisation using NMF typically gives basis signals that resemble physical signals. The decomposition returns underlying *component patterns* that represent the data, along with associated *loadings* at each real space pixel [120]. The *loading maps* indicate regions where the component patterns are significant, and resemble simplified DF images.

To find the factorisation of a matrix $\mathbf{X}$, both matrices $\mathbf{L}$ and $\mathbf{S}$ are set to initial values and then iteratively improved. The initialisation can be from a random distribution or using a more sophisticated approach. The implementation used by HyperSpy sets the initial values using non-negative double singular value decomposition (NNDSVD) which is based on one SVD process approximating the data matrix $\mathbf{X}$ and another one approximating positive sections of the resulting partial SVD factors. This choice of initialisation gives a non-negative starting point suitable for obtaining a sparse factorisation [136, 137].

The effect of precession

Some of the aforementioned data processing options will here be shown in a discussion of the effect of precession on the results obtained using linear matrix decomposition of S(P)ED datasets. The following examples are demonstrated on cropped S(P)ED scans obtained on an Al-Mg-Si alloy studied at a slightly over-

aged condition. This is the same dataset as shown in Figure 3.9. Two scans were obtained, both with ($\phi = 0.5^\circ \approx 9\,\mathrm{mrad}$) and without precession. Figure 3.10 plots the proportion of variance explained by each of the 20 first components obtained using PCA decomposition.

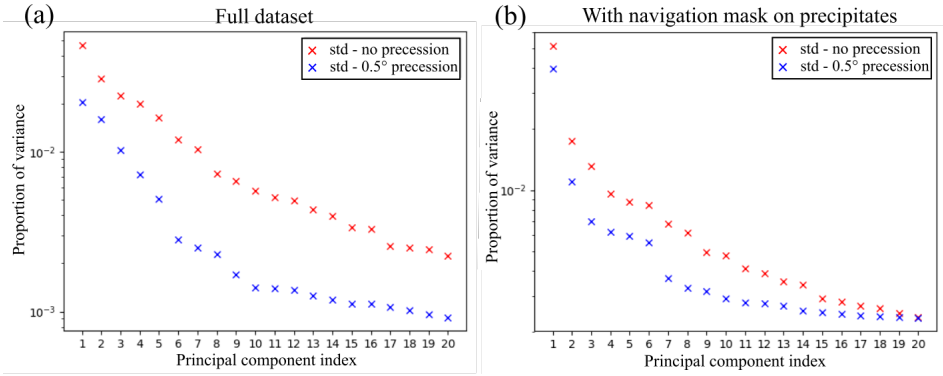

Figure 3.10. Scree plots formed by PCA decomposition (std = standard [128]) using 30 components and centring on the (a) full dataset and (b) pixels located on or near precipitate cross-sections (selected using a navigation mask).

From Figure 3.10a it is seen that for the precessed data, the proportion of variance explained by each component drops off more quickly than without precession. The slope of the datapoints for the precessed scan has more of an 'elbow-shape', whereas the non-precessed data is closer to a straight line. This is a clear demonstration that the precession acts to reduce the number of components needed for a representative reconstruction of the original dataset. Judging from these plots, the precessed data has an approximate dimensionality of 8 and 6 for the full dataset and the scan pixels in proximity of precipitate cross-sections, respectively. For the non-precessed data, it is less clear how many components should be included.

The obtained PCA components are, however, not readily interpretable due to the inclusion of negative values, which has no physical meaning in the context of PED pattern intensities. This is why one usually has to resort to NMF decomposition instead. However, PCA is normally used in a first step to gain an impression of the dimensionality of the data, and thus of how many components are needed in the NMF decomposition. This is particularly important with little or no prior knowledge of the specimen studied.

In the following, NMF decomposition results on S(P)ED data using a navigation mask covering the scan pixels on or near precipitate cross-sections, i.e. the precipitates oriented parallel to the beam (see Figure 3.9b), will be shown. The navigation mask can be seen from the square boxes in loading #1 of Figure 3.11. A

signal mask removing the $\vec{g}_{000}, \vec{g}_{002}$, and $\vec{g}_{022}$ reflections has also been used to avoid oversaturated pixels and to highlight reflections other than those due to the fcc Al matrix. In these scans, acquired in the $[001]_{\mathrm{Al}}$ ZA, a quick visual inspection (Figure 3.9) showed that there are only β'' phase precipitates, and that all 4 orientations of precipitates extended parallel to $[001]_{\mathrm{Al}}$ are present. Therefore, ideally it is expected 5 main components to represent the SPED scan data near precipitate cross-sections: 4 accounting for β'' orientations and 1 due to fcc Al. Figure 3.11 shows 3 selected main NMF components and corresponding loading maps obtained for the precessed and non-precessed dataset.

In Figure 3.11, several things are worth noting with respect to the previous discussions on SPED and data processing. Starting with component #1, it is seen that this component picks out the fcc Al reflections in addition to a significant background intensity. In the non-precessed dataset, one can discern the Kikuchi pattern in this component (highlighted), which is not seen in the precessed component. This was pointed out as an advantage with precession, as the integrating motion will suppress weaker thermal diffuse background scattering [124, 125]. Components #2 and #5 show two different orientations of β'' present in the scan region. Inspection of the scan raw data shows that the numbered precipitates 1-6 and I-IV have equal orientations, respectively. Firstly, it is noted that the extent of precipitate reflections recorded in reciprocal space, indicated by the dashed circle, extends further out in the precessed data, thus intercepting additional reflections compared to the non-precessed scan. This demonstrates another aspect mentioned previously, e.g. in the discussion of Figure 3.8. The reflections of components #2 and #5 for the precessed data also appear more even in intensity, and gradually decreases with increasing scattering angle. This is not the case for the corresponding non-precessed components, which show an uneven intensity distribution. Loading maps #2 and #5 in the precessed scan identify all β'' precipitates of equal orientation. In the non-precessed scan, loading #5 correctly labels the precipitates (albeit some are weak), but loading #2 indicates that additional precipitates have equal orientation, which is incorrect.

Figure 3.12 shows an additional NMF component obtained from the precessed scan data (same as Figure 3.11), revealing another orientation of β'' precipitates present. The component is shown next to a kinematical diffraction simulation of a β'' phase precipitate embedded in a fcc Al matrix as seen from the $[001]_{\mathrm{Al}}$ ZA. The agreement is excellent, confirming the labelling. It is seen that kinematically forbidden reflections are present in the component pattern, i.e. a dynamical effect. 5 precipitates in the scan region (numbered) correspond with this orientation. Similarly, Figure 3.13 shows 4 NMF components and associated loadings of the same β'' orientation as that of Figure 3.12, but obtained for the non-precessed scan

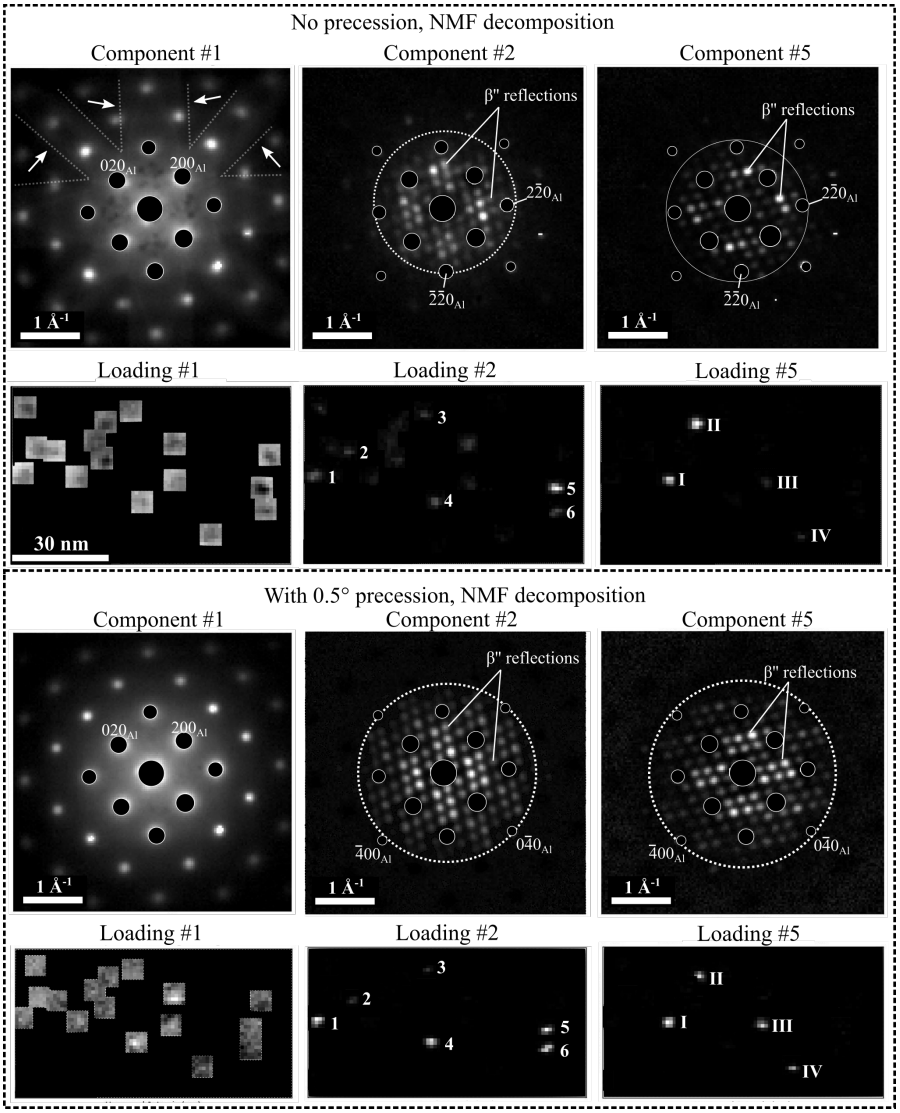

Figure 3.11. Selected NMF components and associated loading maps obtained for S(P)ED scans acquired in the same region with and without precession. The black circles covering the main fcc Al reflections and the square boxes seen in loading #1 represent respectively, the signal- and navigation mask that was used in the NMF decomposition (see HyperSpy documentation [128]). Arrows indicate Kikuchi bands. Numbers and Roman numerals highlight precipitates of identical orientation. The dashed circles indicate the extent of precipitate reflections in reciprocal space.

data. Although all 4 components correspond with the same phase and orientation, different precipitates (numbered 1-5) are picked out in each loading map due to significant variations in diffracted intensities. This shows that a single component of the precessed scan conveys the same information as multiple components in the non-precessed scan.

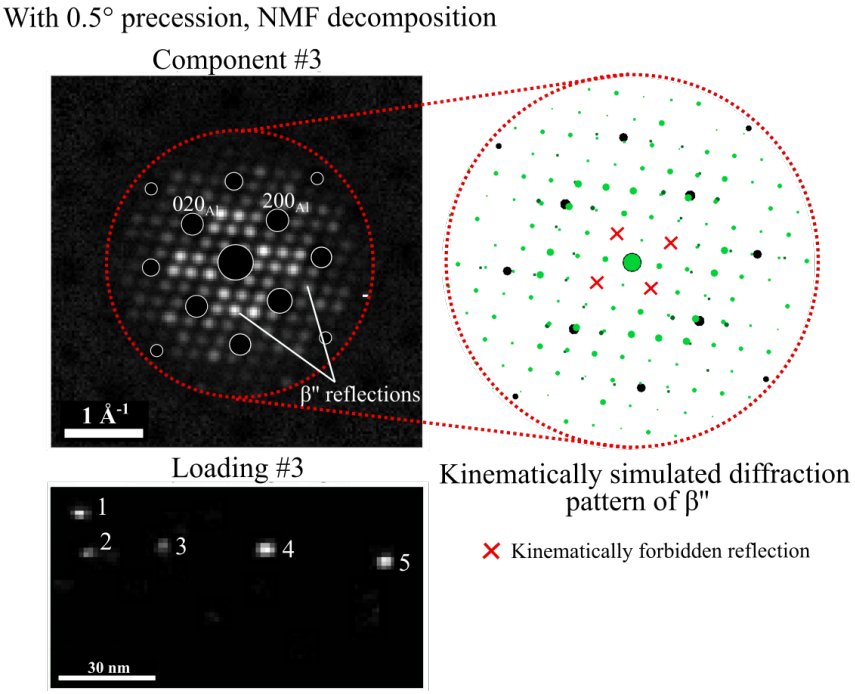

Figure 3.12. NMF component and associated loading #3 obtained for the precessed scan data. A kinematic simulation of a β'' phase precipitate (green) embedded in a fcc Al matrix (black) as seen from the $[001]_{\mathrm{Al}}$ ZA is shown to the right. Numbered precipitates 1-5 correspond with the presented component pattern. This is the same dataset as analysed in Figure 3.11.

All aspects pointed out in this discussion confirm the results of the PCA analysis of Figure 3.10, which showed that there exists significantly less variation across precessed scans, which greatly improves matrix decomposition results. This has major implications, and is the main explanation for the successful application of SPED as used in this thesis. Papers **I**, **II**, **IV**, and **V** have used SPED for statistical assessment of the distribution of precipitate phases. As demonstrated here, this constitutes a powerful approach which could serve as an important tool in future alloy developments.

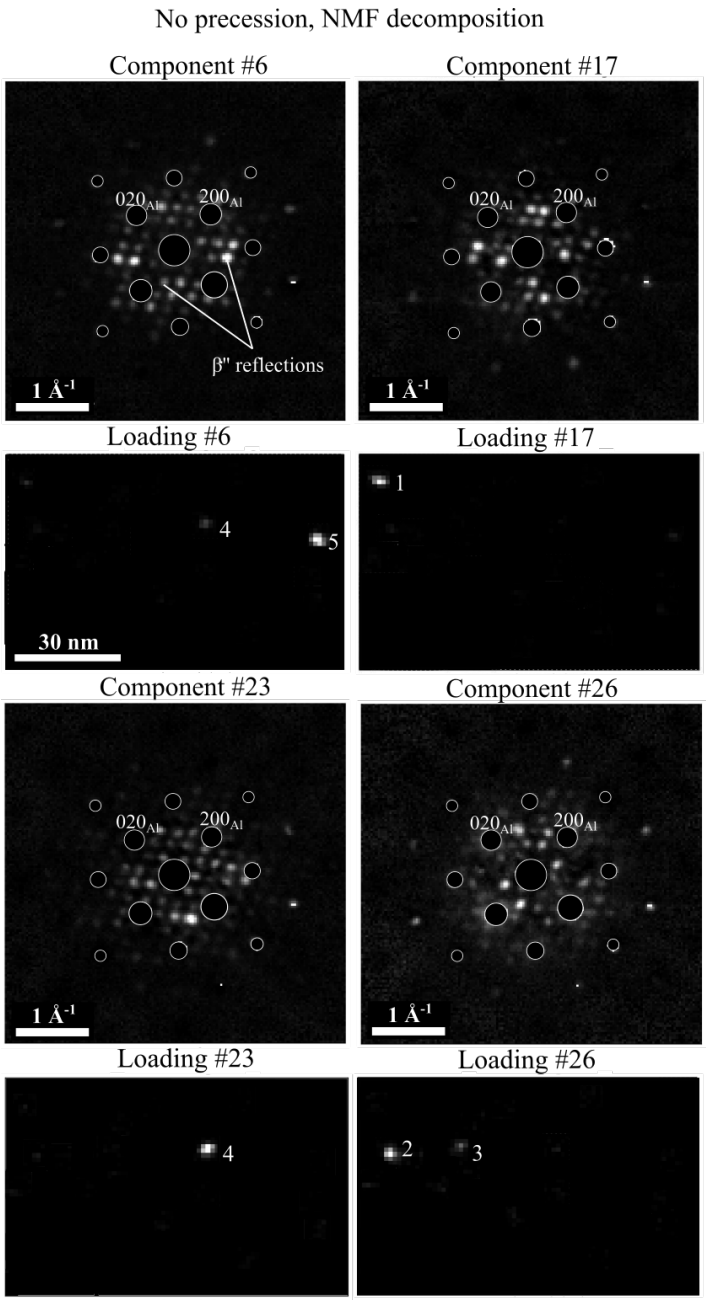

Figure 3.13. 4 NMF components and associated loadings obtained for the non-precessed scan data, showing a single orientation of β'' phase precipitates present in the scan area, cf. Figure 3.12.

PART II

RESEARCH COMMENTARY

Chapter 4

Summary of Papers

This thesis contains seven research papers that comprise the main part of the scientific work done within the PhD project. All papers are focused with the study of metastable precipitate phases formed in age-hardening Al alloys, primarily by the use of TEM. The majority of papers study precipitate phases from the Al-Mg-Si(-Cu) system (6xxx), in addition to one paper (Paper **III**) studying a dispersoid-precipitate aggregate formed in an Al-Cu-Mg-Ag alloy (2xxx). Most papers also make use of the diffraction technique SPED, either directly (Paper **I**–**V**) or indirectly (Paper **VI**), with the exception of Paper **VII**, which combines TEM and APT. As explained in the introduction, section 1.2, all papers have resulted from attempts to advance TEM techniques of interest to the TEM research group and/or from studying materials and research topics of relevance to the AMPERE project. More specifically, all papers fall into one or several of the three following categories: SPED technique development and application, thermomechanical aspects of Al-Mg-Si(-Cu) alloys from Neuman Aluminium Raufoss (AMPERE alloys), and conductivity studies of Al-Mg-Si alloy 6101 from Hydro (AMPERE alloy). This chapter provides a summary of the main findings in each paper produced.

Paper I – Precipitate statistics in an Al-Mg-Si-Cu alloy from scanning precession electron diffraction data

In this paper we wanted to provide a good example demonstrating the added information SPED and related data processing could offer in the quantification of the precipitate microstructure in an Al-Mg-Si-Cu alloy. The alloy and condition studied formed a relatively dense distribution of precipitates, with a number density of $\approx 67\,000\,\mu\mathrm{m}^{-3}$, and with precipitate phases mainly falling into one out of three categories: β'' phase, L phase, or hybrid. The precipitate number density and the relative fraction of phases (%) were first assessed using conventional

TEM methodologies, which include manual counting on high contrast BF images. The categorisation of phases was determined from high magnification BF images, where the geometry of the precipitate cross-section area with respect to the crystallographic directions may often reveal the underlying phase. Cross-sections that were not distinguishable from geometric considerations were simply put in the category hybrid. Secondly, SPED was used to obtain a large $[001]_{\mathrm{Al}}$ ZA scan comprising 247 500 PED patterns, covering an area of $1.34\,\mu\mathrm{m}^2$ in 550×450 pixels, and containing over 3700 precipitates aligned parallel to the beam direction. The number of precipitates was extracted using a blob-detection algorithm on a VDF image formed from precipitate phase reflections, and the number density was subsequently calculated. Information on precipitate types was obtained using NMF decomposition on the PED pattern stack. The resulting NMF component patterns were manually compared to (kinematically) simulated diffraction patterns of phases in the Al-Mg-Si-Cu system, which enabled phase determination. It was shown that the analysis of the data in a single SPED scan yielded precipitate number densities in close agreement to conventional methodologies, giving $(65\,700 \pm 6700)\,\mu\mathrm{m}^{-3}$ and $(67\,800 \pm 5500)\,\mu\mathrm{m}^{-3}$ for the two approaches, respectively. Obtained phase fractions showed significant deviations between the methods. This is concluded to be a consequence of inaccuracy in traditional routines being based on purely geometric considerations. With implications of equal sensitivity in the two approaches, the SPED estimate of phase fractions is considered much more reliable. Due to the increased objectivity of the new approach, the results are more readily reproducible. This has important implications for the validity and use of TEM statistics in future alloy developments, as this requires reliable statistical assessment of precipitates in order to link the microstructure with material properties, e.g. through physically-based models.

Paper II – The evolution of precipitate crystal structures in an Al-Mg-Si(-Cu) alloy studied by a combined HAADF-STEM and SPED approach

This work is focused with the demonstration and explanation of a combined HAADF-STEM and SPED approach used to study the precipitation in an Al-0.80Mg-0.85Si alloy with a low addition of Cu (0.01 at.%). The alloy was manufactured by Neuman Aluminium Raufoss, and is used in applications such as the crash-system and the steering components of automotive vehicles. The alloy was studied at multiple ageing conditions (mainly overaged), using SPED to assess the overall distribution of precipitate phases, and HAADF-STEM to look closely at the atomic structure of the precipitate phases formed. Combining SPED results and precipitate volume fraction measurements by TEM, the total amount of solute atoms locked inside precipitates could be approximated. At peak hardness, the precipitates were predominantly observed as pure β''. Upon further heat treatment, the

precipitates evolved into complex hybrid structures, primarily comprising Al-Mg-Si phases like β'' and U2 in the precipitate interior. Cu-enriched columns and sub-units of Cu-containing phases like Q′/C and β'_{Cu} existed at the precipitate interface. With increased ageing the precipitates coarsened substantially, and exhibited a $\langle 001 \rangle_{\mathrm{Al}}$ projected hexagonal Si network with β'/β'_2 in the precipitate interior. Unit cells/sub-units of Cu-containing phases were still confined to the precipitate interface, but had grown larger in extent. Beyond this point it was seen a slow, but gradual progression inwards into the precipitates by the Cu-containing Q′-phase, with Cu atomic columns incorporating less Cu atoms than what could potentially be accommodated. Q′ was eventually seen to dominate the precipitate structures. The results showed that even a low Cu content (0.01 at.%) can significantly affect the Al-Mg-Si system precipitation, especially during overageing. This has important implications for the recycling of Al alloys, where the inclusion of trace elements is practically unavoidable.

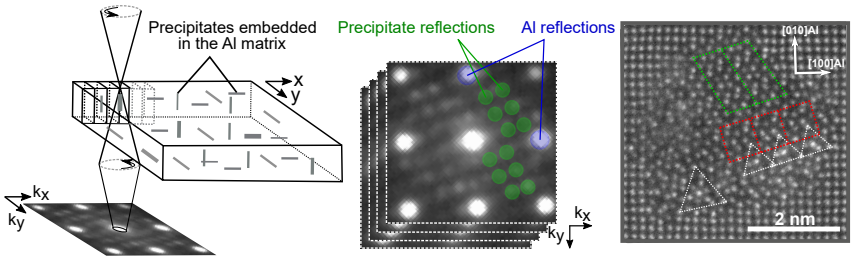

Figure 4.1. Graphical abstract of Paper **II** showcasing the SPED scan data recording and a HAADF-STEM lattice image of a hybrid precipitate cross-section.

Paper III – Crystallographic relationships of T-/S-phase aggregates in an Al–Cu–Mg–Ag alloy

This paper demonstrates a different application of SPED than the former two papers, where it was primarily used for phase mapping. Here, it was demonstrated a methodology for correlating high-resolution (HR)TEM imaging and SPED to allow precise analysis of ORs and disorientations at high spatial resolution ($\approx 1-2\,\mathrm{nm}$). The system studied was an intricate dispersoid-precipitate aggregate in a 2xxx series Al-Cu-Mg-Ag alloy. The aggregates consisted of the T-($Al_{20}Cu_2Mn_3$) phase dispersoid which exhibits rotation twinning, coupled with S-(Al_2CuMg) phase precipitates, and surrounded by fcc Al. T-phase dispersoids are important for limiting recovery and controlling grain growth in Al-Cu alloys. However, these dispersoids can also reduce precipitation hardening by acting as heterogeneous nucleation sites, and may lead to increased susceptibility towards pitting corrosion when galvanically coupled with S-phase precipitates. The crystallographic relationships between the T-phase, S-phase, and surrounding Al matrix were investig-

ated by combining SPED with misorientation analysis in 3-dimensional axis-angle space and HRTEM. ORs were identified between all three phases, confirming previous findings and revealing the S-T ORs for the first time. Differences in S-Al ORs for precipitates formed at T-phase interfaces compared to their non-interfacial counterparts formed in the bulk were also identified.

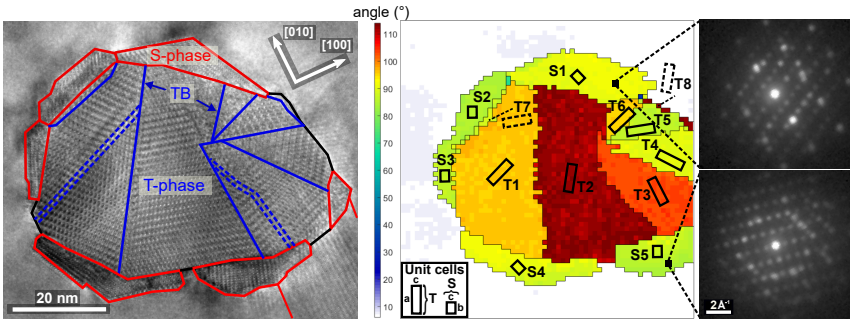

Figure 4.2. Graphical abstract of Paper **III**, showing a HRTEM image of a T-/S-phase aggregate next to orientation mapped SPED data of the same aggregate structure.

Paper IV – *In situ* heating TEM observations of evolving nanoscale Al-Mg-Si-Cu precipitates

In this paper we combined the developed SPED approach for phase mapping with another powerful technique, namely *in situ* heating TEM. The material studied was a high strength Al-Mg-Si-Cu alloy which mainly formed β'' phase and L phase precipitates after moderate thermal ageing. A $[001]_{\mathrm{Al}}$ oriented lamella was prepared by focused ion-beam (FIB), with the orientation determined by scanning electron microscopy (SEM) and electron backscatter diffraction (EBSD). A single region of interest was systematically studied by BF imaging and SPED in order to follow the distribution and identities of transforming precipitates. The distribution and crystal structure of precipitates were determined by SPED at multiple stages, pinpointing the precipitates that underwent phase transformations during heating. The results were compared to conventional TEM studies of the material heat treated *ex situ*. This revealed differences in the transformation kinetics of precipitates in an electron transparent lamella (thickness $\geq$90 nm) to that of macroscopic bulk specimens. The high thermal resistance of the L phase was demonstrated, being one of the main phases remaining after multiple stages of high thermal exposure ($180-240\,^{\circ}\mathrm{C}$). β'' was the main precipitate phase near peak-hardened conditions, and formed a high number density of precipitates. A few % of the β'' precipitates subsequently transformed to β'/Q′ phases, whereas the rest dissolved. To our surprise, two regions at different thicknesses, roughly $130\,\mathrm{nm}$ and $90\,\mathrm{nm}$, showed a very dense microstructure of precipitates and a sparsely populated region at the

same heating stage, respectively. Potential explanations for the latter finding was also discussed.

Paper V – The effect of low Cu additions on precipitate crystal structures in overaged Al-Mg-Si(-Cu) alloys

This work combined HAADF-STEM lattice imaging, SPED-based phase quantification, and DSC to study the effect of low Cu additions on the evolution of precipitate crystal structures in three high strength Al-Mg-Si(-Cu) alloys during overageing. The three alloys, one of which was also studied in Paper **II**, were manufactured by Neuman Aluminium Raufoss. All alloys are intended for applications in the crash-system and the steering components of automotive vehicles. It was found that relatively small changes in the Cu level and the Si:Mg ratio had significant effects on the resulting distribution of precipitate phases, their structural evolution, and their thermal stability. Two Si-rich alloys formed hybrid β' phase and Q$'$ phase precipitates on overageing. A third Mg-rich alloy primarily formed L phase precipitates, which exhibited superior thermal stability. Three distinct Cu-containing sub-units that form the basis for all Al-Mg-Si-Cu precipitate phases were identified: the three-fold symmetric Q$'$/C and the β'_{Cu} sub-units, in addition to a newly discovered C sub-unit. The formation of each sub-unit was discussed, and the atomic structures and connections to other precipitate phases in the Al-Mg-Si(-Cu) system were elaborated. Furthermore, it was presented a careful explanation of the naming conventions used for precipitate phases and phase sub-units, which was seen as necessary due to the increasing numbers of overlapping naming conventions seen in the field. The work provided new insights into the complex precipitation of Cu-added Al-Mg-Si alloys, with implications for material properties and importance in modelling work on the Al-Mg-Si-Cu system.

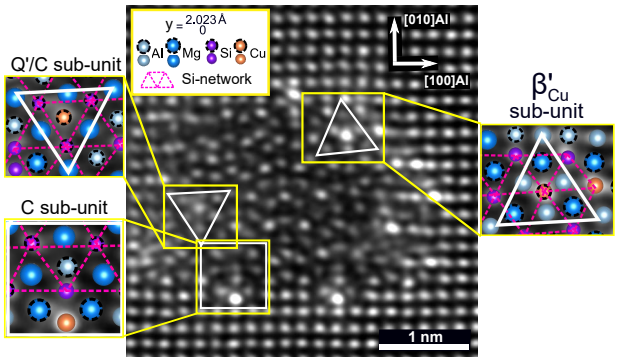

Figure 4.3. Graphical abstract of Paper **V** showing a HAADF-STEM image of a L phase showcasing all 3 identified Cu-containing sub-units of the Al-Mg-Si-Cu system.

Paper VI – Linking mechanical properties to precipitate microstructure in three high strength Al-Mg-Si(-Cu) alloys

In this work we investigated the connection between material strength and ductility to precipitate statistics in three high strength Al-Mg-Si(-Cu) alloys (Cu$\lesssim$0.1 at.%). These were the same alloys as studied in Paper **V**, and these two papers highly complement each other. A range of ageing conditions were examined in order to understand the effect of an evolving precipitate microstructure and the results were used as input for strengthening models. The mechanical properties were obtained by tensile test experiments and microstructure characterisation was attained by TEM. The results showed that minor changes to the Si, Mg, and Cu additions – the total addition (at.%) kept approximately equal – had a significant impact on measured material properties, with corresponding changes in the precipitate microstructure. On the peak strength plateaus, differences as large as 35 MPa in yield strength were measured between the strongest and weakest alloy, obtained as 410 MPa and 375 MPa, respectively. Higher material yield strength correlated well with a refined precipitate microstructure comprising higher number densities of smaller precipitates. Differences with respect to material ductility first appeared after moderate overageing, showing negative correlation with material strength. At significantly overaged conditions the differences in strength exceeded 100 MPa, demonstrating large differences with respect to the thermomechanical stability of these materials, which has important consequences for alloys exposed to elevated temperatures under in-service conditions. The paper illustrated clearly the large differences in material properties that may result from small variations in alloy compositions, and which could be explained based on observed differences in precipitation.

Paper VII – On the microstructural origins of improvements in conductivity by heavy deformation and ageing of Al-Mg-Si alloy 6101

A lean Al-Mg-Si conductor alloy produced by Hydro was studied after two different TMP routes. Conventional solution treatment, quenching, and following artificial ageing at $170\,^{\circ}\mathrm{C}$ was compared to a process applying solution treatment, quenching, pre-ageing ($7\,\mathrm{h}$ at $170\,^{\circ}\mathrm{C}$), 50% thickness reduction by cold-rolling, and subsequent re-ageing at $170\,^{\circ}\mathrm{C}$. Ageing after rolling resulted in a rapid increase of conductivity, maintained at a $2-3\%$IACS gain relative to the conventionally aged material. The main underlying explanation was shown to be an increased solute depletion of the Al matrix after ageing of the deformed material, as quantified by APT. The principal mechanism leading to the rapid increase is proposed to be dislocation-mediated diffusion. By deforming a pre-aged microstructure, the dislocations introduced will be pinned at multiple points on precipitates and solute enriched regions, causing an entangled dislocation microstructure that acts as a

'solute highway' on subsequent ageing. It was also suggested that the difference in electrical conductivity developed in two main stages. In the initial stage, at the onset of re-ageing, a rapid change occurred due to dislocation-mediated diffusion, effectively vacuuming the matrix of solutes. Concurrently, bulk nucleation and growth is mediated by increased vacancy levels after deformation. After roughly $2\,\mathrm{h}$ re-ageing the slopes of the conductivity curves were nearly equal in the two material states, and the subsequent stage is characterised by overageing behaviour, with precipitate coarsening and dissolution of smaller precipitates. Differences in forming precipitate distributions were also observed, as shown by TEM results.

Chapter 5

General Discussion and Outlook

This chapter provides a commentary to the research conducted in this PhD project. It includes the background and motivation behind the different studies, an explanation of the coherence between the papers, as well as a comparison of the research questions answered. Furthermore, the research is put into a broader context of several other relevant and important works published within the field. Finally, the author's thoughts on the outlook of the research topics covered in this thesis are presented.

5.1 Discussion

In 1994, with the aim to establish a viable alternative to convergent beam and plane wave illumination for measuring diffracted intensities suitable for structure determination, Roger Vincent and Paul A. Midgley based at the University of Bristol described their implementation of *a double conical beam-rocking system* [114], which later came to be known as precession electron diffraction (PED). Their key idea was that by using a hollow cone illumination, they could eliminate the excitation errors for a subset of reflections while simultaneously reducing the contribution of non-systematic dynamical perturbations to the diffracted intensities. The advantages of PED were that a far greater number of reflections were seen in a PED pattern than in a conventional (static) diffraction pattern, and the intensities were in many aspects 'more kinematic' in nature, which is crucial for ab-initio structure determination.

Seeing another possibility with PED, Rauch et al. [117] coupled the technique with the microscope scanning system, thus implementing a scanning PED technique, i.e. SPED. SPED was first developed as a technique complementary to electron backscatter diffraction (EBSD) [138] in a SEM, to provide orientation information

in the form of grain structure, texture, misorientation, inverse pole figures, etc. In addition to providing a larger number of reflections to aid accurate indexing, PED also improved the fidelity of the results [118, 119], by effectively averaging out small variations in orientation, thus aiding phase identification. Furthermore, PED helped to reduce the structured background in diffraction patterns, typically from Kikuchi diffraction, by averaging across a large number of orientations, and thus increasing the reliability of peak-finding algorithms [124, 125].

At its 20th year anniversary in 2014, (S)PED had grown to become one of the main techniques in electron crystallography [139]. The technique has been installed on many microscopes, and has been demonstrated to significantly improve orientation and phase mapping [118, 140, 141], strain mapping [122, 123, 142, 143], and 3D interphase crystallography [120]. Particularly, SPED has improved the precission in strain mapping significantly, which is attributable to many of the same effects as mentioned for orientation mapping [144]. Improvements in the precision for strain mapping is of key importance in the semiconductor industry, where strain can be introduced to increase carrier mobilities [145]. Finally, unwanted channeling effects have also been demonstrated to be reduced by the precessing motion in the case of EDS and EELS measurements [126, 127].

Prior to this PhD project, the potential value of SPED in the studies of age-hardening Al alloys had already been explored through the author's Master's thesis [146]. Here, various aspects of SPED and data processing were investigated with the purpose of studying different precipitate phases and dispersoids of the Al-Cu (2xxx) system, including: virtual imaging, data decomposition, orientation mapping, and more. Despite the simplicity and crudeness of the acquisition system, single pixel PED patterns showed surprisingly high sensitivity, and still revealed basic information when pushing the technique to the lower bounds of probe and scanning step sizes. Furthermore, in combination with data visualisation and processing as primarily facilitated through the open-source Python library HyperSpy [128], the SPED data could be analysed in an efficient manner to uncover rich information about the material microstructure. The quality of the results was often comparable to other conventional TEM techniques, such as selected area electron diffraction (SAED), BF, and DF imaging. The results were however processed and extracted off-line, with a plethora of options for further data treatment. An example that illustrated the sensitivity of SPED was the data obtained on an Al-Cu-Li alloy, which formed plate-shaped T_1 (Al_2CuLi) and θ' (Al_2Cu) precipitate phases forming on $\{111\}_{Al}$ and $\{001\}_{Al}$ planes, respectively. The T_1 phase shows particularly high resistance to coarsening in the plate thickness direction [147], and often forms one lattice parameter thick ($\approx 1.39\,\mathrm{nm}$). The diffracting signal from T_1 plates were clearly observed in SPED scan data from the $\langle 001\rangle_{Al}$ ZA, and the signal was suf-

ficiently strong to determine the orientation of the precipitate. The precipitate was embedded in a fcc Al matrix of $\approx 90\,\mathrm{nm}$ thickness. The fact that single pixel PED patterns acquired with a $0.7\,\mathrm{nm}$ diameter probe (non-precessed) could reveal the presence and orientation of a phase comprising only a few % of the illuminated specimen volume at the scan position was an encouraging finding. It was largely due to this and similar observations, combined with the increasing usage of SPED seen in the scientific literature, that it was decided to attempt using SPED to study the $\langle 001 \rangle_{\mathrm{Al}}$ oriented precipitate needles/rods of the Al-Mg-Si-Cu system.

The two first papers of this thesis describe the development and application of SPED combined with related data processing to study the various Al-Mg-Si-Cu precipitate phases and their distributions (Paper **I** and **II**). The first experiments undertaken in the PhD project was to conduct TEM and SPED studies of different ageing conditions of the Neuman Aluminium Raufoss 6082 alloy, Al-0.80Mg-0.85Si at.%, shortened **S** for 'standard'. It became progressively clearer that the structure of precipitate needles/rods in the Al-Mg-Si(-Cu) system, with long axes parallel to $\langle 001 \rangle_{\mathrm{Al}}$ directions, lent themselves rather well for SPED data acquisition in the $[001]_{\mathrm{Al}}$ ZA for the precipitates extended parallel to the beam direction. Starting from peak aged conditions and towards more overaged conditions, the diffraction signal from individual precipitates was normally sufficiently strong to determine its main character. Data decomposition using NMF [120, 134] worked impressively well, and the majority of components showed clear resemblance to kinematic diffraction patterns from expected phases present. Although the main categorisation of phases present was relatively clear, complications arose due to the hybridity of forming phases, as seen from atomically revolved HAADF-STEM observations in this alloy. This resulted in additional component patterns that appeared to comprise a mix of multiple precipitate phase reflections. This hybridity formed due to the small inclusion of Cu in alloy **S**, only 0.01 at.%, which was seen to cause a gradual change in the precipitate crystal structures. However, the results were promising and these were the developments that would eventually form the basis of Paper **II**.

Putting complications aside temporarily, it was clear to us that the development of a SPED approach to study Al alloy precipitates held many advantages over conventional TEM microstructure characterisation methodologies, see e.g. [148]. In order to prove this point we decided to write Paper **I**, providing a clear example of the comparison of SPED vs. conventional TEM methodologies for the characterisation of an Al-1.11Mg-0.50Si-0.16Cu at.% alloy. The alloy was external to the AMPERE project and had been characterised previously by conventional TEM methodologies in the work of Marioara et al. [31], where it is referred to as alloy

K13[1]. In addition to having been previously characterised, this alloy was selected as it primarily formed two different phases at moderately overaged conditions, namely the β'' phase and L phase, which have notably different crystal structures. The fact that we were able to show that analysis of SPED data gave a precipitate number density in close agreement to conventional methodologies was a particularly important finding, as it indicated that SPED had sufficient sensitivity to capture similar numbers of precipitates as the broad beam illumination mode of BF imaging. The number density of precipitates was relatively high ($\approx 67\,000\,\mu\mathrm{m}^{-3}$), and the precipitate volumes were also at the lower end of the spectrum, promoted by the high Mg:Si ratio and significant Cu addition. In combination, this represented a good case for a proof of principle demonstration.

The implication of comparable sensitivities with both techniques provided further support for the main advantage in the SPED-based approach, which was in the statistically improved estimate of precipitate phase fractions (%). The drawbacks with traditional methodologies are that they rely heavily on manual counting and interpretations of BF, TEM high resolution, and/or HAADF-STEM results. This does not scale well with increasing numbers of precipitates, and the analysis holds a highly subjective character. The accuracy in calculated numbers is highly dependent on the knowledge and expertise of the microscopist and the person analysing the data. The SPED-based approach, however, scales rather well, as an increasing scan size and hence increasing precipitate numbers comes at a low price in terms of increased time in analysis of the data. The SPED scan presented covered $1.34\,\mu\mathrm{m}^2$ and over 3700 precipitates aligned parallel to the beam direction, which are considerably more than what could be covered in a manual approach. By offering increased objectivity and improved statistics, this approach may become a valuable resource in verification of modelling work and in the future of Al alloy characterisation and developments.

The study of alloy **S** was subsequently continued, and eventually resulted in Paper **II**. Here it was provided a more careful explanation of the SPED methodology for phase analysis, and a thorough assessment of the effect of low Cu additions on the precipitate crystal structures after prolonged ageing at $180\,^{\circ}\mathrm{C}$. Another important consideration in favour of SPED that was demonstrated in this work, was how a generalisation from a series of, usually, some 10-40 atomically resolved HAADF-STEM images can give a misleading – or perhaps just an incomplete – general picture of the precipitate phases existing in the alloy microstructure. This can especially occur when there exist large variations between precipitate phases formed. There is a risk of selectively probing larger, Cu-containing precipitates

[1]This alloy was patented (# EP2553131A4) and is now an important alloy in the Norwegian industry for production of car steering columns.

due to the strong Z-contrast dependence of HAADF-STEM. Adding to this point, a poor depth of focus due to the focused probe in the HAADF-STEM mode leads to further selective imaging of longer, coarsened precipitates that reach close to the specimen surface. Besides the risk of selectively probing precipitates, rare cases such as the L phase or the Q′/β_2' phase discovered might be missed in a HRTEM/HAADF-STEM study. The images acquired of these phases were obtained after analysing the SPED scan data, where the NMF decomposition results [120, 134], revealed the presence of rare phases in this alloy condition, which were then retrieved and imaged by HAADF-STEM. Again, it was shown how a scanning technique capable of covering large areas necessarily will give a more general picture of precipitate phase distributions. It should also be made clear that the information content of HAADF-STEM is invaluable in assessing the details of the crystal structure of individual precipitate phases. It is the power of the two techniques combined that is highlighted in this work. The results also showed that even a low Cu content (0.01 at.%) can significantly affect the Al-Mg-Si system precipitation, especially during overageing. This has important implications for the recycling of Al alloys, where the inclusion of trace elements is practically unavoidable [7, 149].

Occurring in parallel to the developments that lead to Paper **II**, we wanted to demonstrate other capabilities with SPED in the study of Al alloys than applied as a phase mapping tool. After the author's research visit to prof. Paul A. Midgley's group at the University of Cambridge, we conceived the idea of applying their ongoing developments in interphase crystallography and misorientation spaces [121, 150], to study an intricate dispersoid-precipitate aggregate observed in an Al-Cu-Mg-Ag alloy from the author's Master's thesis. The aggregate comprised T-($Al_{20}Cu_2Mn_3$) phase dispersoids which exhibit rotation twinning [151], coupled with S-(Al_2CuMg) phase precipitates [152], and surrounded by the Al matrix. This system represented an interesting case for studying interphase crystallography, and due to its size it would not have been feasible to study using SEM-EBSD or X-ray approaches. In Paper **III**, by correlated imaging and scanning diffraction, we demonstrated precise analysis of ORs and disorientations at high spatial resolution for this T-/S-phase aggregate. The approach has potential for broad applications within multi-phase materials where phase coherency is decisive for macroscopic properties.

The idea behind Paper **IV** was to combine the developed SPED approach for phase mapping with another powerful technique, namely *in situ* heating TEM. As detailed in the introduction on the motivation behind this PhD project, see section 1.1, understanding the effect of prolonged time and temperature on the microstructure of Al-Mg-Si-Cu alloys has been a central research topic in the AMPERE

project. Up to this point, the approach for studying this topic had been to examine progressively more overaged samples, with electron transparent samples prepared from *ex situ* heated bulk materials. To attempt *in situ* heating TEM was a goal set from the beginning of the PhD work, due to its high relevance by combining: (i) TEM competence building and (ii) studying AMPERE materials and key research topics. TEM *in situ* studies have recently been made very powerful due to large improvements in specimen preparation techniques and the development of TEM holders with high mechanical and thermal stability. Due to the nanoscale nature of the age-hardening precipitates in Al alloys, it was only recently that one has been able to study them *in situ* at the atomic level [153–155]. The main examples are taken from Al-Cu alloys, and the study of the Cu-rich, tetragonal θ' (Al_2Cu) phase [156]. This plate-shaped phase lends itself particularly suitable for observations in STEM mode due to the comparably high atomic number of Cu (Z = 29) to Al (Z = 13). This is not feasible in the Al-Mg-Si system, having Z = 13, 12, and 14, respectively. Previous *in situ* heating studies of precipitates in the Al-Mg-Si alloy system, including X-ray, neutron, and TEM experiments, have measured the overall changes to the distribution of precipitates (lengths, densities, etc.) with thermal exposure [157–159]. We decided to study the Neuman Aluminium Raufoss alloy Al–0.86Mg–0.62Si–0.1Cu (at.%), labelled **M** (for 'Mg'), as it was known that this alloy formed a two-fold distribution of β'' phase and L phase with moderate ageing. From the previous work on alloy K13 [31] (Paper **I**), the L phase had proven advantageous in terms of improving thermomechanical stability, and to confirm this by direct *in situ* observations would be interesting. Different from other previous *in situ* works on Al-Mg-Si(-Cu) alloys, we decided to study a single region of interest, in order to follow directly the distribution and identities of transforming precipitates. This was the only way of directly demonstrating the high thermal resistance of the L phase as compared to the β'' phase. We managed to demonstrate this by showing that a large fraction of L phases remained after multiple stages of high thermal exposure ($180 - 240\,^{\circ}\mathrm{C}$). This finding has important implications as it might be possible to develop alloy compositions and heat treatment procedures which optimise for L phase precipitates, and which could hence yield large improvements in the thermal resistance of Al-Mg-Si-Cu alloys. This is particularly important for alloys that might see elevated temperatures under in-service conditions, such as in heat exchangers and components located near automotive engine rooms.

Another important finding in this paper was the large difference in precipitation kinetics observed in two regions at different specimen thicknesses. After several hours at varying high temperature exposure ($180 - 240\,^{\circ}\mathrm{C}$) a region of $\approx 130\,\mathrm{nm}$ thickness showed a very dense microstructure of coarsened and elongated precipitates, indicating an overaged material state. The main region studied had a

thickness of $\approx 90\,\mathrm{nm}$, and showed a sparsely populated region at the final heating stage, where most precipitates had partially or completely dissolved. The underlying reasons for this difference was discussed, and must be better understood in order to increase transferability to bulk precipitation behaviour. It has previously been shown that there was a significant migration of Si and Mg to the surface of an Al–Mg–Si–Li alloy at $200\,^{\circ}\mathrm{C}$, with concentrations exceeding 10 at.% for both atomic species in the top nanometre of the specimen [160]. Mg was shown to migrate towards GBs, whereas Si was ubiquitous. The many interesting findings and new questions that arose from the *in situ* heating TEM studies were planned to be taken further, with some recent results planned to be shown at the International Conference on Alumiinium Alloys (ICAA17 2020, Grenoble) this year, which was postponed due to the COVID-19 pandemic.

Papers **V** and **VI** showcase the large amount of TEM and material property data accumulated in the AMPERE project in the studies of the three Neuman Aluminium Raufoss Al-Mg-Si(-Cu) alloys labelled **S**, **C**, and **M**. Paper **V** focuses on TEM high resolution studies of the distribution and crystal structures of precipitate phases forming in the three alloys as a function of ageing. Paper **VI** is focused with microstructure-property relationships in the alloys, which is combined with modelling work on yield strength. The alloys are intended for applications in the car crash system and steering column, putting high demands on thermomechanical stability and crashworthiness. Despite having similar compositions, the alloys exhibited significant differences with regards to precipitation and material properties. Particularly, the shift to being Mg-rich with slightly increased levels of Cu in alloy **M** was seen to have advantageous consequences for retained mechanical strength with prolonged ageing. The combined results of these two papers, along with their respective supplementary information, represent a body of data whose level of detail is rarely seen in the field. It is the intent of the authors that these papers spark further investigations on e.g. modelling work of precipitation and strength/work-hardening, as the data has been made readily available for others to use. In Paper **V**, we have also a significant effort to carefully explain the terminology and names used to describe the different Al-Mg-Si(-Cu) precipitate phases and their sub-units. We felt this was needed due to the observed inconsistency seen in the scientific literature. A lot of research is produced every year on the Al-Mg-Si-Cu system, and for ease of navigation through the literature, it is essential to avoid causing unnecessary confusion.

The final study presented in this thesis, Paper **VII**, is a manuscript under preparation that focuses on the electrical properties of a lean 6101 Al-0.54Mg-0.38Si at.% conductor alloy. As pointed out in the introduction, section 1.1, Al is a serious contender for electrical wires in cars and subsea cables due to its high conductivity-

to-weight and strength-to-weight ratio, in addition to significantly lower cost than Cu. Several previous studies have demonstrated how different TMP routes may yield a combination of improved mechanical and electrical properties, such as: by severe plastic deformation (SPD) [59–61], hydrostatic extrusion [161], drawing [92], and rolling [90, 91]. The general impression of the author was that the main focus of previous studies was with demonstrating material property improvements with respect to conductivity and strength, as opposed to focus on the underlying cause and mechanisms behind these improvements. These underlying mechanisms were the focus of this manuscript, which studies the microstructure of Hydro alloy 6101 subjected to two different TMP routes. The difference in conductivity ($2-3\%$IACS) that developed after application of the two different TMP routes, could largely be explained based on the increased solute depletion of the Al matrix after thermal ageing of the deformed material, as compared to the undeformed material. The difference in solute levels of the Al matrix was quantified by APT experiments.

5.2 Outlook

The perhaps biggest paradigm shift in the recent history of TEMs, was the development and successful implementation of aberration corrected lenses in the 1990s [103]. This monumental improvement paved the way for the impressive capabilities of modern day TEMs, which peer at the ultimate length scales of materials – even smaller than the Bohr radius[2], see e.g. [102]. More recently, another revolution is taking place with the introduction of direct electron detectors (DEDs)/direct detection devices (DDDs) for replacing traditional image detectors in TEMs. By building on technologies developed for particle physics, pixelated detectors developed for X-ray imaging have been recently adopted for electron imaging [106, 107]. Traditional image detectors use scintillator and optical transfer path (fiber-coupling or lens) to convert the high energy electrons to photons, which are subsequently transferred to the imaging sensor to form an image. This indirect detection approach has several drawbacks, including: (i) loss of image resolution and sensitivity during the electron-photon conversion, and (ii) the photon transfer as an additional source of noise that degrades the signal-to-noise ratio (SNR) of the detector. DED imaging devices have been developed based on technology advancements in complementary metal oxide semiconductor (CMOS) design and manufacturing, high speed data architectures, vastly increased memory densities, and speed. The elimination of the scintillator and the subsequent optical transfer path has significantly improved the detective quantum efficiency (DQE) – a critical measure of SNR [162]. This new generation of DEDs has revolutionised

[2] $r_0 = 5.29177210903 \cdot 10^{-11}$ m

the field of cryo-electron microscopy (cryoEM) in structural biology [108] and is starting to impact many applications in electron microscopy of materials science, for example: *in situ* microscopy, imaging of beam sensitive materials, quantitative measurements of radiation damage, and quantitative electron microscopy. Of particular relevance to this PhD work, these detectors have revolutionised the field of 4D STEM [163, 164]. 4D STEM is a term used to describe 4D scanning diffraction data comprising 2D diffraction patterns acquired in a 2D region of interest, which therefore includes the main technique applied throughout this work: SPED.

SPED has been a central theme throughout this thesis, and has been used either directly or indirectly in most of the publications resulting from this PhD work. Due to the nanoscale nature of the Al precipitate phases, the applied SPED system had to be pushed to its lower limits in terms of probe and scanning step sizes, with consequential reduction in signal strength. The results were surprisingly good, however, and many useful demonstrations of the capability of this technique have been presented. Modern TEMs are incredibly powerful, and there are still room for significant improvements on several aspects related to SPED. In the author's opinion, the by far greatest potential for improvement relates to the acquisition system, and in coupling SPED with DEDs. Recently, the first realisations of this combination are starting to emerge [165–167]. In order to better grasp the future potential of this combination, it is illustrative to compare key parameters of emerging DED systems with the instrumentation applied for running SPED in this PhD work. Here, SPED has been performed using a NanoMEGAS DigiSTAR scan generator retrofitted to a JEOL 2100F microscope. This system enables the simultaneous scan and acquisition of electron diffraction patterns via imaging the phosphor viewing screen of the microscope using an externally mounted StingRay F-033 camera [119]. A SPED scan for the purpose of studying distributions of precipitates typically comprised 200×200 to 400×400 pixels (real space, (x, y)), each containing a 144×144 pixels PED pattern (reciprocal space, (k_x, k_y)), and where each pixel stores 8-bit (1 byte) data. A $40\,\mathrm{ms}$ dwell time per pixel was usually necessary for obtaining sufficient signal for revealing precipitate structures. Each scan therefore took roughly $0.5 - 2\,\mathrm{h}$ to acquire. The Medipix3 and EMPAD detectors are examples of DEDs offering high frame rates suitable for STEM applications, and therefore ideal candidates for coupling with a S(P)ED system. At the time of writing, the Medipix3 detector is currently sitting in a box at the author's TEM lab, eagerly awaiting to be installed. The Medipix3 detector is a silicon based hybrid pixel detector, developed at CERN, with a CMOS readout architecture consisting of 256×256 pixels. Coupled with the Merlin read-out system [168], the Medipix3 detector offers the option to run in 1-, 6-, or 12-bit mode, and in 12-bit mode it can run at 1200 fps ($0.83\,\mathrm{ms}$ frame time). This is much faster than the time necessary to obtain a single full rotation of the precessing beam,

which precesses at 100 Hz and thus requires $10\,\mathrm{ms}$ per rotation. Most importantly, however, the detector may offer $2\times$ and up to $8\times$ the DQE depending on the signal frequency [107, 169], as compared to the system used here. This entails a tremendous improvement in signal quality. Furthermore, the detector is incredibly robust, and can handle direct exposure of the beam for several hours without suffering any permanent damage.

With such impressive improvements in signal quality, it may be possible to obtain SPED scans giving measurable signals from the very first crystalline structures forming from the solid solution in age-hardenable Al alloys. This was attempted in this PhD work, but the signal drowned in the noise of the detection system. Subsequently, one may track the development of these initial atomic clusters/phases if combined with *in situ* heating TEM as demonstrated Paper **IV**. In the experiments of Paper **IV**, it was necessary to first reduce the temperature to room temperature, re-align the SPED system, and subsequently scan for roughly $1.8\,\mathrm{h}$. Conducting the scan at elevated temperatures could potentially have missed information, and structural transitions/precipitate dissolution would occur between the first and last part of the scanned region due to the significant scan time required. By reducing this time down to minutes, or perhaps even seconds for smaller scan regions, the scan could be conducted at elevated temperatures without need for re-alignment. By running repeated scans after different thermal exposures, the giga-bytes or even tera-bytes of data would enable one to track the crystal structure evolution of all phases present, providing maps of unparalleled detail, showing precipitate formation and dissolution kinetics through all stages from initial clustering to equilibrium phase formation/dissolution (cf. precipitation sequences 2.3 and 2.4). A single study would contain more information than 10-folds of previous *ex situ* studies of selected thermal conditions, and where each condition contains a snap shot of each precipitate's evolution history. Processing such large datasets is not an immidate issue, as several scientific fields have already had to cope with data beyond tera-byte size, e.g. scanning fluorescence microscopy in biophysics. Particularly, related to processing of 4D STEM data, and hence SPED, there already exist many open-source programming libraries fit for the task [128, 129, 170].

Furthermore, it should also be noted that although precessing the beam has been a crucial aspect for obtaining the results in this thesis, this may not be a necessity in the future. Put simply, the key point of precession as utilised here for phase mapping, is to limit the variation across electron diffraction patterns acquired from the same precipitate phases. This greatly reduces the number of significant components as obtained through NMF (cf. section 3.5), which makes the process of labelling manageable. It is however easy to envision applications of other types of data optimisation algorithms, or machine learning approaches, that manage

to perform phase mapping of SED data (notice the absence of P), despite larger variations across electron diffraction patterns from the same phases. The development and applications of new data analysis approaches is progressing at impressive speeds, also within the TEM community. Alternative approaches to NMF, such as data clustering algorithms [137] or convoluted neural networks (CNNs) are powerful options that have shown great promise for similar types of data. A continued push and application of such emerging algorithms is therefore of utmost interest for the future development and analysis of S(P)ED data. Without the need for precession, the full data recording speed of DEDs can be utilised. With this possibility, the comparison between the system used in the author's PhD work (with precession) to that of e.g. the Medipix3-Merlin system (without the need for precession), borders ludicrous. Compare option 1 (the author's system): 400×400 pixel scan, 144×144 pixel PED patterns, 8-bit data, $40\,\mathrm{ms}$ frame time (25 fps), DQE $\lessapprox 0.2$, $1.8\,\mathrm{h}$ scan time, to option 2 (Medipix3-Merlin system): 400×400 pixel scan, 256×256 pixel electron diffraction patterns, 12-bit data, $0.83\,\mathrm{ms}$ frame time (1200 fps), DQE $\lessapprox 0.8$, $2.2\,\mathrm{min}$ scan time. Needless to say, the future of this technique looks as bright as an electron gun.

Chapter 6

Conclusions

Advanced TEM techniques and related data processing have been applied to characterise the metastable precipitate phases forming in age-hardenable Al alloys. Particular emphasis has been on improving the understanding of the connection between precipitate microstructure and the thermomechanial and electrical properties of Al alloys subjected to prolonged exposure at elevated temperatures. The works presented in this thesis fall into one or several of the three following categories: SPED technique development and applications, thermomechanical aspects of Al-Mg-Si(-Cu) alloys for structural applications, and conductivity studies of a lean Al-Mg-Si conductor alloy. SPED has been a key technique applied due to its sensitivity, versatility, and ability to quantitatively study larger areas than traditional TEM techniques. Several examples provided here show how this technique may offer additional or complementary information on precipitate distributions, and how it is emerging as an important technique in future Al alloy developments. There exists a great outlook for the techniques and research topics covered in this work, particularly due to the advent of DEDs being incorporated in TEMs, together with rapid advancements in related data processing alternatives. Finally, it is also emphasised that the majority of approaches and techniques applied throughout this thesis are not limited to studying precipitate phases forming in Al alloys, but have potential for broad applications within multi-phase material systems such as metals, semiconductors, and minerals.

Bibliography

[1] I. Polmear, *Light Alloys*, 4th ed. Oxford, UK: Butterworth-Heinemann, 2005.

[2] J. Rankin, "Energy Use in Metal Production", *High Temperature Processing Symposium 2012*, Available online at: https://publications.csiro.au/rpr/download?pid=csiro:EP12183&dsid=DS3, last accessed on 25.04.2020.

[3] The International Aluminium Institute - *Metallurgical Alumina Refining Energy Intensity* - Available online at: http://www.world-aluminium.org/statistics/metallurgical-alumina-refining-energy-intensity/, last accessed on 25.04.2020.

[4] The International Aluminium Institute - *Primary aluminium smelting energy intensity* - Available online at: http://www.world-aluminium.org/statistics/primary-aluminium-smelting-energy-intensity/, last accessed on 25.04.2020.

[5] IEA - *Tracking report - Iron & Steel* - Available online at: https://www.iea.org/reports/tracking-industry, last accessed on 25.04.2020.

[6] The International Aluminium Institute - *Primary Aluminium Production* - Available online at: http://www.world-aluminium.org/statistics/#histogram, last accessed on 25.04.2020.

[7] J. A. S. Green, *Aluminum recycling and processing for energy conservation and sustainability*. Materials Park, Ohio: ASM International, 2007.

[8] UN, "Sustainable development goal 12", Available online at: https://sustainabledevel un.org/sdg12, last accessed on 10.06.2020.

[9] W. Miller, L. Zhuang, J. Bottema, A. Wittebrood, P. D. Smet, A. Haszler and A. Vieregge, "Recent development in aluminium alloys for the automotive industry", *Materials Science and Engineering A*, vol. 280, pp. 37–49, 2000. DOI: 10.1016/S0921-5093(99)00653-X.

[10] N. Cuppoletta, - *What are the booming materials in the automotive market? Trends for 2020 and beyond* - Available online at: https://www.shapesbyhydro.com/en/material_properties/what-are-the-booming-materials-in-the-automotive-market-trends-for-2020-and-beyond/, last accessed on 25.04.2020.

[11] K. Marthinsen *et al.*, *AMPERE KPN project description* - Available online at: https://prosjektbanken.forskningsradet.no/#/project/NFR/247783, last accessed on 25.04.2020.

[12] J. Verhoeven, *Fundamentals of Physical Metallurgy*, 2nd ed. John Wiley & Sons, 1975.

[13] A. Wilm, "Physikalisch-metallurgische Untersuchungen über magnesiumhaltige Aluminiumlegierungen", *Metallurgie*, vol. 8, p. 225, 1911.

[14] O. H. Duparc, "Alfred Wilm and the beginnings of Duralumin", *Zeitschrift für Metallkunde*, vol. 96, no. 4, 398–404, 2005. DOI: 10.3139/146.018122.

[15] P. D. Merica, R. G. Waltenberg and H. Scott, "The heat treatment of duralumin", *Scientific Papers of the Bureau of Standards*, vol. 15, p. 271, 1919.

[16] D. A. Porter and K. E. Easterling, *Phase Transformations in Metals and Alloys*, 3rd ed. CRC Press, 2009.

[17] H. I. Aaronson, M. Enomoto and J. K. Lee, *Mechanisms of Diffusional Phase Transformations in Metals and Alloys*. CRC Press, 2010.

[18] R. W. Siegel, "Vacancy Concentrations in Metals", *Journal of Nuclear Materials*, vol. 69-7, no. 1-2, 117–146, 1978. DOI: 10.1016/0022-3115(78)90240-4.

[19] J. P. Hirth and J. Lothe, *Theory of dislocations*, 2nd ed. John Wiley & Sons, 1982.

[20] S. Wenner and R. Holmestad, "Accurately measured precipitate–matrix misfit in an Al–Mg–Si alloy by electron microscopy", *Scripta Materialia*, vol. 118, pp. 5–8, 2016. DOI: 10.1016/j.scriptamat.2016.02.031.

[21] Y. Du, Y. A. Chang, B. Y. Huang, W. P. Gong, Z. P. Jin, H. H. Xu, Z. H. Yuan, Y. Liu, Y. H. He and F. Y. Xie, "Diffusion coefficients of some solutes in fcc and liquid Al: critical evaluation and correlation", *Materials Science and Engineering A*, vol. 363, no. 1-2, 140–151, 2003. DOI: 10.1016/S0921-5093(03)00624-5.

[22] M. Mantina, Y. Wang, L. Q. Chen, K. Z. Liu and C. Wolverton, "First principles impurity diffusion coefficients", *Acta Materialia*, vol. 57, no. 14, 4102–4108, 2009. DOI: 10.1016/j.actamat.2009.05.006.

[23] G. A. Edwards, K. Stiller, G. L. Dunlop and M. J. Couper, "The precipitation sequence in Al-Mg-Si alloys", *Acta Materialia*, vol. 46, no. 11, pp. 3893–3904, 1998. DOI: 10.1016/S1359-6454(98)00059-7.

[24] C. D. Marioara, S. J. Andersen, H. W. Zandbergen and R. Holmestad, "The influence of alloy composition on precipitates of the Al-Mg-Si system", *Metallurgical and Materials Transactions A*, vol. 36, no. 13, pp. 691–702, 2005. DOI: 10.1007/s11661-005-1001-7.

[25] T. Saito, E. A. Mørtsell, S. Wenner, C. D. Marioara, S. J. Andersen, J. Friis, K. Matsuda and R. Holmestad, "Atomic Structures of Precipitates in Al–Mg–Si Alloys with Small Additions of Other Elements", *Advanced Engineering Materials*, vol. 20, no. 7, 1800125, 2018. DOI: 10.1002/adem.201800125.

[26] S. J. Andersen, C. D. Marioara, J. Friis, S. Wenner and R. Holmestad, "Precipitates in aluminium alloys", *Advances in Physics: X*, vol. 3, no. 1, pp. 790–814, 2018. DOI: 10.1080/23746149.2018.1479984.

[27] W. F. Miao and D. E. Laughlin, "Effects of Cu content and preaging on precipitation characteristics in aluminum alloy 6022", *Metallurgical Materials Transaction A*, vol. 31, no. 2, pp. 361–371, 2000. DOI: 10.1007/s11661-000-0272-2.

[28] M. Murayama, K. Hono, W. F. Miao and D. E. Laughlin, "The effect of Cu additions on the precipitation kinetics in an Al-Mg-Si alloy with excess Si", *Metallurgical and Materials Transactions A*, vol. 32, no. 2, 239–246, 2001. DOI: 10.1007/s11661-001-0254-z.

[29] H. W. Zandbergen, A. Cerezo and G. D. W. Smith, "Study of precipitation in Al-Mg-Si Alloys by atom probe tomography II. Influence of Cu additions", *Acta Materialia*, vol. 101, 149–158, 2015. DOI: 10.1016/j.actamat.2015.08.018.

[30] A. Bobel, K. Kim, C. Wolverton, M. Walker and G. B. Olson, "Equilibrium composition variation of Q-phase precipitates in aluminum alloys", *Acta Materialia*, vol. 138, 150–160, 2017. DOI: 10.1016/j.actamat.2017.07.048.

[31] C. D. Marioara, S. J. Andersen, J. Røyset, O. Reiso, S. Gulbrandsen-Dahl, T.-E. Nicolaisen, I.-E. Opheim, J. F. Helgaker and R. Holmestad, "Improving thermal stability in cu-containing al-mg-si alloys by precipitate optimization", *Metallurgical and Materials Transactions A*, vol. 45, pp. 2938–2949, 2014. DOI: 10.1007/s11661-014-2250-0.

[32] C. Cayron, L. Sagalowicz and P. A. Buffat, "Structural phase transition in Al-Cu-Mg-Si alloys by transmission electron microscopy study on an Al-4 wt% Cu-1 wt% Mg-Ag alloy reinforced by SiC particles", *Philosophical Magazine A*, vol. 79, no. 11, pp. 2833–2851, 1999. DOI: 10.1080/01418619908212027.

[33] K. Matsuda, Y. Uetani, T. Sato and S. Ikeno, "Metastable phases in an Al-Mg-Si alloy containing copper", *Metallurgical and Materials Transaction A*, vol. 32, no. 6, 1293–1299, 2001. DOI: 10.1007/s11661-001-0219-2.

[34] D. J. Chakrabarti and D. E. Laughlin, "Phase relations and precipitation in Al-Mg-Si alloys with Cu additions", *Progress in Materials Science*, vol. 49, no. 3-4, 389–410, 2004. DOI: 10.1016/S0079-6425(03)00031-8.

[35] C. D. Marioara, S. J. Andersen, T. N. Stene, H. Hasting, J. Walmsley, A. T. J. Van Helvoort and R. Holmestad, "The effect of Cu on precipitation in Al-Mg-Si alloys", *Philosophical Magazine*, vol. 87, no. 23, pp. 3385–3413, 2007. DOI: 10.1080/14786430701287377.

[36] S. J. Andersen, C. D. Marioara, J. Friis, R. Bjørge, Q. Du, I. G. Ringdalen, S. Wenner, E. A. Mørtsell, R. Holmestad, T. Saito, J. Røyset and O. Reiso, "Directionality and column arrangement principles of precipitates in Al-Mg-Si-(Cu) and Al-Mg-Cu linked to line defect in Al", *Materials Science Forum*, vol. 877, pp. 461–470, 2017. DOI: 10.4028/www.scientific.net/MSF.877.461.

[37] T. Saito, C. D. Marioara, S. J. Andersen, W. Lefebvre and R. Holmestad, "Aberration-corrected HAADF-STEM investigations of precipitate structures in Al-Mg-Si alloys with low Cu additions", *Philosophical Magazine*, vol. 94, no. 5, 520–531, 2014. DOI: 10.1080/14786435.2013.857051.

[38] H. S. Hasting, A. G. Frøseth, S. J. Andersen, R. Vissers, J. C. Walmsley, C. D. Marioara, F. Danoix, W. Lefebvre and R. Holmestad, "Composition of β'' precipitates in Al–Mg–Si alloys by atom probe tomography and first principles calculations", *Journal of Applied Physics*, vol. 106, no. 12, 123527, 2009. DOI: 10.1063/1.3269714.

[39] S. Wenner, L. Jones, C. D. Marioara and R. Holmestad, "Atomic-resolution chemical mapping of ordered precipitates in Al alloys using energy-dispersive X-ray spectroscopy", *Micron*, vol. 96, pp. 103–111, 2017. DOI: 10.1016/j.micron.2017.02.007.

[40] R. Vissers, M. A. van Huis, J. Jansen, H. W. Zandbergen, C. D. Marioara and S. J. Andersen, "The crystal structure of the β' phase in Al–Mg–Si alloys", *Acta Materialia*, vol. 55, no. 11, pp. 3815–3823, 2007. DOI: 10.1016/J.ACTAMAT.2007.02.032.

[41] A. H. Geisler and J. K. Hill, "Analyses and interpretations of X-ray diffraction effects in patterns of aged alloys", *Acta Crystallographica*, vol. 1, no. 5, pp. 238–252, 1948. DOI: 10.1107/S0365110X48000661.

[42] S. J. Andersen, C. D. Marioara, R. Vissers, A. Frøseth and H. W. Zandbergen, "The structural relation between precipitates in Al–Mg–Si alloys, the Al-matrix and diamond silicon, with emphasis on the trigonal phase U1-$MgAl_2Si_2$", *Materials Science and Engineering: A*, vol. 444, no. 1-2, pp. 157–169, 2007. DOI: 10.1016/J.MSEA.2006.08.084.

[43] K. Matsuda, Y. Sakaguchi, Y. Miyata, Y. Uetani, T. Sato, A. Kamio and S. Ikeno, "Precipitation sequence of various kinds of metastable phases in Al-1.0mass% Mg2Si-0.4mass% Si alloy", *Journal of Materials Science*, vol. 35, no. 1, pp. 179–189, 2000. DOI: 10.1023/A:1004769305736.

[44] S. J. Andersen, C. D. Marioara, A. Frøseth, R. Vissers and H. W. Zandbergen, "Crystal structure of the orthorhombic U2-$Al_4Mg_4Si_4$ precipitate in the Al–Mg–Si alloy system and its relation to the β' and β'' phases", *Materials Science and Engineering: A*, vol. 390, no. 1-2, pp. 127–138, 2005. DOI: 10.1016/J.MSEA.2004.09.019.

[45] S. D. Dumolt, D. E. Laughlin and J. C. Williams, "Formation of a modified β' phase in aluminum alloy 6061", *Scripta Metallurgica*, vol. 18, no. 12, pp. 1347–1350, 1984. DOI: 10.1016/0036-9748(84)90362-4.

[46] C. Ravi and C. Wolverton, "First-principles study of crystal structure and stability of Al-Mg-Si-(Cu) precipitates", *Acta Materialia*, vol. 52, no. 14, pp. 4213–4227, 2004. DOI: 10.1016/j.actamat.2004.05.037.

[47] C. D. Marioara, J. Nakamura, K. Matsuda, S. Andersen, R. Holmestad, T. Sato, T. Kawabata and S. Ikeno, "HAADF-STEM study of β'-type precipitates in an over-aged Al–Mg–Si–Ag alloy", *Philosophical Magazine*, vol. 92, no. 9, pp. 1149–1158, 2012. DOI: 10.1080/14786435.2011.642319.

[48] C. Wolverton, "Crystal structure and stability of complex precipitate phases in Al-Cu-Mg-(Si) and Al-Zn-Mg alloys", *Acta Materialia*, vol. 49, no. 16, pp. 3129–3142, 2001. DOI: 10.1016/S1359-6454(01)00229-4.

[49] L. Arnberg and B. Aurivillius, "The Crystal Structure of $Al_xCu_2Mg_{12-x}Si_7$, (h-AlCuMgSi)", *Acta Chemica Scandinavica A*, vol. 34a, pp. 1–5, 1980. DOI: 10.3891/acta.chem.scand.34a-0001.

[50] L. Ding, Z. Jia, J.-F. Nie, Y. Weng, L. Cao, H. Chen, X. Wu and Q. Liu, "The structural and compositional evolution of precipitates in Al-Mg-Si-Cu alloy", *Acta Materialia*, vol. 145, pp. 437–450, 2018. DOI: 10.1016/j.actamat.2017.12.036.

[51] M. Torsæter, F. J. H. Ehlers, C. D. Marioara, S. J. Andersen and R. Holmestad, "Applying precipitate-host lattice coherency for compositional determination of precipitates in Al-Mg-Si-Cu alloys", *Philosophical Magazine*, vol. 92, no. 31, pp. 3833–3856, 2012. DOI: 10.1080/14786435.2012.693214.

[52] M. Torsæter, W. Lefebvre, C. D. Marioara, S. J. Andersen, J. C. Walmsley and R. Holmestad, "Study of intergrown L and Q′ precipitates in Al-Mg-Si-Cu alloys", *Scripta Materialia*, vol. 64, no. 9, pp. 817–820, 2011. DOI: 10.1016/j.scriptamat.2011.01.008.

[53] J. W. Martin, *Micromechanisms in particle-hardened alloys*, ser. Cambridge Solid State Science Series. Cambridge UK: Cambridge University Press, 1980.

[54] E. Nembach, *Particle Strengthening of metals and alloys*. New York, USA: Wiley, 1997.

[55] A. H. Cottrell, *Dislocations and Plastic Flow in Crystals*, ser. The International Series of Monographs in Physics. Oxford UK: Clarendon Press, 1958.

[56] D. Hull and D. J. Bacon, *Introduction to dislocations*, 5th ed. Butterworth-Heinemann, 2011. DOI: 10.1016/C2009-0-64358-0.

[57] O. R. Myhr, Ø. Grong and S. J. Andersen, "Modelling of the age hardening behaviour of Al–Mg–Si alloys", *Acta Materialia*, vol. 49, no. 1, pp. 65–75, 2001. DOI: 10.1016/S1359-6454(00)00301-3.

[58] O. R. Myhr, Ø. Grong and K. O. Pedersen, "A Combined Precipitation, Yield Strength, and Work Hardening Model for Al-Mg-Si Alloys", *Metallurgical and Materials Transactions A*, pp. 2276–2289, 2010. DOI: https://doi.org/10.1007/s11661-010-0258-7.

[59] M. Y. Murashkin, I. Sabirov, V. U. Kazykhanov, E. V. Bobruk, A. A. Dubravina and R. Z. Valiev, "Enhanced mechanical properties and electrical conductivity in ultrafine-grained Al alloy processed via ECAP-PC", *Journal of Materials Science*, vol. 48, no. 13, SI, pp. 4501–4509, 2013. DOI: 10.1007/s10853-013-7279-8.

[60] M. Murashkin, A. Medvedev, V. Kazykhanov, A. Krokhin, G. Raab, N. Enikeev and R. Z. Valiev, "Enhanced Mechanical Properties and Electrical Conductivity in Ultrafine-Grained Al 6101 Alloy Processed via ECAP-Conform", *Metals*, vol. 5, no. 4, 2148–2164, 2015. DOI: {10.3390/met5042148}.

[61] X. Sauvage, E. V. Bobruk, M. Y. Murashkin, Y. Nasedkina, N. A. Enikeev and R. Z. Valiev, "Optimization of electrical conductivity and strength combination by structure design at the nanoscale in Al-Mg-Si alloys", *Acta Materialia*, vol. 98, 355–366, 2015. DOI: {10.1016/j.actamat.2015.07.039}.

[62] M. F. Ashby, "The deformation of plastically non-homogeneous materials", *Philosophical Magazine A*, vol. 21, no. 170, pp. 399–424, 1970.

[63] M. Z. Butt and P. Feltham, "Solid-solution hardening", *Journal of Materials Science*, vol. 28, no. 10, pp. 2557–2576, 1993. DOI: 10.1007/BF00356192.

[64] P. Haasen, "Solution hardening in f.c.c. metals", in *Dislocations in Solids*, ser. Dislocations in Metallurgy, F. R. N. Nabarro, Ed., vol. 4, Amsterdam, Netherlands: North-Holland Publishing Company, 1979, pp. 155–190.

[65] J. Friedel, *Dislocations*. Oxford, UK: Pergamon Press, 1964, vol. 1.

[66] F. R. N. Nabarro, *Theory of Crystal Dislocations*. Oxford: Oxford University Press, 1967.

[67] P. D. Nellist and S. J. Pennycook, "The principles and interpretation of annular dark-field Z-contrast imaging", *Advances in Imaging and Electron Physics*, vol. 113, pp. 147–203, 2000. DOI: 10.1016/S1076-5670(00)80013-0.

[68] S. Hillyard and J. Silcox, "Thickness effects in ADF STEM zone axis images", *Ultramicroscopy*, vol. 52, no. 3-4, pp. 325–334, 1993. DOI: 10.1016/0304-3991(93)90043-W.

[69] S. Hillyard, R. F. Loane and J. Silcox, "Annular dark-field imaging: Resolution and thickness effects", *Ultramicroscopy*, vol. 49, no. 1-4, pp. 14–25, 1993. DOI: 10.1016/0304-3991(93)90209-G.

[70] U. F. Kocks, "A statistical theory of flow stress and work-hardening", *Philosophical Magazine*, vol. 13, pp. 541–566, 1966. DOI: 10.1080/14786436608212647.

[71] U. F. Kocks, A. Argon and M. Ashby, "Thermodynamics and kinetics of slip", *Progress in Materials Science*, vol. 19, p1, 1975.

[72] Ø. Ryen, B. Holmedal, K. Marthinsen and T. Furu, "Precipitation, strength and work hardening of age hardened aluminium alloys", *IOP Conference Series: Materials Science and Engineering*, vol. 89, p. 012 013, 2015. DOI: 10.1088/1757-899x/89/1/012013.

[73] K. Misumi, K. Kaneko, T. Nishiyama, T. Maeda, K. Yamada, K. Ikeda, M. Kikuchi, K. Takata, M. Saga and K. Ushioda, "Three-dimensional characterization of interaction between β'' precipitate and dislocation in Al–Mg–Si alloy", *Journal of Alloys and Compounds*, vol. 600, pp. 29–33, 2014. DOI: 10.1016/j.jallcom.2014.02.059.

[74] W. J. Poole, X. Wang, D. J. Lloyd and J. D. Embury, "The shearable–non-shearable transition in Al–Mg–Si–Cu precipitation hardening alloys: implications on the distribution of slip, work hardening and fracture", *Philosophical Magazine*, vol. 85, no. 26-27, pp. 3113–3135, 2005. DOI: 10.1080/14786430500154935.

[75] E. Christiansen, C. D. Marioara, B. Holmedal, O. S. Hopperstad and R. Holmestad, "Nano-scale characterisation of sheared β'' precipitates in a deformed aluminium alloy", *Scientific Reports*, vol. 9, no. 1, p. 17 446, 2019. DOI: 10.1038/s41598-019-53772-4.

[76] K. Teichmann, C. D. Marioara, S. J. Andersen and K. Marthinsen, "TEM study of β' precipitate interaction mechanisms with dislocations and β' interfaces with the aluminium matrix in Al–Mg–Si alloys", *Materials Characterization*, vol. 75, pp. 1–7, 2013. DOI: 10.1016/J.MATCHAR.2012.10.003.

[77] J. F. Nie, B. C. Muddle and I. J. Polmear, "The effect of precipitate shape and orientation on dispersion strengthening in high strength aluminium alloys", *Materials Science Forum*, vol. 530, pp. 217–222, 1996. DOI: 10.4028/www.scientific.net/msf.217-222.1257.

[78] A. Deschamps and Y. Brechet, "Influence of predeformation and ageing of an Al–Zn–Mg alloy—II. Modeling of precipitation kinetics and yield stress", *Acta Materialia*, vol. 47, no. 1, pp. 293–305, 1998. DOI: 10.1016/S1359-6454(98)00296-1.

[79] S. Esmaeili, D. J. Lloyd and W. J. Poole, "A yield strength model for the Al-Mg-Si-Cu alloy AA6111", *Acta Materialia*, vol. 51, no. 8, pp. 2243–2257, 2003. DOI: 10.1016/S1359-6454(03)00028-4.

[80] A. Bahrami, A. Miroux and J. Sietsma, "An Age-Hardening Model for Al-Mg-Si Alloys Considering Needle-Shaped Precipitates", *Metallurgical and Materials Transactions A*, vol. 43, no. 11, pp. 4445–4453, 2012. DOI: 10.1007/s11661-012-1211-8.

[81] B. Holmedal, "Strength contributions from precipitates", *Philosophical Magazine Letters*, vol. 95, no. 12, pp. 594–601, 2015. DOI: 10.1080/09500839.2015.1125029.

[82] M. Yang, H. Chen, A. Orekhov, Q. Lu, X. Lan, K. Li, S. Zhang, M. Song, Y. Kong, D. Schryvers and Y. Du, "Quantified contribution of β'' and β' precipitates to the strengthening of an aged Al–Mg–Si alloy", *Materials Science and Engineering: A*, vol. 774, p. 138 776, 2020. DOI: 10.1016/j.msea.2019.138776.

[83] L. M. Brown and R. K. Ham, "Dislocation-particle interactions", in *Strengthening Methods in Crystals*, ser. Elsevier Materials Science Series, A. Kelly and R. B. Nicholson, Eds., Amsterdam, Netherlands: Elsevier Publishing Company LTD, 1971, pp. 12–129.

[84] A. de Vaucorbeil, W. J. Poole and C. W. Sinclair, "The superposition of strengthening contributions in engineering alloys", *Materials Science and Engineering: A*, vol. 582, pp. 147–154, 2013. DOI: 10.1016/j.msea.2013.06.032.

[85] A. de Vaucorbeil, W. J. Poole and C. Sinclair, "The effect of obstacle strength distribution on the critical resolved shear stress of engineering alloys", *Materials Science Forum*, vol. 794-796, pp. 449–454, 2014. DOI: 10.4028/www.scientific.net/MSF.794-796.449.

[86] N. W. Ashcroft and N. D. Mermin, *Solid State Physics*, 1st ed. Cengage Learning, 1976.

[87] C. Kittel, *Introduction to Solid State Physics*, 8th ed. John Wiley & Sons, 2004.

[88] R. A. Serway, *Principles of Physics*, 2nd ed. Fort Worth, Texas: Saunders College Pub., 1998.

[89] F. Kiessling, P. Nefzger, J. F. Nolasco and U. Kaintzyk, *Overhead Power Lines*, 1st ed. Springer-Verlag Berlin Heidelberg, 2003.

[90] G. Lin, Z. Zhang, H. Wang, K. Zhou and Y. Wei, "Enhanced strength and electrical conductivity of Al-Mg-Si alloy by thermo-mechanical treatment", *Materials Science and Engineering A*, vol. 650, pp. 210–217, 2016. DOI: 10.1016/j.msea.2015.10.050.

[91] C. H. Liu, J. Chen, Y. X. Lai, D. H. Zhu, Y. Gu and J. H. Chen, "Enhancing electrical conductivity and strength in Al alloys by modification of conventional thermo-mechanical process", *Materials & Design*, vol. 87, 1–5, 2015. DOI: {10.1016/j.matdes.2015.07.133}.

[92] J. P. Hou, Q. Wang, Z. J. Zhang, Y. Z. Tian, X. M. Wu, H. J. Yang, X. W. Li and Z. F. Zhang, "Nano-scale precipitates: The key to high strength and high conductivity in Al alloy wire", *Materials & Design*, vol. 132, pp. 148–157, 2017. DOI: 10.1016/j.matdes.2017.06.062.

[93] M. H. Mulazimoglu, R. Drew and J. E. Gruzelski, "Electrical-conductivity of aluminum-rich Al-Si-Mg alloys", *Journal of Materials Science Letters*, vol. 8, no. 3, pp. 297–300, 1989. DOI: 10.1007/BF00725503.

[94] F. R. Fickett, "Aluminum—1. A review of resistive mechanisms in aluminum", *Cryogenics*, vol. 11, no. 5, pp. 349–367, 1971. DOI: 10.1016/0011-2275(71)90036-1.

[95] D. B. Williams and B. C. Carter, *Transmission Electron Microscopy*, 2nd ed. Springer, 2009.

[96] R. Erni, *Aberration-corrected imaging in transmission electron microscopy : an introduction*, 2nd ed. Imperial College Press, 2010.

[97] J. M. Zuo and J. C. H. Spence, *Advanced Transmission Electron Microscopy*, 1st ed. Springer-Verlag New York, 2017.

[98] P. B. Hirsch, A. Howie, R. B. Nicholson, D. W. Pashley and M. J. Whelan, *Electron Microscopy of thin crystals*, 1st ed. Butterworths, 1965.

[99] C. J. Humphreys, "The scattering of fast electrons by crystals", *Reports on Progress in Physics*, vol. 42, 1979.

[100] E. J. Kirkland, *Advanced Computing in Electron Microscopy*, 2nd ed. Springer, 2010. DOI: 10.1007/978-1-4419-6533-2.

[101] L. Reimer and H. Kohl, *Transmission Electron Microscopy: Physics of Image Formation*, 5th ed. Springer-Verlag New York, 2008.

[102] Y. Jiang, Z. Chen, Y. Hang, P. Deb, H. Gao, S. Xie, P. Purohit, M. W. Tate, J. Park, S. M. Gruner, V. Elser and D. A. Muller, "Electron ptychography of 2D materials to deep sub-angstrom resolution", *Nature*, vol. 559, no. 7714, p. 343, 2018. DOI: 10.1038/s41586-018-0298-5.

[103] P. W. Hawkes, "Aberration correction past and present", *Philosophical Transactions of the Royal Society A*, vol. 367, no. 1903, pp. 3637–3664, 2009. DOI: 10.1098/rsta.2009.0004.

[104] M. H. Nielsen, S. Aloni and J. J. D. Yoreo, "In situ TEM imaging of CaCO3 nucleation reveals coexistence of direct and indirect pathways", *Science*, vol. 345, no. 6201, pp. 1158–1162, 2014. DOI: 10.1126/science.1254051.

[105] M. T. McDowell, S. W. Lee, J. T. Harris, B. A. Korgel, C. Wang, W. D. Nix and Y. Cui, "In Situ TEM of Two-Phase Lithiation of Amorphous Silicon Nanospheres", *Nano Letters*, vol. 13, no. 2, pp. 758–764, 2013. DOI: 10.1021/nl3044508.

[106] D. McGrouther, M. Krajnak, I. MacLaren, D. Maneuski, V. O'Shea and P. D. Nellist, "Use of a hybrid silicon pixel (medipix) detector as a stem detector", *Microscopy and Microanalysis*, vol. 21, no. S3, pp. 1595–1596, 2015. DOI: 10.1017/S1431927615008752.

[107] R. N. Clough, G. Moldovan and A. I. Kirkland, "Direct detectors for electron microscopy", *Journal of Physics: Conference Series*, vol. 522, p. 012 046, 2014. DOI: 10.1088/1742-6596/522/1/012046.

[108] G. McMullan, A. R. Faruqi and R. Henderson, "Direct Electron Detectors", in *Resolution Revolution: Recent advances in cryoEM*, ser. Methods in Enzymology, R. A. Crowther, Ed., vol. 579, 2016, pp. 1–17. DOI: 10.1016/bs.mie.2016.05.056.

[109] E. J. Kirkland, R. F. Loane and J. Silcox, "Simulation of annular dark field stem images using a modified multislice method", *Ultramicroscopy*, vol. 23, no. 1, pp. 77–96, 1987. DOI: 10.1016/0304-3991(87)90229-4.

[110] E. J. Kirkland, *Advanced Computing in Electron Microscopy*, 3rd ed. Springer Nature Switzerland, 2020.

[111] S. J. Pennycook and D. E. Jesson, "High-resolution Z-contrast imaging of crystals", *Ultramicroscopy*, vol. 37, no. 1-4, pp. 14–38, 1991. DOI: 10.1016/0304-3991(91)90004-P.

[112] H. Tvedt, *AutomAl 6000 alpha 1.0* - Available online at: http://automal.org, last accessed on 10.06.2020.

[113] J. S. Barnard, A. S. Eggeman, J. Sharp, T. A. White and P. A. Midgley, "Dislocation electron tomography and precession electron diffraction – minimising the effects of dynamical interactions in real and reciprocal space", *Philosophical Magazine*, vol. 90, no. 35-36, pp. 4711–4730, 2010. DOI: 10.1080/14786430903581338.

[114] R. Vincent and P. A. Midgley, “Double conical beam-rocking system for measurement of integrated electron diffraction intensities”, *Ultramicroscopy*, vol. 53, no. 3, pp. 271–282, 1994. DOI: 10.1016/0304-3991(94)90039-6.

[115] T. A. White, A. S. Eggeman and P. A. Midgley, “Is precession electron diffraction kinematical? Part I: "Phase-scrambling" multislice simulations”, *Ultramicroscopy*, vol. 110, no. 7, pp. 763–770, 2010. DOI: 10.1016/j.ultramic.2009.10.013.

[116] A. S. Eggeman, T. A. White and P. A. Midgley, “Is precession electron diffraction kinematical? Part II A practical method to determine the optimum precession angle”, *Ultramicroscopy*, vol. 110, no. 7, pp. 771–777, 2010. DOI: 10.1016/j.ultramic.2009.10.012.

[117] E. Rauch, M. Véron, J. Portillo, D. Bultreys, Y. Maniette and S. Nicolopoulos, “Automatic crystal orientation and phase mapping in tem by precession diffraction”, *Microscopy*, vol. 22, S8–S11, 2008.

[118] E. F. Rauch, J. Portillo, S. Nicolopoulos, D. Bultreys, S. Rouvimov and P. Moeck, “Automated nanocrystal orientation and phase mapping in the transmission electron microscope on the basis of precession electron diffraction”, *Zeitschrift fur Kristallographie*, vol. 225, no. 2-3, pp. 103–109, 2010. DOI: 10.1524/zkri.2010.1205.

[119] P. Moeck, S. Rouvimov, E. F. Rauch, M. Véron, H. Kirmse, I. Häusler, W. Neumann, D. Bultreys, Y. Maniette and S. Nicolopoulos, “High spatial resolution semi-automatic crystallite orientation and phase mapping of nanocrystals in transmission electron microscopes”, *Crystal Research and Technology*, vol. 46, no. 6, pp. 589–606, 2011. DOI: 10.1002/crat.201000676.

[120] A. S. Eggeman, R. Krakow and P. A. Midgley, “Scanning precession electron tomography for three-dimensional nanoscale orientation imaging and crystallographic analysis”, *Nature Communications*, vol. 6, no. 1, 7267, 2015. DOI: 10.1038/ncomms8267.

[121] R. Krakow, D. N. Johnstone, A. S. Eggeman, D. Huenert, M. C. Hardy, C. M. F. Rae and P. A. Midgley, “On the crystallography and composition of topologically close-packed phases in ATI 718Plus (R)”, *Acta Materialia*, vol. 130, pp. 271–280, 2017. DOI: 10.1016/j.actamat.2017.03.038.

[122] J.-L. Rouviere, A. Beche, Y. Martin, T. Denneulin and D. Cooper, “Improved strain precision with high spatial resolution using nanobeam precession electron diffraction”, *Applied Physics Letters*, vol. 103, no. 24, 2013. DOI: 10.1063/1.4829154.

[123] D. Cooper, N. Bernier and J.-L. Rouviere, “Combining 2 nm Spatial Resolution and 0.02% Precision for Deformation Mapping of Semiconductor Specimens in a Transmission Electron Microscope by Precession Electron Diffraction”, *Nano Letters*, vol. 15, no. 8, 5289–5294, 2015. DOI: {10.1021/acs.nanolett.5b01614}.

[124] S. Estrade, J. Portillo, J. Mendoza, I. Kosta, M. Serret, C. Mueller and F. Peiro, "Assessment of misorientation in metallic and semiconducting nanowires using precession electron diffraction", *Micron*, vol. 43, no. 8, pp. 910–915, 2012. DOI: 10.1016/j.micron.2012.03.003.

[125] D. Viladot, M. Veron, M. Gemmi, F. Peiro, J. Portillo, S. Estrade, J. Mendoza, N. Llorca-Isern and S. Nicolopoulos, "Orientation and phase mapping in the transmission electron microscope using precession-assisted diffraction spot recognition: state-of-the-art results", *Journal of Microscopy*, vol. 252, no. 1, pp. 23–34, 2013. DOI: 10.1111/jmi.12065.

[126] Y. Liao and L. D. Marks, "Reduction of electron channeling in EDS using precession", *Ultramicroscopy*, vol. 126, pp. 19–22, 2013. DOI: 10.1016/j.ultramic.2012.11.007.

[127] S. Estrade, J. Portillo, L. Yedra, J. Manuel Rebled and F. Peiro, "EELS signal enhancement by means of beam precession in the TEM", *Ultramicroscopy*, vol. 116, pp. 135–137, 2012. DOI: 10.1016/j.ultramic.2012.03.018.

[128] F. de la Peña, V. T. Fauske, P. Burdet, E. Prestat, P. Jokubauskas, M. Nord, T. Ostasevicius, K. E. MacArthur, M. Sarahan, D. N. Johnstone, J. Taillon, A. Eljarrat, V. Migunov, J. Caron, T. Furnival, S. Mazzucco, T. Aarholt, M. Walls, T. Slater, F. Winkler, B. Martineau, G. Donval, R. McLeod, E. R. Hoglund, I. Alxneit, I. Hjorth, T. Henninen, L. F. Zagonel, A. Garmannslund and A. Skorikov, *Hyperspy/hyperspy v1.5.2*, 2019. DOI: 10.5281/zenodo.3396791.

[129] D. N. Johnstone, P. Crout, S. Høgås, B. Martineau, S. Smeets, J. Laulainen, S. Collins, J. Morzy, E. Prestat, H. Ånes, T. Doherty, T. Ostasevicius and T. Bergh, *Pyxem/pyxem: Pyxem 0.9.2*, version v0.9.2, 2019. DOI: 10.5281/zenodo.3407316.

[130] F. Bachmann, R. Hielscher and H. Schaeben, "Grain detection from 2d and 3d EBSD data—Specification of the MTEX algorithm", *Ultramicroscopy*, vol. 111, no. 12, pp. 1720–1733, 2011. DOI: 10.1016/j.ultramic.2011.08.002.

[131] I. Tanaka, *Nanoinformatics*. Springer Berlin Heidelberg, 2018.

[132] K. Pearson, "On Lines and Planes of Closest Fit to Systems of Points in Space", *Philosophical Magazine*, vol. 2, pp. 559–572, 6 1901.

[133] H. Hotelling, "Analysis of a complex of statistical variables into principal components", *Journal of Educational Psychology*, vol. 24, pp. 417–441, 6 1933. DOI: 10.1037/h0071325.

[134] D. Lee and H. Seung, "Learning the parts of objects by non-negative matrix factorization", *Nature*, vol. 401, no. 6755, 788–791, 1999. DOI: 10.1038/44565.

[135] O. Nicoletti, F. de la Peña, R. K. Leary, D. J. Holland, C. Ducati and P. A. Midgley, "Three-dimensional imaging of localized surface plasmon resonances of metal nanoparticles", *Nature*, vol. 502, pp. 80–84, 2013. DOI: 10.1038/nature12469.

[136] C. Boutsidis and E. Gallopoulos, "SVD based initialization: A head start for nonnegative matrix factorization", *Pattern Recognition*, vol. 41, no. 4, pp. 1350–1362, 2008. DOI: 10.1016/j.patcog.2007.09.010.

[137] B. Martineau, D. N. Johnstone, A. T. J. van Helvoort, P. A. Midgley and A. S. Eggeman, "Unsupervised machine learning applied to scanning precession electron diffraction data", *Advanced Structural and Chemical Imaging*, vol. 5, 2019. DOI: 10.1186/s40679-019-0063-3.

[138] A. J. Schwartz, M. Kumar, B. L. Adams and D. Field, *Electron Backscatter Diffraction in Materials Science*. Springer, 2009.

[139] P. A. Midgley and A. S. Eggeman, "Precession electron diffraction - a topical review", *IUCRJ*, vol. 2, no. 1, 126–136, 2015. DOI: 10.1107/S2052252514022283.

[140] A. Kobler, A. Kashiwar, H. Hahn and C. Kuebel, "Combination of in situ straining and ACOM TEM: A novel method for analysis of plastic deformation of nanocrystalline metals", *Ultramicroscopy*, vol. 128, 68–81, 2013. DOI: 10.1016/j.ultramic.2012.12.019.

[141] E. F. Rauch and M. Veron, "Automated crystal orientation and phase mapping in TEM", *Materials Characterization*, vol. 98, pp. 1–9, 2014. DOI: 10.1016/j.matchar.2014.08.010.

[142] M. P. Vigouroux, V. Delaye, N. Bernier, R. Cipro, D. Lafond, G. Audoit, T. Baron, J. L. Rouviere, M. Martin, B. Chenevier and F. Bertin, "Strain mapping at the nanoscale using precession electron diffraction in transmission electron microscope with off axis camera", *Applied Physics Letters*, vol. 105, no. 19, 2014. DOI: 10.1063/1.4901435.

[143] D. Cooper, T. Denneulin, N. Bernier, A. Beche and J.-L. Rouviere, "Strain mapping of semiconductor specimens with nm-scale resolution in a transmission electron microscope", *Micron*, vol. 80, pp. 145–165, 2016. DOI: 10.1016/j.micron.2015.09.001.

[144] C. Mahr, K. Mueller-Caspary, T. Grieb, M. Schowalter, T. Mehrtens, F. F. Krause, D. Zillmann and A. Rosenauer, "Theoretical study of precision and accuracy of strain analysis by nano-beam electron diffraction", *Ultramicroscopy*, vol. 158, 38–48, 2015. DOI: 10.1016/j.ultramic.2015.06.011.

[145] W. J. Schaff, P. J. Tasker and M. C. F. L. F. Eastman, "Device applications of strained-layer epitaxy", *Semiconductors and Semimetals*, vol. 33, 73–138, 1991.

[146] J. K. Sunde, *Scanning Precession Electron Diffraction Study of 2xxx Series Aluminium Alloys Exhibiting Several Coexisting Strengthening Phases*. NTNU, 2016.

[147] C. Dwyer, M. Weyland, L. Y. Chang and B. C. Muddle, "Combined electron beam imaging and ab initio modeling of T-1 precipitates in Al-Li-Cu alloys", *Applied Physics Letters*, vol. 98, no. 20, 2011. DOI: 10.1063/1.3590171.

[148] S. J. Andersen, "Quantification of the Mg_2Si-β'' and β' phases in AlMgSi alloys by transmission electron microscopy", *Metallurgical and Materials Transactions A*, vol. 26, no. 8, 1931–1937, 1995. DOI: 10.1007/BF02670664.

[149] T. Saito, E. A. Mørtsell, S. Wenner, C. D. Marioara, S. J. Andersen, J. Friis, K. Matsuda and R. Holmestad, "Atomic Structures of Precipitates in Al-Mg-Si Alloys with Small Additions of Other Elements", *Advanced Engineering Materials*, vol. 20, no. 7, 1800125, 2018. DOI: 10.1002/adem.201800125.

[150] R. Krakow, R. J. Bennett, D. N. Johnstone, Z. Vukmanovic, W. Solano-Alvarez, S. J. Laine, J. F. Einsle, P. A. Midgley, C. M. F. Rae and R. Hielscher, "On three-dimensional misorientation spaces", *Proceedings of the Royal Society A*, vol. 473, no. 2206, 2017. DOI: 10.1098/rspa.2017.0274.

[151] Y. Q. Chen, S. P. Pan, B. X. Zhu, X. Liu, W. H. Liu and S. W. Tang, "The evolution of orientation relationships during the transformation of a twin-free T-particle to tenfold T-twins in an Al alloy during homogenisation", *Materials Characterization*, vol. 141, 59–73, 2018. DOI: 10.1016/j.matchar.2018.03.029.

[152] A. W. H. Perlitz, "The crystal structure of Al_2CuMg", *Arkiv för kemi, mineralogi och geologi*, vol. 16B, 1–5, 1943.

[153] S. K. Malladi, Q. Xu, M. A. van Huis, F. D. Tichelaar, K. J. Batenburg, E. Yücelen, B. Dubiel, A. Czyrska-Filemonowicz and H. W. Zandbergen, "Real-time atomic scale imaging of nanostructural evolution in aluminum alloys", *Nano Letters*, vol. 14, no. 1, pp. 384–389, 2014. DOI: 10.1021/nl404565j.

[154] C. Liu, S. K. Malladi, Q. Xu, J. Chen, F. D. Tichelaar, X. Zhuge and H. W. Zandbergen, "In-situ STEM imaging of growth and phase change of individual $CuAl_X$ precipitates in Al alloy", *Scientific Reports*, vol. 7, no. 2184, 2017. DOI: 10.1038/s41598-017-02081-9.

[155] J. Park, R. Kamachali, S.-D. Kim, S.-H. Kim, C.-S. Oh, C. Schwarze and I. Steinbach, "First Evidence for Mechanism of Inverse Ripening from In-situ TEM and Phase-Field Study of δ' Precipitation in an Al-Li Alloy", *Scientific Reports*, vol. 9, 2019. DOI: 10.1038/s41598-019-40685-5.

[156] J. Silcock, T. Heal and H. Hardy, "Structural ageing characteristics of binary aluminium-copper alloys", *Journal of the Institute of Metals*, vol. 82, p. 239, 1953.

[157] C.-S. Tsao, C.-Y. Chen, U.-S. Jeng and T.-Y. Kuo, "Precipitation kinetics and transformation of metastable phases in al–mg–si alloys", *Acta Materialia*, vol. 54, no. 17, pp. 4621–4631, 2006. DOI: 10.1016/j.actamat.2006.06.005.

[158] C. S. T. Chang, F. D. Geuser and J. Banhart, "In situ characterization of β'' precipitation in an Al-Mg-Si alloy by anisotropic small-angle neutron scattering on a single crystal", *Journal of Applied Crystallography*, vol. 48, no. 2, pp. 455–463, 2015. DOI: 10.1107/S1600576715002770.

[159] C. Flament, J. Ribis, J. Garnier, Y. Serruys, F. Leprêtre, A. Gentils, C. Baumier, M. Descoins, D. Mangelinck, A. Lopez, K. Colas, K. Buchanan, P. Donnadieu and A. Deschamps, "Stability of β'' nano-phases in Al-Mg-Si(-Cu) alloy under high dose ion irradiation", *Acta Materialia*, vol. 128, pp. 64–76, 2017. DOI: 10.1016/j.actamat.2017.01.044.

[160] S. P. Cooil, E. A. Mørtsell, F. Mazzola, M. Jorge, S. Wenner, M. T. Edmonds, L. Thomsen, H. W. Klemm, G. Peschel, A. Fuhrich, M. Prieto, T. Schmidt, J. A. Miwa, R. Holmestad and J. W. Wells, "Thermal migration of alloying agents in aluminium", *Materials Research Express*, vol. 3, no. 11, p. 116 501, 2016. DOI: 10.1088/2053-1591/3/11/116501.

[161] K. Majchrowicz, Z. Pakiela, W. Chrominski and M. Kulczyk, "Enhanced strength and electrical conductivity of ultrafine-grained Al-Mg-Si alloy processed by hydrostatic extrusion", *Materials Characterization*, vol. 135, 104–114, 2018. DOI: 10.1016/j.matchar.2017.11.023.

[162] G. McMullan, A. R. Faruqi, D. Clare and R. Henderson, "Comparison of optimal performance at 300 keV of three direct electron detectors for use in low dose electron microscopy", *Ultramicroscopy*, vol. 147, pp. 156–163, 2014. DOI: 10.1016/j.ultramic.2014.08.002.

[163] C. Ophus, "Four-Dimensional Scanning Transmission Electron Microscopy (4D-STEM): From Scanning Nanodiffraction to Ptychography and Beyond", *Microscopy and Microanalysis*, vol. 25, no. 3, 563–582, 2019. DOI: 10.1017/S1431927619000497.

[164] A. S. Eggeman, "Scanning transmission electron diffraction methods", *Acta Crystallographica Section B*, vol. 75, no. 4, SI, pp. 475–484, 2019. DOI: 10.1107/S2052520619006723.

[165] M. Nord, R. Webster, K. P. S. Mcvitie, D. McGrouther, I. MacLaren and G. Paterson, "Fast Pixelated Detectors in Scanning Transmission Electron Microscopy. Part I: Data Acquisition, Live Processing and Storage", 2019. DOI: arXiv:1911.11560.

[166] G. Paterson, R. Webster, A. Ross, K. Paton, T. Macgregor, D. McGrouther, I. MacLaren and M. M. Nord, "Fast Pixelated Detectors in Scanning Transmission Electron Microscopy. Part II: Post Acquisition Data Processing, Visualisation, and Structural Characterisation", 2020. DOI: arXiv:2004.02777.

[167] I. MacLaren *et al.*, "Orientation mapping using scanned precession electron diffraction with a direct electron detector", *Microscopy and Microanalysis*, vol. TBA, TBA, TBA. DOI: TBA.

[168] R. Plackett, I. Horswell, E. N. Gimenez, J. Marchal, D. Omar and N. Tartoni, "Merlin: A fast versatile readout system for medipix3", *Journal of Instrumentation*, vol. 8, no. 01, pp. C01038–C01038, 2013. DOI: 10.1088/1748-0221/8/01/c01038.

[169] M. Pan, "Direct detection and electron counting - a beginning of a new era for electron microscopy", in *European Microscopy Congress 2016: Proceedings*. American Cancer Society, 2016, pp. 342–343. DOI: 10.1002/9783527808465.EMC2016.6293.

[170] M. Nord, *pixStem: Analysis of pixelated STEM data* - Available online at: https://pixstem.org/, last accessed on 04.05.2020.

PART III

PAPERS

Paper I

Jonas Kristoffer Sunde, Øyvind Paulsen, Sigurd Wenner
Randi Holmestad

Precipitate statistics in an Al-Mg-Si-Cu alloy from scanning precession electron diffraction data

Journal of Physics: Conference Series **902** (2017) 012022.
https://doi.org/10.1088/1742-6596/902/1/012022

IOP Conf. Series: Journal of Physics: Conf. Series **902** (2017) 012022 doi:10.1088/1742-6596/902/1/012022

Precipitate statistics in an Al-Mg-Si-Cu alloy from scanning precession electron diffraction data

J K Sunde[1], Ø Paulsen[1], S Wenner[1] and R Holmestad[1]

[1]Department of Physics, Norwegian University of Science and Technology (NTNU), Høgskoleringen 5, N-7491 Trondheim, Norway

E-mail: jonas.k.sunde@ntnu.no

Abstract. The key microstructural feature providing strength to age-hardenable Al alloys is nanoscale precipitates. Alloy development requires a reliable statistical assessment of these precipitates, in order to link the microstructure with material properties. Here, it is demonstrated that scanning precession electron diffraction combined with computational analysis enable the semi-automated extraction of precipitate statistics in an Al-Mg-Si-Cu alloy. Among the main findings is the precipitate number density, which agrees well with a conventional method based on manual counting and measurements. By virtue of its data analysis objectivity, our methodology is therefore seen as an advantageous alternative to existing routines, offering reproducibility and efficiency in alloy statistics. Additional results include improved qualitative information on phase distributions. The developed procedure is generic and applicable to any material containing nanoscale precipitates.

1. Introduction

6xxx series Al(-Mg-Si(-Cu)) alloys form an important group of engineering alloys and are found in a range of applications in buildings and constructions, transportation and marine structures. Increasing industrial demand for materials combining properties such as low weight, high strength, high formability and good corrosion resistance, make Al-based alloys prime candidates for future applications. As an example, this is reflected in their growing impact in the automotive industry [1].

The 6xxx series alloys are characterised by a significant increase in hardness upon short-term thermal ageing. This increase is caused by a large number of small, semi-coherent and metastable needle-shaped precipitates formed along the $\langle 100 \rangle_{\mathrm{Al}}$ directions in the Al matrix from a solid solution of Mg and Si [2]. These nanostructures act as obstacles to dislocation movement through the Al matrix, hence strengthening the material.

The early-stage precipitation sequence in Al-Mg-Si-Cu alloys is normally given as [3–5]

$$\mathrm{SSSS} \rightarrow \text{atomic clusters} \rightarrow \text{GP-zones} \rightarrow \beta'', \mathrm{L} \rightarrow \beta'(\text{-Cu}), \mathrm{U1}, \mathrm{U2}, \mathrm{C}, \mathrm{B}', \mathrm{Q}'.$$

The number and type of the different phases forming throughout the Al matrix are crucially dependent on alloy composition and all prior thermo-mechanical processing. In order to further optimise material properties, detailed and reliable precipitate statistics and its change versus different ageing times, is needed. This is generally acquired through bright-field (BF) and/or dark-field (DF) transmission electron microscopy (TEM) imaging techniques, with subsequent

manual counting and measurements [6]. With recent developments of TEM techniques yielding large, multi-dimensional datasets [7], and corresponding parallel advancements in powerful data processing tools [8], techniques for obtaining the statistics in more objective and reproducible manners are sought. This forms the main motivation behind this work.

2. Materials and methods

The material studied has a nominal composition Al-1.11Mg-0.50Si-0.16Cu (at.%) [9]. From an extruded rod with cylindrical profile (Ø 20 mm) a sample of 10 mm height was cut and solution heat treated at 540 °C for 15 min, before water quenched to room temperature. After 4 h natural ageing it was artificially aged for 6 h at 200 °C, yielding a slightly over-aged condition. TEM samples were made by standard electro-polishing using a Struers Tenupol-5.

Scanning precession electron diffraction (SPED) was performed using a NanoMEGAS DigiSTAR scan generator fitted to a JEOL 2100F TEM operated at 200 kV, with a precession angle of 1° and a step size of 2.28 nm. To get high quality data from the nm-sized precipitates the precession system was aligned using the procedure proposed by Barnard et al. [10]. The main SPED dataset is presented as a virtual dark-field (VDF) image (Figure 1) formed by plotting the intensity of a sub-set of pixels in each PED pattern as a function of probe position. The dataset comprises 247 500 diffraction patterns (DPs) covering an area of $1.34\,\mu m^2$ in 550×450 pixels. The 4D-SPED dataset was primarily analysed using the HyperSpy [8] Python library. An image that highlights the precipitate cross-sections was obtained through principal component analysis, giving a component pattern that closely resembled the sum of precipitate-characteristic reflections. After applying local intensity thresholding, the number of precipitate cross-sections in the scanned area was obtained using a blob-detection algorithm based on the Laplacian of Gaussian method on the pre-processed image. Information on precipitate types was extracted using non-negative matrix factorisation (NMF) with a navigation mask surrounding all precipitate cross-sections detected (Figure 2). The NMF component patterns were compared to (kinematically) simulated DPs of reported phases in the Al-Mg-Si-Cu system. High-angle annular dark-field scanning TEM (HAADF-STEM) images were acquired on a double corrected JEOL ARM200CF microscope operated at 200 kV.

The total area analysed by conventional methods covered approximately $1.1\,\mu m^2$, comparable to the SPED scan area, and was acquired in the same grain. The precipitate number density, ρ [μm^{-3}], was calculated as [6]

$$\rho = \frac{3N_{\parallel}}{A(t + \langle l \rangle)}. \tag{1}$$

Here, $N_{\parallel}$ is the number of precipitate cross-sections in the imaged area, A, while t is the area thickness and $\langle l \rangle$ is the average needle length. The factor 3 accounts for the 3 equivalent $\langle 100 \rangle_{Al}$ directions in which the needles grow, hence assuming an isotropic distribution. The sample thickness, measured by electron energy loss spectroscopy (EELS), gives the highest contribution to the uncertainty in the calculated precipitate number density. The total precipitate number density, $\langle \rho \rangle$, is given as the average of all number densities calculated from single images.

3. Results and discussion

The statistics obtained using conventional and SPED methodologies are presented in Table 1, showing a number density of $(65\,700 \pm 6700)\,\mu m^{-3}$ and $(67\,800 \pm 5500)\,\mu m^{-3}$ for the two approaches, respectively. Considering the high number densities involved, this shows a close agreement between the two methods. It implies that the PED pattern stack has sufficient signal-to-noise ratio to give a number density comparable to that of broad-beam illumination modes.

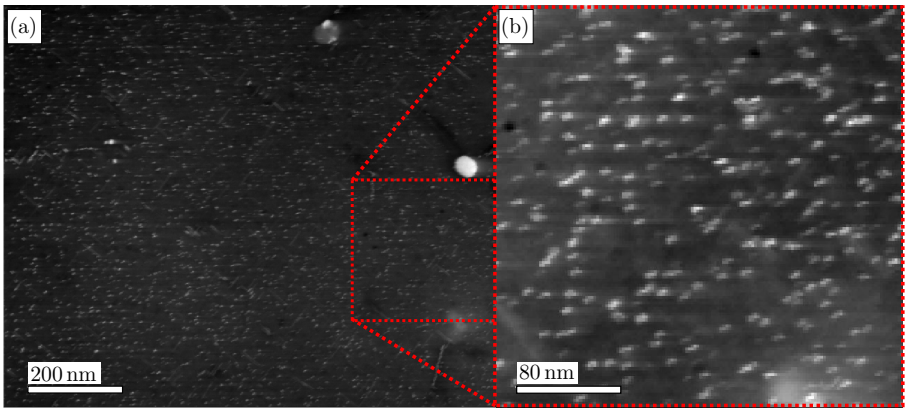

Figure 1. (a) VDF image formed from a SPED scan acquired near a $\langle 100 \rangle_{\mathrm{Al}}$ zone axis using precipitate diffraction spots. The area covers $1.34\,\mu\mathrm{m}^2$ in 550×450 pixels. (b) Enlarged view of the dashed region in (a).

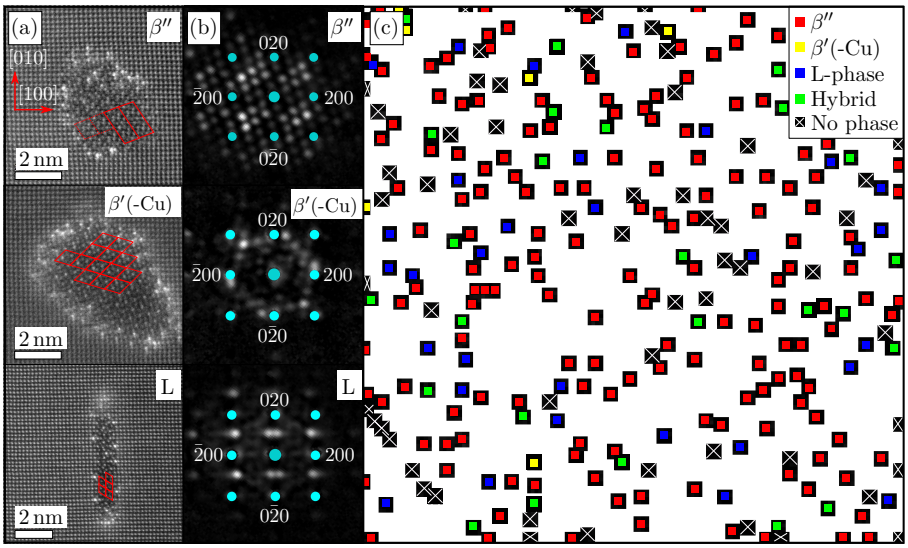

Figure 2. (a) HAADF-STEM images of the three main precipitates observed. Unit cells of the phases are highlighted in red. In the disordered L-phase, parts of the Si-network are marked. (b) NMF component patterns resembling (kinematical) DPs of the corresponding precipitate types in (a). Some aluminium reflections are marked and indexed. (c) Colour-map showing the precipitate phase distribution obtained from loading maps associated with the main NMF component patterns of (b). The area in (c) is the same as in Figure 1 (b).

The transition from Figure 1 (b) to Figure 2 (c) shows how the initial coarse estimate of number density is refined and that in addition, phase fractions are obtained. The latter has excluded those cross-sections which are not associated with a recognisable DP from the phases present. This second refinement is not attainable in manual analysis of BF/DF images where it may be difficult to differentiate between e.g. in-plane and normal orientations of small β'' needles.

Table 1. Precipitate statistics obtained using the two presented methodologies.

Method	β'' [%]	β'(-Cu) [%]	L [%]	Hybrid phase [%]	$\langle\rho\rangle$ [µm^{-3}]
Conventional	54	Unattainable	10	36	65 700±6700
SPED	73	1	12	14	67 800±5500

The precipitate fractions in Table 1 show significant variations, agreeing only on the fractions of the L-phase. This was expected, as the conventional methodology determines precipitate type solely based on shape and orientations relative to the Al matrix, while SPED uses information from reciprocal space. A phase such as β'(-Cu) does normally not extend to the Al interface, and the outer region consists of a narrow layer of other phases (or fractions thereof). Purely geometric considerations must therefore classify less well-defined cross-sections as hybrid. The L-phase has a distinct, narrow cross-section, easily recognised in BF images. Furthermore, since it rarely couples with the other phases, its fraction should be reliable.

4. Conclusions

Computational analysis of SPED data yields precipitate number densities in close agreement to conventional methodologies. Obtained phase fractions show significant deviations between the methods, and is suspected to be a consequence of inaccuracy in traditional routines being based on purely geometric considerations. With implications of equal sensitivity in the two approaches, the SPED estimate of phase fractions is considered more reliable. Due to the increased objectivity of the new analysis, the results are more readily reproducible, which has important implications for the validity and use of TEM statistics in future alloy developments. Further work aims at refining the methodology, making all steps automated and quantifying uncertainties more accurately.

Acknowledgments

All authors extend their gratitude to collaborating researchers Duncan N Johnstone and prof. Paul A Midgley from the University of Cambridge, and prof. Antonius T J van Helvoort from the Norwegian University of Science and Technology.

References

[1] Miller W S, Zhuang L, Bottema J, Wittebrood A J, De Smet P, Haszler A and Vieregge A 2000 *Mater. Sci. Eng.* A **280** 37–49
[2] Totten G E and MacKenzie D S 2003 *Handbook of Aluminium* (New York: Marcel Dekker)
[3] Edwards G A, Stiller K, Dunlop G L and Couper M J 1998 *Acta Mater.* **46** 3893–904
[4] Marioara C D, Andersen S J, Stene T N, Hasting H, Walmsley J, van Helvoort A T J, and Holmestad R 2007 *Phil. Mag.* **87** 3385–413
[5] Ravi C and Wolverton C 2004 *Acta Mater.* **52** 4213–27
[6] Andersen S J 1994 *Metall. Mater. Trans.* A **26** 1931–37
[7] Rauch E F, Portillo J, Nicolopoulos S, Bultreys D, Rouvimov S and Moeck P 2010 *Z. Kristallogr.* **225** 103–9
[8] de la Peña F et al. HyperSpy-1.3 2017 DOI: https://doi.org/10.5281/zenodo.583693
[9] Marioara C D, Andersen S J and Røyset J 2014 *Metall. Mater. Trans.* A **45**, 2938–49
[10] Barnard J S, Johnstone D N and Midgley P A 2017 *Ultramicroscopy* **174** 79–88

Paper II

Jonas Kristoffer Sunde, Calin Daniel Marioara
Antonius T. J. van Helvoort, Randi Holmestad

The evolution of precipitate crystal structures in an Al-Mg-Si(-Cu) alloy studied by a combined HAADF-STEM and SPED approach

Materials Characterization **142** (2018) 458-469.
https://doi.org/10.1016/j.matchar.2018.05.031

Materials Characterization 142 (2018) 458–469

Contents lists available at ScienceDirect

Materials Characterization

journal homepage: www.elsevier.com/locate/matchar

The evolution of precipitate crystal structures in an Al-Mg-Si(-Cu) alloy studied by a combined HAADF-STEM and SPED approach

J.K. Sunde[a,*], C.D. Marioara[b], A.T.J. van Helvoort[a], R. Holmestad[a]

[a] Department of Physics, Norwegian University of Science and Technology (NTNU), Trondheim N-7491, Norway
[b] SINTEF Industry, Trondheim N-7465, Norway

ARTICLE INFO

Keywords:
Al-Mg-Si-Cu alloy
Precipitation
Scanning transmission electron microscopy
Scanning precession electron diffraction
Machine learning

ABSTRACT

This work presents a detailed investigati5on into the effect of a low Cu addition (0.01 at.%) on precipitation in an Al-0.80Mg-0.85Si alloy during ageing. The precipitate crystal structures were assessed by scanning transmission electron microscopy combined with a novel scanning precession electron diffraction approach, which includes machine learning. The combination of techniques enabled evaluation of the atomic arrangement within individual precipitates, as well as an improved estimate of precipitate phase fractions at each ageing condition, through analysis of a statistically significant number of precipitates. Based on the obtained results, the total amount of solute atoms locked inside precipitates could be approximated. It was shown that even with a Cu content close to impurity levels, the Al-Mg-Si system precipitation was significantly affected with overageing. The principal change was due to a gradually increasing phase fraction of the Cu-containing Q′-phase, which eventually was seen to dominate the precipitate structures. The structural overtake could be explained based on a continuous formation of the thermally stable Q′-phase, with Cu atomic columns incorporating less Cu than what could potentially be accommodated.

1. Introduction

Al-based composites and alloys are prime candidates for future applications due to increasing industrial demands for materials combining properties such as high strength, low weight, good formability and corrosion resistance. They are being used to completely or partially replace, or to be combined with other alloys in a range of applications including transport, construction and packaging [1]. The 6xxx series Al(-Mg-Si) alloys form one of the main groups of age-hardening Al alloys. They have demonstrated a combination of properties desirable to the automotive industry [2], and are becoming increasingly utilized in this area [3]. Here, the high strength-to-weight ratio exhibited by these alloys allows for production of lighter vehicles with better fuel efficiency and hence reduced emissions.

6xxx series Al alloys are characterised by a significant increase in hardness upon short-term thermal ageing. The increase is caused by a large number of nano-sized, semi-coherent and metastable precipitates that form in the Al matrix from the solid solution [4,5]. The total alloying addition typically amounts to a few at.%. Needle-shaped precipitates extending along $\langle 100 \rangle_{Al}$ are characteristic of this system, and at peak hardness the microstructure typically comprises a high number density of small β''-needles [6]. The precipitation sequence in Al-Mg-Si alloys is normally given as [7,8]

$$\text{SSSS} \rightarrow \text{solute clusters} \rightarrow \text{GP-zones(pre-}\beta^{*}\text{)} \rightarrow \beta^{*} \rightarrow \beta', \text{U1, U2, B}' \rightarrow \beta, \text{Si,}$$

where SSSS stands for supersaturated solid solution. The different crystal structures can be found elsewhere [9-14].

Many studies have shown that Cu additions in Al-Mg-Si alloys have a positive effect on age-hardening, by providing a higher number density of smaller precipitates [15,16]. This has been explained based on density functional theory calculations using two-body interaction energies, where Cu was found to minimize the total energy in the Al-Mg-Si system [17]. With Cu additions, the 6xxx series precipitation sequence is changed to [18]

$$\text{SSSS} \rightarrow \text{solute clusters} \rightarrow \text{GP-zones} \rightarrow \beta^{*}, \text{L, S, C, } \beta'\text{-Cu, Q}' \rightarrow \text{Q, Si.}$$

See [19-25] for the corresponding crystal structures. This implies that the formation of β'' is suppressed, and other metastable precipitate phases are formed at peak hardness conditions. The different phases can coexist within individual precipitates, forming hybrid precipitate structures. With thermal ageing, this multiphase configuration will undergo continuous changes through diffusive transformations,

* Corresponding author.
E-mail address: jonas.k.sunde@ntnu.no (J.K. Sunde).

https://doi.org/10.1016/j.matchar.2018.05.031
Received 2 March 2018; Received in revised form 22 April 2018; Accepted 21 May 2018
Available online 24 May 2018

entailing a complex interplay that occurs on the atomic scale.

The metastable precipitates in the Al-Mg-Si-Cu system are all structurally connected through a mutual network of Si atomic columns. This network exhibits a projected near hexagonal symmetry with $a = b \approx 4$ Å, $c = n \cdot 4.05$ Å, n being an integer. Here, the lattice constant c is parallel to the needle/rod/lath axis [18]. The precipitates can be described as stacks of atomic columns in $\langle 100 \rangle_{Al}$ directions adapting to the Al lattice periodicity. They are defined through different arrangements of Al, Mg and Cu atomic columns situated *in-between*, or for certain phases with Cu columns *replacing*, the Si network columns [26]. Mixed element occupancy of atomic columns is also possible. The projected Si network is fragmented in the case of the β''-phase because of a high coherency with the Al matrix.

This work focuses on the influence of low amounts of Cu (0.01 at.%/0.03 wt.%) because of a reported considerable effect on precipitation when present in higher concentrations ($\gtrsim$ 0.4 wt.%) [23,27-29]. Previous studies evaluating the effect of low Cu additions looked at lean extruded alloys ($\lesssim$ 0.1 wt.%) [26,30,31]. High-resolution transmission electron microscopy (TEM) studies found that $\simeq$ 0.1 wt.% Cu had limited effect on the Al-Mg-Si system precipitation, merely affecting the precipitation kinetics and number densities. However, the precipitates were disordered, with sub-units of known metastable precipitates in the Al-Mg-Si-Cu system. Any significant difference in material hardness with $\lesssim$ 0.1 wt.% Cu was not measured. It remains interesting to assess the atomic scale effects of near impurity level Cu additions, and with prolonged ageing times.

Existing methodologies in microstructure quantification of Al alloys by TEM yield information on precipitate morphologies and distributions [32], including lengths, projected cross-section areas, number densities and volume fractions [18]. Despite being one of the main obtained microstructure parameters, the total precipitate volume fraction by itself is difficult to clearly relate to any measured material property. What is missing is a statistical assessment of the precipitate phase fractions at each ageing condition, which would enable refinement of the total volume fraction into a volume fraction per phase. Each phase has a different chemical composition, and hence locks different amounts of solute elements inside the structure. The amount and chemical identity of solutes left in solid solution have considerable effect on many material properties, including conductivity, ductility, corrosion and hardness.

Detailed information regarding coexisting phases and the presence of trace elements inside precipitates can be obtained using e.g. atomically resolved high-angle annular dark-field scanning transmission electron microscopy (HAADF-STEM). Other options include nanobeam diffraction and atom-probe tomography (APT). Despite offering insight to the crystal structure and elemental composition of individual precipitates, the drawback with these approaches is poor statistics, as only a limited number of precipitates can be studied. Especially with larger variations in phases exhibited at each ageing condition, this is a limitation for accurately calculating the precipitate phase fractions.

The possibility for large variations in Al-Mg-Si-Cu phases existing requires a complementary technique capable of probing a substantial number of precipitates, from which one can infer an overall picture of the frequency of phases. It has been demonstrated that scanning precession electron diffraction (SPED) combined with a machine learning approach can give information on the precipitate phase fractions in the microstructure of Al-Mg-Si-Cu alloys [33]. This scanning technique has the potential of probing a larger number of precipitates than feasible by (S)TEM lattice imaging and APT. The SPED technique was developed further in this work, and combined with HAADF-STEM. This allowed evaluation of both the crystal structure in individual precipitates, as well as a quantitative analysis of precipitate phase fractions using a substantial number of precipitates in each ageing condition.

The developed technique was employed to achieve the following goals:

- To obtain an improved understanding of the precipitate crystal structure evolution that occurs during ageing
- To elaborate the effect of low Cu additions in the Al-Mg-Si system on precipitation in the overageing stage

In the first part, the combined HAADF-STEM and SPED methodology used throughout this work is presented along with supporting evidence. In the second part, the obtained results are presented and evaluated.

2. Experimental Procedure

2.1. Material and Heat Treatment

The material studied was an Al-Mg-Si alloy (6082) with low Cu addition obtained from the materials manufacturer Neuman Aluminium Raufoss (Raufoss Technology). The composition is given in Table 1. A cylinder sample (Ø 20 mm, 10 mm height) was cut from an extruded bar and subjected to solution heat treatment at 540 °C for 12 min, and then water-quenched to room temperature. 10 min natural ageing occurred before the material was set to artificial ageing at 180 °C in an oil bath. The peak hardness condition was obtained after 3 h ageing, and the additional overaged conditions studied in this work were obtained after 24 h, 1 week, 2 weeks and 1 month total ageing.

2.2. TEM Specimen Preparation

TEM samples were made by standard electro-polishing. Al discs with 3 mm diameter and thicknesses of approximately 100 µm were electro-polished using a Struers Tenupol-5. The applied electrolyte comprised 1/3 nitric acid (HNO_3) and 2/3 methanol (CH_3OH), and was kept at −30 °C to −25 °C. The applied voltage was set to 20 V (0.2 A). Prior to SPED and HAADF-STEM experiments, the specimens were cleaned using a Fischione 1020 Plasma Cleaner to reduce the risk of carbon contamination build-up during data acquisition.

2.3. Electron Microscopy

A JEOL 2100F microscope operated at 200 kV was used for conducting the SPED experiments. SPED was performed using a NanoMEGAS DigiSTAR scan generator retrofitted to the instrument. This system enables the simultaneous scan and acquisition of electron diffraction patterns (DPs) via imaging the phosphor viewing screen of the microscope using an externally mounted camera [34].

The microscope was operated in nanobeam diffraction mode when performing SPED, using a non-precessed probe diameter of 0.5, 0.7 or 1.0 nm. The probe semi-convergence angle was 1.0 mrad. The precession angle employed was 0.5, 0.7 or 1.0°, and the precession frequency was set to 100 Hz. The scan step size was selected as 0.76, 1.52 or

Table 1
Nominal elemental composition of the (6082) Al-Mg-Si(-Cu) alloy studied in this work.

Element	Al	Si	Mg	Cu	Fe	Mn	Cr
at.%	bal.	0.85	0.80	0.01	0.12	0.25	0.08
wt.%	bal.	0.88	0.72	0.03	0.24	0.51	0.16

2.28 nm depending on the material condition studied. Exposure times used were 20 or 40 ms per pixel. The double-rocking probe required for PED was aligned following the method set out by Barnard et al. [35]. A typical dataset comprised 400 × 400 PED patterns (≈ 3.2 GB) and required on average 1 h and 30 min to acquire.

HAADF-STEM images were recorded on a double-corrected JEOL ARM200F microscope operated at 200 kV using a detector collection angle of 42–178 mrad. Conventional precipitate statistics were obtained using a JEOL 2100 microscope (200 kV). The specimen thickness was measured by electron energy loss spectroscopy (EELS). All TEM experiments were conducted in the $\langle 001 \rangle_{Al}$ zone axis of the Al matrix.

2.4. SPED Data Analysis

The obtained 4D SPED datasets, comprising a 2D PED pattern at each position of a 2D area scan, were analysed using the HyperSpy [36] Python library. The different processing steps are illustrated in Fig. 1. Initial visualisation of the precipitates present in the scan areas was obtained using virtual dark-field (VDF) images. These were formed by plotting the intensity within a selected sub-set of diffracting pixels, a *virtual aperture*, as a function of probe position. An annular aperture was selected sufficiently large and positioned so as to include diffraction spots from all precipitates lying parallel to the beam direction, verified by TEM images from the same region.

The positions (x_i,y_i) of the precipitates were extracted from the VDF images using a *local maxima filtering* and a *blob detection* algorithm based on the Laplacian of Gaussian, both building on Scikit-image project implementations [37]. Using the obtained precipitate coordinates, a boolean mask covering the immediate neighbourhood of the precipitate centres (x_i,y_i), referred to as a *navigation mask* was constructed. In addition, a boolean mask covering the PED pattern Al reflections, a *signal mask*, was formed. The latter was obtained by applying background subtraction to a bulk Al PED pattern followed by intensity thresholding.

An unsupervised learning approach based on non-negative matrix factorization (NMF) [38] was applied to the SPED data, using only the regions of interest marked by the obtained masks, i.e. the pixels covering each precipitate and the pixels falling in-between the Al reflections. The NMF algorithm approximates the 4D dataset, **S**, by the product of two matrices, **Q** and **R**, by minimizing the error function under a positivity requirement

$$\min_{\mathbf{Q},\mathbf{R}} ||\mathbf{S} - \mathbf{QR}||_F,\ \mathbf{Q} \geq 0,\ \mathbf{R} \geq 0. \tag{1}$$

The inherent condition of positive matrices **Q** and **R** ensures more physically meaningful results, being a rational choice in light of the positive nature of PED pattern intensities recorded. The decomposition returned underlying *component patterns* that represent the data, along with associated *loadings* at each real space pixel [39]. The *loading maps* indicate regions where the component patterns are significant, and resemble simplified dark-field images, see Fig. 1.

In the case of mixed PED patterns in individual pixels, i.e. patterns composed of reflections from multiple phases, one obtains loading maps with overlapping regions of intensity. Here, the PED patterns have been separated into individual components. This is the key towards unraveling the multiple phase information that can be contained in single pixel PED patterns. This was also attempted by cross-correlation and peak finding approaches, but for the weak precipitate phase reflections, these approaches were deemed inadequate.

The decomposition takes as input the number of components that will approximate the total dataset. Ideally, in the regions selected by the obtained masks, the number of components should equal the number of unique phases present multiplied by the number of allowed orientations, given by their orientation relationship with the Al matrix. This requires the scan area to remain in zone axis orientation. However, this is approximately achieved as long as the bending over the scanned area is smaller than the applied precession angle. Furthermore, the integrating operation of the precession averages out some of the effects from dynamical scattering, and acts to make the PED patterns more 'kinematic-like' [40]. This reduces the number of components needed considerably, and is crucial for machine learning decomposition routines to work. Realistically, due to non-ideal microscope alignments, imperfect masks, disordered phases, strain, dynamical effects and large area tilts, 4-5 times the ideal number of components needed to be included. Through trial-and-error, it was found that 80–120 components were necessary to represent the features of interest in the SPED data. Using a larger number introduced components associated with noise.

After decomposition, the NMF component patterns were manually compared with simulated (kinematic) DPs from known Al-Mg-Si-Cu precipitate phases. Once identified, the associated loading maps provided direct interpretation of real space positions of each phase. The loadings of the identified NMF components were then normalized and summed

$$I_i(x, y) = \sum_j^N I_j(x, y).$$

Here, (x,y) denotes scan pixel coordinate and I_j denotes the normalized loading map for the jth component pattern. The index j runs over all N component patterns matched to phase i, e.g. as a result of the different orientations allowed by the orientation relationship to the Al matrix. Subsequently, a 3D data matrix **D** built from all M phases identified was formed, where elements of **D**, $D_{x,y,i} = D_i(x,y) = I_i(x,y)$, denote the loading value in pixel (x,y) from phase i. The net result is a reconstructed and simplified description of the diffraction data, built from loading maps associated with component patterns matched to precipitate phases from the Al-Mg-Si-Cu system.

The data matrix **D** formed the basis for calculating an average phase fraction for phase i, denoted f_i, using

$$f_i \approx P^{-1} \cdot \sum_k^P \left(D_i(x_k, y_k) / \sum_i^M D_i(x_k, y_k) \right) \tag{2}$$

Here, the sum runs over all precipitate pixels (x_k,y_k), for a total number of P pixels, determined as those pixels which have a significant loading sum $\sum_i D_i(x, y)$.

In summary, a decomposition algorithm based on NMF was applied to the diffraction data from precipitates lying parallel to the beam direction. The decomposition results were matched with phases existing in the material, and combined to form a simplified representation of the SPED scan data. Finally, precipitate phase fractions were estimated using a pixel-based calculation where each precipitate PED pattern has been divided into a sum of the identified phase patterns.

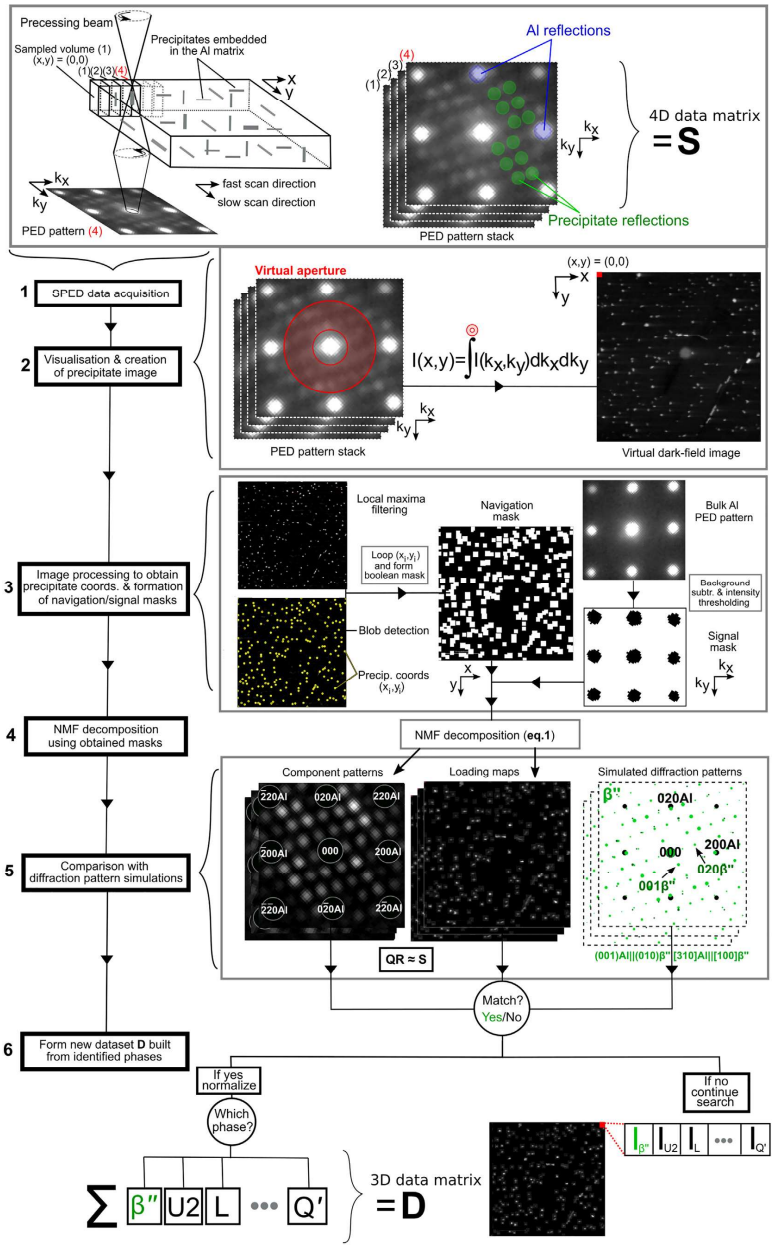

Fig. 1. Flow diagram showing the SPED experiment and the data processing applied to the acquired scan data. Details are explained in the associated text.

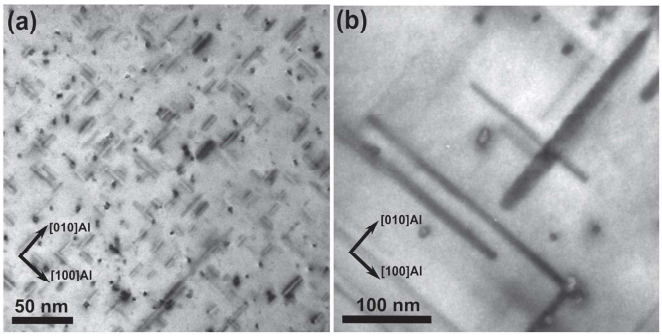

Fig. 2. Bright-field image of the (a) 3 h (peak hardness) and (b) 1 month artificial ageing condition of the Al-Mg-Si(-Cu) alloy studied.

3. Results and Discussion

3.1. Conventional TEM Analysis

Fig. 2 shows the large transformation of the Al alloy microstructure when subjected to prolonged ageing at 180 °C. At 3 h ageing (peak hardness) the microstructure comprises a high number density of small needles, with an average length of (15 ± 1) nm and (13 ± 1) nm^2 average cross-section area. After 1 month total ageing, the precipitates have coarsened considerably, measuring (352 ± 15) nm in average needle length and (63 ± 10) nm^2 in average cross-section area.

HAADF-STEM images of precipitates from the five ageing conditions studied are shown in Fig. 3. The precipitates presented were selected from a series of images, and evaluated as representative for each ageing condition. Starting with Fig. 3a acquired at 3 h ageing, the precipitate is seen to be a pure β''-phase. Some of the atomic columns appear brighter than the other corresponding columns due to partial occupancy of Cu. This is for instance seen at the Al(/Si_3) columns in the highlighted unit cell. Cu (Z_{Cu} = 29) is observed with a higher contrast than the other elements Mg (Z_{Mg} = 12), Al (Z_{Al} = 13), and Si (Z_{Si} = 14) due to the $Z^{1.7-2.0}$ atom column scattering power at high angles for HAADF-STEM imaging [41]. For some precipitates (not shown), Cu-enriched columns could be seen at the precipitate interface. This has been observed previously, and has been proposed as a mechanism to suppress misfit dislocations [42].

Fig. 3b shows a precipitate at 24 h ageing. In this condition we see that β'' is still dominant, but many additional phases are now present, forming a fragmented hybrid structure. Unit cells and sub-units of the U2-phase connect to the unit cells of β''. At the lower part of the image, sub-units of Cu-containing phases such as Q′/C and β'-Cu are seen, which have Cu columns located *in-between* and *replacing* the Si network, respectively. These phases are conspicuous due to their high Cu content. Several precipitates at this condition showed the same tendency, with a predominantly Al-Mg-Si containing β''/U2 interior, and Cu-enrichment, as well as randomly positioned sub-units of Cu-containing phases at the precipitate interface. This is similar to earlier results [26,43], showing β''/disordered precipitates at under-aged and peak hardness conditions for alloys with higher Cu content. The positions of Cu enriched columns in the β''-phase for the 3 h and 24 h conditions seem to agree with the findings of Li et al. [44], which found that Cu incompletely substitutes for Mg_1 and Si_3 (here, Al) columns. In rare cases, Si_2 columns also showed partial Cu occupancy.

After 1 week ageing (Fig. 3c) it is seen that a large transformation of the precipitate structure has occurred. The precipitates have coarsened considerably. The largest phase fraction, often dominating the precipitate interior, is now that of the β'-phase. Detailed image analysis revealed that there exists a pattern of varying intensity at the Si column positions. Many regions showed a significantly higher intensity at Si_1 columns as compared to the Si_2 columns, which were more uniform in intensity. These regions are likely associated with a β' structure as reported by Vissers et al. [10]. There evidence was given for a structure with an addition of 1 extra Si atom per 3 × 4.05 Å in the *c*-direction at the Si_1 columns. This leads to a higher column occupancy, and hence a higher intensity at the Si_1 site. However, in other regions the difference between Si_1 and Si_2 column intensities was less distinct, meaning that the atomic modulation of Si_1 columns has not developed. The border between the regions is not very clear, and there exists a tiling of the two.

The difference is more evident in diffraction data, where the presence of added reflections (Fig. 3c–d) indicates a structural disparity. Image analysis and DP simulations indicate that the regions without clear modulation of Si_1 columns instead have a space group symmetry similar to β'-Cu(/Ag) (P-62m) [22]. The difference in space group symmetry gives a trigonal, as opposed to hexagonal symmetry surrounding the corner Si columns in the proper β' unit cell ($P6_3/m$), see Fig. 3c–d. The change of symmetry relative to proper β' seems to be related to the different Si_1 column occupancies, which necessarily affect the bonding to the neighbouring atomic columns. The difference is difficult to assess in HAADF-STEM images, as the deviating structure can lie somewhere in-between the two symmetries. However, with the diffraction approach employed throughout this work, the two variants can clearly be separated, and in order to distinguish them, the notation β'-2 will be used to denote the structure that deviates from proper β', see Fig. 4.

Analysis of atomic column Z-contrast indicates that β'-2 is isostructural with β'-Cu(/Ag) [22], but having Cu replaced by Si, and Al by Mg. This is probably due to the smaller size of the Si atoms as compared to Cu, which allows for more space to be occupied by the larger atom size of Mg. β'/β'-2 are the main precipitate constituents in the 1 week condition, often linked through a narrow strip of U2 unit cells/sub-units to the Al matrix or phases at the interface. The interface comprises unit cells and sub-units of Al-Mg-Si-Cu phases, most notably Q′/C. Compared with the 24 h condition, the region of Cu-containing phases at the interface has grown in extent. β'' was not frequently observed in the 1 week condition.

After 2 weeks ageing (Fig. 3d) many precipitates show a modest coarsening relative to the 1 week condition. The phases coexisting are similar to the 1 week case. From a series of images, the main observed development of the precipitate structure seems to be the progression of the Q′-phase towards the precipitate interior. Several grouped unit cells of Q′ can now be seen.

At 1 month total ageing (Fig. 3e) there is limited further coarsening

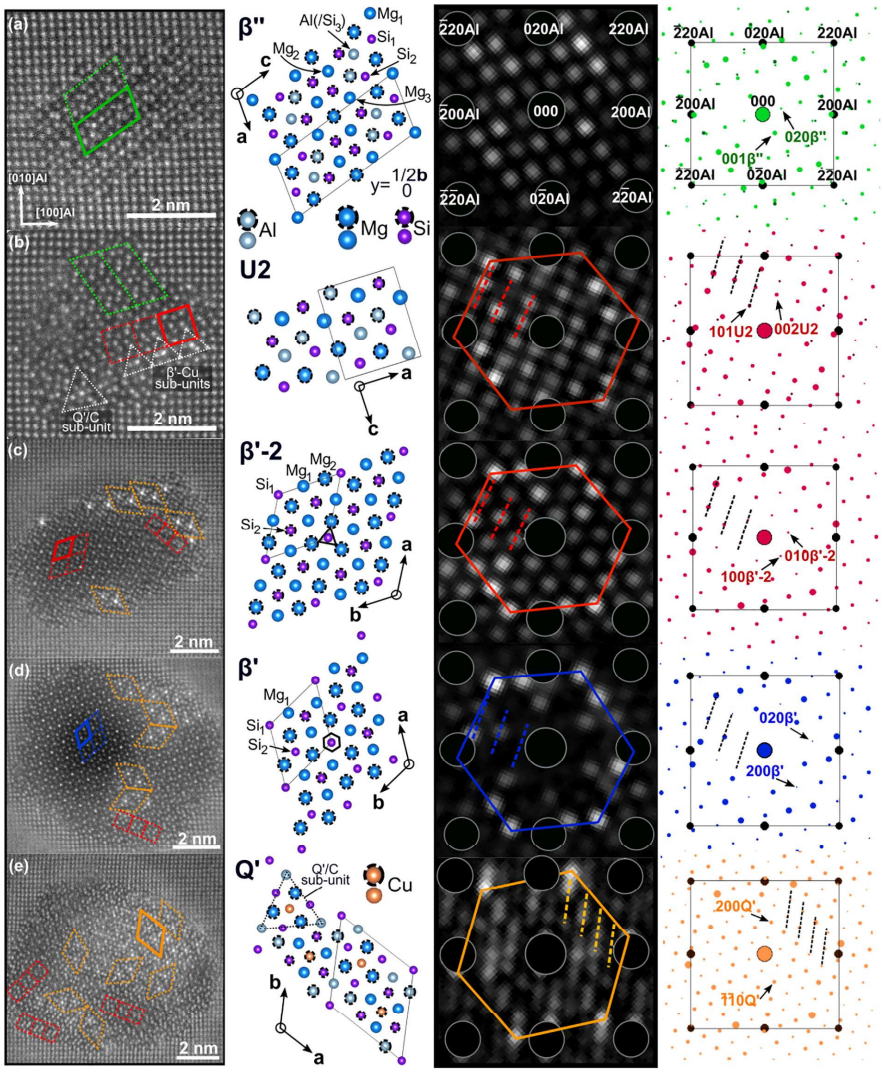

Fig. 3. (a–e) HAADF-STEM images of precipitates, precipitate crystal structures based on existing literature, NMF component patterns from SPED data decomposition and matching (kinematic) DP simulations. They are from representative precipitates for each of the ageing conditions studied; 3 h, 24 h, 1 week, 2 weeks and 1 month artificial ageing at 180 °C, respectively. One unit cell of the displayed structures is marked with solid lines, and repeated unit cells are dashed. The hybrid character of the precipitates are indicated, showing several unit cells and sub-units from different phases. Solid and dashed lines in component patterns and matching simulated DPs are guiding aids for the characteristic features of the precipitates.

of precipitates. Similar to the 1 week–2 weeks transition, there seems to be a further development of the Q′ takeover of the precipitate structures. Qualitatively, for some precipitates there seems to be a near 50/50 division of β'/β'-2 vs. Q′. Apart from these phases, there are still lines of U2 unit cells or sub-units linking or 'gluing' the other coexisting phases together. This was the observed behaviour of the U2-phase in all conditions with disordered precipitate structures. Such U2 characteristics have also been observed in the β'-Cu(/Ag) phase [22].

In addition to the phases previously discussed, the L-phase was also observed in all alloy conditions (Fig. 5). This was however first revealed when the areas were revisited after SPED analysis. Its presence remained low in numbers and stable with ageing, often linked with

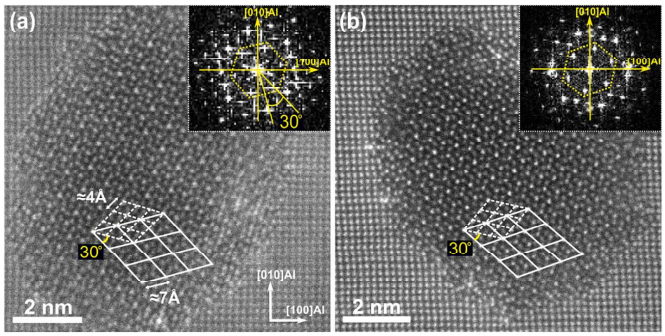

Fig. 4. HAADF-STEM images showing (a) β'-2 and (b) β'. The insets show fast Fourier transforms (FFTs) of the lattice images. There is a slight, but noticeable difference between the FFTs in (a) and (b) indicating a small symmetry difference between the two β' types.

microstructure defects such as dislocation lines. This is in agreement with previous studies of this phase [45].

In summary, the main observed precipitate phase evolution begins with a β'' to β'/β'-2 transition. Looking at the role of Cu in the initial stages, the atoms likely start out at the β''/Al interface, where they act to suppress the misfit strain. Subsequently, and in agreement with previous studies, Cu atoms enter the β'' unit cell preferentially at the Si_3 (Al) and Mg_1 sites. In addition, sub-units of Cu-containing phases (Fig. 3b) are formed at the precipitate interface. In the next evolution stage, there occurs a slow movement inwards by the Q′-phase, gradually taking over the precipitate interior. Cu has a low diffusion coefficient in the Al matrix, which supports the slow kinetics of Cu-containing phases observed [46]. The observed evolution is likely to terminate when there is too few additional Cu atoms left in solid solution to drive the diffusion, and can be followed qualitatively by HAADF-STEM imaging.

3.2. Assessment of the Information Content in SPED Data

In order to obtain statistical support for the observed evolution indicated by atomically resolved imaging, SPED combined with a machine learning approach was pursued. This scanning technique can cover areas over 1 μm^2 in nm-sized steps, which could include 10 s to 1000 s of precipitate cross-sections depending on the thermomechanical pre-processing applied to the material. This increased sampling forms the basis for improved statistics complementary to conventional high-resolution TEM analysis. For the alloy conditions studied in this work, it was necessary to adapt the step size and hence the scanned area to include a significant number of precipitates, especially for the longest ageing times, as seen from Fig. 2b.

The VDF image presented in Fig. 6c shows a selection of 188 precipitates, acquired for the 24 h alloy condition. Comparison with bright-field and dark-field TEM images (Fig. 6a–b) indicates that all precipitates (parallel to the beam direction) are detected. The principal loading maps obtained by NMF decomposition and matched with precipitate phases existing are shown in Fig. 6e–j. This shows how the technique can be used for phase mapping in the alloy microstructure. Fig. 6d shows the sum of the loading maps, i.e. the reconstructed dataset based on the six identified precipitate phase classes (β'', U2, β'-2, Q′, L, hybrid/disordered). The hybrid class denotes component patterns that comprise a mix of individually identifiable patterns from Al-Mg-Si-Cu phases. Hybrid components are likely to arise in cases where either one of the phases in the mix does not occur in any individual PED pattern, probably caused by the spatial confinement of the phase, which does not extend beyond the scan pixel size. The disordered class denotes component patterns which do not clearly resemble any of the DP simulations, but which contain certain features of interest, such as the Si network hexagon. Comparison with the DF/VDF images (Fig. 6b–c) indicates that this reconstructed representation covers the precipitates seen in the area.

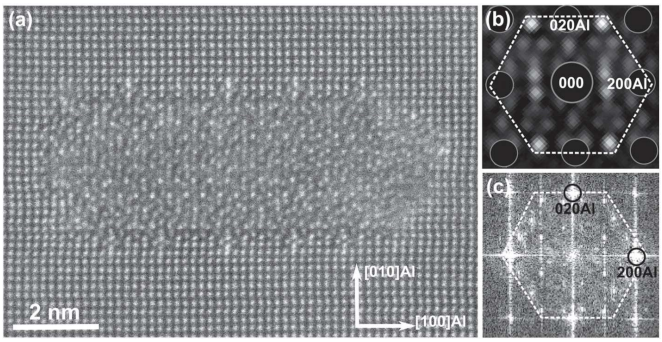

Fig. 5. (a) HAADF-STEM image of a L-phase formed on a dislocation line in the 24 h ageing condition. The associated component pattern (b) shows agreement with the FFT of the lattice image (c). The projected hexagonal Si network is indicated, which is aligned along $\langle 100 \rangle_{Al}$ directions for the L-phase.

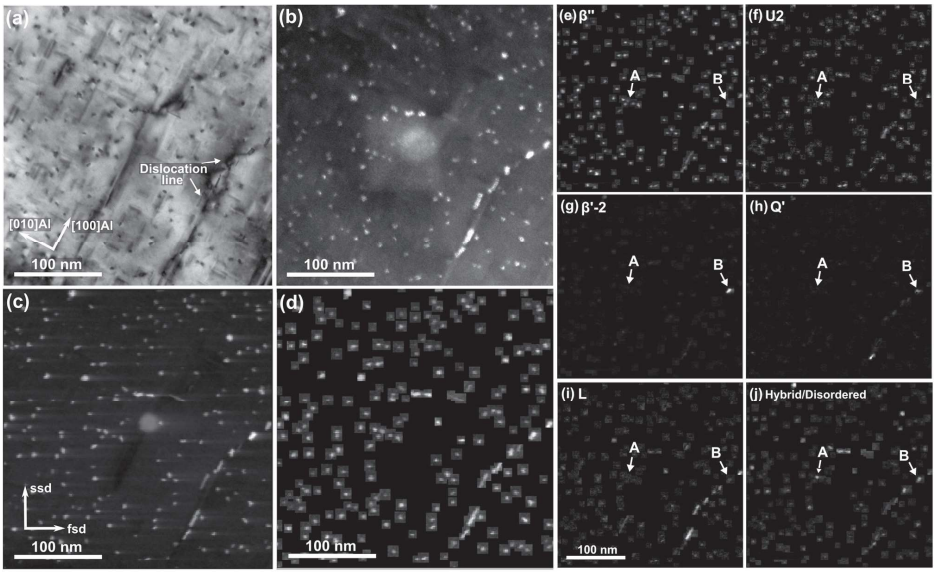

Fig. 6. (a) Bright-field and (b) dark-field image acquired in a SPED scan area near the $[001]_{Al}$ zone axis. (c) VDF image constructed from precipitate reflections. (d) Reconstruction of the SPED data from NMF component patterns matched with precipitate phases existing. (e–j) Loading maps from each of the identified phases in the SPED scan area. The two precipitates **A** and **B** are imaged by HAADF-STEM in Fig. 7. *ssd* and *fsd* denote slow scan- and fast scan direction, respectively.

Examples of main component patterns obtained by NMF decomposition for the different alloy conditions are shown in Fig. 3a–e. These components show good agreement with (kinematic) simulations of DPs for known Al-Mg-Si-Cu precipitate structures.

It is observed from the loading maps that several precipitates have multiple overlapping pixels of intensity coming from different phases. This shows how phases are revealed down to the sub-precipitate level, i.e. multiple phases within a single precipitate are resolved. The reliability of the decomposition was assessed by correlating the NMF results with atomic resolution images acquired from some of the very same precipitates, e.g. the precipitates labeled **A** and **B** in Fig. 6e–j, which are shown in Fig. 7a–b, respectively.

The precipitate imaged in Fig. 7a shows a particularly disordered crystal structure, with near absence of complete crystal structure unit cells. Sub-units of phases in the Al-Mg-Si-Cu system can however be discerned. The most significant loading map and its associated component pattern is shown. The pattern shows no clear match with any of the simulated DPs of single phases in Fig. 3. However, the feature of importance is the presence of a hexagonal network with reciprocal spacing in agreement with the projected Si network spacing of the Al-Mg-Si(-Cu) system. In addition, the periodicity in diffraction spot rows highlighted agrees with that of the Q′-phase, which is also seen from the FFT of the lattice image. The HAADF-STEM image agrees with the presence of a projected hexagonal Si network. HAADF-STEM and SPED both conclude that the precipitate is disordered, but an underlying Si network is present. A few unit cells and sub-units of U2, β' and Q′ (highlighted in Fig. 7a) can be seen. The loading map is most significant in the lower region of the precipitate, which agrees with the position of the Q′ sub-units. Additional loadings were obtained for this precipitate (not shown). The additional loadings individually described less than 20% of the precipitate pixels, and their associated component patterns all showed the Si network hexagon.

The second precipitate imaged (Fig. 7b) shows a coarsened structure located on a dislocation line in the scan area, see Fig. 6. Precipitate phases located near dislocation lines were less frequent in this alloy condition (Fig. 6e–j), and have likely coarsened as a result of solute segregation or pipe diffusion of elements such as Cu. They hence show a faster ageing response relative to the bulk precipitates. The HAADF-STEM image shows the presence of a projected hexagonal Si network permeating the structure. The largest phase fraction comprising this precipitate is β'-2, seen as a bright hexagonal network of Si columns. Additionally, highlighted in the left part of the image is a smaller region of Q′ unit cells, whose structure is shown in Fig. 3e, having Cu columns situated *in-between* the Si network. Another defining characteristic of this phase is an interface oriented along $\langle 150 \rangle_{Al}$ directions, highlighted in the image. Furthermore, as β'/β'-2 does not extend to the Al matrix interface [47], there exists a narrow layer of different Al-Mg-Si-Cu phase sub-units.

The second and third columns of Fig. 7b show how the SPED analysis provides information about the phases coexisting inside this precipitate. The two main loading maps and associated component patterns obtained are shown. Comparison to DP simulations (Fig. 3) identifies the two components as Q′ (top) and β'-2 (bottom), respectively. The defining features are also indicated in the FFTs of the lattice images. The loading maps indicate the phase presence in each pixel. Apart from a visible effect of afterglow in the fast scan direction, the loading maps correspond reasonably well with the HAADF-STEM image.

The main strength of the SPED technique lies in the ability to scan large areas containing a substantial number of precipitates, while still preserving high spatial resolution. This forms the basis for objective evaluation of the precipitate phase occurrence using a representative distribution of precipitates. Generalizing from a series of 10-20 HAADF-STEM images can give a misleading conclusion on precipitate phase fractions in the alloy microstructure, especially when the variations between precipitate phases exhibited are relatively large. There is a risk

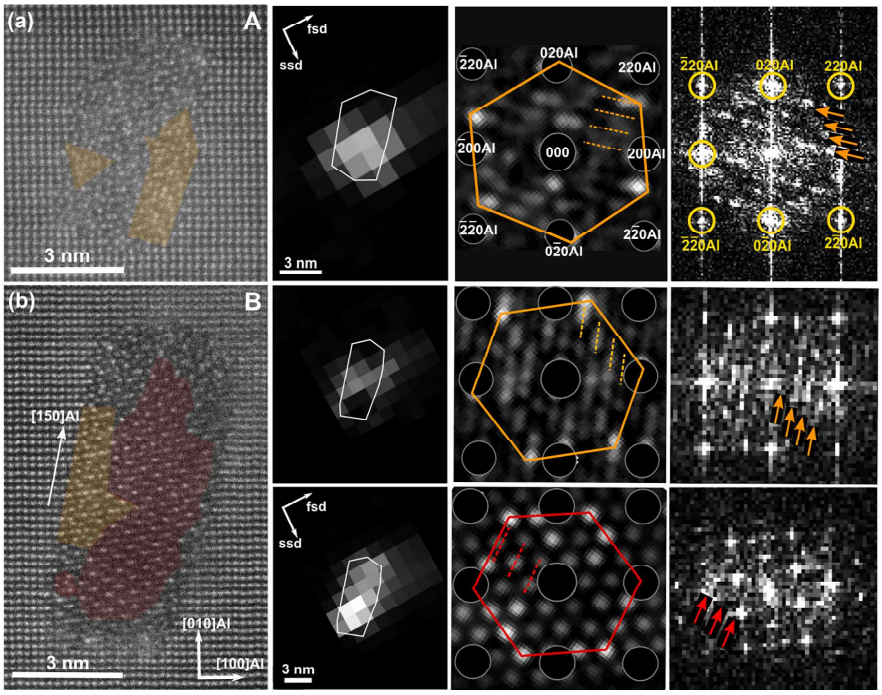

Fig. 7. (a) and (b) show HAADF-STEM lattice images and SPED decomposition results for precipitates labeled **A** and **B** in Fig. 6. The first column shows precipitate lattice images. The second and third columns show the main loading maps and associated component patterns from NMF decomposition, respectively. The fourth column shows FFTs of the lattice image areas highlighted. The red and orange highlighted regions show unit cells/sub-units of *β′*-2 and Q′, respectively. The outlines of the precipitate cross-sections are overlaid on the loading maps. Characteristic precipitate features in component patterns and image FFTs are indicated.

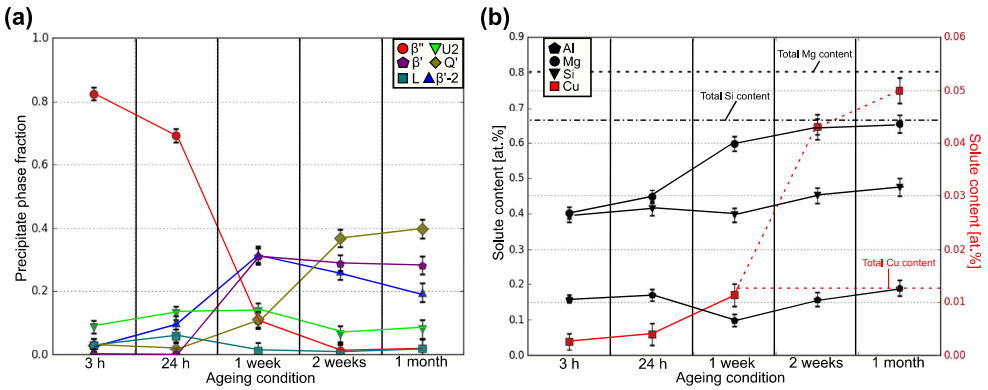

Fig. 8. Plots of (a) average precipitate phase fractions (Eq. (2)) and (b) the total amount of solute atoms locked inside precipitates at each ageing condition studied. The incorporation of Si into dispersoids is taken into account for the marked total Si solute content (dashed-dotted line) using an estimate based on the Alstruc microstructure solidification model [48].

of selectively probing larger, Cu-containing precipitates due to the strong Z-contrast dependence of HAADF-STEM. Adding to this point, a poor depth of focus leads to further selective imaging of longer, coarsened precipitate needles that reach the specimen surface.

Besides the risk of selectively probing precipitates, rare cases such as the L-phase (Fig. 5) or the Q′/β′-2 phase (Fig. 7b) might be missed in a HAADF-STEM analysis. These images were acquired after analysing the SPED scan data, where the precipitate PED patterns from the dislocation line revealed the presence of rare phases in this alloy condition (Fig. 6e–j). It becomes clear that a scanning technique capable of covering large areas will give a more general picture of phase distributions, and hence an improved estimate of precipitate phase fractions in the alloy microstructure. The SPED scan data presented in this work covers precipitate numbers ranging from 520 (3 h condition) to 101 (1 month condition). The scan areas and hence the number of precipitates can be further upscaled [33], and comes at a relatively low cost in increased analysis time.

The main limiting factors with SPED are currently due to the acquisition system. The diffraction from particularly small precipitates falls close to the noise threshold. In addition, adverse effects of afterglow is observed, see the second column of Fig. 7. This has an effect on the recorded PED patterns in the fast scan direction, and for large and strongly diffracting precipitates this effect is pronounced. It is however unlikely that the main characteristic of a precipitate is miscalculated due to this effect, as the relative intensities remain similar. There are technical solutions coming to solve these issues.

3.3. Quantification of Precipitate Phase Fractions

Fig. 8 summarizes the main findings from the SPED analysis for the five ageing conditions and the total of approximately 1200 precipitates identified. Fig. 8a shows the average precipitate phase fractions estimated from a representative distribution of precipitates in each ageing condition. Errors in individual precipitate phase fractions were estimated based on comparison with high-resolution images, which takes into account the adverse effects introduced by the SPED acquisition system. This error was subsequently scaled according to the number of precipitates in the recorded SPED scan, N, assuming linearly independent measurements of phase fractions for each precipitate. The plot showcases the main precipitate phase evolution that occurs during ageing.

In line with the HAADF-STEM results, the presence of β″ is seen to drop quickly with increased ageing time. At the 1 week condition it has dropped to 10%. Furthermore, it confirms the distinct transformation of

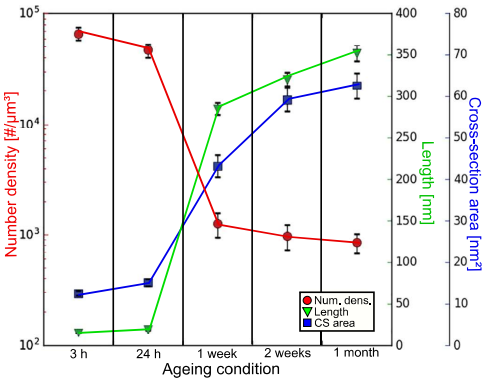

Fig. 9. Plot of the precipitate statistics at each ageing condition studied.

Table 2
Average composition and crystal lattice parameters of the precipitate phases found in the Al-Mg-Si(-Cu) alloy studied.

Precip. phase	Chemical composition	Lattice parameters [Å]	Ref.
β″	$Al_5Mg_{14}Si_{14}$	a = 15.16, b = 4.05,β = 105.3°, c = 6.74	[9]
β′/β′-2	$Mg_6Si_{3.33}$	$a = b$ = 7.15, c = 4.05,γ = 120°	[10]
U2	AlMgSi	a = 6.75, b = 4.05, c = 7.94	[11]
L	$Al_{20}Mg_{44}Si_{33}Cu_2$	a = 10.32, b = 4.05,β = 100.9°, c = 8.10	[21]
Q′	$Al_6Mg_6Si_7Cu_2$	$a = b$ = 10.32, c = 4.05,γ = 120°	[49]

precipitate crystal structures from the 24 h to the 1 week condition. The main phases present changes from β″ and U2 to β′/β′-2, and it is interesting to note that the onset of β′-2 formation seems to occur before β′. The 1 week condition also shows an increasing Q′ phase fraction (≈11%). At this condition Q′ is predominantly observed inside bulk precipitates, unlike earlier conditions where it was mainly detected near microstructure defects.

With further ageing there are different developments for the three main phase fractions β′, β′-2 and Q′. The β′-2 phase fraction is seen to gradually decrease from 1 week to 1 month ageing, whereas β′ stays nearly constant at about 30%. As was observed in HAADF-STEM images, the Q′ phase fraction increases steadily as a function of ageing time, and is seen from the plot to reach a phase fraction of ≈ 40% at 1 month ageing. The precipitate cross-section area exhibits a modest growth from 2 weeks to 1 month ageing, seen from Fig. 9. Interpretation of the observed β′/β′-2 evolution suggests that in order for the β′ phase fraction to stay nearly constant, with limited cross-section area increase and with a gradually increasing fraction of Q′, both or either one of two effects are occurring:

- β′-2 transforms into β′ with increased ageing time.
- β′ remains stable, and the formation of Q′ occurs preferentially at β′-2 regions.

As previously discussed, the observed evolution is likely to end when there are too few Cu atoms left in solid solution. Using the obtained phase fractions together with measured precipitate statistics, one can estimate the amount of solute atoms locked inside precipitates. The different phases have different chemical compositions and unit cell parameters, see Table 2. The compositions listed are in the case of the β″-phase based on an average composition using three structures [9]. For the disordered L-phase, the composition was estimated using HAADF-STEM images, assuming a C-phase atom column density [21]. β′-2 was assumed to have the same average composition as β′.

The precipitate phase fractions were first used to convert a measured overall volume fraction (VF) into a volume fraction per phase, VF_i. Subsequently, the precipitate phase unit cell parameters and composition were used to convert a volume fraction per phase into a solute fraction per phase (SF_i). This was calculated using a conversion factor, k, relating the two parameters

$$VF_i = k \cdot SF_i.$$

The conversion factor is defined as

$$k = \left(\frac{\text{equiv. \#Al atoms in } V_{UC,i}}{\text{\#atoms in } UC_i}\right)\cdot\left(\frac{\text{\#atoms in } UC_i}{\text{\#non-Al atoms in } UC_i}\right),$$

where UC_i denotes the unit cell of phase i and $V_{UC,i}$ is its corresponding volume. Finally, the solute fractions were summed up to give a total

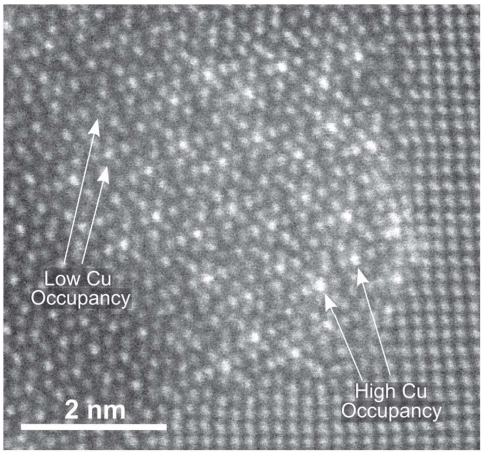

Fig. 10. HAADF-STEM image of a precipitate containing Q′. The varying intensity in the indicated atomic columns implies different Cu occupancies.

solute content locked inside precipitates.

The results are presented in Fig. 8b, which shows the development of total solute content of main elements locked in precipitates during ageing. Besides a dip in the Al solute fraction, and a constant (or small decrease) in the solute fraction of Si in the 24 h to 1 week transition, Al, Mg, Si and Cu content in precipitates gradually increases with ageing. The noted exception for Al and Si solute fractions at 24 h to 1 week ageing is due to the formation of *β′/β′*-2. Unlike the other phases observed, which have Si:Mg ratios close to one, *β′/β′*-2 show the largest deviation with an average composition of $Mg_6Si_{3.33}$. This necessarily leads to a larger incorporation of Mg than Si in the precipitate structure, which is dissolved back into the solid solution. These structures also contain no Al, which explains the decrease of the Al solute fraction. The combined total solute content in precipitates is monotonously increasing with increased ageing time, meaning that the orders of magnitude decline in number density seen from Fig. 9 are compensated by the diffusive growth of large precipitates.

The Cu solute content remains low in the 3 h to 24 h transition. At this stage, the Cu content in precipitates is mainly attributed to the L and Q′-phase having formed near microstructure defects, such as dislocation lines. HAADF-STEM images show that there additionally exists an incorporation of Cu in e.g. the *β″* structure and a Cu-enrichment at the precipitate interface. This contributes however little to the total Cu content inside precipitates.

At the 1 week condition there is a significantly increased phase fraction of Q′, which leads to a higher content of Cu in precipitates. This further increases rapidly with ageing, due to a continuously increasing Q′ phase fraction. At 1 month ageing a total solute fraction of 0.05 at.% Cu is obtained, which far surpasses the total Cu content of 0.013 at.% in the alloy, marked in Fig. 8b. The reason is that the calculation assumes a maximum Cu incorporation in the Q′ structure of ≈ 10%, which is based on the stated composition $Al_6Mg_6Si_7Cu_2$. However, it is observed here that there exists only a partial occupancy of Cu in the Cu atomic columns of the Q′ structure. This is clearly seen in HAADF-STEM images, see Fig. 10. The Cu content instead varies between 0 and 10%, leading to an overestimate using the maximum value.

What can be concluded is that the Q′ phase fraction near the 1 week condition has the *potential* to incorporate nearly all the Cu in the material, being the only phase with a significant Cu content. However, instead the phase continues to form, with less Cu than what can be accommodated in the structure. This explains how even a Cu content almost down to impurity levels can considerably affect the Al-Mg-Si system precipitation. The Q′ structure is more thermally stable than *β′/β′*-2, evident by its gradual dominance of the precipitate structure with overageing. Several HAADF-STEM images showed that the Cu occupancy was higher at the precipitate interface, where the Q′ unit cells initially are formed. This supports the indication of an inwards movement into the precipitate structures by the Q′-phase, which occurs through a slow diffusive process. The slow transformation is due to the low diffusivity of Cu in the Al matrix [46].

Different from other phases, the U2 and L phase fractions remain stable ($\lesssim$ 16%) throughout the total ageing process. This is in agreement with HAADF-STEM lattice images, where the U2-phase is seen to form lines of unit cells in all conditions, forming the 'glue' between the other phases, or the interface to the Al matrix. Among the Al-Mg-Si containing phases, this is the phase that remains most stable in number with ageing.

The L-phase also remains stable and low in numbers. This is thought to be due to the similarity in the number of microstructure defects in the samples studied, such as grain boundaries or dislocation lines, to which the L-phase is associated. This is clear from the presented 24 h condition SPED scan (Fig. 6i), where a dislocation line contains nearly all the L-phases in this area. The L-phase is known to have high thermal stability, and forms in the bulk at higher alloy Cu contents [45].

4. Conclusions

This work has demonstrated that combining HAADF-STEM and SPED resulted in a more accurate evaluation and quantification of the precipitate crystal structure evolution that occurs during ageing of a low Cu content Al-Mg-Si alloy. NMF decomposition of SPED data could be used to resolve phases within individual precipitates, and allowed for a statistically sound number of precipitates to be included in the analysis, beyond what is achievable by other techniques. The results enabled an estimate of precipitate phase fractions at each ageing condition, which were used to approximate the total solute content locked inside precipitates throughout the total ageing process.

At peak hardness, the precipitates were predominantly observed as pure *β″*. Upon further heat treatment, the precipitates evolved into complex hybrid structures, primarily comprising Al-Mg-Si phases like *β″* and U2 in the precipitate interior. Cu-enriched columns and sub-units of Cu-containing phases like Q′/C and *β′*-Cu existed at the precipitate interface. With increased ageing the precipitates coarsened substantially, and exhibited a projected hexagonal Si network with *β′/β′*-2 in the precipitate interior. Unit cells/sub-units of Cu-containing phases were still confined to the precipitate interface, but had grown larger in extent. Beyond this point was seen a slow, but gradual progression inwards into the precipitates by the Cu-containing Q′-phase, with Cu atomic columns incorporating less Cu atoms than what could potentially be accommodated. Q′ was eventually seen to dominate the precipitate structures. It is expected that this trend would continue until most Cu atoms have been drained from the solid solution. The results show that even a low Cu content (0.01 at.%) can significantly affect the Al-Mg-Si system precipitation, especially during overageing.

The study demonstrates the potential of SPED when combined with other TEM techniques and data analysis including machine learning. The high information content in each SPED scan can continually be explored, and with the advent of powerful and dedicated machine learning approaches and improved detector technologies, this can potentially uncover further insights to the material microstructure.

Data Availability

The TEM images presented in this work are given in raw/unprocessed form. The raw/processed scanning diffraction data required to reproduce these findings cannot be shared at this time as the data

also forms part of an ongoing study.

Acknowledgements

JKS, CDM and RH acknowledge the support from the AMPERE project (247783), a Knowledge building Project for Industry, co-financed by The Research Council of Norway (RCN), and the industrial partners Norsk Hydro, Sapa, Gränges, Neuman Aluminium Raufoss (Raufoss Technology) and Nexans. The (S)TEM work was carried out on the NORTEM infrastructure (NFR 197405) at the TEM Gemini Centre, Trondheim, Norway. All the authors extend their gratitude to collaborating researchers Duncan N. Johnstone and prof. Paul A. Midgley from the University of Cambridge.

References

[1] G.E. Totten, D.S. MacKenzie, Handbook of Aluminum, Vol. I and II Marcel Dekker, New York, 2003.
[2] W.S. Miller, L. Zhuang, J. Bottema, A.J. Wittebrood, P. De Smet, A. Haszler, A. Vieregge, Recent development in aluminium alloys for the automotive industry, Mater. Sci. Eng. A 280 (2000) 37–49.
[3] Aluminium Content in Cars, Summary Report Ducker Worldwide LLC, (2016) http://www.ducker.com/.
[4] M. Murayama, K. Hono, Pre-precipitate clusters and precipitation processes in Al-Mg-Si alloys, Acta Mater. 47 (1999) 1537–1548.
[5] S.P. Ringer, K. Hono, Microstructural evolution and age hardening in aluminium alloys: atom probe field-ion microscopy and transmission electron microscopy studies, Mater. Charact. 44 (2000) 101–131.
[6] S.J. Andersen, H.W. Zandbergen, J. Jansen, C. Træholt, U. Tundal, O. Reiso, The crystal structure of the β''-phase in Al-Mg-Si alloys, Acta Mater. 49 (1998) 3283–3298.
[7] G.A. Edwards, K. Stiller, G.L. Dunlop, M.J. Couper, The precipitation sequence in Al-Mg-Si alloys, Acta Mater. 46 (1998) 3893–3904.
[8] C.D. Marioara, S.J. Andersen, H.W. Zandbergen, R. Holmestad, The influence of alloy composition on precipitates of the Al-Mg-Si system, Metall. Mater. Trans. A 36 (2005) 691–702.
[9] H.S. Hasting, A.G. Frøseth, S.J. Andersen, R. Vissers, J.C. Walmsley, C.D. Marioara, F. Danoix, W. Lefebvre, R. Holmestad, Composition of β'' precipitates in Al-Mg-Si alloys by atom probe tomography and first principles calculations, J. Appl. Phys 106 (2009) 123527.
[10] R. Vissers, M.A. van Huis, J. Jansen, H.W. Zandbergen, C.D. Marioara, S.J. Andersen, The crystal structure of the β' phase in Al–Mg–Si alloys, Acta Mater. 55 (2007) 3815–3823.
[11] S.J. Andersen, C.D. Marioara, R. Vissers, A. Frøseth, H.W. Zandbergen, The structural relation between precipitates in Al-Mg-Si alloys, the Al-matrix and diamond silicon, with emphasis on the trigonal phase U1-$MgAl_2Si_2$, Mater. Sci. Eng. A (2007) 157–169.
[12] S.J. Andersen, C.D. Marioara, A. Frøseth, R. Vissers, H.W. Zandbergen, Crystal structure of the orthorhombic U2-$Al_4Mg_4Si_4$ precipitate in the Al-Mg-Si alloy system and its relation to the β' and β'' phases, Mater. Sci. Eng. A 390 (2005) 127–138.
[13] S.D. Dumolt, D.E. Laughlin, J.C. Williams, Formation of a modified β' phase in aluminium alloy 6061, Scr. Metall. 18 (1984) 1347–1350.
[14] A.H. Geisler, J.K. Hill, Analyses and interpretations of X-ray diffraction effects in patterns of aged alloys, Acta Crystallogr. 1 (1948) 238–252.
[15] W.F. Miao, D.E. Laughlin, Effects of Cu content and preageing on precipitation characteristics in aluminium alloy 6022, Metall. Mater. Trans. A 31 (2000) 361–371.
[16] M. Murayama, K. Hono, W.F. Miao, D.E. Laughlin, The effect of Cu additions on the precipitation kinetics in an Al-Mg-Si alloy with excess Si, Metall. Mater. Trans. A 32 (2001) 239–246.
[17] S. Hirosawa, F. Nakamura, T. Sato, First-principles calculation of interaction energies between solutes and/or vacancies for predicting atomistic behaviors of microalloying elements in aluminum alloys, Mater. Sci. Forum 561-565 (2007) 283–286.
[18] C.D. Marioara, S.J. Andersen, T.N. Stene, H. Hasting, J. Walmsley, A.T.J. van Helvoort, R. Holmestad, The effect of Cu on precipitation in Al–Mg–Si alloys, Philos. Mag. 87 (2007) 3385–3413.
[19] L. Sagalowicz, G. Hug, D. Bechet, P. Sainfort, G. Lapasset, A study of the structural precipitation in the Al-Mg-Si-Cu system, Proceedings of the 4th International Conference on Aluminium Alloys (ICAA4) (1994) 644–651.
[20] H. Perlitz, A. Westgren, The crystal structure of Al_2CuMg, Arkiv. Kemi, Min. Geol. 16B (1943) 1–5.
[21] M. Torsæter, F.J.H. Ehlers, C.D. Marioara, S.J. Andersen, R. Holmestad, Applying precipitate–host lattice coherency for compositional determination of precipitates in Al–Mg–Si–Cu alloys, Philos. Mag. 92 (2012) 3833–3856.
[22] C.D. Marioara, J. Nakamura, K. Matsuda, S.J. Andersen, R. Holmestad, T. Sato, T. Kawabata, S. Ikeno, HAADF-STEM Study of β'-type precipitates in an over-aged Al–Mg–Si–Ag alloy, Philos. Mag. 92 (2012) 1149–1158.
[23] L. Arnberg, B. Aurivillius, The crystal structure of $Al_5Cu_2Mg_{12-x}Si_7$, (h-AlCuMgSi), Acta Chem. Scand. A 34 (1980) 1–5.
[24] C. Wolverton, Crystal structure and stability of complex precipitate phases in Al-Cu-Mg-(Si) and Al-Zn-Mg alloys, Acta Mater. 49 (2001) 3129–3142.
[25] C. Ravi, C. Wolverton, First-principles study of crystal structure and stability of Al–Mg–Si–(Cu) precipitates, Acta Mater. 52 (2004) 4213–4227.
[26] T. Saito, C.D. Marioara, S.J. Andersen, W. Lefebvre, R. Holmestad, Aberration-corrected HAADF-STEM investigations of precipitate structures in Al-Mg-Si alloys with low Cu additions, Philos. Mag. 94 (2014) 520–531.
[27] D.J. Chakrabarti, D.E. Laughlin, Phase relations and precipitation in Al-Mg-Si alloys with Cu additions, Prog. Mater Sci. 49 (2004) 389–410.
[28] C. Cayron, L. Sagalowicz, O. Beffort, P.A. Buffat, Structural phase transition in Al-Cu-Mg-Si alloys by transmission electron microscopy study on an Al-4 wt.% Cu-1 wt.% Mg-Ag alloy reinforced by SiC particles, Philos. Mag. 79 (1999) 2833–2851.
[29] K. Matsuda, Y. Uetani, T. Sato, S. Ikeno, Metastable phases in an Al-Mg-Si alloy containing copper, Metall. Mater. Trans. A 32 (2001) 1293–1299.
[30] T. Saito, C.D. Marioara, J. Røyset, K. Marthinsen, R. Holmestad, The effects of quench rate and pre-deformation on precipitation hardening in Al–Mg–Si alloys with different Cu amounts, Mater. Sci. Eng. A 609 (2014) 72–79.
[31] T. Saito, S. Muraishi, C.D. Marioara, S.J. Andersen, J. Røyset, R. Holmestad, The effects of low Cu additions and predeformation on the precipitation in a 6060 Al-Mg-Si alloy, Metall. Mater. Trans. A 44 (2013) 4124–4135.
[32] S.J. Andersen, Quantification of the Mg_2Si β'' and β' phases in AlMgSi alloys by transmission electron microscopy, Metall. Mater. Trans. A 26 (1995) 1931–1937.
[33] J.K. Sunde, Ø. Paulsen, S. Wenner, R. Holmestad, Precipitate statistics in an Al-Mg-Si-Cu alloy from scanning precession electron diffraction data, J. Phys.: Conf. Ser 902 (2017) 012022.
[34] P. Moeck, S. Rouvimov, E.F. Rauch, M. Véron, H. Kirmse, I. Häusler, W. Neumann, D. Bultreys, Y. Maniette, S. Nicolopoulos, High spatial resolution semi-automatic crystallite orientation and phase mapping of nanocrystals in transmission electron microscopes, Cryst. Res Technol. 46 (2011) 589–606.
[35] J.S. Barnard, D.N. Johnstone, P.A. Midgley, High-resolution scanning precession electron diffraction: alignment and spatial resolution, Ultramicroscopy 174 (2017) 79–88.
[36] F. de la Peña, et al., HyperSpy - 1.3 (2017), http://dx.doi.org/10.5281/zenodo.583693.
[37] S. van der Walt, J.L. Schönberger, J. Nunez-Iglesias, F. Boulogne, J.D. Warner, N. Yager, E. Gouillart, T. Yu and the scikit-image contributors, scikit-image: Image processing in Python, PeerJ 2 (e453) (2014)http://dx.doi.org/10.7717/peerj.453.
[38] D.D. Lee, H.S. Seung, Learning the parts of objects by non-negative matrix factorization, Nature 401 (1999) 788–791.
[39] A.S. Eggeman, R. Krakow, P.A. Midgley, Scanning precession electron tomography for three-dimensional nanoscale orientation imaging and crystallographic analysis, Nat. Commun. 6 (2015) 7267.
[40] R. Vincent, P.A. Midgley, Double conical beam-rocking system for measurement of integrated electron-diffraction intensities, Ultramicroscopy 53 (1994) 271–282.
[41] P.D. Nellist, S.J. Pennycook, The principles and interpretation of annular dark-field Z-contrast imaging, Adv. Imag. Electron Phys 113 (2000) 148–203.
[42] T. Saito, F.J.H. Ehlers, W. Lefebvre, D. Hernandez-Maldonado, R. Bjørge, C.D. Marioara, S.J. Andersen, E.A. Mørtsell, R. Holmestad, Cu atoms suppress misfit dislocations at the β''/Al interface in Al-Mg-Si alloys, Scr. Mater. 110 (2016) 6–9.
[43] L. Ding, Z. Jia, J.F. Nie, Y. Weng, L. Cao, H. Chen, X. Wu, Q. Liu, The structural and compositional evolution of precipitates in Al-Mg-Si-Cu alloy, Acta Mater. 145 (2018) 437–450.
[44] K. Li, A. Béché, M. Song, G. Sha, X. Lu, K. Zhang, Y. Du, S.P. Ringer, D. Schryvers, Atomistic structure of Cu-containing β'' precipitates in an Al–Mg–Si–Cu alloy, Scr. Mater. 75 (2014) 86–89.
[45] C.D. Marioara, S.J. Andersen, J. Røyset, O. Reiso, S. Gulbrandsen-Dahl, T.E. Nicolaisen, I.E. Opheim, J.F. Helgaker, R. Holmestad, Improving thermal stability in Cu-containing Al-Mg-Si alloys by precipitate optimization, Metall. Mater. Trans. A 45 (2014) 2938–2949.
[46] Y. Du, Y.A. Chang, B. Huang, W. Gong, Z. Jin, H. Xu, Z. Yuan, Y. Liu, Y. He, F.Y. Xie, Diffusion coefficients of some solutes in fcc and liquid Al: critical evaluation and correlation, Mater. Sci. Eng. A 363 (2003) 140–151.
[47] K. Teichmann, C.D. Marioara, S.J. Andersen, K. Marthinsen, TEM Study of β' precipitate interaction mechanisms with dislocations and β' interfaces with the aluminium matrix in Al–Mg–Si alloys, Mater. Charact. 75 (2013) 1–7.
[48] A.-L. Dons, E.K. Jensen, Y. Langsrud, E. Trømborg, S. Brusethaug, The alstruc microstructure solidification model for industrial aluminum alloys, Metall. Mater. Trans. A 30 (1999) 2135–2146.
[49] S. Wenner, L. Jones, C.D. Marioara, R. Holmestad, Atomic-resolution chemical mapping of ordered precipitates in Al alloys using energy-dispersive X-ray spectroscopy, Micron 96 (2017) 103–111.

Paper III

Jonas Kristoffer Sunde, Duncan N. Johnstone, Sigurd Wenner,
Antonius T. J. van Helvoort, Paul A. Midgley, Randi Holmestad

Crystallographic relationships of T-/S-phase aggregates in an Al–Cu–Mg–Ag alloy

Acta Materialia **166** (2019) 587-596.
https://doi.org/10.1016/j.actamat.2018.12.036

Acta Materialia 166 (2019) 587–596

Contents lists available at ScienceDirect

Acta Materialia

journal homepage: www.elsevier.com/locate/actamat

Full length article

Crystallographic relationships of T-/S-phase aggregates in an Al–Cu–Mg–Ag alloy

Jonas K. Sunde [a, *], Duncan N. Johnstone [b], Sigurd Wenner [c], Antonius T.J. van Helvoort [a], Paul A. Midgley [b], Randi Holmestad [a]

[a] Department of Physics, Norwegian University of Science and Technology (NTNU), Høgskoleringen 5, N-7491, Trondheim, Norway
[b] Department of Materials Science and Metallurgy, University of Cambridge, 27 Charles Babbage Road, CB3 0FS, Cambridge, UK
[c] Materials and Nanotechnology, SINTEF Industry, Høgskoleringen 5, N-7491, Trondheim, Norway

ARTICLE INFO

Article history:
Received 21 September 2018
Received in revised form
14 December 2018
Accepted 19 December 2018
Available online 24 December 2018

Keywords:
Aluminium alloy
Orientation relationships
Dispersoid-precipitate aggregate
ACOM-TEM
Scanning precession electron diffraction

ABSTRACT

T-($Al_{20}Cu_2Mn_3$) phase dispersoids are important for limiting recovery and controlling grain growth in Al-Cu alloys. However, these dispersoids can also reduce precipitation hardening by acting as heterogeneous nucleation sites and may lead to increased susceptibility towards pitting corrosion when galvanically coupled with S-(Al_2CuMg) phase precipitates. The interplay between T- and S-phases is therefore important for understanding their effect on the mechanical and electrochemical properties of Al-Cu-Mg alloys. Here, the crystallographic relationships between the T-phase, S-phase, and surrounding Al matrix were investigated in an Al-1.31Cu-1.14Mg-0.13Ag-0.10Fe-0.28Mn (at.%) alloy by combining scanning precession electron diffraction with misorientation analysis in 3-dimensional axis-angle space and high-resolution transmission electron microscopy. Orientation relationships are identified between all three phases, revealing S-T orientation relationships for the first time. Differences in S-Al orientation relationships for precipitates formed at T-phase interfaces compared to their non-interfacial counterparts were also identified. These insights provide a comprehensive assessment of the crystallographic relationships in T-/S-phase aggregates, which may guide future alloy design.

1. Introduction

2xxx series Al alloys are Cu-containing age-hardenable alloys widely used in the aerospace industry due to their high strength-to-weight ratio, good formability, and high damage tolerance [1,2]. Alloys based on the Al-Cu-Mg system are particularly common owing to their high fracture toughness and fatigue resistance [3,4]. Al-Cu-Mg alloys obtain most of their strength from a distribution of atomic clusters, Guinier-Preston-Bagaryatsky (GPB) zones [5], and precipitates of different metastable phases that are formed throughout the Al matrix during heat treatment. Commercial alloys typically have an atomic ratio Cu:Mg > 1 which eventually leads to formation of equilibrium S-(Al_2CuMg) and/or θ-(Al_2Cu) precipitates preceded by their precursor phases [6–9]. Ag additions to this alloy system have been found to increase strength by modifying and enhancing the age hardening response [10–12]. This is achieved by promoting Ω-(Al_2Cu) phase formation over θ′(Al_2Cu) [13,14] leading to a denser distribution of finer precipitates. Mn additions reduce the detrimental effects on mechanical properties from Fe impurities by forming dispersoids during high temperature homogenisation. In Al-Cu-Mg alloys the main dispersoid phase is T ($Al_{20}Cu_2Mn_3$, Bbmm, $a = 23.98$ Å, $b = 12.54$ Å, $c = 7.66$ Å [15]) which effectively pins grain boundaries, limits recrystallisation, accumulates dislocations, and resists recovery after forming [16–18]. The T-phase dispersoid can increase the sensitivity to micro-crack initiation but can on the other hand prevent fast and continuous crack propagation [19]. The T-Al interface can act as a heterogeneous nucleation site for phases such as Ω, θ(θ′), and S(S′) [20–22] creating dispersoid aggregates and reducing normal intra-granular precipitation.

Although the contribution of Cu and Mg in precipitation of various phases results in a higher strength and mechanical performance, the phases formed generally lead to a significant drop in corrosion resistance [4]. Extensive research has been devoted to study different aspects of corrosion in these alloys, including localized corrosion, galvanic coupling between phases and stress-corrosion cracking [23–27]. Several studies point out the S- and

* Corresponding author.
E-mail address: jonas.k.sunde@ntnu.no (J.K. Sunde).

https://doi.org/10.1016/j.actamat.2018.12.036
1359-6454/

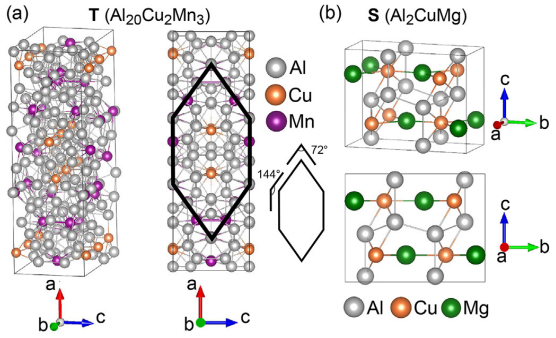

Fig. 1. Crystal structures of the (a) T- and (b) S-phase. A flattened hexagonal subunit in the T-phase is indicated and is relevant in twinning of this structure.

T-phase as most important particularly with regards to initiation of pitting corrosion, especially when the two phases are in contact forming a galvanic couple [28].

T-phase dispersoids tend to adopt rod-like morphologies with their long axes along $\langle 001\rangle_{Al}$ directions. In cross-section, the morphology is typically a lath or a shell-shaped structure [29]. Internal faulting, particularly twinning, is common, and successive twinning transforms the cross-section from a lath to a shell-shaped structure [30]. The crystal structure of the S-phase has been subject to much debate but there is now broad consensus around the Perlitz-Westgren structure (Al_2CuMg, Cmcm, $a = 4.00$ Å, $b = 9.23$ Å, $c = 7.14$ Å) [31,32]. The T- and S-phase crystal structures are shown in Fig. 1.

Crystallographic orientation relationships (ORs) between the T-phase, S-phase, and Al matrix, as well as the internal structure of the T-phase, have been the subject of numerous studies across a range of compositions and thermo-mechanical treatments. Reported ORs are summarised in Table 1 and Table 2. Three ORs have been observed between the T-phase and Al matrix [33], all with the $[010]_T$ axis aligned along $\langle 001\rangle_{Al}$ but with different coincident planes. When viewed along the $[010]_T$ axis, the twinning is seen as a $\sim 36°$ rotation about the axis with $\{101\}_T$ as the twin plane, which can yield structures exhibiting pseudo 10-fold symmetry [34].

Different crystallographic relationships between the S-phase and Al matrix have been reported, the most frequent of which is that discovered by Bagaryatsky [35] (OR(I) in Table 2) corresponding to type I S-phase. However, rotations of several degrees away from this S-Al OR are observed. This has led several authors [9,36–39] to distinguish a second OR (e.g. OR(II-IV) in Table 2) rotated by 3° to as much as 9° about the $[100]_S//[001]_{A1}$ axis away from OR(I), and is potentially associated with a second type of S-phase (type II). It has been suggested that the two ORs may be extrema of a continuous or near continuous distribution of rotation angles [37]. The rotation has been rationalized in terms of a competition between elastic strains due to lattice mismatch between coherent interfaces formed at each OR [38]. Some studies found that type II S-phase grows at the expense of type I, and that type II is the more stable phase [9,40]. Studies conducted by Styles et al. [40,41] concluded that there are no significant differences in crystal structure between the two types, but that type I has a deficiency of Cu which may explain observed variations in lattice parameters between the two types. S-phases adopting OR(I) tend to be lath-like with atomically sharp interfaces, whereas precipitates following the second OR tend to be rod-shaped with stepped interfaces [39]. The ratio of type I relative to type II S-phases is among others dependent on ageing times and temperature [40], as well as quenching rate from homogenisation and whether cold work is applied prior to ageing [9,42]. S-T ORs and S-Al ORs for S-phase precipitates nucleated on T-phase dispersoids have been less studied [20].

In this work, scanning precession electron diffraction (SPED) is applied in combination with misorientation analysis in axis-angle space and high-resolution imaging to understand the structure of dispersoid aggregates comprised of T-phase dispersoids and S-phase precipitates surrounded by the Al matrix. In addition, a comparison is made between S-Al misorientations for S-phase precipitates decorating T-phase dispersoids and those located away from T-phase interfaces. Knowledge of these crystallographic relationships will enhance understanding of the effect of T-/S-phase aggregates on mechanical and electrochemical properties in Al-Cu-Mg alloys.

Table 1
Reported T-Al orientation relationships [33]. **n** denotes a unit vector that runs parallel to the axis of rotation.

OR	Parallelism	Axis-angle
(I)	$\{200\}_T$ // $\{200\}_{Al}$, $\langle 010\rangle_T$ // $\langle 001\rangle_{Al}$ (// **n**)	**n**, 0°
(II)	$\{200\}_T$ // $\{40\bar{3}\}_{Al}$, $\langle 010\rangle_T$ // $\langle 001\rangle_{Al}$	**n**, 36.87°
(III)	$\{200\}_T$ // $\{301\}_{Al}$, $\langle 010\rangle_T$ // $\langle 001\rangle_{Al}$	**n**, 18.43°

Table 2
Reported S-Al orientation relationships I [35], II [36], III [37,38], and IV [39].

OR	Parallelism	Axis-angle
(I)	$\{001\}_S$ // $\{012\}_{Al}$, $\langle 100\rangle_S$ // $\langle 001\rangle_{Al}$ (// **n**)	**n**, 26.57°
(II)	$\{001\}_S$ // $\{0\bar{5}2\}_{Al}$, $\langle 100\rangle_S$ // $\langle 001\rangle_{Al}$	**n**, 21.80°
(III)	$\{0\bar{2}1\}_S$ // $\{014\}_{Al}$, $\langle 100\rangle_S$ // $\langle 001\rangle_{Al}$	**n**, 18.84°
(IV)	$\{043\}_S$ // $\{021\}_{Al}$, $\langle 100\rangle_S$ // $\langle 001\rangle_{Al}$	**n**, 17.55°

2. Material & methods

2.1. Material

The nominal composition of the Al alloy studied in this work is shown in Table 3. The as-received material was an extruded rod pre-heated to 400 °C and extruded at 390 °C. From the extruded rod a cylinder (Ø = 20 mm, height = 10 mm) was cut and solution heat treated at 440 °C for 1 h before water-quenched to room temperature. The material was then directly set to artificial ageing at 170 °C conducted in an oil-bath, avoiding any natural ageing effects. The material was studied in an over-aged condition, which was obtained after 4 days of ageing.

Electron transparent thin film specimens were prepared from 3 mm diameter discs of material ground to a thickness of ~100 μm before further thinning by electrolytic polishing. Electro-polishing was performed using a Struers Tenupol-5 operated at a voltage of 20 V (current 0.2 A). The electrolytic solution comprised a 2:1 mixture of methanol:nitric acid and was held at a temperature in the range −30 °C to −25 °C. Prior to SPED and high resolution microscopy, the specimens were cleaned using a Fischione 1020 Plasma Cleaner to reduce the risk of carbon contamination build-up during data acquisition.

Table 3
Nominal composition of the Al alloy studied.

Element	Al	Cu	Mg	Ag	Fe	Mn
at.%	bal.	1.31	1.14	0.13	0.10	0.28
wt.%	bal.	3.00	1.00	0.50	0.20	0.55

2.2. Electron microscopy

High-resolution transmission electron microscopy (HRTEM) and SPED were performed using a JEOL 2100F (S)TEM operated at 200 kV and fitted with a NanoMEGAS ASTAR system [43,44] to enable the simultaneous scan and acquisition of precession electron diffraction patterns at each probe position. SPED was performed with the microscope operated in nanobeam diffraction mode. The probe convergence semi-angle was measured as 1.0 mrad. The precession angle employed was $0.5 - 1.0^{\circ}$ and the precession frequency was set to 100 Hz. The scan step size was in the range 0.76 – 2.28 nm and the exposure time per pixel was 20 – 40 ms. Diffraction patterns were recorded using a Stingray camera photographing the microscope's fluorescent screen. The double-rocking probe required for PED was aligned following the method detailed by Barnard et al. [45]. High-angle annular dark-field STEM (HAADF-STEM) was performed using a double corrected JEOL ARM 200F microscope operated at 200 kV using a detector collection angle of 42–178 mrad.

2.3. Phase & orientation mapping

Phase and orientation maps were formed using the pattern matching approach of Rauch et al. [46] in which the 2-dimensional PED pattern recorded at each probe position in a 2-dimensional area scan is matched against a library of simulated diffraction patterns, for all asymmetric orientations of the expected phases. Prior to this pattern matching, a background subtraction was applied to each PED pattern using a routine implemented in the pyXem Python library [47–49], and the template matching parameters in the ASTAR software were tuned to obtain good agreement between the matching results and HRTEM images of the same particles, as detailed in Supplementary Information (SI).

Orientation mapping results were analysed using the Matlab toolbox MTEX [50], following procedures described by Krakow et al. [51]. Crystallographic domains in the dispersoid aggregates were typically defined using regions with a common phase and orientation within a threshold of 10°, which was found to give good agreement with the same phases observed in HRTEM images. Orientation relationships between these crystallographic domains were investigated by calculating the misorientation between neighbouring pixels across all domain boundaries. This misorientation data was then visualised, for each type of phase boundary by plotting the disorientation between adjacent domains as a vector in the appropriate symmetry reduced region (*fundamental zone*) of a 3-dimensional misorientation space [51]. The vector space chosen was the *axis-angle space* in which a disorientation is represented by a vector $\boldsymbol{\rho}$:

$$\boldsymbol{\rho} = \omega \boldsymbol{n} \tag{1}$$

where $\boldsymbol{n}$ is a unit vector parallel to the axis of rotation and ω is the angle of rotation [°]. This representation is preferred over other mappings because the rotation angle is simply read from the plot and it is sufficient for visualisation.

3. Results

3.1. TEM observations

Conventional TEM imaging was performed to obtain an overview of the phases present, which were identified based on characteristic morphology and lattice structure in high-resolution images, as shown in Fig. 2, Fig. 3, and Fig. 4(a,d). A high number density of Ω-phase precipitates were observed throughout the Al matrix, as well as elongated S-phase precipitates and T-phase dispersoids. The Ω-phase exists as thin, hexagonal shaped plates formed on $\{111\}_{Al}$. S-phase precipitates were more inhomogeneously distributed, growing as rods or laths on $\{021\}_{Al}$ planes and extending along $\langle 100\rangle_{Al}$ directions. S-phase precipitates were frequently observed clustered together, having formed heterogeneously on T-phase dispersoids or in wall-structures of adjoining S-phase precipitates on underlying dislocation networks, in

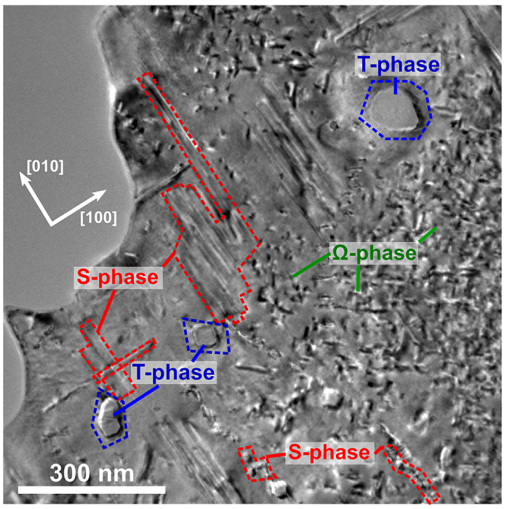

Fig. 2. TEM image of the over-aged Al-Cu-Mg-Ag alloy microstructure as viewed near the $[001]_{Al}$ zone axis. The main phases observed are indicated.

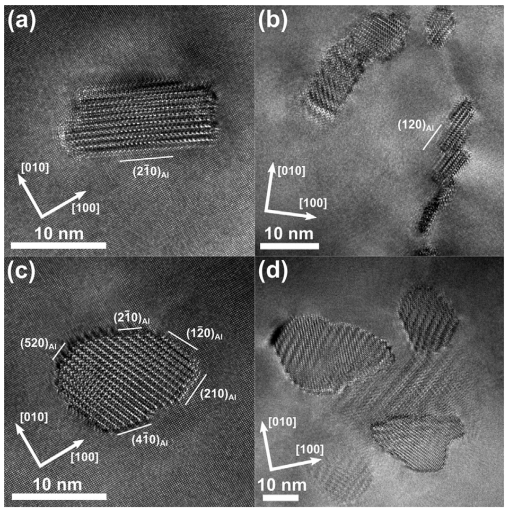

Fig. 3. Different variations of S-phases in the alloy microstructure as observed near the $[001]_{Al}$ zone axis. (a) A single lath-shaped S-phase. (b) A wall-structure of adjoining S-phases nucleated on a dislocation network. (c) A single rod-shaped S-phase. (d) A cluster of coarsened S-phases.

agreement with previous reports [20,52] (see Fig. 3(b,d) and Fig. 4(a,d)). Both lath- and rod-shaped S-phase cross-sections were observed, laths being more frequent. A smaller number of individual S-phase precipitates, likely formed by homogeneous bulk nucleation, was also observed (Fig. 3(a,c)). Moiré fringes can be observed in some images, e.g. Fig. 3(b,d), which are attributed primarily to overlap between the S-phase cross-sections and surrounding Al. Whilst this suggests a more diverse range of precipitate morphologies than is evident from these projection images this does not affect assessment of orientation relationships between phases.

Dispersoids were identified as T-phase and all of these were decorated by S-phase precipitates at prior T-Al interfaces (see Fig. S1-24 in SI). Typically, 1-10 S-phases were observed at each dispersoid. No Ω-phases were observed at the T-phase interfaces. Morphologically, both shell-shaped (Fig. 4(a)) and lath-shaped (Fig. 4(d)) T-phase dispersoids were observed, and all exhibited some degree of rotation-twinned substructure. T-phase cross-section diameters or diagonals were measured in the range 45–75 nm, and cross-section aspect ratios varied between 1.1 and 1.9. S-phase precipitates were observed to grow both parallel and perpendicular to the T-phase elongation axis. S-phase precipitate lengths were measured as (136±19) nm and (146±24) nm for S-phases at T-phase interfaces (i.e. S-phases with elongation perpendicular to the T-phase axis) and non-interfacial S-phases, respectively. Cross-section areas for the two categories were (93±8) nm^2 and (69±8) nm^2, respectively. This indicates a slight coarsening of S-phase precipitates decorating T-phase dispersoids.

3.2. Dispersoid aggregates

Dispersoid aggregates comprise the T-phase dispersoid, interfacial S-phases, and surrounding Al matrix. The structure of 10 such aggregates was investigated in detail using correlated HRTEM and SPED data, as shown in Fig. S1-20. Two examples are presented in Fig. 4, showing a shell- and lath-shaped T-phase exhibiting pronounced and limited rotation-twinning, respectively. Comparing HRTEM images and SPED mapping results from the same dispersoid aggregates demonstrates that the primary crystallographic features were accurately captured in the SPED data analysis. T-phase substructures such as anti-phase boundaries (APBs), micro twins, and twin boundaries (TBs) confined to a limited number of hexagon subunits in width (multilayers) [34,53] could not be resolved by SPED, but are often associated with pixels of lower reliability and/or index value in pattern matching (Fig. S1-20). In total, 43 S-phases at the interface of T-phases were mapped by SPED. The disorientation data for each type of phase boundary shown in the following is the combined data extracted from all SPED scans recorded in the present work.

3.2.1. T-phase orientation relationships

Crystallographic relationships between rotated domains of the T-phase (T-T) and across the T-Al interface were assessed by plotting disorientations within the corresponding fundamental zones of axis-angle space as shown in Fig. 5, with previously reported T-Al ORs (Table 1) highlighted. T-T domain boundary disorientations (Fig. 5(a)) are clustered near a ~36° rotation about $[010]_T$

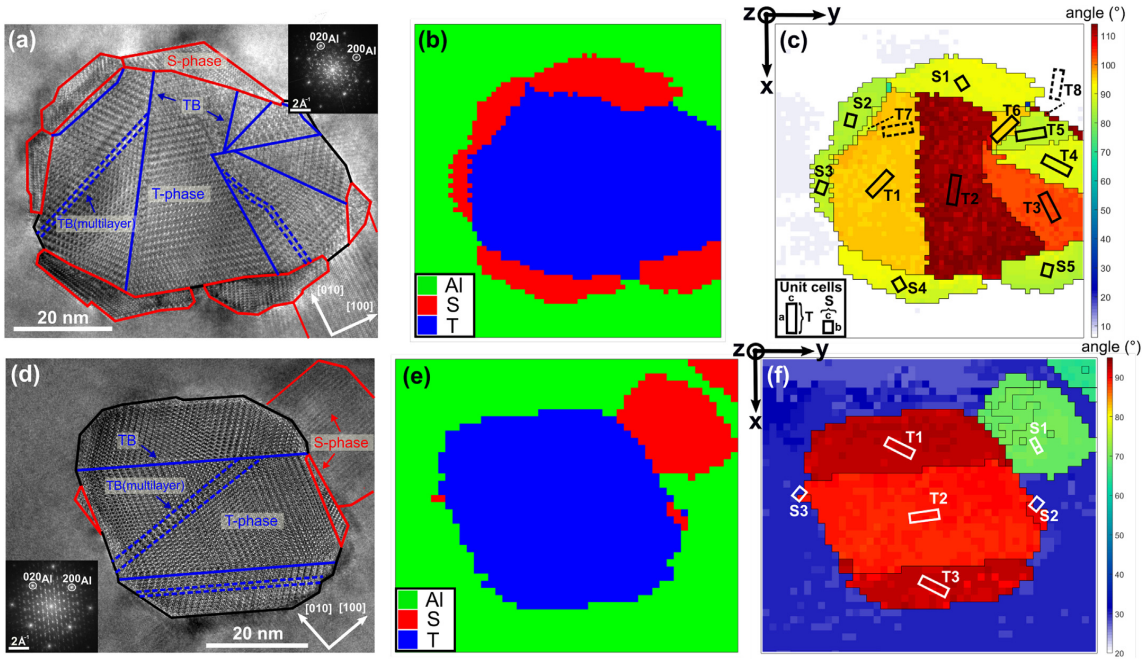

Fig. 4. Structure of a (a–c) shell-shaped and (d–f) lath-shaped T-/S-phase aggregate. (a,d) HRTEM images of the aggregates with S-phases and T-phase TBs/TB multilayers indicated. Inserts show the image fast fourier transforms. (b,e) Phase maps obtained via template matching of SPED data. (c,f) Orientation maps showing the disorientation angle ω taken about an axis $\boldsymbol{\rho}$ (Eq. (1)) at each probe position relative to the specimen reference frame (x,y,z). The average orientation of each labelled domain/phase is indicated by drawn unit cells of the T- and S-phase (not to scale).

corresponding to twinning [34]. Two smaller clusters are also observed at 0° and ~72°, the latter corresponding to twice the twinning angle. Both are associated with disorientations across domains in the rotation-twin centres, i.e. the regions from which the twin domains seemingly emanate. In this region, each domain shares a small boundary to other domains that can be rotated relative to it by 0°, ~36°, or ~72°. Data points away from these disorientation clusters were likely misindexed pixels as a result of local disorder, e.g. the unresolved APBs, micro twins or TB multilayers. The spread in T-T TB disorientations (FWHM of angle distribution) of ~1.2° is taken as an indication of angular resolution, which is consistent with estimated angular resolution for spot pattern based indexation [54].

T-Al disorientations (Fig. 5(b)) form 3 main clusters near previously reported T-Al ORs. The 2 clusters situated at negative angles along the $[010]_T//[001]_{A1}$ axis correspond, by symmetry, with those at equivalent positive values, i.e. near ORs (II) and (III). There is a spread of rotations $\sim 4^{\circ}$ away from the exact angles described by the ORs, primarily about the $[010]_T//[001]_{A1}$ axis since most data points are distributed parallel to this axis. This implies that there exists a deviation of $\pm 4^{\circ}$ from exact OR parallelisms across the T-Al interface. The cluster spread is less pronounced perpendicular to the $[010]_T//[001]_{A1}$ axis, implying that the $[010]_T$ elongation axis remains reasonably parallel to the $[001]_{A1}$ direction. A 5° radius sphere of disorientations about OR(I), OR(II), and OR(III) accounts for 7%, 30%, and 50% of all disorientation data points, respectively.

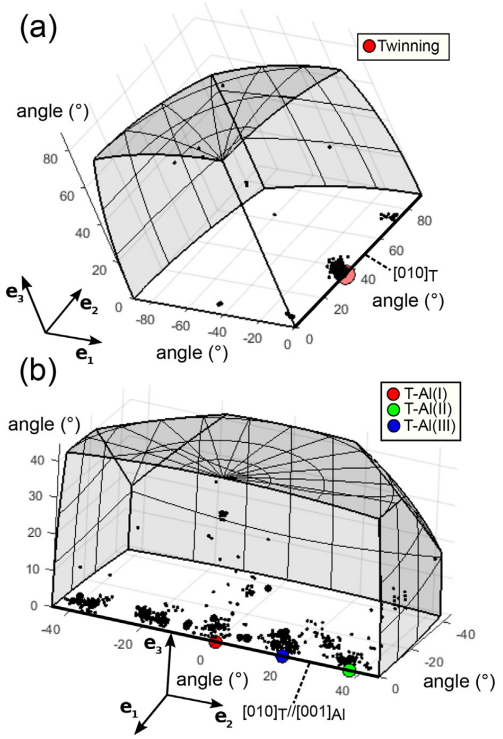

Fig. 5. T-phase disorientations and previously reported orientation relationships plotted in corresponding fundamental zones of axis-angle space. (a) T-T disorientations across 34 boundaries. (b) T-Al disorientations across 51 boundaries.

The substructure of T-phase dispersoids are observed in HAADF-STEM, as shown in Fig. 6. APBs (Fig. 6(c)) form where there exists a band one single hexagon subunit in width rotated (by the twinning angle) with respect to the surrounding twin domain. A micro twin forms when a second band rotated with respect to the first appears. A TB multilayer appears as a narrow band, usually 2–5 hexagon subunits in width. Another more complex feature is transition regions (Fig. 6(b)), which comprise different geometrical structures formed by various hexagon subunit tessellations. The T-phase substructures that extend to the T-Al interface are likely the main explanation for misindexed data points in Fig. 5(b) that are spread at significant distances away from the main observed disorientation clusters. The bright regions in Fig. 6 are primarily due to incorporation of Ag in the S- and T-phase. Additional HAADF-STEM images are presented in Fig. S23 and Fig. S24.

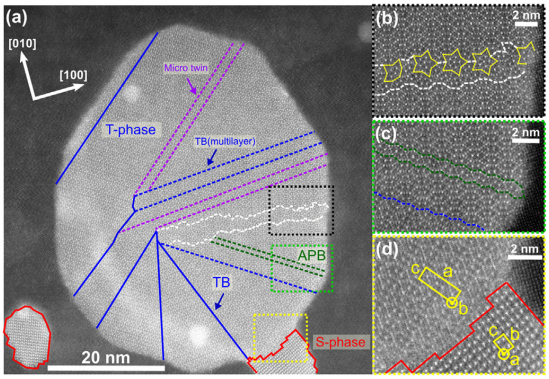

Fig. 6. (a) HAADF-STEM image of a T-phase dispersoid with a S-phase precipitate at the prior T-Al interface as viewed near the $[001]_{A1}$ zone axis. TBs/TB multilayers, micro twins, APB, and a transition region are observed. (b) Transition region comprising different tessellations of the hexagonal subunit. (c) An APB and a TB multilayer. (d) S-T phase boundary with unit cells indicated.

3.2.2. S-Al orientation relationships

S-Al disorientations for S-phase precipitates situated at T-phase interfaces and non-interfacial counterparts are shown in Fig. 7, with previously reported S-Al ORs (Table 2) highlighted. In both cases, the disorientations cluster together near the $[100]_S//[001]_{A1}$ axis. The cluster of disorientations for S-phases situated away from T-phase interfaces (Fig. 7(b)) is more clearly placed at the $[100]_S//[001]_{A1}$ axis, whereas the disorientations for interfacial S-phases (Fig. 7(a)) show a dense population slightly off axis. This implies that there exists more deviation from exact $[100]_S//[001]_{A1}$ parallelism when S-phase precipitates decorate the T-Al interfaces. S-phase precipitates placed away from T-Al interfaces are more strictly confined to in-plane ($(001)_{A1}$) rotations about $[100]_S//[001]_{A1}$ configuration.

S-Al interfaces for S-phase precipitates not decorating T-phases show a disorientation angle distribution shifted towards OR(I), with a dense population between OR(I) and OR(II) (~5° spread). For S-phases at T-phase interfaces the disorientations are more evenly spread across a ~9° range of rotations. A 2° radius sphere of disorientations around OR(I-IV) accounts for 48%, 35%, 9%, and 4% of all disorientation data points in the case of S-phases at T-phase interfaces, respectively. Corresponding

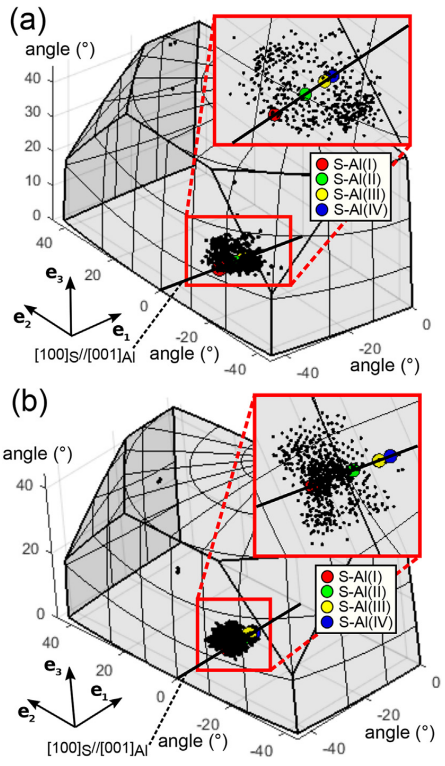

Fig. 7. S-Al disorientations and previously reported orientation relationships plotted in fundamental zones of axis-angle space. (a) S-Al disorientations across 43 boundaries for S-phases situated at T-phase interfaces. (b) S-Al disorientations across 57 boundaries for S-phases placed away from T-phase interfaces.

numbers are 78%, 9%, 3%, and 1% for S-phases located away from T-phase interfaces.

3.2.3. S-T orientation relationships

S-T phase boundary disorientations are shown in Fig. 8. The majority of disorientations fall close to the $[100]_S//[010]_T$ axis, and is consistent with HRTEM (Fig. 4(a,d)) and HAADF-STEM (Fig. 6(d)) images, showing that the **a**- and **b**-axis of the S- and T-phase respectively, runs near parallel to $[001]_{Al}$. Several clear disorientation clusters can be seen, indicating the formation of several definite S-T crystallographic ORs. By sampling potential low index ORs placed along the $[100]_S//[010]_T$ axis, corresponding to a range of 90–120° in disorientation angles, the most probable crystallographic ORs were determined. The ORs were determined as those candidate ORs which accounted for the largest percentage of disorientations, falling within a $n[°]$ radius sphere of disorientations centred on the exact OR value, n being an integer. The analysis yielded 3 ORs highlighted in Fig. 8. These ORs encompassed 26%, 27%, and 9% of all data points, using a 3° radius sphere for ORs (I-III), respectively. The corresponding parallelisms and axis-angle representations are shown in Table 4.

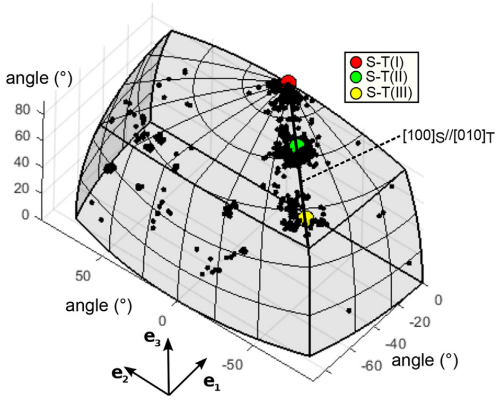

Fig. 8. S-T disorientations across 43 boundaries and proposed orientation relationships plotted in the corresponding fundamental zone of axis-angle space.

Table 4
S-T orientation relationships inferred from measured disorientations.

OR	Parallelism	Axis-angle
(I)	$\{001\}_S$ // $\{001\}_T$, $\langle 100\rangle_S$ // $\langle 010\rangle_T$ (// **n**)	**n**, 90°
(II)	$\{011\}_S$ // $\{001\}_T$, $\langle 100\rangle_S$ // $\langle 010\rangle_T$	**n**, 96°
(III)	$\{013\}_S$ // $\{100\}_T$, $\langle 100\rangle_S$ // $\langle 010\rangle_T$	**n**, 112°

3.3. Orientation spread

Disorientations between phases in the T-/S-phase aggregates generally showed significant spread about ORs described by plane parallelisms. This was investigated by direct inspection of SPED raw data and mapping results for each dispersoid aggregate, e.g. as shown in Fig. 9. The misorientation angle across S-T boundaries (Fig. 9(a)) varied over the range 86–113°. The range was not continuously populated, but rather showed clustering about the angles corresponding with S-T ORs(I-III) (Table 4), consistent with the axis-angle representation of the combined S-T disorientations in Fig. 8. Spatially, the misorientation angle changed abruptly where the S-phase crossed T-phase TBs (indicated by arrows in Fig. 9(a)). The misorientation angle across S-Al boundaries spanned the range 18–27°, again consistent with the combined axis-angle representation of S-Al disorientations for interfacial S-phase precipitates in Fig. 7(a). The population of angles showed a continuous, or near continuous distribution across this range. Particularly for S-phase precipitates crossing T-phase TBs, the full range of rotations was observed.

Taking S1 in Fig. 9(a) as an example, at the S1-T1 boundary the misorientation angles indicate that S-T OR(III) is followed. Moving from left to right crossing the T1-T2 TB, S1 makes a sharp adjustment at the S1-T2 interface to S-T OR(II) in order to accommodate the large changes in interface structure necessary to adjust to the rotation-twinned T2 domain. Crossing the T2-T6 TB, S-T OR(III) is re-established as the T-phase has rotated in the opposite direction back to T1 orientation (see Fig. 4(c)). The transition involves ~16° rotations of the S1-T interface. Adjustments are also observed at the phase boundary between S1 and the surrounding Al matrix. The S1-Al boundary exhibits a 18–27° range of misorientation angles, gradually increasing from left to right. Comparing with reported

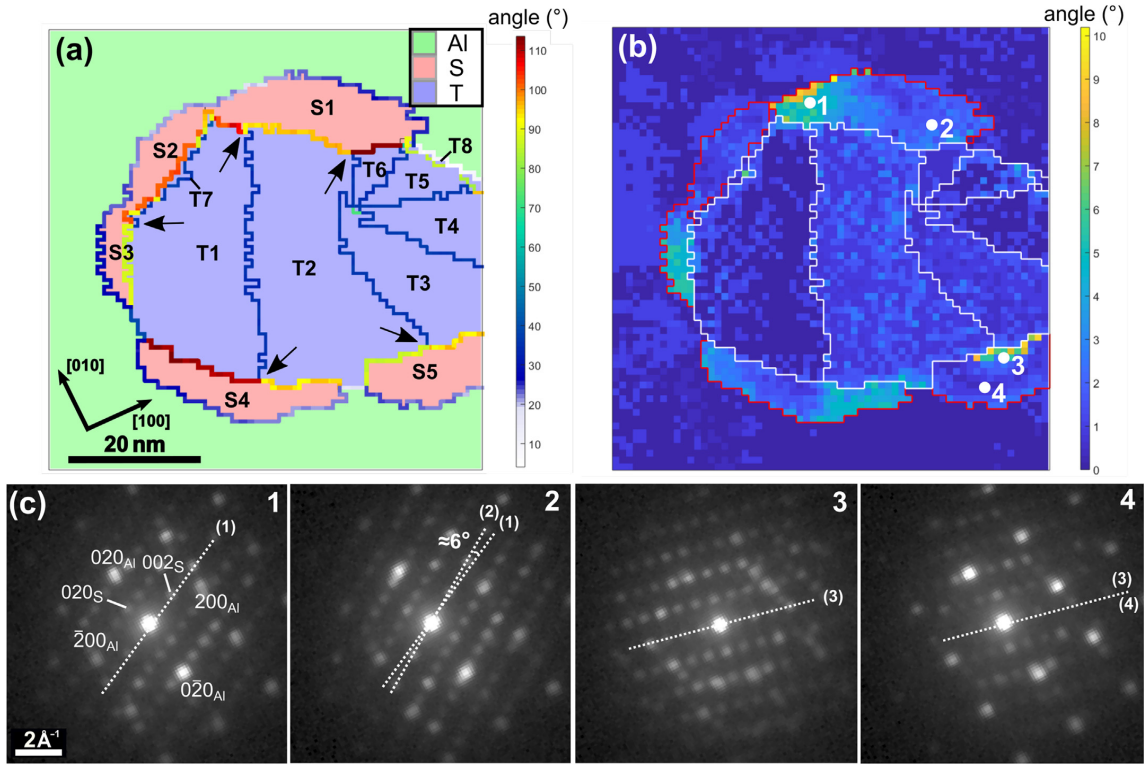

Fig. 9. (a) Phase map of a T-/S-phase aggregate with phase/domain boundaries coloured according to the misorientation angle between neighbouring pixels. Arrows highlight abrupt changes in misorientation angle across S-T boundaries. This is the same dispersoid aggragate as shown in Fig. 4(a). (b) Misorientation with respect to the mean for each phase/domain, respectively. T-phase domains are highlighted by white lines, and red lines mark S-phase cross-sections. (c) The PED patterns from the numbered pixels 1–4 in (b). Dashed lines (1–4) from the associated PED pattern 1–4 is drawn to compare orientations. (For interpretation of the references to colour in this figure legend, the reader is referred to the Web version of this article.)

plane parallelisms this nearly corresponds to a continuous or near continuous rotation from S-Al OR(I) to OR(IV).

The misorientation with respect to the mean of each crystallographically distinct domain is shown in Fig. 9(b) and reveals significant variation inside individual S-phase precipitates. The largest deviations are observed where the S-phase crosses T-phase TBs. The deviation from the mean reach ~9° for the interfacial S-phases, compared with variations below ~3° within T-phase domains and the surrounding Al matrix.

The PED patterns presented in Fig. 9(c) are from marked positions in Fig. 9(b) and verify the discussed orientation variation of the T-/S-phase aggregates. The patterns show a significant in-plane ($(001)_{A1}$) rotation about the $[100]_S//[001]_{A1}$ axis within S1 (pattern 1–2), and an out-of-plane tilt of the S-phase structure away from this axis within S5 (pattern 3–4), which is apparent from the asymmetric intensity distribution and is consistent with the observation of phase boundary misorientations tilted away from simple parallelisms in addition to significant rotations about the parallel direction. As observed in axis-angle space, the largest tilts (spread of data points perpendicular to main axes) occur for S-phase precipitates in dispersoid aggregates (Fig. 7(a)), an example of which is shown here.

4. Discussion

The combined TEM and SPED study presented here provides new insights to the inter-phase relations of T-/S-phase aggregates. In the following, these findings are interpreted in light of previous reports on the phases studied separately.

The T-phase dispersoid forms during the homogenisation process at temperatures above 400 °C [55]. Depending on the time and temperature at this stage the T-phase undergoes different degrees of rotation-twinning, which consequently affect the morphology. Long times and higher temperatures favour shell-shaped structures exhibiting pronounced twinning. A pseudo 10-fold symmetry centre can develop from successive twinning of T-twin domains. This symmetry centre is built from five differently oriented T-twin domains, each with a mirrored version, and which has three underlying T-Al ORs (Table 1). A recent study [30] has shown that the reported ORs can continually change as the T-phase undergoes rotation-twinning, requiring as much as 9° rotation of T-twin domains about the $[010]_T//[001]_{Al}$ axis, which likely results from the increase in interface energy caused by the twinning. The lattice mismatch of the T-phase hexagon subunit with $(200)_{A1}$ and $(002)_{A1}$ is largest for T-Al OR(III) (6.7% and 8.6%, respectively), which is only

found in T-phases with multiple T-twin domains [29,30,33]. Large rotations at the T-Al interface were also observed in the misorientation analysis conducted here, which measured up to ~8° rotations about previously reported ORs (I-III), seen from Fig. 5(b). OR(III) was found to be the most frequent, which is reasonable as the majority of T-phase dispersoids analysed exhibited pronounced rotation-twinning (see Fig. S1-20).

Similarly, the misorientation analysis of non-interfacial S-phase precipitates showed several degrees variation from reported OR parallelisms. This was found to be approximately confined to a ~5° range of rotations (Fig. 7(b)), a smaller number of data points reaching larger rotations. Previous reports show similar results, with upper bounds reaching $6-9^{\circ}$ [37–39] rotation away from OR(I) reported by Bagaryatsky [35]. This attests to the preference for heterogeneous nucleation.

It has hence been shown that both the S- and T-phase individually show in-plane ($(001)_{A1}$) rotations of several degrees from reported ORs with the Al matrix. The upper bounds of the range of rotation angles exhibited by S-phase precipitates situated away from T-phase interfaces corresponds well with the noted rotation that occur at the T-Al interface. The similarity may indicate why the T-Al interface is energetically favourable for S-phase nucleation and subsequent growth, and it reasons the finding of crystallographic ORs between the two phases. The correspondence of angles implies that the S-phase has the capability of accommodating the full rotation imposed by the maximum rotation at the T-Al interface. In the present study, S-phase precipitates were observed on all studied T-phase dispersoids, which suggests a good structural match between the two phases. These S-phases were seen to exhibit up to ~9° rotation about an axis near $[100]_S//[001]_{Al}$ configuration (Fig. 7(a)), in close agreement with the magnitude of the range of rotations (~8°) observed at the T-Al interface (Fig. 5(b)). As previously mentioned, the population of orientation angles exhibited by S-phase precipitates decorating T-phase interfaces was more spread towards larger angles than for the non-interfacial S-phases. This is to be expected as the S-phase has to accommodate the large rotations occurring at the T-Al interface.

The majority of S-phase precipitates in dispersoid aggregates seems to have grown preferentially along the T-Al interface. This is indicated by the observation that many S-phase precipitates in projection form caps at the prior T-Al interface, seen from Fig. 4, Fig. S1-20 and Fig. S23-24. This hence maximises the S-T interface area. Interfacial S-phase cross-sections typically have a narrow extension normal to the S-T interface. This implies that the S-T interface is energetically preferable as compared to S-Al interfaces. The interfacial S-phases have to adjust to local changes in both the T-phase structure and the surrounding Al matrix. The interface of the T-phase to which the S-phase has to conform is a complex rotation-twinned structure, often complicated further by regions of geometrical defects (see Fig. 6 and Fig. S23-24). If the S-T interface incorporates a TB, significant adjustments of the S-phase structure must have resulted to maintain a definite crystallographic OR to each of the T-twin domains and the Al matrix, simultaneously. Furthermore, because the S-phase cross-section usually is narrow normal to the S-T interface, the structural adjustment must be a rather sharp transition in orientation in close proximity of the TB at the S-T interface. Misorientation angles across phase boundaries show that this is indeed the case, with the S-T interface shifting to a different OR across the TB (Fig. 9(a)). These changes in configuration involve rotations of several degrees of the S- and T-phase structures. The rotation is mainly about the $[100]_S//[010]_T$ axis, but tilts away from this configuration also occur (see Fig. 8).

The T-phase dispersoid often shows less orientation variation compared to the S-phase precipitates near the S-T phase boundaries, as the misorientation-to-mean-plot shows (Fig. 9(b)). This is because the phases are formed at different stages in material heat treatment. The rotations observed at T-Al interfaces must already be in place after quenching from homogenisation, unless the S-phase nucleation and growth can cause the T-phase dispersoid to bend. Due to the comparatively small size of interfacial S-phases relative to the T-phase dispersoid, this is not thought to occur. The S-phase nucleates and grows under artificial ageing (170 °C), which is too low in temperature for any significant changes in the T-phase structure to occur [55,56]. The large local rotation of the S-phase structure near the TB is likely associated with a significant shear strain.

Some of the observed S-phase cross-sections at T-phase interfaces were likely formed by the coalescence of two initially separate S-phases. An example of this case was observed near a T-phase TB (see Fig. S13). The final morphology of S-phase precipitates in dispersoid aggregates can be seen as a balance between S-Al, S-T, and potentially S-S interface energies, reduction of lattice parameter misfits, and resulting shear strain.

The comparison between S-phase precipitates in dispersoid aggregates and S-phase precipitates formed away from T-phase interfaces provides further insight to the phase boundary energetics and the different inter-phase relations. Non-interfacial S-phases do not have to maintain a simultaneous OR with the T-phase in addition to the surrounding Al matrix. There is hence less need for large local adjustments in interface configurations, and the structure rotation that potentially arise from a variation in S- and/or (locally) Al lattice parameters [9,37,38] stays more confined about the $[100]_S//[001]_{A1}$ axis, as observed from Fig. 7(b). Furthermore, the range of orientation angles exhibited is smaller for non-interfacial S-phases (~5°). Although S-phases at T-phase interfaces exhibit a broader range of disorientation angles with respect to the surrounding Al matrix (~9°), the range is still approximately confined to the crystallographic limits proposed by Winkelman et al. [37] studying S-phases formed away from T-phase interfaces (Fig. 7(a)).

It is noteworthy that, the Ω-phase, which was the most abundant phase in the studied alloy microstructure, exhibits a high resistance to coarsening [57] and remains small and uniformly dispersed. These precipitates are therefore likely the most significant contributors to strengthening in this over-aged condition. No Ω-phase precipitates were observed at T-Al interfaces, which may be explained by S(S′) nucleating more easily and depleting the matrix of the solute supersaturation (mainly Cu) required to support the nucleation and growth of Ω [22].

5. Conclusions

SPED based orientation mapping combined with misorientation analysis in 3-dimensional axis-angle space and correlated HRTEM has been applied to study T-/S-phase aggregates in an Al-Cu-Mg-Ag alloy. The analysis revealed that:

- T-phase dispersoids show a rotation-twinned substructure characterised by $\sim 36^{\circ}$ rotation about $[010]_T$ with $\{101\}_T$ as twin boundary planes. Dispersoids with a low number of twin domains (<3) tend to be lath-shaped, and T-phases showing more pronounced twinning have up to 10 domains, and exhibit shell-shaped cross-sections.
- T-Al interfaces follow the previously reported T-Al ORs(I-III), but show significant rotations ($\pm 4^{\circ}$) about the $[010]_T//[001]_{A1}$ axis relative to exact OR parallelisms.
- S-Al interfaces for S-phases formed away from dispersoids show a disorientation angle distribution clustered about S-Al OR(I), mainly confined within a continuous (or near continuous) spread of $\sim 5^{\circ}$ rotation towards OR(II). These S-phase

precipitates showed a relatively strong confinement to rotations about the $[100]_S//[001]_{A1}$ axis.

- S-Al interfaces for S-phase precipitates in dispersoid aggregates exhibit a continuous (or near continuous) range of disorientation angles between 18 and 27° about the $[100]_S//[001]_{A1}$ axis. These rotations are roughly confined within the crystallographic limits between S-Al OR(I) and OR(IV) ($\sim 9^{\circ}$ rotation). In addition, these S-phases showed more out-of-plane tilts away from $[100]_S//[001]_{A1}$ configuration compared to the non-interfacial counterparts.
- Our work has found the following 3 ORs between S-phase precipitates and T-phase dispersoids:
  (I) $\{001\}_S$ // $\{001\}_T$, $\langle 100\rangle_S$ // $\langle 010\rangle_T$
  (II) $\{011\}_S$ // $\{001\}_T$, $\langle 100\rangle_S$ // $\langle 010\rangle_T$
  (III) $\{013\}_S$ // $\{100\}_T$, $\langle 100\rangle_S$ // $\langle 010\rangle_T$
- Axes-angle representation of S-Al, S-T and T-Al disorientations show several degrees deviation from reported/obtained crystallographic ORs. This is seen as a necessary consequence of changes in interface orientation and structure in maintaining simultaneous crystallographic ORs between S, T and Al.

We have demonstrated a methodology of correlating imaging and scanning diffraction techniques to allow precise analysis of orientation relationships and disorientations at high spatial resolution. The approach has potential for broad applications within multi-phase materials such as metals, semiconductors and minerals, where phase coherency is decisive for macroscopic properties.

Acknowledgements

JKS and RH acknowledge support from the AMPERE project (NFR247783), a Knowledge-building Project for Industry, co-financed by The Research Council of Norway, and the industrial partners Hydro, Gränges, Neuman Aluminium Raufoss (Raufoss Technology) and Nexans. RH and SW acknowledge funding from the Research Council of Norway NFR221714. PAM acknowledges funding from the ERC 291522-3DIMAGE, and the EPSRC Grant no. EP/R008779/1. DNJ acknowledges the EPSRC NanoDTC Cambridge EP/L015978/1 and the University of Cambridge for funding. The (S)TEM work was carried out on the NORTEM infrastructure (NFR197405) at the TEM Gemini Centre, Trondheim, Norway.

Appendix A. Supplementary data

Supplementary data to this article can be found online at https://doi.org/10.1016/j.actamat.2018.12.036.

References

[1] E.A. Starke Jr., J.T. Staley, Application of modern aluminum alloys to aircraft, Prog. Aero. Sci. 32 (1996) 131–172.
[2] G.E. Totten, D.S. MacKenzie, Handbook of Aluminum, vols. I and II, Marcel Dekker, New York, 2003.
[3] J.C. Williams, E.A. Starke Jr., Progress in structural materials for aerospace systems, Acta Mater. 51 (2003) 5775–5799.
[4] T. Dursun, C. Soutis, Recent developments in advanced aircraft aluminium alloys, Mater. Des. 56 (2014) 862–871.
[5] L. Kovarik, S.A. Court, H.L. Fraser, M.J. Mills, GPB zones and composite GPB/GPBII zones in Al-Cu-Mg alloys, Acta Mater. 56 (2008) 4804–4815.
[6] A. Guinier, Heterogeneities in solid solutions, Solid State Phys. 9 (1959) 293–398.
[7] S.C. Wang, M.J. Starink, Precipitates and intermetallic phases in precipitation hardening Al-Cu-Mg-(Li) based alloys, Int. Mater. Rev. 50 (2005) 193–215.
[8] S.P. Ringer, K. Hono, I.J. Polmear, T. Sakurai, Nucleation of precipitates in aged Al–Cu–Mg–(Ag) alloys with high Cu:Mg ratios, Acta Mater. 44 (1996) 1883–1898.
[9] S.C. Wang, M.J. Starink, Two types of S phase precipitates in Al-Cu-Mg alloys, Acta Mater. 55 (2007) 933–941.
[10] J.T. Vietz, I.J. Polmear, The influence of small additions of silver on the ageing of aluminium alloys: observations on Al-Cu-Mg alloys, J. Inst. Met. 94 (1966) 410–417.
[11] J.A. Taylor, B.A. Parker, I.J. Polmear, Precipitation in Al–Cu–Mg–Ag casting alloy, Met. Sci. 12 (1978) 478–482.
[12] D. Bakavos, P.B. Prangnell, B. Bes, F. Eberl, The effect of silver on microstructural evolution in two 2xxx series Al-alloys with a high Cu:Mg ratio during ageing to a T8 temper, Mater. Sci. Eng. A 491 (2008) 214–223.
[13] R.N. Lumley, I.J. Polmear, The effect of long term creep exposure on the microstructure and properties of an underaged Al-Cu-Mg-Ag alloy, Scripta Mater. 50 (2004) 1227–1231.
[14] N. Sano, K. Hono, T. Sakurai, K. Hirano, Atom-probe analysis of Ω and θ' phases in al Al–Cu–Mg–Ag alloy, Scripta Metall. Mater. 25 (1991) 491–496.
[15] Z. Shen, C. Liu, Q. Ding, S. Wang, X. Wei, L. Chen, J. Li, Z. Zhang, The structure determination of $Al_{20}Cu_2Mn_3$ by near atomic resolution chemical mapping, J. Alloy Compd. 601 (2014) 25–30.
[16] W.X. Feng, F.S. Lin, E.A. Starke Jr., The effect of minor alloying elements on the mechanical properties of Al-Cu-Li alloys, Metall. Trans. A 15 (1984) 1209–1220.
[17] L.D. Castillo, E.J. Lavernia, Microstructure and mechanical behavior of spray-deposited Al-Cu-Mg(-Ag-Mn) alloys, Metall. Mater. Trans. A 31 (2000) 2287–2298.
[18] S. Cheng, Y.H. Zhao, Y.T. Zhu, E. Ma, Optimizing the strength and ductility of fine structured 2024 Al alloy by nano-precipitation, Acta Mater. 55 (2007) 5822–5832.
[19] Z.Q. Feng, Y.Q. Yang, Y.X. Chen, B. Huang, M.S. Fu, M.H. Li, J.G. Ru, In-situ TEM investigation of fracture process in an Al-Cu-Mg alloy, Mater. Sci. Eng. A 586 (2013) 259–266.
[20] Z. Feng, Y. Yang, B. Huang, X. Luo, M. Li, Y. Chen, M. Han, M. Fu, J. Ru, HRTEM and HAADF-STEM tomography investigation of the heterogeneously formed S(Al_2CuMg) precipitates in AlCuMg alloy, Philos. Mag. 93 (2013) 1843–1858.
[21] A.K. Mukhopadhyay, G. Eggeler, B. Skrotzki, Nucleation of Ω phase in an Al–Cu–Mg–Mn–Ag alloy aged at temperatures below 200 °C, Scripta Mater. 44 (2001) 545–551.
[22] L.M. Wang, H.M. Flower, T.C. Lindley, Precipitation of the Ω phase in 2024 and 2124 aluminium alloys, Scripta Mater. 41 (1999) 391–396.
[23] K. Urushino, K. Sugimoto, Stress-corrosion cracking of aged Al–Cu–Mg alloys in NaCl solution, Corros. Sci. 19 (1979) 225–236.
[24] R. Parvizi, R.K.W. Marceau, A.E. Hughes, M.Y. Tan, M. Forsyth, Atom probe tomography study of the nanoscale heterostructure around an Al20Mn3Cu2 dispersoid in aluminium alloy 2024, Langmuir 30 (2014) 14817–14823.
[25] R. Parvizi, A.E. Hughes, M.Y. Tan, R.K.W. Marceau, M. Forsyth, P. Cizek, A.M. Glenn, Probing corrosion initiation at interfacial nanostructures of AA2024-T3, Corros. Sci. 116 (2017) 98–109.
[26] J. Wang, B. Zhang, B. Wu, X.L. Ma, Size-dependent role of S phase in pitting initiation of 2024Al alloy, Corros. Sci. 105 (2016) 183–189.
[27] N. Birbilis, R.G. Buchheit, D.L. Ho, M. Forsyth, Inhibition of AA2024-T3 on a phase-by-phase basis using an environmentally benign inhibitor, cerium dibuthyl phosphate, Electrochem. Solid St. 8 (2005) 180–183.
[28] J. Wang, B. Zhang, Y.T. Zhou, X.L. Ma, Multiple twins of a decagonal approximant embedded in S-Al_2CuMg phase resulting in pitting initiation of a 2024Al alloy, Acta Mater. 82 (2015) 22–31.
[29] Y.Q. Chen, S.P. Pan, W.H. Liu, X. Liu, C.P. Tang, Morphologies, orientation relationships, and evolution of the T-phase in an Al-Cu-Mg-Mn alloy during homogenisation, J. Alloy Compd. 709 (2017) 213–226.
[30] Y.Q. Chen, S.P. Pan, B.X. Zhu, X. Liu, W.H. Liu, S.W. Tang, The evolution of orientation relationships during the transformation of a twin-free T-particle to tenfold T-twins in an Al alloy during homogenisation, Mater. Charact. (2018) 59–73.
[31] H. Perlitz, A. Westgren, The crystal structure of Al_2CuMg, Ark. Kemi Min. Geol. 16B (1943) 1–5.
[32] C. Wolverton, Crystal structure and stability of complex precipitate phases in Al-Cu-Mg-(Si) and Al-Zn-Mg alloys, Acta Mater. 49 (2001) 3129–3142.
[33] Y.Q. Chen, D.Q. Yi, Y. Jiang, B. Wang, D.Z. Xu, S.C. Li, Twinning and orientation relationships of T-phase precipitates in an Al matrix, J. Mater. Sci. 48 (2013) 3225–3231.
[34] Z.Q. Feng, Y.Q. Yang, B. Huang, N.H. Li, Y.X. Chen, J.G. Ru, Crystal substructures of the rotation-twinned T ($Al_{20}Cu_2Mn_3$) phase in 2024 aluminum alloy, J. Alloy Compd. 583 (2014) 445–451.
[35] Y.A. Bagaryatsky, Zh. Tekh. Fiz. 18 (1948) 827.
[36] J. Majimel, G. Molenat, F. Danoix, D. Blavette, G. Lapasset, M.J. Casanove, A study of the hardening precipitation in a 2650 aluminium alloy for aeronautics, Mater. Sci. Forum 396 (2002) 1025–1030.
[37] G.B. Winkelman, K. Raviprasad, B.C. Muddle, Orientation relationships and lattice matching for the S phase in Al-Cu-Mg alloys, Acta Mater. 55 (2007) 3213–3228.
[38] L. Kovarik, M.K. Miller, S.A. Court, M.J. Mills, Origin of the modified orientation relationship for S(S")-phase in Al-Mg–Cu alloys, Acta Mater. 54 (2006) 1731–1740.
[39] V. Radmilovic, R. Kilaas, U. Dahmen, G.J. Shiflet, Structure and morphology of S-phase precipitates in aluminum, Acta Mater. 47 (1999) 3987–3997.
[40] M.J. Styles, C.R. Hutchinson, Y. Chen, A. Deschamps, T.J. Bastow, The coexistence of two S (Al_2CuMg) phases in Al-Cu-Mg alloys, Acta Mater. 60 (2012) 6940–6951.
[41] M.J. Styles, R.K.W. Marceau, T.J. Bastow, H.E.A. Brand, M.A. Gibson,

C.R. Hutchinson, The competition between metastable and equilibrium S (Al2CuMg) phase during the decomposition of Al–Cu–Mg alloys, Acta Mater. 98 (2015) 64–80.
[42] T.S. Parel, S.C. Wang, M.J. Starink, Hardening of an AlCuMg alloy containing Types I and II S phase precipitates, Mater. Des. 31 (2010) S2–S5.
[43] Nanomegas, ASTAR - Application Notes Nanoscale TEM Orientation Imaging Analysis, 2016, pp. 1–32. www.nanomegas.com.
[44] P. Moeck, S. Rouvimov, E.F. Rauch, M. Véron, H. Kirmse, I. Häusler, W. Neumann, D. Bultreys, Y. Maniette, S. Nicolopoulos, High spatial resolution semi-automatic crystallite orientation and phase mapping of nanocrystals in transmission electron microscopes, Cryst. Res. Technol. 46 (2011) 589–606.
[45] J.S. Barnard, D.N. Johnstone, P.A. Midgley, High-resolution scanning precession electron diffraction: alignment and spatial resolution, Ultramicroscopy 174 (2017) 79–88.
[46] E.F. Rauch, J. Portillo, S. Nicolopoulos, D. Bultreys, S. Rouvimov, P. Moeck, Automated nanocrystal orientation and phase mapping in the transmission electron microscope on the basis of precession electron diffraction, Z. Kristallogr. 225 (2010) 103–109.
[47] pyxem.github.io/pyxem - Version 0.5.1.
[48] F. de la Peña, et al., HyperSpy - 1.3.1 (2018), https://doi.org/10.5281/zenodo.592838.
[49] F. de la Peña, et al., Electron microscopy (big and small) data analysis with the open source software package HyperSpy, Microsc. Microanal. 23 (S1) (2017) 214–215.
[50] F. Bachmann, R. Hielscher, H. Schaeben, Texture analysis with MTEX free and open source software toolbox, Solid State Phenom. 160 (2010) 63–68.
[51] R. Krakow, R.J. Bennett, D.N. Johnstone, Z. Vukmanovic, W.S. Alvarez, S.J. Lainé, J.F. Einsle, P.A. Midgley, C.M.F. Rae, R. Hielscher, On three-dimensional misorienation spaces, Proc. Royal Soc. A 473 (2017) 20170274.
[52] Z.Q. Feng, Y.Q. Yang, B. Huang, X. Luo, M.H. Li, M. Han, M.S. Fu, Variant selection and the strengthening effect of S precipitates at dislocations in Al-Cu-Mg alloy, Acta Mater. 59 (2011) 2412–2422.
[53] J. Wang, B. Zhang, Z.B. He, B. Wu, X.L. Ma, Atomic-scale mapping of twins and relevant defective structures in $Al_{20}Cu_2Mn_3$ decagonal approximant, Philos. Mag. 96 (2016) 2457–2467.
[54] E.F. Rauch, M. Véyron, Automated crystal orientation and phase mapping in TEM, Mater. Charact. 98 (2014) 1–9.
[55] F. Zupani, D. Wang, C. Gspan, T. Boncina, Precipitates in a quasicrystal-strengthened Al-Mn-Be-Cu alloy, Mater. Charact. 106 (2015) 93–99.
[56] Y.Q. Chen, S.P. Pan, S.W. Tang, W.H. Liu, C.P. Tang, F.Y. Xu, Formation mechanisms and evolution of precipitate-free zones at grain boundaries in an Al-Cu-Mg-Mn alloy during homogenization, J. Mater. Sci. 51 (2016) 7780–7792.
[57] C.R. Hutchinson, X. Fan, S.J. Pennycook, G.J. Shiflet, On the origin of the high coarsening resistance of Ω plates in Al–Cu–Mg–Ag alloys, Acta Mater. 49 (2001) 2827–2841.

Paper IV

Jonas Kristoffer Sunde, Sigurd Wenner
Randi Holmestad

In situ heating TEM observations of evolving nanoscale Al-Mg-Si-Cu precipitates

Journal of Microscopy (2019).
https://doi.org/10.1111/jmi.12845

Journal of Microscopy

Journal of Microscopy, Vol. 00, Issue 00 2019, pp. 1–5 doi: 10.1111/jmi.12845
Received 29 June 2019; accepted 7 November 2019

In situ heating TEM observations of evolving nanoscale Al–Mg–Si–Cu precipitates

JONAS KRISTOFFER SUNDE*, SIGURD WENNER† & RANDI HOLMESTAD*
*Department of Physics, Norwegian University of Science and Technology (NTNU), Trondheim, Norway
†Materials and Nanotechnology, SINTEF Industry, Trondheim, Norway

Key words. Aluminium alloys, *in situ* transmission electron microscopy, phase mapping, precipitation, scanning precession electron diffraction.

Summary

This research concerns the precipitation and subsequent dissolution of precipitate phases in an Al–0.86Mg–0.62Si–0.1Cu (at.%) alloy subjected to varying thermal exposure during an *in situ* heating transmission electron microscope (TEM) experiment. The distribution and crystal structure of precipitates were determined by a scanning diffraction approach at multiple stages, pinpointing the precipitates that underwent phase transformations during heating. Obtained results were compared with TEM studies of the material heated *ex situ*. This revealed differences in the transformation kinetics of precipitates in an electron transparent lamella (thickness $\gtrsim 90$ nm) to that of macroscopic bulk specimens.

Introduction

Age-hardenable Al alloys are an important group of structural materials that are strengthened by nanosized, metastable precipitates formed during thermal ageing. The precipitates are conventionally studied using the TEM, with electron transparent specimens prepared from materials heat treated to different stages. Due to improvements in specimen preparation techniques and the advent of TEM heating holders with high mechanical and thermal stability, it has now become possible to study the evolution of precipitates *in situ* (Malladi *et al.*, 2014; Liu *et al.*, 2017; Park *et al.*, 2019).

Al–Mg–Si(–Cu) alloys are important in automotive and construction applications, and form characteristic needle- or lath-shaped precipitates with long axes parallel to $<100>_{Al}$ upon ageing (Edwards *et al.*, 1998; Marioara *et al.*, 2007). Previous *in situ* heating studies of precipitates in this alloy system have measured the overall changes to the distribution of precipitate parameters (lengths, densities, etc.) (Tsao *et al.*, 2006; Chang *et al.*, 2015; Flament *et al.*, 2017). We have here conducted an *in situ* heating TEM study, using bright-field imaging and scanning precession electron diffraction (SPED) combined with data post-processing to study the distribution and identities of transforming precipitates. A single region of interest was systematically studied, enabling tracking of the evolution of individual precipitate phases. The results were compared to conventional TEM studies of the material heat treated *ex situ* (Sunde *et al.*, 2019).

Correspondence to: Jonas Kristoffer Sunde, Department of Physics, NTNU, N-7491 Trondheim, Norway. Tel: +47 90918060; e-mail: jonas.k.sunde@ntnu.no

Material and methods

An extruded Al–0.86Mg–0.62Si–0.1Cu (at.%) alloy was subjected to solution heat treatment (SHT) at 540°C for 12 min, and subsequently water-quenched to room temperature (RT). The specimens heat treated *ex situ* were kept 10 min at RT before artificial ageing at 180°C. A peak-hardened material was obtained after approximately 3 h ageing. TEM specimens were made by standard electro-polishing using a Struers Tenupol-5 applying a 1:2 nitric acid:methanol mixture ($T \approx -25$°C).

Electron backscatter diffraction was conducted in a Hitachi SU6600 FE scanning electron microscope (SEM) on an electropolished TEM specimen which enabled mapping and identification of grains close to $\langle 001 \rangle_{Al}$ orientation. The specimen had been heat treated 20 min at 180°C *ex situ* to initiate the precipitation in bulk conditions. Subsequently, a focused ion beam (FIB) lamella of a $\langle 001 \rangle_{Al}$-oriented grain was prepared and mounted on a DENSsolutions nanochip using a FEI Helios G4 FIB. The chip was placed in a DENSsolutions D6 wildfire TEM holder which kept the specimen at 180–240°C in-between SPED scans. A JEOL 2100F microscope (200 kV) was used to run the *in situ* heating and SPED experiments. SPED was conducted using a NanoMEGAS ASTAR system. The nanobeam diffraction probe semi-convergence angle was 1.0 mrad and the precession angle employed was 1.0°. The scan step size was selected as 1.52 nm and pixel exposure time was 40 ms. SPED scans were recorded with the temperature held at RT ($T = 23$°C) and typically comprised 400×400 pixels, thus covering an area of $\sim 600 \times 600$ nm^2 and taking

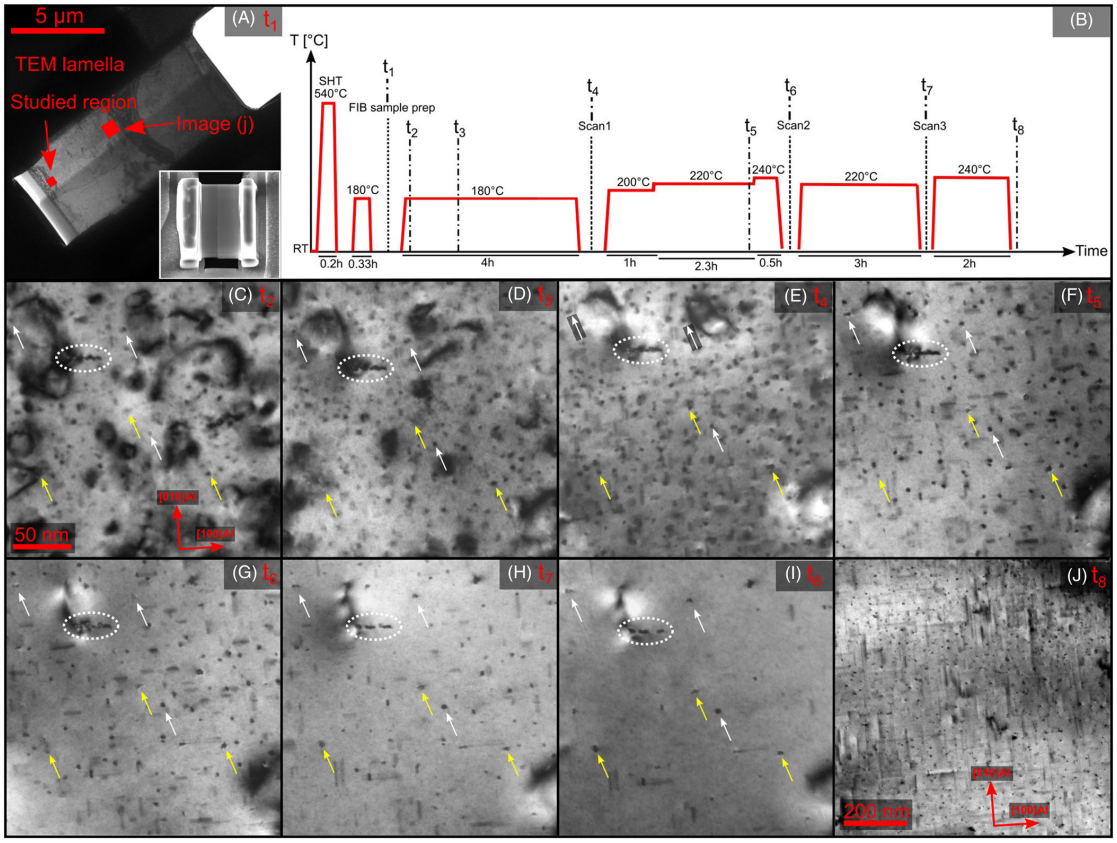

Fig. 1. (A) TEM image of the FIB prepared lamella. Insert shows a SEM image of the ion-milled lamella mounted across the heating holder SiN window using a C-weld. (B) A schematic of the heat treatment procedure. (C–I) Bright-field images acquired at indicated times (t_x) in the region highlighted in image (A) (~90nm thickness). White and yellow arrows indicate *L* and (β''/)β'/Q′ phases, respectively, that remain in the studied region after all stages of heating. The white dashed oval highlights coarsened precipitates that have formed on an underlying dislocation, and acts as a point of reference between images. (J) Bright-field image acquired in the indicated region of image (A) (~130 nm thickness).

approximately 1.5 h to acquire. Specimen thickness was measured by electron energy loss spectroscopy. The obtained 4D SPED datasets, comprising a 2D PED pattern at each position of a 2D area scan, were analysed using the HyperSpy (de la Peña et al., 2019) Python library. The diffraction data were decomposed using an unsupervised machine learning algorithm based on non-negative matrix factorization, and subsequently matched with phases of the Al–Mg–Si–Cu system (Sunde *et al.*, 2018).

Results and discussion

Figure 1 shows the evolution of the alloy microstructure after exposure to subsequent stages of heating. The time–temperature evolution is indicated in schematic B, showing the times (t_X) at which bright-field images and SPED scans were obtained. In the initial stages ($t_1 - t_3$), the needle-shaped character of the majority of precipitates was hard to discern, and many likely existed as small atomic clusters or Guinier–Preston zones. Dislocations and surface impurities introduced by FIB (dark regions of Figs. 1C,D) gradually annealed out. At t_4 (image E), the needle morphology was clearly visible, and a high density of small precipitates had formed. The thermal exposure at this point corresponded with near peak hardness in isothermally heated bulk specimens. Figure 2 shows the phase mapping results obtained from SPED data. Figure 2(A) was constructed from SPED scan1 acquired at t_4, and shows that the majority of precipitates in the region were β''. There was also a significant presence of *L*-phase and β'/Q′-phase precipitates.

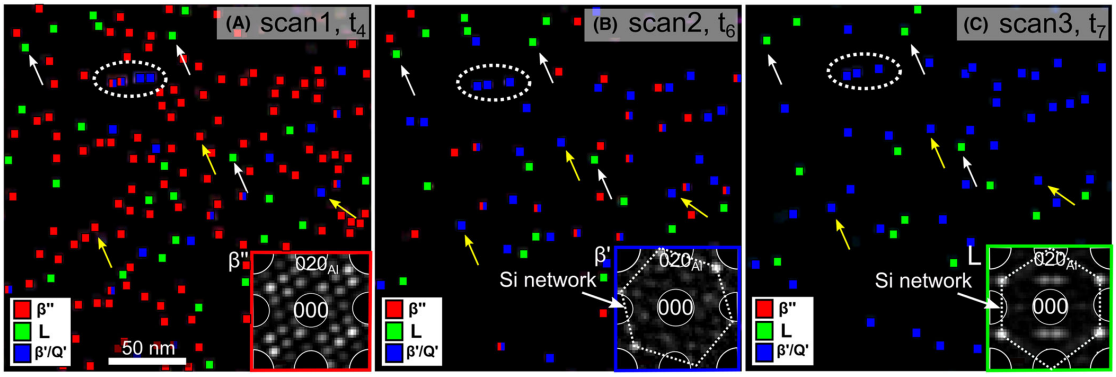

Fig. 2. (A–C) Phase maps constructed from SPED scan decomposition results. The inserts show decomposition component patterns matched with indicated phases.

Table 1. Precipitate statistics and proportion of the total volume fraction of precipitate phases existing in the microstructure after isothermal ageing at 180°C conducted *ex situ* and *in situ*.

Condition	Needle length (nm)	Number density (#/μm^3)	β'' (%)	L (%)	β'/Q' (%)	U2 (%)
3 h *ex situ*	11.2 ± 0.6	(10.7 ± 1.1) × 10^4	69 ± 5	12 ± 2	11 ± 2	8 ± 3
4.3 h *in situ* (t_4)	8.4 ± 0.8	(13.5 ± 1.5) × 10^4	72 ± 5	13 ± 3	15 ± 3	–
24 h *ex situ*	13.0 ± 1.0	(8.0 ± 0.8) × 10^4	47 ± 4	21 ± 2	24 ± 2	8 ± 3

After subsequent heating stages at $T > 180$°C the precipitates coarsened and subsequently dissolved. The phase map in Figure 2(B) at t_6 shows a low presence of remaining β'' precipitates, and at time t_7 (Fig. 2C), there were none left. At this stage, there were only *L*-phase and β'/Q'-phase precipitates present. The six precipitates indicated by white and yellow arrows that existed throughout the full heating experiment support current hypotheses regarding the precipitation in this alloy system: The *L*-phase precipitates remained fixed as *L* phases through the full experiment, and could be traced back to 1 h ageing (not shown). This observation indicates that this phase exhibits a separate evolution, likely tracing back to the clustering stage. No new *L*-phase precipitates were formed. The high thermal stability of this phase was also clearly demonstrated, as the majority of the *L*-phase precipitates at t_4 remained at t_6 and t_7 (Marioara *et al.*, 2014). Two out of three yellow marked precipitates started out as β'' precipitates (t_4), but were at t_6 seen to have transformed to β', in agreement with established knowledge about the precipitation in these alloys (Edwards *et al.*, 1998; Marioara *et al.*, 2007). The surrounding β'' precipitates at t_4 which were subsequently dissolved are thought to free solute to the matrix surrounding the evolving β' precipitates.

Table 1 shows a comparison of measured precipitate statistics at time t_4 to that of *ex situ* heated specimens studied after 3 and 24 h isothermal ageing at 180°C, corresponding with a peak-hardened and a slightly overaged condition, respectively. Bright-field images of the material microstructures for the conditions listed in Table 1 are shown in Figure 3. It is observed that the precipitate statistics in the studied region of the *in situ* heated lamella (thickness ~ 90 nm) showed a more refined microstructure of smaller precipitates relative to the isothermally heated bulk specimens. This indicated that the material was still in an underaged state. This is thought to have occurred primarily due to a lack of solutes which instead have diffused towards the top and bottom surfaces of the TEM lamella. It has previously been shown that there was a significant migration of Si and Mg to the surface of an Al–Mg–Si–Li alloy at 200°C, with concentrations exceeding 10 at.% for both atomic species in the top nanometre of the specimen (Cooil *et al.*, 2016). Mg was shown to migrate towards grain boundaries (GBs), whereas Si was ubiquitous. It is important to note that the surface oxide was removed by Ar^+ bombardment in the cited study. The specimen in the present study was exposed to air before insertion into the TEM, and therefore formed several nanometre thick surface oxide layers. Due to the similarities in element additions and temperature, surface segregation of solutes is also thought to have occurred for the alloy studied in this work. Decreased levels of precipitate forming elements, most notably Si, are thought to be the main reason for the observed reduction in precipitate growth as compared to specimens prepared

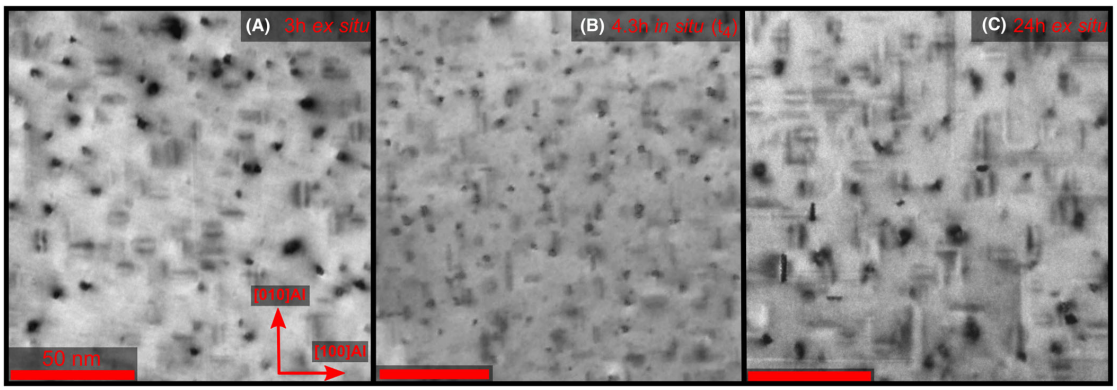

Fig. 3. (A–C) Bright-field TEM images of the alloy microstructures after (A) 3 h *ex situ*, (B) 4.3 h *in situ* and (C) 24 h *ex situ* ageing at 180°C. All scale bars equal 50 nm.

from bulk conditions. In addition, because the TEM lamella is free to bend and expand in one dimension, different from a bulk material, strain relaxation could also have contributed to reduced precipitate growth. Heterogeneous nucleation of precipitates in cold worked materials is known to accelerate precipitation significantly, with dislocations acting as high-diffusion pathways. However, as the bulk material was not subjected to any cold deformation and the resulting division of precipitate types formed was similar, the effect is thought to be less important than surface segregation of solutes.

The precipitates in the studied region did not grow larger than 30 nm in length (see Fig. 1H). In a thicker region of the specimen (Fig. 1J, ∼130 nm thickness), some precipitates grew to reach above 100 nm in length, similar to significantly overaged conditions in the isothermally aged bulk material (Sunde *et al.*, 2019). There is a striking difference between the scarcely populated region of Figure 1(I) to that of Figure 1(J), both acquired at the same condition. The dissolution of precipitate phases in a thin region of the lamella further indicated that the concentration of solutes (and potentially vacancies) in the specimen had developed in a significantly different manner than for the bulk material.

As the material was pre-aged before FIB specimen preparation, the vacancy concentration was likely near equilibrium concentration initially. Before *in situ* ageing, below the surface oxide layers, the top and bottom surfaces of the material were rich in dislocations and Ga^+ ions from the FIB. Metal/amorphous interfaces serve as dislocation sinks (Legros *et al.*, 2009; De Knoop & Legros, 2014), and the initial bright-field imaging observations showed that the dislocations and surface impurities were annealed out after a relatively short time. It is not known whether the metal/oxide interfaces act as net sources or sinks of vacancies. *In situ* observations of precipitate-free zones (PFZs) surrounding dispersoids near the studied region showed that the PFZs grew at similar rates as for PFZs surrounding dispersoids and GBs in the bulk material. The comparable growth rates are taken as a qualitative indication that the concentration of vacancies in the lamella was comparable to that of the bulk material.

Our hypothesis regarding precipitate dissolution is that with a driving force causing solutes to segregate to the specimen surfaces with ageing, the precipitates that were positioned near or grew to reach in proximity of the surfaces dissolved, thus initiating the formation of PFZs. Subsequently, the continued segregation of solutes to the surfaces lead to further growth of the PFZ regions, and the growing PFZs reached precipitate phases buried progressively deeper in the lamella thickness, causing further dissolution. In addition, the lack of solutes through the lamella thickness might eventually have caused dissolution of the remainder precipitate phases. High-resolution high-angle annular dark-field scanning TEM imaging was attempted at t_5, but the precipitates were buried too deep in the material to be imaged, which supports the PFZ hypothesis. Future experiments will attempt SHT and re-ageing *in situ* to see whether the experiment can be repeated on the same lamella. Thickness effects will also be studied more carefully to assess the transferability of the results to bulk precipitation behaviour.

Conclusions

The high thermal resistance of the *L* phase was demonstrated, being one of the main phases remaining after multiple stages of high thermal exposure (180–240°C). β'' was the main precipitate phase near peak-hardened conditions, and formed a high number density of precipitates. A few percentage of the β'' precipitates subsequently transformed to β'/Q' phases, whereas the rest dissolved. Specimen thickness had a pronounced effect on the ageing kinetics, and additional experiments comparing *in situ* and *ex situ* heating TEM results are necessary to investigate this aspect further.

Acknowledgements

The authors acknowledge support from the AMPERE project (NFR 247783), a knowledge building project for industry, cofinanced by the Research Council of Norway (NFR), and the industrial partners Hydro, Gränges, Neuman Aluminium Raufoss (Raufoss Technology) and Nexans. The (S)TEM work was carried out on the NORTEM infrastructure (NFR 197405) at the TEM Gemini Centre, Trondheim, Norway.

Conflict of interest

The authors declare no conflict of interest.

References

Chang, C.S.T., De Geuser, F. & Banhart, J. (2015) In situ characterization of β'' precipitation in an Al-Mg-Si alloy by anisotropic small-angle neutron scattering on a single crystal. *J. Appl. Crystallogr.* **48**, 455–463. https://doi.org/10.1107/S1600576715002770.

Cooil, S.P., Mørtsell, E.A., Mazzola, F. *et al.* (2016) Thermal migration of alloying agents in aluminium. *Mater. Res. Exp.* **3**(11). https://doi.org/10.1088/2053-1591/3/11/116501.

De Knoop, L. & Legros, M. (2014) Absorption of crystal/amorphous interfacial dislocations during in situ TEM nanoindentation of an Al thin film on Si. *Scr. Mater.* **74**, 44–47. https://doi.org/10.1016/j.scriptamat.2013.10.003.

de la Peña, F., Prestat, E. Fauske, V.T. et al. (2019) Hyperspy/hyperspy: v1.5.2. https://doi.org/10.5281/zenodo.3396791.

Edwards, G.A., Stiller, K., Dunlop, G.L. & Couper, M.J. (1998) The precipitation sequence in Al-Mg-Si alloys. *Acta Mater.* **46**(11), 3893–3904. https://doi.org/10.1016/S1359-6454(98)00059-7.

Flament, C., Ribis, J., Garnier, J. *et al.* (2017) Stability of β'' nano-phases in Al-Mg-Si(-Cu) alloy under high dose ion irradiation. *Acta Mater.* **128**, 64–76. https://doi.org/10.1016/j.actamat.2017.01.044.

Legros, M., Cabié, M. & Gianola, D.S. (2009) In situ deformation of thin films on substrates. *Microsc. Res. Technol.* **72**(3), 270–283. https://doi.org/10.1002/jemt.20680.

Liu, C., Malladi, S.K., Xu, Q., Chen, J., Tichelaar, F.D., Zhuge, X. & Zandbergen, H.W. (2017) In-situ STEM imaging of growth and phase change of individual $CuAl_X$ precipitates in Al alloy. *Sci. Rep.* **7**, 2184. https://doi.org/10.1038/s41598-017-02081-9.

Malladi, S.K., Xu, Q., Van Huis, M.A. *et al.* (2014) Real-time atomic scale imaging of nanostructural evolution in aluminum alloys. *Nano Lett.* **14**(1), 384–389. https://doi.org/10.1021/nl404565j.

Marioara, C.D., Andersen, S.J., Røyset, J., *et al.* (2014) Improving thermal stability in Cu-containing Al-Mg-Si Alloys by precipitate optimization. *Metal. Mater. Trans. A* **45**(7), 2938–2949. https://doi.org/10.1007/s11661-014-2250-0.

Marioara, C.D., Andersen, S.J., Stene, T.N., Hasting, H., Walmsley, J., van Helvoort, A.T.J. & Holmestad, R. (2007) The effect of Cu on precipitation in Al-Mg-Si alloys. *Philos. Mag.* **87**(1), 3385–3413. https://doi.org/10.1080/14786430701287377.

Park, J., Kamachali, R.D., Kim, S.D., Kim, S.H., Oh, C.S., Schwarze, C. & Steinbach, I. (2019) First evidence for mechanism of inverse ripening from in-situ TEM and phase-field study of δ' precipitation in an Al-Li alloy. *Sci. Rep.* **9**(1), 1–11. https://doi.org/10.1038/s41598-019-40685-5.

Sunde, J.K., Marioara, C.D. & Holmestad, R. (2019) The effect of low Cu additions on precipitate crystal structures in overaged Al-Mg-Si(-Cu) alloys. *Submitted.*

Sunde, J.K., Marioara, C.D., van Helvoort, A.T. & Holmestad, R. (2018) The evolution of precipitate crystal structures in an Al-Mg-Si(-Cu) alloy studied by a combined HAADF-STEM and SPED approach. *Mater. Charact.* **142**(1), 458–469. https://doi.org/10.1016/j.matchar.2018.05.031.

Tsao, C.S., Chen, C.Y., Jeng, U.S. & Kuo, T.Y. (2006) Precipitation kinetics and transformation of metastable phases in Al-Mg-Si alloys. *Acta Mater.* **54**(17), 4621–4631. https://doi.org/10.1016/j.actamat.2006.06.005.

Paper V

Jonas Kristoffer Sunde, Calin Daniel Marioara
Randi Holmestad

The effect of low Cu additions on precipitate crystal structures in overaged Al-Mg-Si(-Cu) alloys

Materials Characterization **160** (2020) 110087.
https://doi.org/10.1016/j.matchar.2019.110087

Materials Characterization 160 (2020) 110087

Contents lists available at ScienceDirect

Materials Characterization

journal homepage: www.elsevier.com/locate/matchar

The effect of low Cu additions on precipitate crystal structures in overaged Al-Mg-Si(-Cu) alloys

Jonas K. Sunde[a,*], Calin D. Marioara[b], Randi Holmestad[a]

[a] Department of Physics, Norwegian University of Science and Technology (NTNU), Trondheim N-7491, Norway
[b] Materials and Nanotechnology, SINTEF Industry, Trondheim N-7465, Norway

ARTICLE INFO

Keywords:
Aluminium alloys
Precipitation
Scanning transmission electron microscopy
Scanning electron diffraction
Differential scanning calorimetry

ABSTRACT

This study concerns the effect of low Cu additions (≲0.1 at.%) on the precipitate crystal structure evolution in three Al-Mg-Si(-Cu) alloys during overageing. The evolution was assessed through a combination of atomic resolution scanning transmission electron microscopy, scanning electron diffraction, and differential scanning calorimetry. It was found that relatively small changes in the Cu level and the Si:Mg ratio had significant effects on the resulting distribution of precipitate phases, their structural evolution, and their thermal stability. Two Si-rich alloys formed hybrid β' phase and Q′ phase precipitates on overageing. A third Mg-rich alloy primarily formed L phase precipitates, which exhibited superior thermal stability. Three distinct Cu-containing sub-units that form the basis for all Al-Mg-Si-Cu precipitate phases were identified: the three-fold symmetric Q′/C and the β_{Cu}' sub-units, in addition to a newly discovered C sub-unit. The formation of each sub-unit was discussed, and the atomic structures and connections to other precipitate phases in the Al-Mg-Si(-Cu) system were elaborated. The work presented provides new insights into the complex precipitation of Cu-added Al-Mg-Si alloys, with implications for material properties. The results obtained will be of importance in future alloy and process development, and are thought to be of high value in modelling work on the quaternary Al-Mg-Si-Cu system.

1. Introduction

Heat treatable (age hardenable) 6xxx series Al-Mg-Si(-Cu) alloys form an important group of medium strength engineering alloys widely applied in the transportation and construction sector. This alloy series can be tailored to exhibit a favourable combination of properties, including good formability, high strength-to-weight ratio, and good corrosion resistance [1, 2]. The 6xxx series Al alloys obtain a large increase in hardness when subjected to short-term thermal ageing. The hardening is due to a high number of nano-sized and metastable precipitate phases that form and distribute throughout the Al matrix [3, 4]. The various phases have different atomic structures, and therefore differ in mechanical properties. The phases also vary in atomic matchings at the precipitate-matrix interface, which cause different levels of interfacial strain. Dislocation movement is impeded by both the atomic structure of precipitate phases and the interfacial strain, which results in material strengthening. Consequently, the properties of an alloy depend strongly on the precipitate types and the microstructures they produce.

The total addition of precipitate forming elements Mg, Si, and Cu typically amounts to < 2 at.% in wrought 6xxx series Al alloys. Changes in the Cu level and the Si:Mg ratio may have a pronounced effect on the resulting distribution of precipitates (types, sizes, density, etc.). Rod- or lath-shaped precipitates with long axes parallel to $\langle 100 \rangle_{Al}$ are characteristic of the Al-Mg-Si-Cu system. In the Cu-free system, the established precipitation sequence is given as [5, 6]

$$\begin{aligned} \text{SSSS} &\rightarrow \text{solute clusters} \rightarrow \text{GP-zones} \\ &\rightarrow \beta'' \rightarrow \beta', \text{U1, U2, B}' \rightarrow \beta, \text{Si,} \end{aligned} \tag{1}$$

where SSSS denotes a supersaturated solid solution.

There is a large commercial interest in Cu additions in Al-Mg-Si alloys as it is demonstrated to increase the age hardening response, and to promote a higher number density of smaller precipitates that exhibit improved thermal stability [7-12] . The addition of Cu leads to a more complex precipitation sequence, that can be stated as [7, 13-16]

$$\begin{aligned} \text{SSSS} &\rightarrow \text{solute clusters} \rightarrow \text{GP-zones} \\ &\rightarrow \beta'', \text{L} \rightarrow \beta_{Cu}', \text{S, Q}', \text{C} \rightarrow \text{Q, Si.} \end{aligned} \tag{2}$$

All metastable precipitate phases in the Al-Mg-Si(-Cu) system are structurally related due to a common network of Si atomic columns along the precipitate lengths [13]. In $\langle 100 \rangle_{Al}$ projection, this network exhibits a near hexagonal symmetry with $a = b \approx 4$ Å. For the β'' phase, the network is partly fragmented due to a high coherency with

* Corresponding author.
E-mail address: jonas.k.sunde@ntnu.no (J.K. Sunde).

https://doi.org/10.1016/j.matchar.2019.110087
Received 25 September 2019; Received in revised form 15 November 2019; Accepted 19 December 2019
Available online 30 December 2019

the Al matrix [17]. The different types of precipitates are distinguished based on how their Al, Mg, and Cu atomic columns are positioned with respect to the Si-network columns. Al and Mg are always positioned in-between the Si-network columns, and Cu is positioned in-between (Q′ phase and C phase), or replacing parts of the Si-network columns (β_{Cu}′ phase) [18]. The precipitate atomic columns can also exhibit variations in atomic modulation and/or mixed element occupancy. In the precipitation sequence Eq. (2), the frequently used notations QP and QC are not included, being instead interpreted as fragments of Al-Mg-Si (-Cu) phases on the Si-network and the β_{Cu}′ phase, respectively. The details of this discussion are presented in the reviews conducted by Saito et al. [19] and Andersen et al. [20].

As noted, Cu additions are generally associated with several favourable effects, but are on the other hand also causing an increased susceptibility towards corrosion [21]. Pitting- and intergranular corrosion (IGC), are the two most common corrosion modes observed in this alloy system [22]. IGC mainly occurs when the alloys are artificially aged and when Cu > 0.1 wt.% and/or contain excess Si compared to the β phase stoichiometry (Mg_2Si) [23]. IGC is thought to propagate due to the presence of a continuous Cu film along grain boundaries (GBs), and an increase in IGC resistance at overaged conditions is thought to be due to the induced discontinuity in this film [24, 25]. If this is the case, then the key towards limiting IGC is therefore to maximize Cu absorption in bulk precipitates, leaving less Cu available to form a continuous Cu film at the GBs [26]. Further research is necessary to improve alloy compositions and thermomechanical processing routines that lead to alloys exhibiting satisfactory corrosion properties, as well as enhanced strength and thermal stability. Therefore, it is important to obtain an improved understanding of how Cu is incorporated into the precipitate structures, which was explored in the present study.

Due to the aforementioned considerations it was decided to focus on low Cu additions ($\lesssim$0.1 at.%). At these Cu levels, fragmentation and hybridization often prevails, with the different phase unit cells and substructures of the Al-Mg-Si- and the Cu-added system often coexisting within individual precipitates [18, 27]. Low level additions are also highly relevant on the subject of Al alloy recycling. There are vast energy savings in re-using Al alloys, and recycling is an important activity in the industry [28]. Recycled Al alloys will inevitably contain certain levels of trace elements, which might induce undesirable changes to the precipitation, as relatively low amounts of solute elements are needed to form precipitates. These changes could have consequences for the mechanical properties of the alloy. The influence of Cu as a trace element on precipitation was another aspect studied through this work.

In the present work, atomic resolution scanning transmission electron microscopy (STEM) was used to assess the precipitate structures, and the distribution of 1000s of precipitate phases was quantified using a recently developed scanning precession electron diffraction (SPED) approach [29, 30]. Electron microscopy results were linked to bulk material phase transformations measured by differential scanning calorimetry (DSC). The combination of techniques provided a detailed assessment of the evolution of phases in the alloy microstructures as a function of overageing, with particular focus on the role of Cu.

2. Experimental procedures

2.1. Materials and heat treatments

Three Al-Mg-Si(-Cu) alloys with different, albeit low Cu additions were studied. Table 1 shows the compositions of the alloys. The compositions of alloys S and C correspond with the high strength commercial alloy 6082, whereas alloy M falls outside of this range. On comparison with alloys S and C, alloy M differs by being Mg-rich, has a higher level of Cu, and lower concentration of the dispersoid (/primary particle) forming elements Mn and Cr. The alloys were delivered as extruded rods (Ø 30 mm). Approximately 10 mm height cylinders were cut from the rods and set to solution heat treatment at 540 °C for 12 min conducted in a salt bath. Subsequently, the specimens were water-quenched to room temperature and kept at this temperature for 10 min before they were artificially aged at 180 °C conducted in an oil bath. The material conditions selected for TEM studies were chosen as follows: alloy S — 3 h, 12 h, 24 h, 1 week, 2 weeks, and 1 month ageing; alloy C — 3 h, 12 h, 24 h, and 1 week ageing; alloy M — 3 h, 24 h, and 1 month ageing.

Table 1
Nominal compositions of the three Al-Mg-Si(-Cu) alloys studied.

Alloy	Al	Si	Mg	Cu	Fe	Mn	Cr
S at.%	Bal.	0.85	0.80	0.01	0.12	0.25	0.08
S wt.%	Bal.	0.88	0.72	0.03	0.24	0.51	0.16
C at.%	Bal.	0.85	0.71	0.04	0.10	0.22	0.07
C wt.%	Bal.	0.88	0.64	0.09	0.20	0.45	0.14
M at.%	Bal.	0.62	0.86	0.10	0.13	0.13	0.01
M wt.%	Bal.	0.64	0.77	0.23	0.26	0.26	0.02

2.2. Preparation of TEM specimens

The heat treated material cylinders were cut to 1 mm height and then mechanically polished with gradually finer grades of SiC-paper until they reached a thickness of roughly 100 μm. Al discs of 3 mm diameter were punched out from the polished cylinders. Subsequently, the discs were electro-polished using a Struers Tenupol-5 applying an electrolytic solution comprising a 2:1 mixture of methanol:nitric acid, kept between −30 °C and -25 °C. The voltage was set to 20 V (current 0.2 A). A Fischione 1020 Plasma Cleaner was used on each specimen prior to TEM studies in order to minimize carbon contamination.

2.3. Electron microscopy

Initial visualization of the alloy microstructures was done using bright-field TEM imaging, which was attained using a JEOL 2100 microscope operated at 200 kV. A double corrected JEOL ARM200F microscope (200 kV) was used to obtain atomically resolved high-angle annular dark-field (HAADF) STEM lattice images. The detector collection angle used was 42–178 mrad.

SPED experiments were performed using a JEOL 2100F microscope (200 kV). The microscope is equipped with a NanoMEGAS ASTAR system which makes it possible to simultaneously scan the electron beam while recording electron diffraction patterns. The diffraction patterns that were formed on the phosphor viewing screen of the microscope were captured using an external Allied Vision StingRay camera [31]. The nanobeam diffraction mode was used when running SPED, and the beam alignment for PED was done using the procedure described by Barnard et al. [32]. The following parameters were used when acquiring SPED data: probe diameter — 0.5–2.0 nm (non-precessed); probe semi-convergence angle — 1.0 mrad; precession angle — 0.5, 0.7, or 1.0°; precession frequency — 100 Hz; scan step size — 0.76, 1.52, or 2.28 nm; and exposure time — 20 or 40 ms per pixel. The precipitate distribution (sizes, density, etc.) change with thermal ageing, and the acquisition parameters had to be adjusted to cover representative numbers of precipitates for each alloy and ageing condition.

SPED can be classified as a 4D-STEM technique, and each dataset is composed of 2D PED patterns associated with each pixel in a 2D scan area. The HyperSpy [33] Python library was used for data visualization and analysis. The SPED data formed the basis for estimating average precipitate phase fractions in the microstructure of the different alloys after various ageing times. The details of the SPED data analysis is elaborated in a previously related work by Sunde et al. [30].

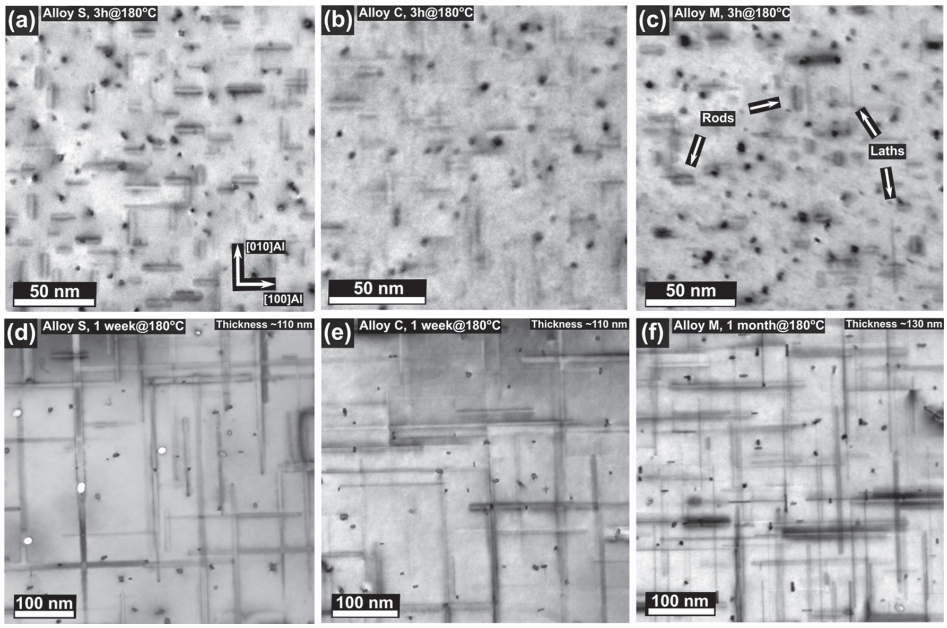

Fig. 1. (a–f) Bright-field TEM images of indicated alloys and ageing times. All images are acquired near the $[001]_{Al}$ zone axis.

Table 2
Average precipitate parameters in alloys S, C, and M for selected ageing conditions.

Alloy & condition	Cross-section area	Length rods	Length laths
S 3 h	(13 ± 1) nm^2	(14 ± 1) nm	–
S 1 week	(45 ± 3) nm^2	(242 ± 7) nm	–
C 3 h	(10 ± 1) nm^2	(13 ± 1) nm	–
C 1 week	(55 ± 3) nm^2	(181 ± 6) nm	–
M 3 h	(10 ± 1) nm^2	(11 ± 1) nm	(25 ± 2) nm
M 1 month	(43 ± 3) nm^2	(136 ± 4) nm*	(136 ± 4) nm*

* Coarsened precipitates lying in-plane were not clearly separable as rods and laths and were assumed to be approximately equal in size.

2.4. Thermal analysis by DSC

DSC experiments were conducted for alloys S and C, and employed a Hitachi DSC7020 using a heating rate of ~0.2 K s^{-1} (10 K min^{-1}) scanned from RT (~25 °C) up to 500 °C. Specimens were measured relative to a thermodynamically inert reference specimen of pure aluminium with equal geometry, using nitrogen as purge gas. The specimens were cut to cubic geometry (5:5:5 [mm], h:l:w) with masses of (21 ± 1) mg. DSC experiments were conducted on four material conditions: as-solutionized (~10 min natural ageing), 3 h, 24 h, and 1 week ageing at 180 °C. This corresponds to an as-solutionized, peak aged, medium overaged, and significantly overaged condition, respectively. DSC diagrams are presented using excess specific heat capacity, c_p [J g^{-1} K^{-1}], calculated as [34]

$$c_p = \frac{\dot{Q}_S - \dot{Q}_B}{m_S \cdot \epsilon},$$

where $\dot{Q}_S$ and $\dot{Q}_B$ are the specimen and baseline heat flows, respectively. m_S denotes the specimen mass, and ϵ is the heating rate. The baseline heat flow was obtained by scanning a pure Al specimen against another pure Al reference specimen in the DSC device using identical scan parameters as for the scanned alloy conditions.

3. Results and discussion

3.1. Assessment of the precipitate crystal structure evolution by TEM

The transformations of the alloy microstructures after different ageing times at 180 °C are shown in Fig. 1. At 3 h ageing (peak aged), the microstructures comprised high densities of short rods with characteristic β'' strain fields on either side, running parallel to the main growth direction. In alloy M, longer and narrow lath-shaped precipitates were also visible (highlighted). As will be shown in the following, these precipitates are mainly L phases, and do not exhibit the same strain contrast characteristic of β''. After 1 week ageing, the precipitates in alloys S and C had coarsened considerably as compared to the 3 h condition. The precipitates in alloy M exhibited high resistance towards coarsening, and after 1 month ageing they were still smaller than the precipitates at the 1 week ageing condition in alloys S and C. The average precipitate lengths and the average cross-section areas measured for alloys S, C, and M for the conditions imaged in Fig. 1 are listed in Table 2.

The crystal structures of the main Al-Mg-Si(-Cu) precipitate phases relevant to this work are shown in Fig. 2. HAADF-STEM lattice images of precipitates from corresponding ageing times for alloys S and C are shown in Fig. 3. Fig. 4 shows precipitates from the three studied ageing conditions for alloy M. Fast Fourier transform (FFT) filtering was applied to reduce noise using a circular band pass mask removing all periods shorter than 1.5 Å. Chosen precipitates were evaluated as representative for each ageing condition, but it should be noted that large variations were observed. The same images without highlighting are presented in **Fig. SI 1** and **Fig. SI 2** in the **Supplementary Information (SI)**. **Figs. SI 3–5** present additional HAADF-STEM images of precipitates in all studied alloys and ageing conditions.

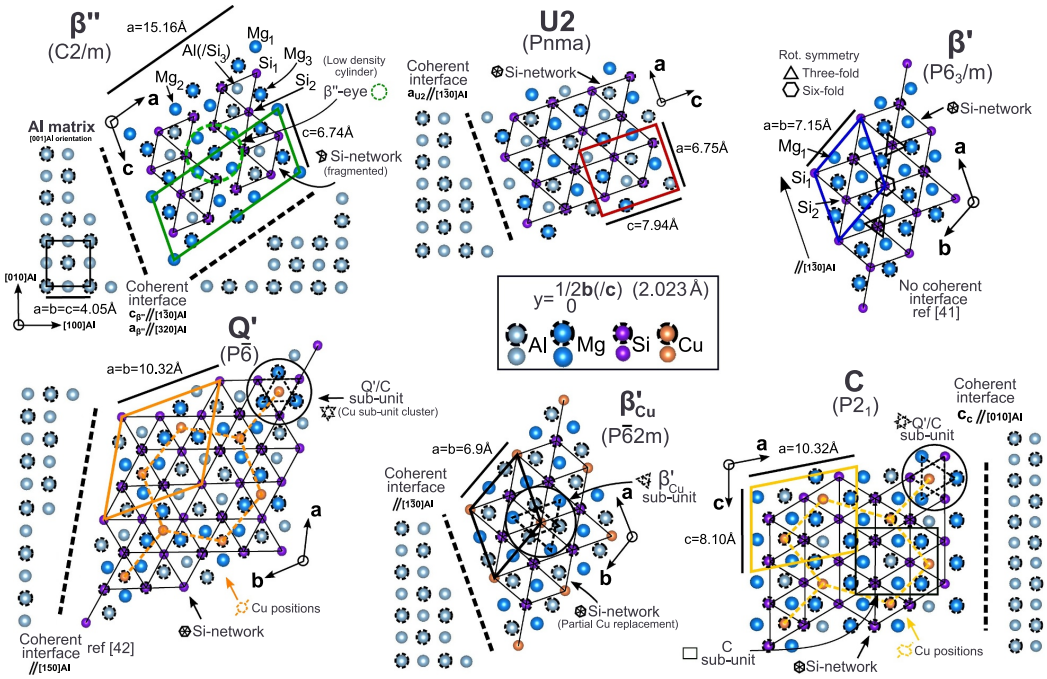

Fig. 2. The crystal structures of the main precipitate phases observed in the present work. Unit cells, sub-units, and other key structural features are indicated. Phase unit cells are shown in coloured full lines. Coherent precipitate-matrix interfaces are indicated for the different phases. The notation $\mathbf{a}_A$, $\mathbf{b}_A$, and $\mathbf{c}_A$ for a given phase A denotes the main crystallographic vectors spanning the unit cell of phase A. The references used for the precipitate crystal structures are shown in **Table SI 1** in the **Supplementary Information (SI)**. (For interpretation of the references to colour in this figure legend, the reader is referred to the web version of this article.)

3.1.1. Peak aged precipitates (3 h ageing)

The vast majority of precipitates in alloys S and C at 3 h ageing was pure β'', see Fig. 3a–d. Some atomic columns in the β'' structures showed higher intensity than the other corresponding columns due to partial occupancy of Cu. Cu (Z_{Cu} = 29) exhibits a higher contrast in the HAADF-STEM imaging mode than the other precipitate forming elements Mg (Z_{Mg} = 12), Al (Z_{Al} = 13), and Si (Z_{Si} = 14) due to the $Z^{1.7-2.0}$ atom column scattering power dependency at high angles [35]. The incorporation of Cu in β'' structures was observed to be higher for alloy C than for S, which was as expected due to its higher Cu content. This finding was also supported by the observation of individual β_{Cu}' sub-units in the β'' structures, which were seen in some precipitates in alloy C (e.g. Fig. 3c), but not in alloy S. β_{Cu}' is the Cu-containing equivalent to the isostructural Ag-containing β' phase [36]. The presence of this sub-unit in alloy C was an indication of accelerated phase transformation kinetics occurring for alloy C in comparison to alloy S, which is mainly attributed to the increased Cu content of alloy C.

In the following, the description of precipitate structures uses terms such as phase, sub-unit, hybrid, and fragmented. Here, a precipitate phase means a crystal structure consisting of at least one full unit cell of a phase such as those in the precipitation sequences Eqs. (1) and (2). A sub-unit is used to denote a structural unit that forms part of a precipitate phase unit cell. The term hybrid is used to describe a precipitate that exhibits multiple coexisting phases, all of which form multiple complete phase unit cells. I.e. hybrid precipitates comprise more than one clearly identifiable phase. A fragmented precipitate structure is used to describe a precipitate that comprises multiple phase sub-units or single stray unit cells. Fragmented precipitate structures contain no dominating phase(s). For the latter case, we avoid the term disordered, which is not a clear term in this context. As noted, all precipitate phases in this alloy system build on an underlying Si-network, and comprise structural units that adhere to this network. Therefore, the precipitates are never truly disordered.

Precipitates in alloy M exhibited notable differences as compared to alloys S and C at 3 h ageing (see Fig. 4a–d). The precipitates can be divided into two types: a fragmented/β'' type (Fig. 4a, b) and an overall fragmented type containing no dominant phase (Fig. 4c, d). The fragmented/β'' type showed significantly increased Cu incorporation as compared to the β'' precipitates in alloys S and C. The β_{Cu}' and the Q′/C sub-units were observed (Fig. 4a), in addition to complete unit cells of Q′ and U2 (Fig. 4b). The precipitate shown in image Fig. 4c is classified as L phase. The L phase displays local regions containing unit cells of Q′ and C phases (or sub-units), ordered on the Si-network, which aligns with $\langle 100 \rangle_{Al}$. The Si arrangement is the main ordering observed for this phase [37, 38]. Image Fig. 4d shows a precipitate lacking an ordered, permeating Si-network. Furthermore, it does not contain any phase unit cells, and is therefore described as a fragmented precipitate, denoted S phase [16].

There was a tendency of Cu enrichment in certain atomic columns along the precipitate-matrix interface for both types of precipitates in alloy M. Cu segregation to the interface of β'' type precipitates has been observed previously, and was proposed as a mechanism to suppress misfit dislocations [39]. However, here the Cu segregation often takes on a special configuration, highlighted in Fig. 4b, c. In a recent investigation by Weng et al. [40], the same Cu segregation was observed in L type precipitates. It was proposed to arise due to a strong covalent bonding between Cu and Si, where the Si column forms part of the Si-network. As will be shown in the following, this Cu segregation was observed in the majority of all precipitate types in alloy M. On closer inspection, the sub-structure associated with this Cu segregation is seen to be a sub-unit of the C phase, and is therefore denoted as C sub-unit in the following.

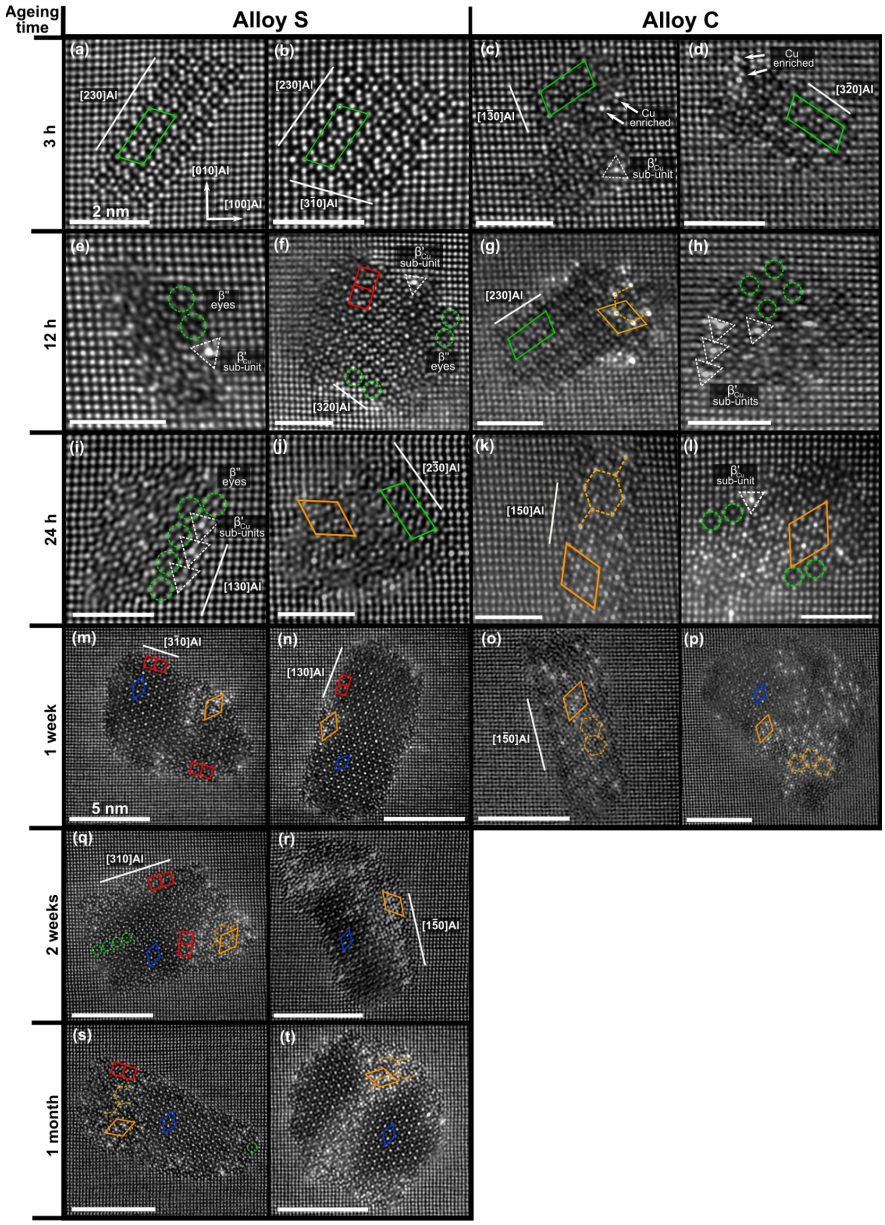

Fig. 3. (a–t) HAADF-STEM lattice images of precipitates from indicated alloys and ageing conditions. A few unit cells, sub-units, and other key structural features of the identified Al-Mg-Si-Cu phases are highlighted, using the marking shown in Fig. 2. Al matrix directions that run parallel to the adjacent precipitate interfaces are indicated. The scale bars (a–l) equal 2 nm, and the scale bars (m–t) correspond to 5 nm.

The observations made for alloy M indicated that the increased Cu content in this alloy as compared to both alloys S and C lead to further enhanced phase transformation kinetics. Some precipitates in alloy M had already formed complete cells of Q′ and C, sub-units of which were not observed in alloys S and C. β_{Cu}' sub-units were also more frequent in alloy M as compared to alloy C. In addition to being promoted by increased Cu levels, the fragmentation and formation of L phases were also due to the increased Mg:Si ratio in alloy M as compared to alloys S and C.

Three distinct Cu-containing sub-units were observed up to this point: the Q′/C sub-unit, the β_{Cu}' sub-unit, and a newly discovered C sub-unit. The atomic configuration of these sub-units are shown in Fig. 2. The differences between the three-fold symmetric sub-units of Q′/C and β_{Cu}' include the positioning of the Cu column with respect to the Si-network columns. For β_{Cu}', the Cu column *replaces* a Si-network column, whereas for Q′/C the column is located *in-between* the network.

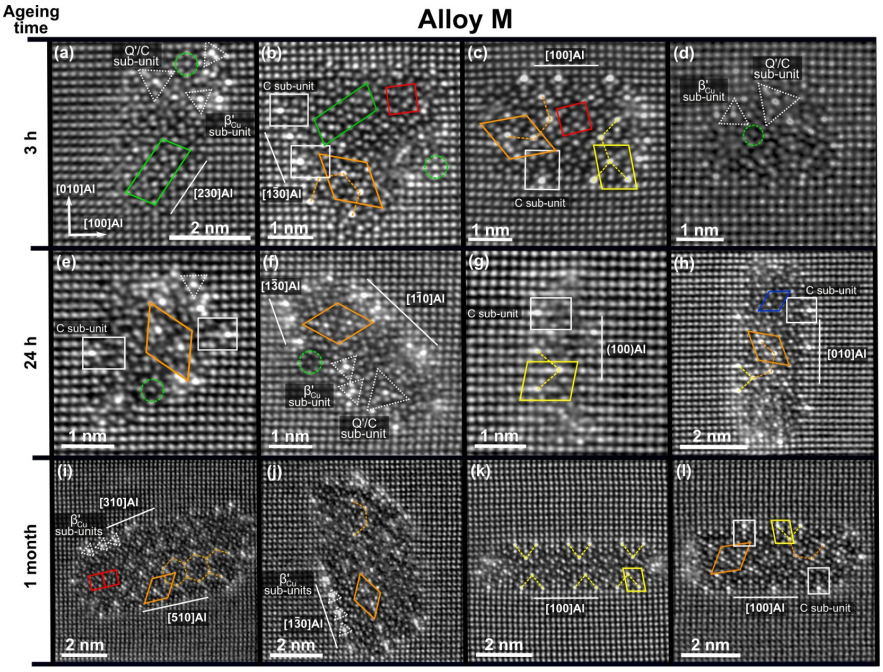

Fig. 4. (a–l) HAADF-STEM lattice images of precipitates from indicated ageing conditions in alloy M. A few unit cells, sub-units, and other key structural features of the identified Al-Mg-Si-Cu phases are highlighted, using the marking shown in Fig. 2. Al matrix directions that run parallel to the adjacent precipitate interfaces are indicated.

Furthermore, the structures differ in the atomic species and interatomic distances of the triangular sites surrounding the center Cu atom. A Mg and a Si triangle is placed at the same atomic height as the Cu atom for the β_{Cu}' and the Q′/C sub-unit, respectively. An Al and a Mg triangle is shifted $c/2 \approx 2.023$ Å in height relative to the center Cu atom for the β_{Cu}' and the Q′/C sub-unit, respectively.

3.1.2. Classification of Al-Mg-Si(-Cu) phases and sub-units

In the literature, there exists other notations for some of the phases and sub-units in the Al-Mg-Si(-Cu) system, some of which are included in Fig. 2. The multiple conventions cause confusion and may lead to misunderstandings. Therefore, for the sake of clarification, **Table SI 1** shows an overview of the present work's labelling together with other existing notations. **Fig. SI 6** shows a flow chart for classifying the different Cu-containing phases.

The Q′/C sub-unit is referred to as a *(Cu) sub-unit cluster* in the work of Cayron et al. [13] and Ding et al. [43], and is proposed as a key building block in the evolution of phases in the Al-Mg-Si-Cu system. In the work of Maeda et al. [44] the same term is used, but then indicating a β_{Cu}' sub-unit. The Q′/C sub-unit is discriminated, and there referred to as a Q′ sub-unit cell. Hence, there exists an inconsistency in the terminology used to denote these structural units, which needs to be resolved.

We argue here that it is important to differentiate between the two flavours of Cu-centered, three-fold symmetric sub-units Q′/C and β_{Cu}'. This is because their atomic configurations differ, and hence their formation and subsequent evolution will vary. In addition to the C sub-unit, these in total three sub-units constitute the building blocks for the subsequent formation of all Cu-containing phases in this alloy system. **Fig. SI 7** shows an atomic overlay of a precipitate containing all three sub-units, which serves as a useful illustration of the configuration of the sub-units and how these relate to the Si-network.

3.1.3. Medium overaged precipitates (12 h & 24 h ageing)

At 12 h ageing, unit cells of phases other than β'' were present in alloys S and C (Fig. 3e–h), including U2, β', and Q′ (not all shown). This often resulted in a hybrid precipitate structure comprising multiple coexisting phases. Clearer differences between alloys S and C had emerged, the most prominent being the increased proportion of Cu-containing phase unit cells and sub-units in alloy C. In alloy S, unit cells of U2 were often observed to connect to the unit cells of β'', or its sub-units (β''-eyes). The β_{Cu}' sub-unit was also observed for some precipitates, with or without a strong presence of Cu in the center column, and mainly observed at the precipitate-matrix interface. For alloy C, almost all precipitates showed multiple Cu-containing sub-units of β_{Cu}' in addition to Q′/C. For some precipitates, complete unit cells of Q′ could be seen (e.g. Fig. 3g). The sub-units were not only observed at the precipitate-matrix interface, but also in the precipitate interior. Despite noted differences, β'' remained the dominant phase in both alloys at 12 h ageing.

At 24 h ageing (Fig. 3 i–l), the hybrid character had developed further in alloys S and C. Pure β'' phases were less common. For alloy S, the precipitates typically showed a predominantly Al-Mg-Si containing β'' phase and U2 phase interior, and some Cu enrichment, as well as a few sub-units of β_{Cu}' and Q′/C at the precipitate-matrix interface. For the precipitates exhibiting a high degree of fragmentation (e.g. Fig. 3i), unit cells of β'' were no longer present, but reduced to rows of- or individual β''-eyes. The observations are similar to other reports showing β''/fragmented precipitates at underaged and peak hardness conditions for alloys with higher Cu content [18, 43]. For alloy C, an increased proportion of the precipitate structures comprised Cu-containing phases, in particular Q′. Fig. 3k shows a pure Q′ phase with characteristic lath-shaped morphology and coherent $\langle 150 \rangle_{Al}$ interfaces. This was not observed in alloy S at any ageing condition. Corresponding precipitates in alloy M at 24 h ageing (see Fig. 4 e–h) exhibited two

main precipitate types: hybrid rods (mainly S phase) and hybrid/fragmented laths with $\{100\}_{Al}$ habit planes (mainly L phase). Most precipitates showed significant Cu incorporation. Q′ phase and C phase unit cells were observed, as well as β_{Cu}' and Q′/C sub-units. β' was also observed at this stage (Fig. 4h). Many precipitates in alloy M had developed an ordered Si-network permeating the precipitate structures. This further supports the indicated acceleration in transformation kinetics as compared to alloys S and C.

3.1.4. Significantly overaged precipitates (≥1 week ageing)

After 1 week ageing a large transformation of the precipitate structures in alloys S and C had taken place, and the precipitates had coarsened considerably (see Fig. 3m–p). For alloy S, the main phases observed were β' and β_2'. These phases often dominated the interior of the precipitates. β' and β_2' are closely related structures, differing primarily in the atomic modulation of the Si_1 column (see Fig. 2). The structure of proper β' has 1 extra Si atom per 3 × 4.05 Å in the *c*-direction at the Si_1 columns, i.e. a $\frac{3}{4}a_{Al}$ repeat distance [45]. This leads to a higher column occupancy, and hence a higher intensity at the Si_1 site. β_2' shows absence of clear modulation, and is readily identified in a diffraction based approach due to a slight variation in space group symmetry [30]. In the following, β' and β_2' are together denoted as $\beta_{(2)}'$. $\beta_{(2)}'$ was often linked by a row of U2 unit cells/sub-units to the Al matrix or phases at the precipitate-matrix interface. Q′/C sub-units and full unit cells of Q′ were commonly observed at the interface. In alloy C, the Q′ phase had now progressed to become the dominant phase observed. As shown in Fig. 3o, almost pure Q′ phases with characteristic $\langle 150\rangle_{Al}$ interfaces were sometimes observed. In addition to Q′, $\beta_{(2)}'$ was also frequently seen. An ordered Si-network had been established in the precipitates of alloys S and C. The β_{Cu}' sub-unit was no longer observed in either alloy, which indicated that this sub-unit either dissolved or underwent a structural transition. No further ageing of alloy C was conducted, as the precipitates were thought to show limited subsequent change.

After 2 weeks ageing of alloy S, many precipitates showed modest coarsening relative to the 1 week condition, and the phases coexisting were similar to the 1 week state (see Fig. 3q, r). From the observation of a series of images, the main development seemed to be the increased extent of the Q′ phase, which now reached further into the precipitate interior. Multiple grouped Q′ unit cells were frequently observed.

At 1 month total ageing of alloy S there was limited further coarsening of the precipitates (see Fig. 3s, t). Similar to the 1 week–2 weeks transition, there seemed to be a further development of the Q′ takeover of the precipitate structures. In some precipitates there was now a near 50/50 division of $\beta_{(2)}'$ phase and Q′ phase. In addition to these phases, rows of U2 unit cells often formed the interfaces between the $\beta_{(2)}'$ and Q′ phases. The U2 phase was also often observed at the precipitate-matrix interface, particularly in the interlayer separating the $\beta_{(2)}'$ phase from the Al matrix. The interlayer forms because the $\beta_{(2)}'$ phase does not form coherent interfaces towards Al [41]. The Q′ phase however forms coherent interfaces along $\langle 150\rangle_{Al}$ [42]. Several precipitates at 1 month ageing for alloy S showed many similarities with precipitates in alloy C at the 1 week condition. This further attested to the differences observed in phase transformation kinetics caused by the differences in the Cu content of these alloys.

Precipitates in alloy M after 1 month ageing showed significant differences as compared to alloy S after 1 month ageing, and compared to alloy C after 1 week ageing (see Fig. 4i–l). There were still two main precipitate types: hybrid rods (mainly S phase), which mainly comprised Q′ and $\beta_{(2)}'$, and laths with $\{100\}_{Al}$ habit planes. The lath-shaped precipitates were most frequent, are were predominantly L phase (see Fig. 5b), but C phase was also observed (see Fig. 4k). Atomic columns at the precipitate interfaces often showed clear Cu segregation. For the rod-shaped precipitates this often resulted in formation of rows of β_{Cu}' sub-units. For the lath-shaped precipitates this was manifested as C sub-units and C unit cells. The precipitates of alloy M had coarsened substantially less than for alloys S and C in the overageing stages, which is likely due to the stabilising effect of the Cu enriched interfaces, which has been demonstrated for the C sub-unit on the interfaces of L phase precipitates [12, 46]. The β_{Cu}' sub-unit was not observed in the overaged precipitates in alloys S and C. In alloy M however, the β_{Cu}' sub-unit was commonly observed at the precipitate-matrix interface, also after 1 month total ageing. The β_{Cu}' sub-unit did not grow to form complete unit cells.

3.2. Quantification of the precipitate phase evolution based on SPED data

The lattice image results provide detailed insight to the complexity and interplay of the different phases in the Al-Mg-Si-Cu system. However, in order to provide stronger statistical support for the proposed evolution of precipitate phases inferred from lattice image observations, a recently developed SPED approach was applied [29, 30]. This approach enables determination of precipitate types for a large number of precipitates, obtained in large, representative areas of the alloy microstructures. Fig. 5 presents phase mapping results obtained from a SPED scan acquired in the microstructure of alloy M at the 1 month ageing condition. For the purpose of visualization, three groups of phases in this ageing condition are mapped using RGB colouring: Q′/C (red), L (green), and $\beta_{(2)}'$ (blue) (see Fig. 5b). The L phase (green) is seen to have a widespread presence, in agreement with lattice image observations. Some pixels appear mixed, e.g. as indicated by purple colouring. This corresponds to a mix of $\beta_{(2)}'$ (blue) and Q′/C (red). Such hybrid $\beta_{(2)}'$ and Q′ phase precipitates were also observed in lattice images (not shown).

Fig. 6 summarizes the main findings from the SPED experiments. These bar plots show the average precipitate phase fractions estimated in each ageing condition for alloys S, C, and M, encompassing a total of more than 5000 scanned precipitates. Additional SPED mapping results from which the plots in Fig. 6 are based are shown in **Figs. SI 8–10**. In accordance with TEM observations and established knowledge on the precipitation in the Al-Mg-Si(-Cu) system, Fig. 6 shows that the β'' phase dominates at the peak aged condition (3 h), and subsequently drops off with overageing. For alloys S and C, it is seen that the main transformation of phases occurred between the 24 h and the 1 week state. In this transition stage, the fraction of β'' is seen drop, and is replaced by an increased fraction of $\beta_{(2)}'$ phase and Q′ phase. At the 1 week ageing condition, the relative fraction $Q'/\beta_{(2)}'$ is shown to be much higher in alloy C as compared to alloy S, which agrees well with lattice image observations (see Fig. 3m–p). It is also seen that alloy S after 1 month ageing has a similar division of phases to that of alloy C after 1 week ageing. This is also in good agreement with the development inferred from lattice image observations.

SPED also showed that L type precipitates were present in alloys S and C. In alloy S, the L phase was often linked with microstructure defects such as dislocation lines [30]. This is in agreement with previous studies of this phase [12, 37, 38]. The same applies for alloy C, but here the phase mapping results indicated that a low number of L phases could also be observed away from microstructure heterogeneities.

Alloy M differs as expected notably from alloys S and C in the evolution of phases. At the 3 h condition, the microstructure is seen to comprise a lower fraction of β'' phase, and a higher fraction of L and $\beta_{(2)}'$ phases as compared to alloys S and C. A similar difference is observed at the 24 h condition, where the fraction of L and $\beta_{(2)}'$ phases has increased further for alloy M. The SPED analysis also shows that there is a widespread presence of the β'' phase at the 24 h condition. This result was not evident from HAADF-STEM imaging. At the 1 month condition, alloy M is dominated by the L phase. This evolution differs from that of alloys S and C, where it is $\beta_{(2)}'$ and Q′ that eventually dominate. SPED analysis results serve to demonstrate that there is a need for improvements in precipitate statistics in order to make general statements about the precipitation of age hardening Al alloys.

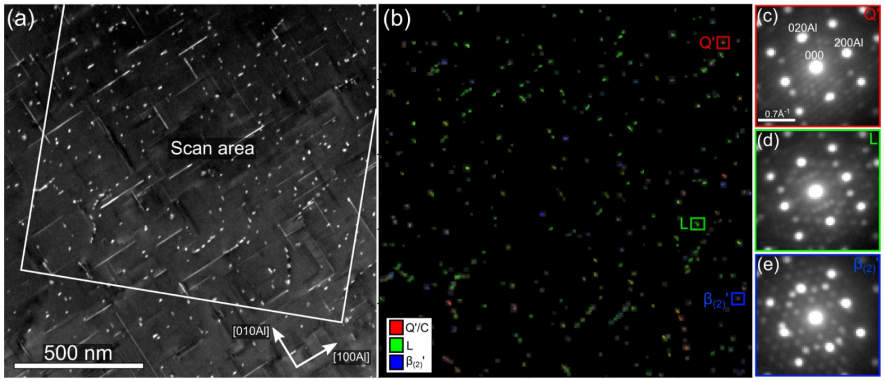

Fig. 5. (a) Dark-field TEM image of alloy M in the 1 month ageing condition. SPED scan area is indicated. The image was acquired near the $[001]_{Al}$ zone axis. (b) Phase map constructed from analysed SPED data showing 437 precipitate cross-sections. Three groups of phases are mapped using RGB colouring: Q′/C (red), L (green), and $\beta_{(2)}'$ (blue). (c–e) Individual pixel PED patterns (raw) from indicated precipitates in (b). (For interpretation of the references to colour in this figure legend, the reader is referred to the web version of this article.)

3.3. Connection between microstructure observations and bulk material phase transformations measured by DSC

In general, energy has to be supplied if chemical bonds are to dissociate, which refers to an endothermic reaction. In exothermic reactions, energy is released, which indicates that new chemical bonds have been formed. For Al alloys, dissolution of precipitate phases corresponds to an endothermic reaction, and precipitation belongs to exothermic reactions. The results from the DSC experiments conducted on alloys S and C are presented in Fig. 7. The main endo- and exothermic peaks are indicated in Roman numerals I–IX. The precipitation events are (coarsely) interpreted as follows: exothermic peak I — GP-zone and/or cluster formation; endothermic peak II — dissolution of GP-zones/clusters; exothermic peak III — β'' precipitation; endothermic peak IV — β'' dissolution; exothermic peak V — β' (/and Q′) formation; endothermic peak VI — β' (/and Q′) dissolution; exothermic peak VII — Q precipitation; exothermic peak VIII — β precipitation; endothermic peak IX — β (/and Q) dissolution.

It is important to emphasize that this is a simplified interpretation of the complex precipitation reactions previously elaborated through the study of precipitate structures. As shown, there were additional phases forming in these alloys, such as U2 and L phases. The vast majority of precipitates were also hybrid, each comprising multiple coexisting phases. It is here aimed at a qualitative understanding of the curves.

The curves from both alloys in all scanned ageing conditions nearly overlap up to the point of peak V. This indicates that all precipitation events up to this point were of similar character. The differences in the DSC curves occurred in the final stages of heating. It is seen that there are differences in the curves for alloys S and C between peaks V and IX for all ageing conditions. The differences observed between peaks V and VII are thought to arise due to variations in the formation and dissolution rate of hybrid Q′ phase and $\beta_{(2)}'$ phase precipitates. The HAADF-STEM and SPED experiments showed that these alloys formed different relative precipitate phase fractions of $Q'/\beta_{(2)}'$, seen from Fig. 3m–p and Fig. 6a, b. Differences in the relative fraction of Q′ phase to $\beta_{(2)}'$ phase implies differences in the kinetics of precipitate formation and dissolution, which are thought to have given rise to the variation observed.

The main differences between the DSC curves are observed at the subsequent formation and dissolution of equilibrium phases, i.e. cubic β phase and hexagonal Q phase. The formation/dissolution of pure diamond structure Si is thought to be approximately equal for alloys S and C due to the nearly equal levels of Si additions and the similar Si:Mg ratio, and is therefore left out of the interpretation of the curves. Peak VII and peak VIII were interpreted as being due to the separate precipitation of the Q phase and the β phase, respectively. This interpretation again followed from the measurement of an increased relative precipitate phase fraction $Q'/\beta_{(2)}'$ in alloy C as compared to alloy S at the 1 week isothermal ageing condition (see Fig. 6a, b). Furthermore, the precipitates in alloy C were sometimes observed to hold defining pure Q′ phase characteristics, such as coherent $\langle 150\rangle_{Al}$ precipitate-matrix interfaces (see Fig. 3o). The precipitates of alloy C exhibiting the highest relative precipitate phase fraction $Q'/\beta_{(2)}'$ and defining interfaces are thought to be the precipitates that have subsequently transformed to equilibrium Q phase. For alloy S, peak VII is apparently missing, which means that this alloy does not form Q phase. This indicated that the predominantly $\beta_{(2)}'$ precipitates of this alloy (see Fig. 3m, n and Fig. 6a) transformed as pure β' phase precipitates, i.e. having formed equilibrium β in the final precipitation stage.

For alloy C, the heat signals of peak VII and peak VIII have some overlap, causing the exothermic effect of Q precipitation to appear as a local minimum on a larger exothermic β precipitation peak. The integrated peak area of peak VIII (β) is much larger than peak VII (Q), implying that also for alloy C the main equilibrium phase is β. This was expected considering the low total Cu addition. Peak VIII is also shifted to a higher temperature in the case of alloy C, indicating that the formation of β has a higher energy barrier in this alloy. Peak VII (Q phase formation) could also potentially be missing from the DSC curve of alloy S due to complete overlap with peak VIII (β phase formation), i.e. that there is an insufficient amount of heat released for the Q phase formation to be detected. This difference in equilibrium phase precipitation is an interesting finding, which shows support for a suggestion made by Bobel et al. [11], who suggested that the presence of small Cu additions determine the stability of hexagonal Q phase or cubic β phase upon ageing to equilibrium conditions.

3.4. Evaluation of the formation of Cu-containing sub-units

β'' was the dominant phase in all alloys studied at the peak hardened condition (3 h), as seen from Fig. 6. Therefore, in order to understand the subsequent evolution of the precipitate crystal structures at the atomic level, it is reasonable to start by inspecting how Cu enters and affects the crystal structure of the β'' phase (see Fig. 8). There are six distinct atomic positions in the β'' structure: Mg_1, Mg_2, Mg_3, Si_1, Si_2, and Al/(Si_3) (see Fig. 2). Density functional theory (DFT) calculations have shown that Cu atoms have highest affinity for the Al/(Si_3)

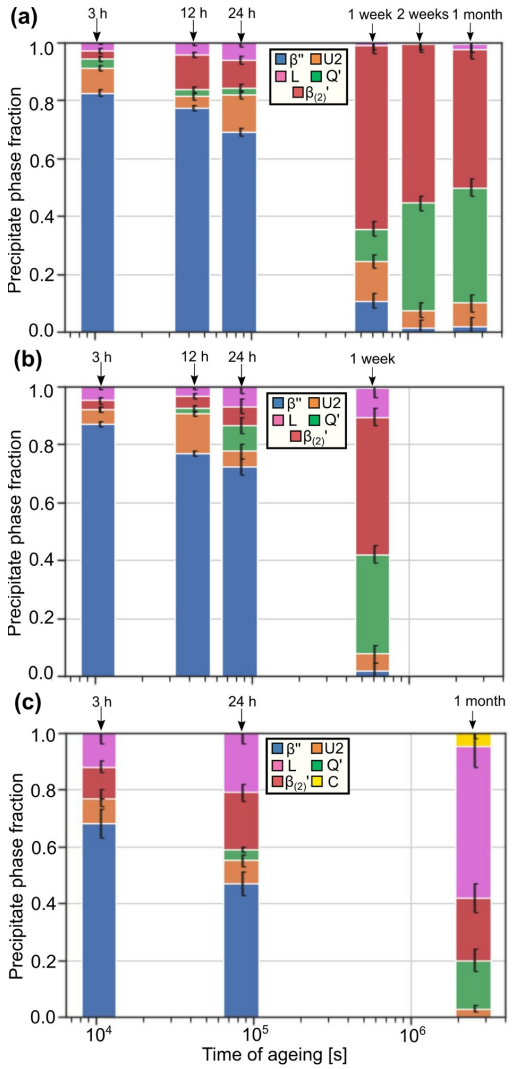

Fig. 6. Bar plots showing average precipitate phase fractions in alloy (a) S, (b) C, and (c) M in each indicated ageing condition. The numbers are estimated from SPED data.

positions, a moderate affinity for the Si_1 position, and to some extent also the Si_2 position [39]. The Mg positions were shown not to be favoured.

Cu has not previously been demonstrated to show clear occupation of the Si_1 and Si_2 positions in the β'' structure. However, the similarities in the structures of the β''-eye and the GPB-zones in the Al-Mg-Cu system [47], in addition to some support from DFT calculations, indicate that these might be potential points of entry for Cu atoms. The Si_1 and Si_2 columns are situated on the Si-network. These columns are also in proximity of both Al and Mg columns which is also part of the β_{Cu}' sub-unit. Therefore, a gradual replacement of either the Si_1 or Si_2 column by Cu may be the probable starting point of the β_{Cu}' sub-unit. Fig. 8a–d shows lattice images and atomic overlays of a pure β'' precipitate and a precipitate containing β'' phase and β_{Cu}' sub-units. On comparison of the images in Fig. 8a, b and in Fig. 8c, d, it is seen that the Cu column of β_{Cu}' is positioned in close proximity of the Si_1 and Si_2 positions of the pure β'' structure. The triangular β_{Cu}' site is observed to interrupt the ordering of the β''-eyes. The net effect of this structural change is inclusion of Cu, and the establishment of an increasingly ordered Si-network, which is favoured on the basis of lattice image observations. Hence, in contrast to the GPB-zones of the Al-Mg-Cu system, the structure of β''-eyes in the Al-Mg-Si-Cu system seems to be immediately perturbed by the inclusion of Cu, which forms β_{Cu}' sub-units near the Si_1 and Si_2 positions. Another interesting remark is that although the interfaces towards the Al matrix are identical for the structures in Fig. 8c and d, there is a shift in the heights of the corresponding atomic positions in the remainder of the precipitate structures that are not in the immediate neighbourhood of the β_{Cu}' sub-units. In fact, all atomic positions in the left-hand row of three β''-eyes in Fig. 8c are shifted $1/2a_{Al}$ in height relative to the corresponding row of three β''-eyes in Fig. 8d. This indicates that there are additional, non-site specific structural changes occurring in the transformation towards post β''-phases, which in this case may have been triggered by the Cu inclusions.

Previous TEM reports have shown that Cu mainly enriches the Al ($/Si_3$) columns of the β'' structure [48, 49], which as noted was also favoured from DFT-based calculations. Observations of multiple β'' lattice images show that this is also supported from this work. Fig. 8e–h shows lattice images of a pure β'' precipitate and a precipitate containing β''-eyes and a Q′ unit cell. On comparison of the images in Fig. 8e, f and in Fig. 8g, h, it is seen how the β'' structure connects to the Q′ unit cell. The positioning of the Cu column corresponds well with the Al($/Si_3$) site of the β'' structure. As the Al($/Si_3$) column is positioned in-between the Si-network, enrichment of this column leads to a Cu-containing column characteristic of the Q′ (and C) phase. This shows that Cu enrichment of the Al($/Si_3$) column is one possible starting point for the formation of Q′/C sub-units.

The C sub-unit only existed at the precipitate-matrix interface (see Fig. 4), and therefore differs notably from the β_{Cu}' and the Q′/C sub-units. Hence, the C sub-unit does not form as the result of Cu inclusions in a structure such as β'', but rather due to an interaction with the atoms positioned at the precipitate-matrix interface. The Cu column of this sub-unit is not embedded in- or replacing the Si-network columns, but rather positioned externally to it (see **Fig. SI 7**). The C sub-unit was frequently observed in alloy M, and only very rarely in alloy C. It therefore seems that an increased Mg:Si ratio is necessary in order to form this sub-unit. The C sub-unit was observed in a Mg-rich (Mg:Si ≈ 2:1) alloy containing only 0.01 wt.% Cu [40]. It is therefore the high Si:Mg ratio, and not the total Cu content that is preventing alloys S and C from forming notable numbers of C sub-units.

4. Conclusions

A combination of HAADF-STEM lattice imaging, SPED-based phase quantification, and DSC has been applied to study the effect of low Cu additions on the evolution of precipitate crystal structures in three Al-Mg-Si(-Cu) alloys during overageing. Generally, the precipitates in all alloys studied showed a gradually increasing proportion of Cu-containing phases with overageing, and accelerated phase transformation kinetics were observed with higher Cu content.

Three different Cu-containing sub-units were identified as the building blocks for all Al-Mg-Si-Cu phases. They are

- β_{Cu}' sub-units
- Q′/C sub-units
- C sub-units

The origins of the two first sub-units were discussed based on how Cu inclusions would alter the β'' crystal structure. The latter only forms at the precipitate-matrix interface, and primarily in Mg-rich alloys.

Two Si-rich alloys and one Mg-rich alloy were studied, and the main findings can be summarised as

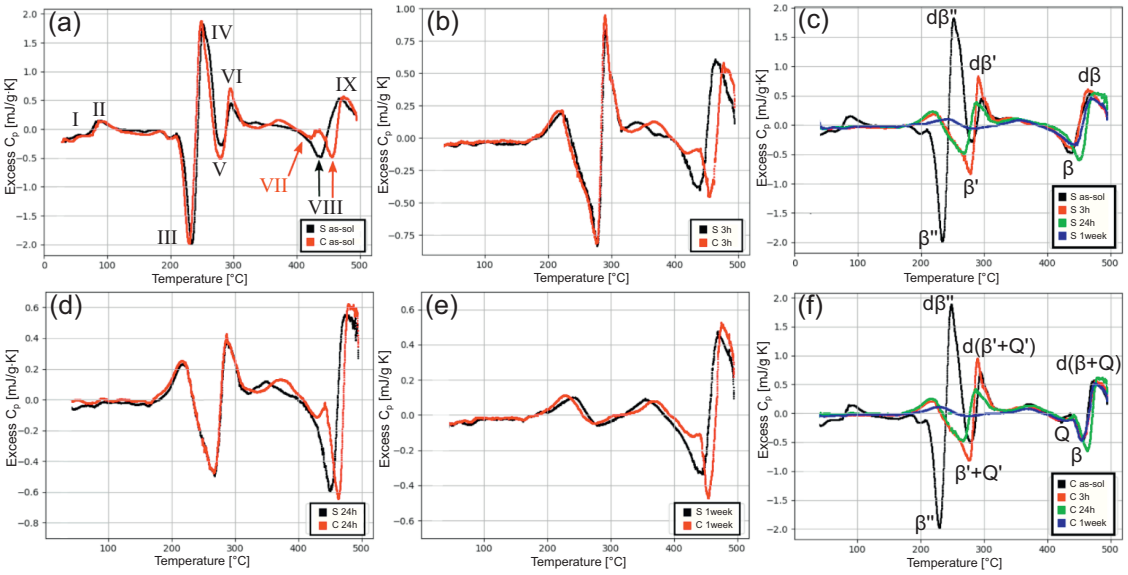

Fig. 7. Excess specific heat capacity measured as a function of temperature obtained from experimental DSC curves for alloys S and C in the ageing conditions: (a) as-solutionized (as-sol) (b) 3 h (d) 24 h (e) 1 week. (c) Combined measurements for alloy S and (f) combined measurements for alloy C. The main endo- and exothermic peaks (I–IX) are indicated. A and dA denote formation and dissolution of a given phase A, respectively.

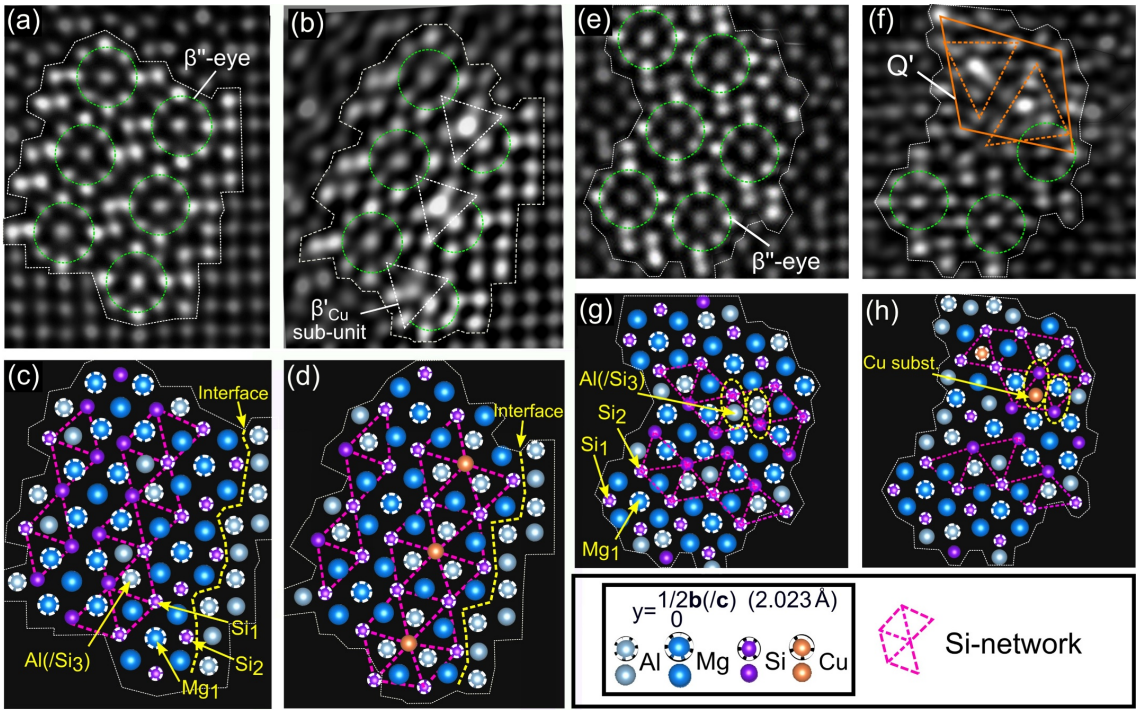

Fig. 8. (a–d) Side-by-side lattice images and atomic overlays of a pure β'' and a hybrid precipitate containing β'' and β_{Cu}' sub-units. (e–h) Side-by-side lattice images and atomic overlays of a pure β'' and a hybrid precipitate containing β''-eyes and a Q′ unit cell. Atomic overlay of the lattice images have been constructed according to the rules of Andersen et al. [17].

- Hybrid $\beta_{(2)}'$ phase and Q′ phase precipitates were formed upon overageing in the Si-rich alloys, and the evolution involved a gradually increasing phase fraction of the Cu-containing Q′ phase
- Minor changes to the Cu level in the Si-rich alloys determined the stability of hexagonal Q phase relative to cubic β phase
- L phase precipitates existed in all conditions in the Mg-rich alloy, and exhibited significantly improved thermal stability as compared to the hybrid $\beta_{(2)}'$ phase and Q′ phase precipitates in the Si-rich alloys

Our study demonstrates how relatively small changes in alloy compositions can cause significant changes to the precipitation. The differences in precipitation were inferred from the analysis of 1000s of precipitate phases enabled by the SPED approach. The improved statistics and the increased objectivity this approach offers validate it as a powerful tool that will be of importance in future alloy design.

Declaration of competing interest

The authors declare that they have no known competing financial interests or personal relationships that could have appeared to influence the work reported in this paper.

Acknowledgments

The authors acknowledge support from the AMPERE project (NFR 247783), a knowledge building project for industry, co-financed by The Research Council of Norway (NFR), and the industrial partners Hydro, Gränges, Neuman Aluminium Raufoss (Raufoss Technology), and Nexans. The electron microscopy work was done using instruments of the NORTEM infrastructure (NFR 197405) at the TEM Gemini Centre. JKS acknowledges support from the Norwegian-Japanese Aluminium Alloy Research and Education Collaboration, INTPART (NFR 249698), which enabled a 1 month research stay at Kobe Steel, Ltd. in Moka, Tochigi, Japan. All authors extend their gratitude towards Kobe Steel, Ltd. for the assistance in conducting DSC experiments.

Appendix A. Supplementary Information

The **Supplementary Information** following this publication presents additional HAADF-STEM lattice images, conventions regarding classification of Al-Mg-Si(-Cu) phases, an atomic overlay of a precipitate lattice image, as well as additional SPED phase mapping results from selected ageing conditions in the studied alloys. The **Supplementary Information** is available to download from [https://doi.org/10.1016/j.matchar.2019.110087]. The raw SPED data required to reproduce these findings cannot be shared at this time due to technical limitations, but are available upon reasonable request.

References

[1] G.E. Totten, D.S. MacKenzie, Handbook of Aluminum, vol. I and II, Marcel Dekker, New York, 2003.
[2] W.S. Miller, L. Zhuang, J. Bottema, A.J. Wittebrood, P. De Smet, A. Haszler, A. Vieregge, Recent development in aluminium alloys for the automotive industry, Mater. Sci. Eng. A 280 (2000) 37–49.
[3] M. Murayama, K. Hono, Pre-precipitate clusters and precipitation processes in Al-Mg-Si alloys, Acta Mater. 47 (1999) 1537–1548.
[4] A.K. Gupta, D.J. Lloyd, S.A. Court, Precipitation hardening in Al-Mg-Si alloys with and without excess Si, Mater. Sci. Eng. A 316 (2001) 11–17.
[5] G.A. Edwards, K. Stiller, G.L. Dunlop, M.J. Couper, The precipitation sequence in Al-Mg-Si alloys, Acta Mater. 46 (1998) 3893–3904.
[6] C.D. Marioara, S.J. Andersen, H.W. Zandbergen, R. Holmestad, The influence of alloy composition on precipitates of the Al-Mg-Si system, Metall. Mater. Trans. A 36 (2005) 691–702.
[7] W.F. Miao, D.E. Laughlin, Effects of Cu content and preageing on precipitation characteristics in aluminium alloy 6022, Metall. Mater. Trans. A 31 (2000) 361–371.
[8] M. Murayama, K. Hono, W.F. Miao, D.E. Laughlin, The effect of Cu additions on the precipitation kinetics in an Al-Mg-Si alloy with excess Si, Metall Mater. Trans. A 32 (2001) 239–246.
[9] Z. Jia, L. Ding, L. Cao, R. Sanders, S. Li, Q. Liu, The influence of composition on the clustering and precipitation behavior of Al-Mg-Si-Cu alloys, Metall. Mater. Trans. A 48 (2014) 459–473.
[10] M.W. Zandbergen, A. Cerezo, G.D.W. Smith, Study of precipitation in Al–Mg–Si alloys by atom probe tomography II. Influence of Cu additions, Acta Mater. 101 (2015) 149–158.
[11] A. Bobel, K. Kim, C. Wolverton, M. Walker, G.B. Olson, Equilibrium composition variation of Q-phase precipitates in aluminum alloys, Acta Mater. 138 (2017) 150–160.
[12] C.D. Marioara, S.J. Andersen, J. Røyset, O. Reiso, S. Gulbrandsen-Dahl, T.-E. Nicolaisen, I.-E. Opheim, J.F. Helgaker, R. Holmestad, Improving thermal stability in Cu-containing Al-Mg-Si alloys by precipitate optimization, Metall. Mater. Trans. A 45 (2014) 2938–2949.
[13] C. Cayron, L. Sagalowicz, O. Beffort, P.A. Buffat, Structural phase transition in Al-Cu-Mg-Si alloys by transmission electron microscopy study on an Al-4 wt% Cu-1 wt % Mg-Ag alloy reinforced by SiC particles, Philos. Mag. 79 (1999) 2833–2851.
[14] K. Matsuda, Y. Uetani, T. Sato, S. Ikeno, Metastable phases in an Al-Mg-Si alloy containing copper, Metall. Mater. Trans. A 32 (2001) 1293–1299.
[15] D.J. Chakrabarti, D.E. Laughlin, Phase relations and precipitation in Al–Mg–Si alloys with Cu additions, Prog. Mater. Sci. 49 (2004) 389–410.
[16] C.D. Marioara, S.J. Andersen, T.N. Stene, H. Hasting, J. Walmsley, A.T.J. van Helvoort, R. Holmestad, The effect of Cu on precipitation in Al-Mg-Si alloys, Philos. Mag. 87 (2007) 3385–3413.
[17] S.J. Andersen, C.D. Marioara, J. Friis, R. Bjørge, Q. Du, I.G. Ringdalen, S. Wenner, E.A. Mørtsell, R. Holmestad, T. Saito, J. Røyset, O. Reiso, Directionality and column arrangement principles of precipitates in Al-Mg-Si-(Cu) and Al-Mg-Cu linked to line defect in Al, Mater. Sci. Forum 877 (2017) 461–470.
[18] T. Saito, C.D. Marioara, S.J. Andersen, W. Lefebvre, R. Holmestad, Aberration-corrected HAADF-STEM investigations of precipitate structures in Al-Mg-Si alloys with low Cu additions, Philos. Mag. 94 (2014) 520–531.
[19] T. Saito, E.A. Mørtsell, S. Wenner, C.D. Marioara, S.J. Andersen, J. Friis, K. Matsuda, R. Holmestad, Atomic structures of precipitates in Al-Mg-Si alloys with small additions of other elements, Adv. Eng. Mater. 20 (2018) 1800125.
[20] S.J. Andersen, C.D. Marioara, J. Friis, S. Wenner, R. Holmestad, Precipitates in aluminium alloys, Adv. Phys. X 3 (2018) 790–813.
[21] W.J. Liang, P.A. Rometsch, L.F. Cao, N. Birbilis, General aspects related to the corrosion of 6xxx series aluminium alloys: exploring the influence of Mg/Si ratio and Cu, Corros. Sci. 76 (2013) 119–128.
[22] G. Svenningsen, M.H. Larsen, J.C. Walmsley, J.H. Nordlien, K. Nisancioglu, Effect of artificial aging on intergranular corrosion of extruded AlMgSi alloy with small Cu content, Corros. Sci. 48 (2006) 1528–1543.
[23] S.K. Kairy, P.A. Rometsch, K. Diao, J.F. Nie, C.H.J. Davies, N. Birbilis, Exploring the electrochemistry of 6xxx series aluminium alloys as a function of Si to Mg ratio, Cu content, ageing conditions and microstructure, Electrochim. Acta 190 (2016) 92–103.
[24] M.H. Larsen, J.C. Walmsley, O. Lunder, R.H. Mathiesen, K. Nisancioglu, Intergranular corrosion of copper-containing AA6xxx AlMgSi aluminum alloys, J. Electrochem. Soc. 155 (2008) 550–556.
[25] S.K. Kairy, T. Alam, P.A. Rometsch, C.H.J. Davies, R. Banerjee, N. Birbilis, Understanding the origins of intergranular corrosion in copper-containing Al-Mg-Si alloys, Metall. Mater. Trans. A 47 (2016) 985–989.
[26] C.D. Marioara, A. Lervik, J. Grønvold, O. Lunder, S. Wenner, T. Furu, R. Holmestad, The correlation between intergranular corrosion resistance and copper content in the precipitate microstructure in an AA6005a alloy, Metall Mater Trans A 49 (2018) 5146–5156.
[27] T. Saito, S. Muraishi, C.D. Marioara, S.J. Andersen, J. Røyset, R. Holmestad, The effects of low cu additions and predeformation on the precipitation in a 6060 Al-Mg-Si alloy, Metall. Mater. Trans. A 44 (2013) 4124–4135.
[28] J.A.S. Green, Aluminum Recycling and Processing for Energy Conservation and Sustainability, 91 ASM International, Materials Park, OH, 2007, pp. 109–134.
[29] J.K. Sunde, Ø. Paulsen, S. Wenner, R. Holmestad, Precipitate statistics in an Al-Mg-Si-Cu alloy from scanning precession electron diffraction data, J. Phys.: Conf. Ser. 902 (2017) 12022.
[30] J.K. Sunde, C.D. Marioara, A.T.J. van Helvoort, R. Holmestad, The evolution of precipitate crystal structures in an Al-Mg-Si(-Cu) alloy studied by a combined HAADF-STEM and SPED approach, Mater. Charact. 142 (2018) 458–469.
[31] P. Moeck, S. Rouvimov, E.F. Rauch, M. Véron, H. Kirmse, I. Häusler, W. Neumann, D. Bultreys, Y. Maniette, S. Nicolopoulos, High spatial resolution semi-automatic crystallite orientation and phase mapping of nanocrystals in transmission electron microscopes, Cryst. Res. Technol. 46 (2011) 589–606.
[32] J.S. Barnard, D.N. Johnstone, P.A. Midgley, High-resolution scanning precession electron diffraction: alignment and spatial resolution, Ultramicroscopy 174 (2017) 79–88.
[33] F. de la Peña, et al., HyperSpy - 1.5.2, (2019), https://doi.org/10.5281/zenodo.3396791.
[34] S.M. Sarge, G.W.H. Höhne, W.F. Hemminger, Calorimetry: Fundamentals, Instrumentation and Applications, Wiley-VCH Verlag GmbH & Co. KGaA, Weinheim, Germany, 2014.
[35] P.D. Nellist, S.J. Pennycook, The principles and interpretation of annular dark–field Z–contrast imaging, Adv. Imag. Electron Phys. 113 (2000) 148–203.
[36] C.D. Marioara, J. Nakamura, K. Matsuda, S.J. Andersen, R. Holmestad, T. Sato, T. Kawabata, S. Ikeno, HAADF-STEM study of β'-type precipitates in an over-aged Al-Mg-Si-Ag alloy, Philos. Mag. 92 (2012) 1149–1158.
[37] M. Torsæter, F.J.H. Ehlers, C.D. Marioara, S.J. Andersen, R. Holmestad, Applying precipitate–host lattice coherency for compositional determination of precipitates

in Al-Mg-Si-Cu alloys, Philos. Mag. (2012) 3833–3856.
[38] M. Torsæter, W. Lefebvre, C.D. Marioara, S.J. Andersen, J.C. Walmsley, R. Holmestad, Study of intergrown L and Q′ precipitates in Al-Mg-Si-Cu alloys, Scripta Mater. 64 (2011) 817–820.
[39] T. Saito, F.J.H. Ehlers, W. Lefebvre, D. Hernandez-Maldonado, R. Bjørge, C.D. Marioara, S.J. Andersen, E.A. Mørtsell, R. Holmestad, Cu atoms suppress misfit dislocations at the β″/Al interface in Al-Mg-Si alloys, Scr. Mater. 110 (2016) 6–9.
[40] Y. Weng, Z. Jia, L. Ding, K. Du, H. Duan, Q. Liu, X. Wu, Special segregation of Cu on the habit plane of lath-like β′ and QP2 precipitates in Al-Mg-Si-Cu alloys, Scripta Mater. 151 (2018) 33–37.
[41] K. Teichmann, C.D. Marioara, S.J. Andersen, K. Marthinsen, TEM study of β′ precipitate interaction mechanisms with dislocations and β′ interfaces with the aluminium matrix in Al-Mg-Si alloys, Mater. Charact. 75 (2013) 1–7.
[42] C.D. Marioara, J. Friis, E. Hersent, A. Oskarsson, A transmission electron microscopy study of precipitate phases that form during operation in a heat exchanger alloy, Mater. Charact. 149 (2019) 218–225.
[43] L. Ding, Z. Jia, J.F. Nie, Y. Weng, L. Cao, H. Chen, X. Wu, Q. Liu, The structural and compositional evolution of precipitates in Al-Mg-Si-Cu alloy, Acta Mater. 145 (2018) 437–450.
[44] T. Maeda, K. Kaneko, T. Namba, Y. Koshino, Y. Sato, R. Teranishi, Y. Aruga, Structural and compositional study of precipitates in under-aged Cu-added Al-Mg-Si alloy, Sci. Rep. 8 (2018) 16629.
[45] R. Vissers, M.A. van Huis, J. Jansen, H.W. Zandbergen, C.D. Marioara, S.J. Andersen, The crystal structure of the β′ phase in Al-Mg-Si alloys, Acta Mater. 55 (2007) 3815–3823.
[46] J.K. Sunde, S. Wenner, R. Holmestad, In situ heating TEM observations of evolving nanoscale Al-Mg-Si-Cu precipitates, J. Microsc. (2019), https://doi.org/10.1111/jmi.12845.
[47] L. Kovarik, S.A. Court, H.L. Fraser, M.J. Mills, GPB zones and composite GPB/GPBII zones in Al-Cu-Mg alloys, Acta Mater. 56 (2008) 4804–4815.
[48] S. Wenner, L. Jones, C.D. Marioara, R. Holmestad, Atomic-resolution chemical mapping of ordered precipitates in Al alloys using energy-dispersive X-ray spectroscopy, Micron 96 (2017) 103–111.
[49] K. Li, A. Béché, M. Song, G. Sha, X. Lu, K. Zhang, Y. Du, S.P. Ringer, D. Schryvers, Atomistic structure of Cu-containing β″ precipitates in an Al-Mg-Si-Cu alloy, Scr. Mater. 75 (2014) 86–89.

Paper VI

Jonas Kristoffer Sunde, Feng Lu, Calin Daniel Marioara
Bjørn Holmedal, Randi Holmestad

Linking mechanical properties to precipitate microstructure in three high strength Al-Mg-Si(-Cu) alloys

To be submitted.

Linking mechanical properties to precipitate microstructure in three high strength Al-Mg-Si(-Cu) alloys

Jonas K. Sunde[a,*], Feng Lu[b,*], Calin D. Marioara[c], Bjørn Holmedal[b], Randi Holmestad[a]

[a]*Department of Physics, Norwegian University of Science and Technology (NTNU), N-7491 Trondheim, Norway*
[b]*Department of Materials Science and Engineering, NTNU, N-7491 Trondheim, Norway*
[c]*Materials and Nanotechnology, SINTEF Industry, N-7465 Trondheim, Norway*

Abstract

The mechanical properties of age hardenable Al alloys depend strongly on the precipitate microstructure. This work presents an investigation into the connection between material strength and ductility to precipitate statistics in three high strength Al-Mg-Si(-Cu) alloys (Cu$\lesssim$0.1 at.%). A range of ageing conditions were examined in order to understand the effect of an evolving precipitate microstructure, and the results were used as input for strengthening models. The mechanical properties were obtained by tensile test experiments and microstructure characterisation was attained by transmission electron microscopy. The results showed that minor changes to the Si, Mg, and Cu additions – the total addition (at.%) kept approximately equal – had a significant impact on measured material properties with corresponding changes in the precipitate microstructure. On the peak strength plateaus, differences as large as 35 MPa in yield strength were measured between the strongest and weakest alloy, obtained as 410 MPa and 375 MPa, respectively. Higher material yield strength correlated well with a refined precipitate microstructure comprising higher number densities of smaller precipitates. Differences with respect to material ductility first appeared after moderate overageing, showing negative correlation with material strength. At significantly overaged conditions the differences in strength exceeded 100 MPa, demonstrating large differences with respect to the thermomechanical stability of these materials, which has important consequences for alloys exposed to elevated temperatures under in-service conditions. The highly comprehensive body of data presented should serve as a valuable reference in the development of strengthening models for the Al-Mg-Si-Cu system, and will hopefully spark further investigations on the topics covered.

Keywords: 6xxx Al alloys, Precipitation, Yield strength, Transmission electron microscopy, Strengthening models, Microstructure-property relationships

1. Introduction

Al-Mg-Si(-Cu) alloys are important age hardenable alloys for extruded products in marine, automotive, and building construction applications. They are widely used due to their low cost, ease of fabrication and machinability, and to a combination of attractive material properties, including high strength, low weight, nice surface finish, and good corrosion resistance. A few hours thermal ageing at elevated temperatures (170–230 °C) may double – or in some cases nearly triple – the strength of these alloys as compared to their as-quenched (T4) state. This is caused by the formation and growth of a high density of nanosized rod- and/or lath-shaped precipitate phases with long axes parallel to $\langle 100 \rangle_{\mathrm{Al}}$ that act as barriers to dislocation motion.

High strength Al-Mg-Si(-Cu) alloys are becoming increasingly utilised in applications such as the crash-system and the steering components of automotive vehicles [2]. It is therefore important to study and optimise the properties that impact the crashworthiness of such alloys. The yield strength, σ_{y}, is particularly important for resisting deformation, and the ability to work harden affects the energy absorption capacity. The material ductility (e.g. true fracture strain, ϵ_{f}) is also important as low values could cause cracking and failure. Additionally, for components that might see elevated temperatures under in-service conditions the thermomechanical stability is important, and the change of σ_{y} with prolonged ageing is highly relevant in this regard.

Depending on alloy composition and thermomechanical processing (TMP) various precipitate phases may form, and the different phases of the Al-Mg-Si- and the Cu-added system have been thoroughly characterised [3, 4, 5, 6]. Furthermore, the precipitate number density, N, length, l, and cross-section area, a, will vary. These parameters together determine the volume fraction of precipitates, $V_{\mathrm{f}} = N \cdot l \cdot a$. As the different precipitate phases have different crystal structures, compositions, interface coherence, and interfacial strain, they influence material properties differently. This poses a challenge in optimising alloy compositions and TMP routes for achieving pre-defined material properties, such as a given σ_{y} or ϵ_{f}. This is the reason why a lot of research on the aspects of TMP, materials testing, modelling, and characterisation of these alloys is produced ev-

*Corresponding author(s)
Email addresses: jonas.k.sunde@ntnu.no (Jonas K. Sunde), feng.lu@ntnu.no (Feng Lu)

Table 1. Compositions of the Al-Mg-Si(-Cu) alloys studied. The last column shows the estimated total concentrations of precipitate forming elements left in solid solution immediately after quenching.

Alloy	Al	Si	Mg	Cu	Fe	Mn	Cr	Si†+ Mg + Cu
S at./wt. %	bal.	0.85/0.88	0.80/0.72	0.01/0.03	0.12/0.24	0.25/0.51	0.08/0.16	1.52/1.44
C at./wt. %	bal.	0.85/0.88	0.71/0.64	0.04/0.09	0.10/0.20	0.22/0.45	0.07/0.14	1.46/1.42
M at./wt. %	bal.	0.62/0.64	0.86/0.77	0.10/0.23	0.13/0.23	0.13/0.26	0.01/0.02	1.46/1.48

† The incorporation of Si into dispersoids was taken into account using an estimate based on the thermal history of the material and the Alstruc microstructure solidification model [1].

ery year.

One of the fundamental interactions that determines the mechanical properties of age hardenable Al alloys is that occurring between precipitates and moving dislocations. Al has a fcc crystal lattice, causing dislocations to move in close packed $\langle 110 \rangle_{\mathrm{Al}}$ directions and on $\{111\}_{\mathrm{Al}}$ planes. There are two main types of precipitate-dislocation interactions: either the mobile dislocations pass through the precipitate (shearable), or they bypass the precipitate, e.g. via the Orowan looping process (non-shearable) [7, 8, 9]. Whether a particular precipitate is sheared or bypassed depends on several factors, where interface coherence and cross-section area on the $\{111\}_{\mathrm{Al}}$ slip planes are the most important.

Up to the peak hardened state, the most common precipitate phase existing in the microstructure of Al-Mg-Si alloys is the needle-shaped β'' phase [10]. In alloys that are Mg-rich (Mg/Si (at.%) > 1) and that contain a low addition of Cu (0.05–0.3 Cu at.%), β'' may coexist with the lath-shaped L phase precipitate [6, 2, 11]. *In situ* investigations performed on an Al-Mg-Si-Cu alloy containing both β'' and L phases suggest that both shearing and bypassing of precipitates occur at room temperature, and that increasing temperature facilitates cross-slip and bypassing [12, 13]. Which of the β'' or L precipitates are sheared/bypassed was not determined, but there exists strong evidence that β'' is shearable [14, 15, 16, 17]. In overaged conditions the precipitates are to a larger extent non-shearable [18], i.e. they remain undeformed while the matrix around them is deformed. Typical phases existing in overaged, low Cu containing Al-Mg-Si alloys are β', Q′ and L phase [6]. Several studies have made attempts to estimate the value of the critical dimension that determines the transition point between shearable and non-shearable precipitates for the various precipitate phases existing in this alloy system, e.g. [16, 18]. The critical dimension, r_{c}, where this transition occurs is important in order to model the strength in these alloys, as the obstacle strength, $F(r)$, is usually separated into a weak ($r \leq r_{\mathrm{c}}$) and strong ($r > r_{\mathrm{c}}$) regime.

Despite the complexity of the underlying strengthening mechanisms, many yield strength models developed for Al-Mg-Si-Cu alloys capture the general evolution of material strength with ageing to a reasonable extent. The crudest models assume a single precipitate type approximated as equivalent spherical volumes, whereas more advanced models also take into account the $\langle 100 \rangle_{\mathrm{Al}}$ oriented, rod-/lath-shaped nature of the precipitates and their size distribution [7, 8, 9, 19, 20, 21, 22, 23, 24, 25, 26].

In this work we have studied three high strength Al-Mg-Si(-Cu) alloys with nearly equal alloying additions (at.%). Mechanical properties (σ_{y}, ϵ_{f}) were inferred from tensile test experiments and microstructure characterisation was obtained by transmission electron microscopy (TEM), providing precipitate statistics (N, l, a, V_{f}) at a range of ageing conditions. Microstructure characterisation results were used as input for three recognized yield strength models [21, 23, 25] which were compared with experimental findings. The combination of materials testing, characterisation, and modelling work provided a comprehensive evaluation of microstructure-property relationships existing in these alloys.

2. Experimental details

2.1. Materials and heat treatments

Three Al-Mg-Si(-Cu) alloys labelled S, C, and M, were designed with similar alloying additions (at.%), and minor differences in the Si:Mg ratios and Cu content, see **Table 1**. The alloys were manufactured by Neuman Aluminium Raufoss and were delivered as extruded rods (Ø30 mm). 10 mm height cylinder specimens cut perpendicular to the extrusion direction were set to solution heat treatment (SHT) at 540 °C for 12 min in a salt bath, and then water-quenched to room temperature. The specimens were kept at room temperature for 10 min before they were set to artificial ageing (AA) at 180 °C in an oil bath. AA was conducted for a series of holding times from 20 min to 1 month total ageing, which spanned underaged (UA) – through peak aged – to significantly overaged (OA) material conditions. A schematic of the heat treatment procedure is shown in **Fig. 1**.

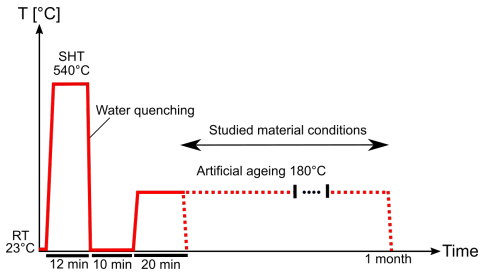

Fig. 1. Heat treatment procedure applied for studied Al-Mg-Si(-Cu) alloys.

2.2. Mechanical testing and conductivity measurements

The cylinder specimens were used for serial hardness and conductivity measurements after different ageing times. Vickers hardness (VH1) tests were carried out on a Leica VMHT MOT hardness tester. 10 indentation marks were inserted concentrically around the cylinder surface, a few mm from outer edge and center, and formed the basis for calculating an average value for each ageing condition. Conductivity was measured using a Foerster Sigmatester 2.069. Each value was determined as the average of 5 measurements on the specimen surface.

Tensile tests were conducted on Ø10 mm, 78 mm height cylinders with 18 mm gauge length and Ø6 mm inner diameter pulled parallel to the extrusion direction. The specimens were machined from the centre part of the extruded rods, and the dimensions are shown in **Fig. 2**. A universal tensile test machine and an optical measurement technique [27] were employed for tensile testing. The tests were conducted at room temperature using a load speed of 0.54 mm/min. 3 parallel specimens were tested to get the average value of tensile properties. The radius of the minimal cross-section area, a, the curvature radius of the necking region, R, and the corresponding load were measured using the optical measurement technique during experiments. These parameters were used as inputs for the Gromada necking correction approach [28], and the corrected stress-strain curve until fracture were then calculated for each condition. Material yield strength, σ_y, was obtained from the curves using the offset method. Assuming volume consistency, true strain can be estimated from the measurements of radius, a, therefore, the true fracture strain was obtained at the occurrence of fracture for each condition, $\epsilon_f = \ln(A_0/A_f) = 2\ln(a_0/a_f)$, where A denotes the cross-section area in the necking region (subscript 0 = initial, f = at fracture).

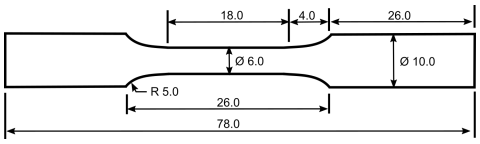

Fig. 2. Dimensions in mm for tensile test specimens.

2.3. Electron microscopy

Thin foils for TEM experiments were prepared by further cutting and grinding the cylinder specimens used for hardness/conductivity measurements down to disks with thicknesses of about 100 µm, and then punching them into several smaller Ø3 mm disks. Twin-jet polishing in a Struers Tenupol-5 was used to further thin the disks to electron transparency. The electrolytic solution comprised a 2:1 mixture of methanol:nitric acid, maintained at roughly −25 °C.

Precipitate statistics were obtained using a JEOL 2100 microscope operated at 200 kV and equipped with a Gatan Imaging Filter (GIF). The specimen thickness was measured by electron energy loss spectroscopy using the t/λ (log-ratio) methodology with an electron mean free path $\lambda \approx 130$ nm for 200 keV electrons in the $\langle 100 \rangle_{Al}$ zone axis of fcc Al. Existing methodologies in microstructure quantification of Al alloys by TEM give precipitate dimensions and distributions [29], including N, l, a, and V_f. The width of precipitate free zones (PFZs) perpendicular to grain boundaries (GBs) were determined from annular dark-field scanning TEM (ADF-STEM) images obtained on a JEOL 2100F microscope (200 kV).

3. Results

3.1. Hardness and electrical conductivity

The hardness and the electrical conductivity of the alloys as a function of ageing time are shown in **Fig. 3**. It is seen that alloys C and M both started out higher in hardness than alloy S, and after 10 min ageing these were at roughly 80 compared to 65 HV1, respectively. Subsequently, all alloys showed a similar rate of hardness increase, all reaching close to peak hardness after roughly 2 h ageing, with values ranging from 122 HV1 for alloy S to 128 HV1 for alloy M. The hardness then remained nearly constant, and all alloys exhibited a similar duration in the peak hardness plateau, from approximately 2 h to 12 h ageing. At 12 h ageing, alloys S and C exhibited comparable hardness values, 122 HV1, and the rate of hardness decrease with following overageing was similar in the two alloys. Only after 4 days of ageing had a significant hardness difference between alloys S and C again developed, and beyond this point alloy C stayed roughly 8 HV1 higher than for alloy S.

Alloy M differed strikingly from alloys S and C with overageing. At 12 h ageing alloy M measured 126 HV1, and with further ageing it maintained a substantially higher hardness than alloys S and C for all subsequent conditions, indicating a considerably improved thermomechanical stability. After roughly 5 days ageing the hardness difference relative to alloys S and C was at a maximum, and it stayed nearly constant with further ageing. At 5 days ageing and beyond the hardness difference was near 19 HV1 relative to alloy C, and about 23 HV1 to alloy S. After 1 month accumulated ageing, the hardness of alloys S and C measured 70 and 75 HV1, respectively, which was within 5 HV1 of their corresponding 10 min ageing measurements. Alloy M measured 94 HV1 at 1 month ageing, which was still significantly higher than the 10 min value at ≈80 HV1.

The conductivity of alloy M started out at 24.4 MS/m after 10 min ageing, higher than both alloys S and C at ≈23.5 MS/m. Following, the conductivity of alloys S and C increased at a higher rate than M. Near peak hardness (≈ 3 h) all alloys exhibited similar conductivity values, measuring roughly 26 MS/m. Beyond moderate overageing (> 24 h) the ordering high-to-low was reversed relative to the hardness at corresponding ageing times. The ordering high-to-low in terms of conductivity was here: alloy S, alloy C, and alloy M. Final values reached after 1 month ageing were 28.3, 28.0, and 27.7 MS/m for alloys S, C, and M, respectively.

The material conditions selected for TEM experiments were chosen based of the plots in **Fig. 3**, and are shown in **Table 2**. With the aim to understand the effect of an evolving microstructure on the overall strength and ductility of the material, a range

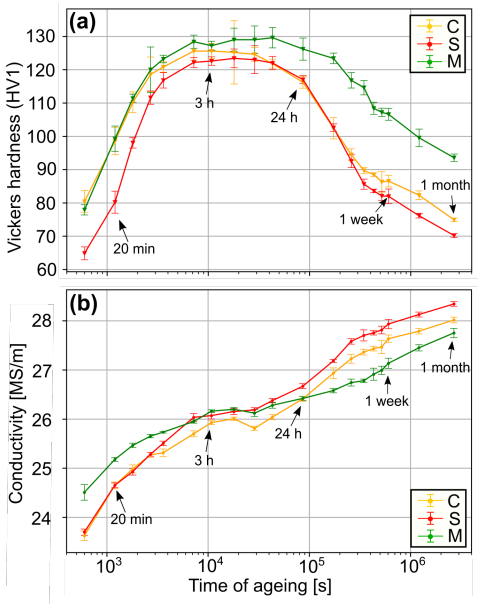

Fig. 3. (a) Vickers hardness (HV1) and (b) electrical conductivity as a function of ageing at 180 °C.

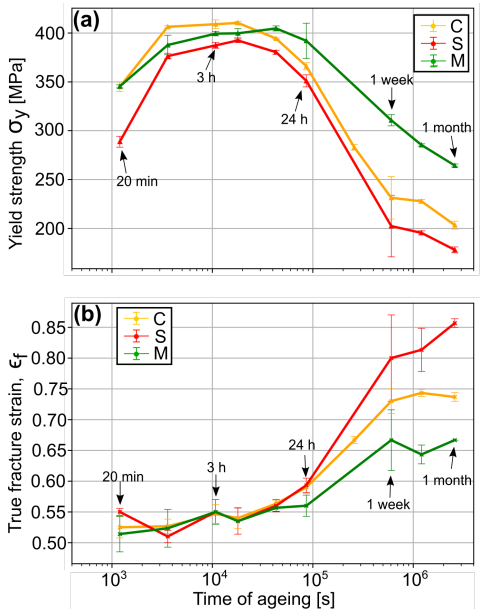

Fig. 4. Material tensile properties obtained from true stress-strain curves, showing (a) yield strength, σ_y, and (b) true fracture strain, ϵ_f, as a function of ageing time.

of conditions were selected, encompassing UA, peak hardened, and significantly OA material conditions.

Table 2. Ageing conditions selected for TEM experiments.

Alloy	Time of ageing at 180 °C
S	20 min, 3 h, 12 h, 24 h, 1 week, 2 weeks, 1 month
C	20 min, 3 h, 12 h, 24 h, 3 days, 1 week
M	20 min, 3 h, 24 h, 1 month

3.2. Tensile properties

Tensile test experiments were performed on several material conditions, including all conditions selected for TEM studies. The true stress-strain curves for all ageing conditions in each alloy are shown in the **Supplementary Information (SI)** in section **SI 1**, with following tables showing the parameters of the fitted 4-term Voce equation for each curve. The main results obtained from the true stress-strain curves are presented in **Fig. 4**, showing the material yield strength, σ_y, and the true fracture strain, ϵ_f.

The main trends of the σ_y-plot in **Fig. 4a** show good agreement with the Vickers hardness plot in **Fig. 3a**. One exception is due to alloy C, which in the σ_y-plot is no longer sandwiched in-between alloys S and M in value. At UA and peak aged conditions alloy C obtained highest σ_y-values, with a peak value of 410 MPa at 5 h ageing, compared to 392 MPa (5 h) and 406 MPa (12 h) for alloys S and M, respectively. In agreement with measured hardness, alloy M reigns supreme at OA conditions (>12 h). At significantly OA conditions (>1 week), alloy M stayed roughly 60 and 100 MPa higher in σ_y as compared to alloys C and S, respectively. Alloy C stays close to- but exhibits consistently higher σ_y than alloy S with overageing. σ_y at 20 min ageing is also notably higher than the value at significantly OA conditions (>1 week ageing) for all alloys. In the case of hardness, these outer extremes of UA vs OA values were in much closer agreement, with the exception of alloy M.

ϵ_f remained comparable for all alloys (51%-55%) up to the onset of overageing, i.e. 12 h. Beyond this point the differences became progressively larger, and the ordering high-to-low was alloy S, C, and M, respectively, reversed with respect to the σ_y-ordering at corresponding conditions. Final values reached after 1 month ageing were 86% for alloy S, 74% for alloy C, and 67% for alloy M.

3.3. Quantification of precipitate statistics by TEM

Bright-field TEM images of the precipitate microstructures in the three alloys after various ageing times are shown in **Fig. 5**. At 20 min ageing (**Fig. 5a-c**), a very dense microstructure of atomic clusters/GP-zones and small precipitates existed, with main growth dimension rarely exceeding 9 nm in length for all alloys. Near the peak hardened state at 3 h ageing (**Fig. 5d-f**) the microstructures comprised high densities of short β'' precipitates with characteristic strain contrast (dark lines) running parallel to the main growth direction. In alloy M, longer and narrow lath-shaped L phase precipitates were also present (highlighted). After 1 week ageing, the precipitates in alloys S and C had grown very large as compared to the 3 h condition (**Fig.**

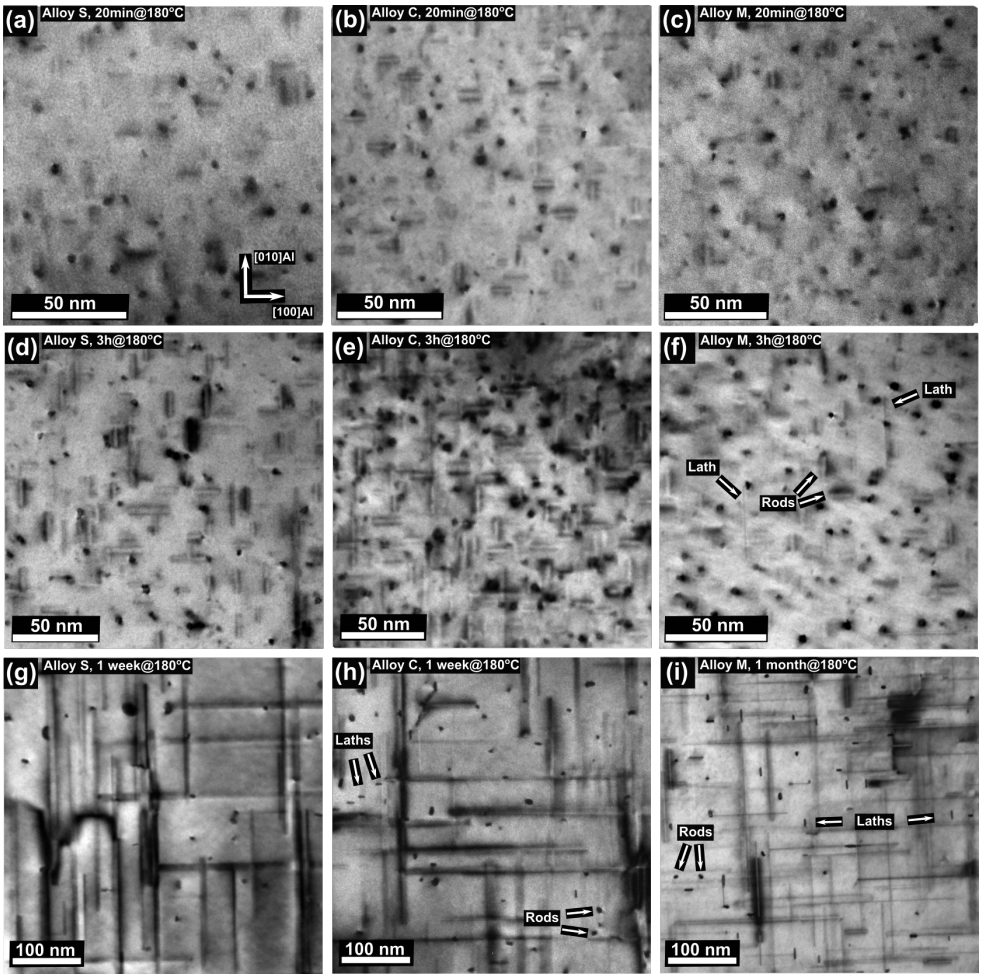

Fig. 5. (a-i) Bright-field TEM images of indicated alloys and ageing times. All images are acquired near the $[001]_{Al}$ zone axis.

5g,h). In addition, the precipitate density has been reduced significantly as expected for overaged conditions. The precipitates in alloy M demonstrated a high resistance towards coarsening, and at 1 month ageing (**Fig. 5i**) their average size was still smaller than the precipitates at the 1 week ageing condition in alloys S and C. The development in average precipitate cross-section areas and lengths are shown in **Fig. 6**. In the overaged conditions imaged it is also easy to classify the cross-sections as either lath-type or rod-type. Narrow, lath-shaped cross-sections extended along $[010]_{Al}$ and $[100]_{Al}$ directions are visible in both alloy C and M (highlighted). It is also clear that the presence of lath-type precipitates are more frequent in alloy M at this overaged condition. These precipitates are either L phase or C phase precipitates [30]. The rod-type precipitates present are β' phase and Q′ phase precipitates. It is important to note that also Q′ phase precipitates can exhibit a lath-type morphology, but its interface will run along $\langle 150 \rangle_{Al}$ directions, see e.g. [31]. Alloy S does not show any clear presence of lath-type precipitates. The distribution of precipitate phases in these alloys was quantified by a scanning diffraction approach in the related work by Sunde et al. [6].

The precipitate number density was calculated as $N = 3N_{\parallel}/(A(t + \bar{l}_m))$, where $N_{\parallel}$, is the number of precipitate cross-sections in the image, A is the field of view area, t is thickness in the centre of the image, and $\bar{l}_m$ is the average measured precipitate length. The factor 3 accounts for the 3 growth directions of the precipitates, hence assuming an uniform distribution. The volume fraction was subsequently calculated as $V_f = N \cdot l \cdot a$. N and V_f were calculated for all alloys for the conditions selected for TEM studies, and the results are shown in **Fig. 7**. All numerical values for the measured and calculated precipitate statistics are shown in **Table SI 4**, **Table SI 5**, and **Table**

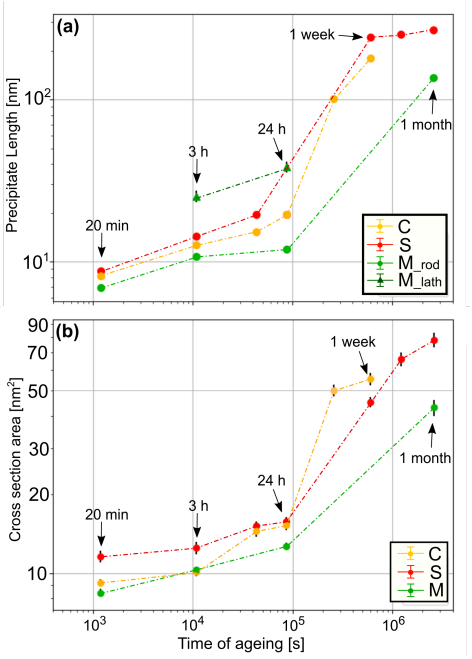

Fig. 6. (a) Average length and (b) cross-section area for precipitates in all ageing conditions studied in alloys S, C, and M.

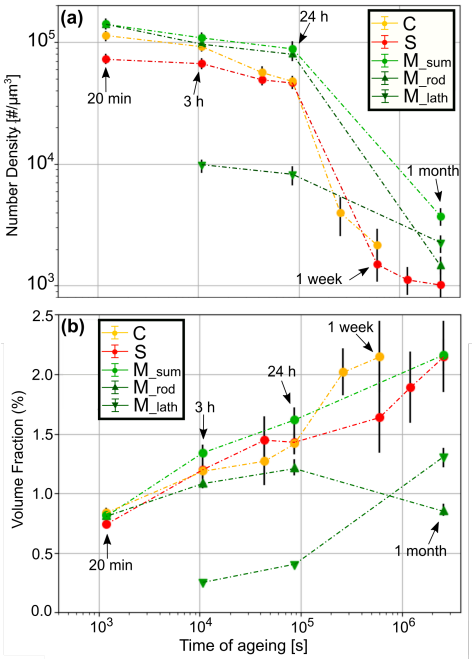

Fig. 7. (a) Precipitate number density and (b) precipitate volume fraction in each alloy and ageing condition.

SI 6 in **SI 2**, for alloys S, C, and M, respectively.

As seen from **Fig. 6** and **Fig. 7**, there are clear differences between the alloys despite their similar compositions. In terms of average precipitate parameters l and a (**Fig. 6a,b**), the rod-type precipitates of alloy M have consistently smaller dimensions as compared to the precipitates of alloys S and C, for all conditions studied. The lath-type precipitates were longer at 3 h and 24 h ageing, but these were in relatively low numbers at these ageing conditions, see **Fig. 7a**. Lath-type precipitates are also present at the 1 month condition in alloy M, but the coarsened precipitates lying in-plane were not clearly separable as rods and laths (see **Fig. 5i**) and were assumed to be approximately equal in size. Comparing the precipitates of alloy C to S, the length of the former stays smaller for all corresponding conditions. The cross-section areas of the precipitates in alloy C also stays smaller than for S up to 24 h ageing, but then becomes larger with significant overageing.

The precipitate number density (see **Fig. 7a**) is consistently higher for alloy M, followed by alloy C, and lastly S. The difference between alloy M as compared to both C and S becomes larger with prolonged ageing. It is seen that for alloy M the number density of rod-type precipitates drops off by more than an order of magnitude with ageing, whereas the lath-type precipitates stay at the same order of magnitude even after 1 month ageing. The thermal resistance of lath-type precipitate phases, i.e. C- and L-phase, has also been demonstrated previously [2, 32]. Comparing the number density for alloys C and S, it is seen that alloy C starts out significantly higher than alloy S, but that the difference decreases up to the point of moderate overageing (24 h). At the significantly OA state at 1 week ageing, alloy C is again higher in number density as compared to alloy S.

The volume fraction (see **Fig. 7b**) does not display as clear differences as were seen for the other precipitate statistical parameters due to the uncertainties in calculated values. The main source of uncertainty is due to the thickness estimation by EELS ($\Delta t/t \approx 10\%$). However, the lower number density of precipitates in alloy S seems to be compensated by the increased size of precipitate parameters (l and a), making the volume fraction comparable to alloys C and M. The volume fraction of alloy C is similar to that of alloy M for the same reason, but it seems that the volume fraction of alloy M is somewhat larger up to the point of moderate overageing (24 h). It is also seen that for alloy M the lath-type precipitates dominate over rod-type precipitates at the significantly overaged condition (1 month).

The PFZ width perpendicular to GBs were also measured in each condition studied, see **Fig. 8**. The PFZ widths are nearly equal for alloys S and C, but differs notably for alloy M, being lower than all corresponding conditions in alloys S and C. After 1 month ageing there is a large difference between the PFZ width in alloy S at 267 ± 18 nm to that of alloy M at 172 ± 8 nm.

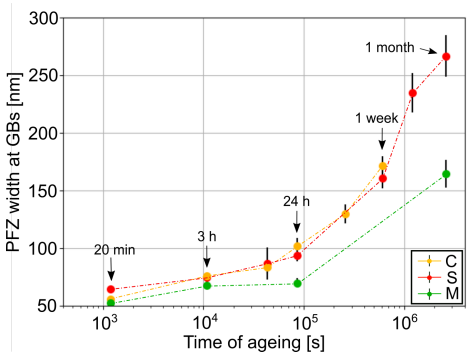

Fig. 8. Average measured PFZ width perpendicular to GBs in each alloy and ageing condition.

4. Discussion

4.1. Microstructure-property relationships

With few exceptions, it is generally observed that alloy M exhibited the highest strength and hardness with ageing, followed by alloy C, and lastly alloy S, see **Fig. 3a** and **Fig. 4a**. It is also generally observed from the microstructure results in **Fig. 6** and **Fig. 7** that alloy M showed the most refined precipitate microstructure, with smaller precipitate parameters, l and a, and higher precipitate number densities, N. Alloy C places second and alloy S is last. Although the precipitates in alloy C at 1 week ageing had a larger cross-section area than those of alloy S, the average precipitate volume, $\bar{V}_\mathrm{p} = \bar{l} \cdot \bar{a}$, was smaller for alloy C, which also had a somewhat higher number density. The precipitate statistics of alloys S and C were closest in value between the 24 h and the 1 week ageing conditions, which were also the conditions where the measured hardness and strength were the most similar, see **Fig. 3a** and **Fig. 4a**.

At a fixed volume fraction, with precipitates of similar types and morphology, a denser distribution of smaller precipitates is generally stronger than a sparse distribution of coarse precipitates, due to the statistically increased number of dislocation pinning points in each slip plane. The observed refinement in precipitate microstructure thus supports alloy M having the highest strength, followed by alloy C, and lastly alloy S.

An exception not immediately explained by this reasoning is the slightly increased strength of alloy C as compared to alloy M between 1 h and 5 h ageing. The calculated number densities at 3 h ageing were similar, at $(93 \pm 9) \cdot 10^3$ compared to $(109 \pm 12) \cdot 10^3$ for alloys C and M, respectively, and within the uncertainty of the measurement errors. Furthermore, the hardness seen in **Fig. 3a** showed that alloy M was harder than alloy C at all corresponding ageing conditions. The precipitate cross-section areas were comparable at UA and 3 h ageing, which implies that the obstacle strengths should be similar. However, as previously noted, alloy M also has a significant presence of lath-type precipitates, most notably L phase, which has a different aspect ratio and crystal structure than the β'' precipitate phase, and will therefore differ in dislocation obstacle strength. From microstructure observations, it is therefore less evident how to explain the relative strength difference between alloys C and M at these conditions. As noted, it could be due to the uncertainties in measured precipitate statistics, or it could potentially indicate that L phase precipitates are weaker dislocation obstacles than β'' phase precipitates at smaller precipitate volumes.

With subsequent overageing, the number density of alloy M at 24 h and 1 month ageing was significantly higher than that of corresponding OA conditions in alloys S and C, see **Fig. 7**. For alloy M the precipitate parameters l and a did also not grow as fast as that of alloys S and C, see **Fig. 6**. This supports the measurement of a significantly higher material strength at these conditions. The conductivity plots seen in **Fig. 3b** also indicates that there occurred a slower coarsening of precipitates in alloy M beyond 24 h ageing relative to alloys S and C, as a lower conductivity normally correlates with a higher solute solution content in the matrix, and hence a reduced uptake of solutes in precipitates. It is also supported by the observation of a significantly reduced PFZ width at GBs in alloy M as compared to alloys S and C, see **Fig. 8**, which again indicates that more solute remained in solute solution for alloy M as compared to alloys S and C with overageing.

The true fracture strain of the alloys, see **Fig. 4b**, showed no significant differences between the alloys up to the point of moderate overageing, at about 24 h. After this point, there is a reversal of ordering high-to-low with respect to material strength, in general agreement with experimental findings. This also supports literature findings which suggest that material ductility is mainly determined by the presence of larger, coarse particles in the alloys. For instance, it has been shown that coarse particles and precipitates on GBs are the most important sites for nucleation and growth of intergranular ductile fracture [33]. Alloy M has about half the Mn-content and a much lower Cr-content than alloys S and C, see **Table 1**, and therefore formed significantly fewer dispersoids. Based on the observed true fracture strain the distribution of dispersoids is therefore not crucial in terms of explaining material ductility, but rather the precipitate distribution at OA conditions. Some studies also point to the PFZ width as important for explaining ductility, as PFZs may act to localise strain and accelerate void nucleation and growth at GB particles [34, 35]. The microstructure observations support that alloy M should exhibit the lowest ductility at overaged conditions, as this alloy has the smallest PFZ at GBs (see **Fig. 8**) and the highest density of coarse precipitates (see **Fig. 7**). At the 1 week ageing condition alloys C and S had similar PFZ widths but it was measured a higher number density of precipitates in alloy C than for S (see **Fig. 7**). Alloys C and S also have similar levels of dispersoids due to their similar Mn-content and overall composition (see **Table 1**). Therefore, the increased material strength for alloy C as compared to alloy S, which follows from an increased number density of precipitates in alloy C, is the main underlying explanation for the observation of a lower ductility in alloy C in comparison to alloy S at overaged conditions.

It is generally seen that a refinement of the precipitate distribution – with smaller precipitate parameters l and a and an increased density N of precipitates – correlates well with a higher

material hardness and yield strength. The substantially retained strength of alloy M as compared to alloys S and C at OA conditions is seen as a consequence of the increased resistance towards coarsening and dissolution exhibited by the precipitates in this alloy. The formation of L phase precipitates is particularly important for explaining the observed differences [6], due to the improved thermal resistance of this phase compared to the β'' phase [2, 32].

4.2. Strength modelling

The study presented here is a suitable test case for modelling work as it provides material testing results and a quantification of the alloy microstructure at a range of ageing conditions from UA to signficiantly OA conditions. There exists many strengthening models for the 6xxx series Al alloy system which attempt to link microstructure parameters such as grain size, texture, precipitate size distribution, etc., to the macroscopic yield strength, σ_y. A number of different strengthening mechanisms are operative at room temperature, the most important of which is that due to the precipitates, σ_p. In addition, one must add the contribution from solute solution strengthening, σ_{ss}, as well as the intrinsic strength of pure Al, σ_i. If the latter is experimentally measured on a material of comparable grain size to that of the alloy under consideration, this also accounts for grain size strengthening effects. The contributions are typically added linearly [21, 22]:

$$\sigma_y = \sigma_p + \sigma_{ss} + \sigma_i. \tag{1}$$

In estimating the solid solution strengthening, the contribution from each element is typically also added linearly, given as [7, 36]

$$\sigma_{ss} = \sum_i k_i C_i^{\frac{2}{3}}, \tag{2}$$

where k_i is the scaling factor and C_i is the mass fraction of a specific element in solid solution (wt.%).

The strengthening contribution from the distribution precipitate needles and/or laths growing along $\langle 100 \rangle_{Al}$ directions is more challenging to estimate. In the following, we have applied three selected models, see **Table 3**, for predicting the contribution σ_p. The NaMo, Esmaeili, and Holmedal models [21, 23, 25] have shown good agreement with selected experimental findings, and are recognized in the scientific literature. The models have here been modified as compared to their originally presented forms, with the intent to put them into a common framework, which is described in the work of Holmedal [25]. In the paper by Holmedal, the precipitate contribution to the stress is calculated using Kocks statistics [8, 9], which are based on numerical line-tension simulations of a dislocation gliding through an array of obstacles. Using recent line-tension simulations by Vaucorbeil et al. [37, 38], Holmedal estimated the tensile stress using the following equation:

$$\sigma_p = M\tau = 0.9M(2\beta)\mu b\sqrt{n}\bar{f}^{\frac{3}{2}}\left(1 - \frac{1}{6}\bar{f}^5\right). \tag{3}$$

Here, M is the Taylor factor, τ is the critical resolved shear stress, μ is the shear modulus of the Al matrix, b is the Burgers vector, and n is the density of obstacles per area slip plane. $\bar{f} = \bar{F}/2\beta\mu b^2 = \cos(\phi_c/2)$ is the non-dimensional mean obstacle strength, where $\bar{F}$ is the mean obstacle strength, $\beta\mu b^2$ is the line tension of the dislocations, $\beta \approx 1/2$ is a constant, and ϕ_c is the obstacle breaking angle of the dislocation. Note that **Eq. 3** is applied here for all models, replacing the Friedel statistics, $\sigma_p = M\mu b\sqrt{n}\bar{f}^{\frac{3}{2}}$, on which the original models by Deschamps [20], Myhr et al. [21], and by Esmaeili et al. [23] were based. Note also that the two special cases of weak and strong obstacles distinguished in the Esmaeili model are here merged, using instead the approach by Holmedal. This makes this model more general, while its predictions remain essentially the same for the two special cases.

The way to derive the non-dimensional mean obstacle strength, $\bar{f}$, is sligtly different for the considered models. The Esmaeili model can be regarded as a simplified version of the Holmedal model, where $\bar{f}$ is estimated simply as a function of the mean cross-sectional area of the precipitates. In the more complex approach by Holmedal, the statistical distribution of different number of pinning points per particle depending on its length, and with pinning points of strength that depends on its cross sectional area, are accounted for. This requires numerical integration of

$$\bar{f} = \frac{1}{N\bar{l}}\int f\phi_l l dl, \tag{4}$$

for a strength, $f(a)$, and size distribution, ϕ_l, of precipitates with length l and cross sectional area $a = l^2/\Omega^2$. Note that the size distribution here is not normalized, i.e. $\int \phi_l dl = N$. It is assumed that the aspect ratio Ω is a function of l, i.e. a strong correlation between the length and cross-section area distributions. For a sufficiently narrow size distribution the Esmaeili and Holmedal models become equal.

Table 3. Strengthening models for estimating σ_p. For a detailed description of the models the cited works should be consulted.

Key equations	References
$n = \frac{3V_f}{2\pi\bar{r}_{eq}^2}$, $f\left(r_{eq}\right) = \min\left(\frac{r_{eq}}{\bar{r}_{\mathrm{eq,3h}}}, 1\right)$	[20, 21, 22] (NaMo)
$n = \frac{V_f}{2\pi\bar{r}^2}$, $\bar{f}\left(\bar{r}\right) = \min\left(\frac{\bar{r}}{\bar{r}_{3h}}, 1\right)$	[23, 19] (Esmaeili model)
$n = \frac{\sqrt{3}}{3}N\bar{l}$, $f\left(a\right) = \min\left(\frac{a}{\bar{a}_{3h}}, 1\right)$	[25, 27] (Holmedal model)

The models by Deschamps et al. [20], and later the NaMo model [21], consider volume-equivalent spherical precipitates, for which $4\pi r_{eq}^3/3 = al$. For each precipitate, the obstacle strength is assumed to depend on its volume, i.e. a function $f(r_{eq})$, and the non-dimensional mean obstacle strength is integrated numerically from the precipitate size distribution as

$$\bar{f} = \frac{1}{N} \int f \phi_{r_{eq}} \mathrm{d}r. \quad (5)$$

This integral does not account for that larger particles pierce more glide planes and therefore contribute with more pinning points than for smaller particles. An alternative expression for shearable spherical particles, similar to **Eq. 4**, may be found in [25]. However, since the particles considered in this work are not spherical anyway, this difference must be expected to be of second order. For the obstacle strengths, expressions similar as reported for the respective models were used, see **Table 3**.

TEM measurements gave distributions of precipitate lengths, l, and cross-section areas, a, at each studied ageing condition, with average values shown in **Fig. 6**. The distribution of precipitate lengths, ϕ_l , were found to be best fitted using a log-normal function

$$\phi_\mathrm{l} = \frac{N}{l\sqrt{2\pi \ln(1 + s/\bar{l}^2)}} \exp\left(-\frac{\ln\left(l\sqrt{1 + s/\bar{l}^2}/\bar{l}\right)^2}{2\ln(1 + s/\bar{l}^2)} \right), \quad (6)$$

where s is the variance of the distribution. Generally, two precipitates of equal length may have different cross-section areas. The two are however correlated, and the aspect ratio $\Omega = l/\sqrt{a}$ may for simplicity be assumed to change as some function $\Omega(l)$ of the needle length, i.e. a direct correlation between the statistical distributions of needle lengths and cross-section areas. Using the average precipitate cross-section area, $\bar{a}$, and the average precipitate length, $\bar{l}$, measured at each ageing condition, the average precipitate aspect ratio was calculated as $\bar{\Omega} = \bar{l}/\sqrt{\bar{a}}$, and a function $\Omega(l)$ was fitted to the calculated values, see **SI 3**. The obtained function $\Omega(l)$ enabled conversion from measured distributions of precipitate lengths to cross-section areas and corresponding precipitate radii. In order to apply the NaMo model, where the precipitates are assumed to be spherical, the radii were calculated by equating $V_\mathrm{sphere} = \left(\frac{l}{\Omega(l)}\right)^2 \cdot l$, thereby converting to a distribution of volume equivalent spherical precipitates. A minor correction also had to be made to account for rod-shaped precipitates with a circular cross-section in the Esmaeili model, compared to square cross-sections in the Holmedal model.

Important for the application of all strengthening models is the critical dimension defining the transition point between shearable and non-shearable precipitates. This transition point was selected as the relevant dimension (cross-section area, length, or radius) calculated from the average precipitate parameters at 3 h ageing, i.e. near peak strength.

The macroscopic yield strength for each alloy was calculated using **Eq. 1**. The intrinsic strength of pure Al, σ_i, was obtained experimentally, using the methodology and parameters described in the experimental section. The solute solution strengthening, σ_ss, was calculated using **Eq. 2**, where C_i for Mg, Si, and Cu was approximated from measured precipitate volume fractions, precipitate phase fractions as obtained by scanning precession electron diffraction (SPED) experiments, and known precipitate phase chemical compositions, see **SI 4**. This methodology is elaborated in the related works by Sunde et al. [39, 6]. Finally, the precipitate strengthening contribution, σ_p, was calculated by applying the three selected models. The parameter values used in the calculations are shown in **Table 4**.

Table 4. Values used for model parameters.

Parameter	Numerical value
σ_i	35 MPa ⋆
k_Si, k_Mg, and k_Cu	66.3, 29.0, and 46.4 MPa/wt.% †
M	3.05 ‡
$\mathrm{r_c^{NaMo}}$, $\mathrm{r_c^{Esmaeili}}$, $\mathrm{a_c^{Holmedal}}$	$\bar{r}_\mathrm{3h}^\mathrm{NaMo}$, $\bar{r}_\mathrm{3h}^\mathrm{Esmaeili}$, $\bar{a}_\mathrm{3h}^\mathrm{Holmedal}$
μ	19.8 GPa
β	0.47 [21]

⋆ Obtained from tensile tests on pure aluminium.
† Taken from [21].
‡ Calculated from the measured extruded texture using the ALAMEL crystal plasticity model [40].

Figure 9, **Figure 10**, and **Figure 11** show the comparison between the three applied models and the experimentally measured macroscopic yield strength for alloys S, C, and M, respectively, as a function of ageing. It is generally observed that the models capture the overall trend of the experimental results to a reasonable extent. The Holmedal model particularly obtains an excellent agreement for most conditions in all alloys. The Esmaeili model also shows a generally good agreement with experimental results. For alloys S and C it generally underestimates the strength up to the point of moderate overageing (24 h). For alloy M it overestimates the strength quite significantly at 3 h, where it predicts this to be the highest among all alloys and ageing conditions. The NaMo model obtains the best overall fit with the UA condition at 20 min ageing, and then generally predicts a similar strength as the Esmaeili model up to the point of moderate overageing (24 h). Subsequently, at significantly OA conditions (> 24 h ageing), the NaMo model underestimates the strength by > 40 MPa for all conditions.

The underestimation of the strength at OA conditions by the NaMo model is most likely a consequence of the underlying simplification of using a spherical precipitate geometry. The geometry of a precipitate is important as it affects how many $\{111\}_\mathrm{Al}$ slip planes a precipitate of a given volume V_p intersects. A spherical precipitate of radius r will act as a dislocation obstacle for a slip plane located within a distance $\pm r$ from the precipitate centre. A needle-shaped precipitate will act as a dislocation obstacle in any $\{111\}_\mathrm{Al}$ slip plane located within a distance $\pm l\cos\theta = \pm l/\sqrt{3}$ from the precipitate centre, where $\theta = 54.74°$ is the angle between the glide-plane normal and the needle direction. As seen from **Fig. 6**, the precipitates grow to reach lengths that are several 10s of times longer than their diameter/thickness, which implies that the strengthening effect per precipitate is greater for needle-shaped precipitates as compared to equivalent volume spherical precipitates. In the models applied, this has consequences for the calculation of n, i.e. the

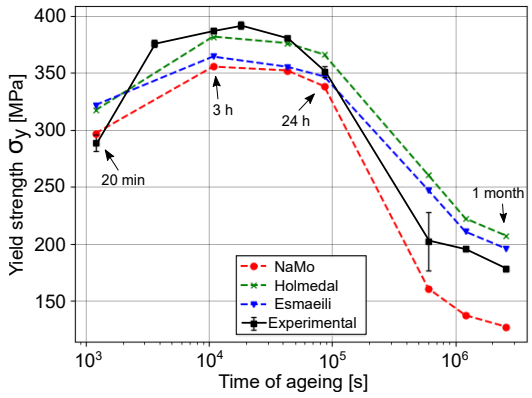

Fig. 9. Experimental results and model predictions of yield stress as a function of ageing for alloy S.

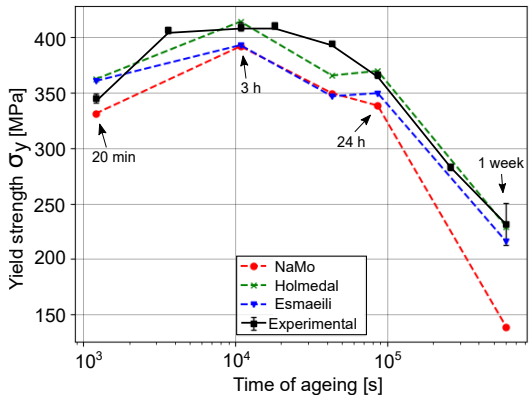

Fig. 10. Experimental results and model predictions of yield stress as a function of ageing for alloy C.

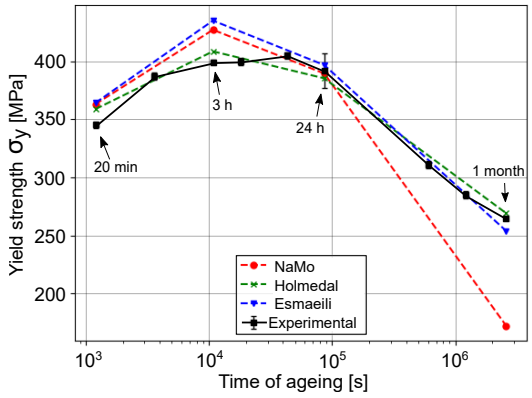

Fig. 11. Experimental results and model predictions of yield stress as a function of ageing for alloy M.

density of obstacles per area slip plane.

The relative differences between the models and experimental results in the range 20 min $\leq t \leq$ 24 h show the same trend for alloys S and C shown in **Figure 9** and **Figure 10**, and differ somewhat for alloy M, see **Figure 11**. The similarities in the predictions for alloys S and C were expected as the compositions of these alloys are very similar, and with both alloys showing a similar overall precipitation behaviour [6]. For alloy M, all models overestimate the strength at 3 h ageing, and the NaMo and Esmaeili model predicts this as the highest among all alloys and ageing times, which is supported by the measurement of the highest number density of precipitates. Part of the reason for this overestimation must lie in the coexistence of two precipitate classes, namely β'' and L phase precipitates. The L phase precipitates are generally observed to be longer than β'' precipitates at moderately aged conditions, see **Fig. 5f** and **Fig. 6a**, and hence have higher aspect ratios, Ω. The length distribution fitting assumes a single precipitate type, ϕ_l, and the cross-section area a for a precipitate of a measured length l is approximated using the fitted aspect ratio $\Omega(l)$. As the majority of precipitates present are β'', this will overestimate the cross-section area of L phase precipitates due to their increased length as compared to β'' precipitates. This in turn will overestimate the strength contribution of L phase precipitates. The different crystal structures of these precipitate phases also implies that they will have different critical cross-section areas or radii defining the shearable/non-shearable transition point, which is here assumed to be equal, and set to the average values measured at 3 h ageing.

The application of the Esmaeili model does not entail a numerical integration of the precipitate size distribution, but instead uses calculated average precipitate parameter values. The observation that this model also significantly overestimates the strength of alloy M at 3 h ageing requires another explanation besides the overestimated cross-sections areas of L phase precipitates. It further suggests that a significant fraction of the precipitates at this condition still should be considered weak, and therefore that the critical radius, $r_c > r_{3h}$. This implies that the L phase precipitates are weaker dislocation obstacles than the β'' precipitates at moderately aged conditions ($t < t_{peak}$). This is also a reasonable conclusion to make from the observation of a higher number density of precipitates in alloy M than for alloy C at 3 h ageing, but the measurement of a higher strength for alloy C. It was measured a number density of roughly 10000 and 100000 ($\#/\mu m^3$) lath- and rod-type precipitates in alloy M at 3 h ageing, respectively, compared to 93000 rod-type precipitates in alloy C ($\Delta N/N \approx 10\%$). The length of the rod-type precipitates in alloy C at 3 h ageing was somewhat longer than for alloy M, at 12.6 nm compared to 10.7 nm, respectively, with nearly equal cross-section areas. It should also be noted that alloy C has a significantly higher number density of dispersoids than alloy M at all ageing conditions, due to its increased content of dispersoid forming elements, most notably Mn, see **Table 1**. Although not quantified, this comprises an added strengthening contribution which is larger for alloys C and S as compared to alloy M. The similarities in obtained numbers, also accounting for measurements errors, make it difficult

to draw any strong conclusions. However, the change from a general underestimation (alloys S and C) to an overestimation (alloy M) of the strength at 3 h ageing suggests that the L phase precipitates does not provide as high strengthening potential per precipitate as for β'' precipitates at this condition, and therefore the critical dimension $r_c > r_{3h}$ for L phase precipitates. Simulations of interactions between moving dislocations and β'' and L phase at the atomic level would provide more insight into this observation.

5. Conclusions

A combination of hardness-, conductivity- and tensile testing, TEM precipitate microstructure quantification, and strength modelling have been applied to better understand material-property relationships in three high strength Al-Mg-Si(-Cu) alloys of similar compositions at a range of ageing conditions.

It was found that relatively small changes in alloy compositions caused significant differences in the precipitate microstructures, with corresponding significant differences in the measured material properties, including macroscopic yield strength and true fracture strain. The Mg-rich and highest Cu content alloy M showed a refined microstructure with higher number densities of smaller precipitates at all ageing conditions, as compared to the more Si-rich alloys S and C. Furthermore, alloy M also formed lath-shaped L phase precipitates of high aspect ratio exhibiting large resistance towards coarsening. Comparing alloys S and C, the higher Cu content of alloy C caused an increased refinement of the precipitate microstructure. An increased refinement in precipitate parameters generally correlated well with an increased material yield strength, and the peak strengths obtained were 392, 410, and 406 MPa for alloys S, C, and M, respectively. Three strengthening models were applied using the calculated precipitate microstructure parameters, and the results showed a generally good agreement with experimental results, with some interesting exceptions.

Material ductility, assessed from measured true fracture strain, remained comparable for all alloys up to moderate overageing, where a higher material strength corresponded with a lower material ductility. The difference became progressively larger with further overageing.

It is the authors' intent that the large body of data presented in this study should encourage further studies and developments, particularly on the aspect of modelling work for the Al-Mg-Si-Cu system.

Acknowledgements

All authors acknowledge support from the AMPERE project (NFR 247783), a knowledge building project for industry, co-financed by The Research Council of Norway (NFR), and the industrial partners Hydro, Gränges, Neuman Aluminium Raufoss (Raufoss Technology), and Nexans. The (S)TEM work was carried out on the NORTEM infrastructure (NFR 197405) at the TEM Gemini Centre, Trondheim, Norway.

Data availability

The **Supplementary Information** following this publication presents tensile test data, parameters of Voce equation fitted flow stress-strain curves until fracture, numerical values for TEM precipitate statistics, calculated solute solution levels at each ageing condition, and fitting of precipitate length distribution data.

References

[1] A. L. Dons, E. K. Jensen, Y. Langsrud, E. Tromborg, and S. Brusethaug. The Alstruc microstructure solidification model for industrial aluminum alloys. *Metallurgical and Materials Transaction A*, 30(8):2135–2146, 1999.

[2] C. D. Marioara, S. J. Andersen, J. Røyset, O. Reiso, S. Gulbrandsen-Dahl, T.-E. Nicolaisen, I.-E. Opheim, J. F. Helgaker, and R. Holmestad. Improving thermal stability in Cu-containing Al–Mg–Si alloys by precipitate optimization. *Metallurgical and Materials Transactions A*, 45:2938–2949, 2014.

[3] G. A. Edwards, K. Stiller, G. L. Dunlop, and M. J. Couper. The precipitation sequence in Al-Mg-Si alloys. *Acta Materialia*, 46(11):3893–3904, 1998.

[4] C. Cayron, L. Sagalowicz, L. Sagalowicz, and P. A. Buffat. Structural phase transition in Al-Cu-Mg-Si alloys by transmission electron microscopy study on an Al-4 wt% Cu-1 wt% Mg-Ag alloy reinforced by SiC particles. *Philosophical Magazine A*, 79(11):2833–2851, 1999.

[5] C. D. Marioara, S. J. Andersen, T. N. Stene, H. Hasting, J. Walmsley, A. T. J. Van Helvoort, and R. Holmestad. The effect of Cu on precipitation in Al-Mg-Si alloys. *Philosophical Magazine*, 87(23):3385–3413, 2007.

[6] J. K. Sunde, C. D. Marioara, and R. Holmestad. The effect of low Cu additions on precipitate crystal structures in overaged Al-Mg-Si(-Cu) alloys. *Materials Characterization*, page 110087, 2019.

[7] J. Friedel. *Dislocations*, volume 1. Pergamon Press, Oxford, UK, 1964.

[8] U. F. Kocks. A statistical theory of flow stress and work-hardening. *Philosophical Magazine*, 13:541–566, 1966.

[9] A. S. Argon U. F. Kocks and M. F. Ashby. Thermodynamics and kinetics of slip. *Progress in Materials Science*, 19:1–281, 1975.

[10] J. Jansen C. Trætholt U. Tundal S. J. Andersen, H. W. Zandbergen and O. Reiso. The crystal structure of the β'' phase in Al–Mg–Si alloys. *Acta Materialia*, 46(9):3283–3298, 1998.

[11] J. Ribis A. Lopez K. Buchanan, K. Colas and J. Garnier. Analysis of the metastable precipitates in peak-hardness aged Al-Mg-Si(-Cu) alloys with differing Si contents. *Acta Materialia*, 132:209–221, 2017.

[12] M. Vivas, P. Lours, C. Levaillant, A. Couret, M.-J. Casanove, and A. Coujou. Determination of precipitate strength in aluminium alloy 6056-T6 from transmission electron microscopy in situ straining data. *Philosophical Magazine A*, 76(5):921–931, 1997.

[13] F. Delmas, M. Vivas, P. Lours, M.-J. Casanove, A. Couret, and A. Coujou. Straining mechanisms in aluminium alloy 6056. in-situ investigation by transmission electron microscopy. *Materials Science and Engineering A*, 340(1):286 – 291, 2003.

[14] Ø. Ryen, B. Holmedal, K. Marthinsen, and T. Furu. Precipitation, strength and work hardening of age hardened aluminium alloys. *IOP Conference Series: Materials Science and Engineering*, 89:012013, 2015.

[15] K. Misumi, K. Kaneko, T. Nishiyama, T. Maeda, K. Yamada, K. Ikeda, M. Kikuchi, K. Takata, M. Saga, and K. Ushioda. Three-dimensional characterization of interaction between β'' precipitate and dislocation in AlMgSi alloy. *Journal of Alloys and Compounds*, 600:29 – 33, 2014.

[16] W. J. Poole, X. Wang, D. J. Lloyd, and J. D. Embury. The shearablenon-shearable transition in AlMgSiCu precipitation hardening alloys: implications on the distribution of slip, work hardening and fracture. *Philosophical Magazine*, 85(26-27):3113–3135, 2005.

[17] E. Christiansen, C. D. Marioara, B. Holmedal, O. S. Hopperstad, and R. Holmestad. Nano-scale characterisation of sheared β'' precipitates in a deformed aluminium alloy. *Scientific Reports*, 9(1):17446, 2019.

[18] K. Teichmann, C. D. Marioara, S. J. Andersen, and K. Marthinsen. TEM study of β' precipitate interaction mechanisms with dislocations and β'

interfaces with the aluminium matrix in AlMgSi alloys. *Materials Characterization*, 75:1–7, 2013.

[19] B. C. Muddle J. F. Nie and I. J. Polmear. The effect of precipitate shape and orientation on dispersion strengthening in high strength aluminium alloys. *Materials Science Forum*, 530:217–222, 1996.

[20] A. Deschamps and Y. Brechet. Influence of predeformation and ageing of an Al–Zn–Mg alloy–II. Modeling of precipitation kinetics and yield stress. *Acta Materialia*, 47(1):293 – 305, 1998.

[21] O. R. Myhr, Ø. Grong, and S.J. Andersen. Modelling of the age hardening behaviour of Al–Mg–Si alloys. *Acta Materialia*, 49(1):65–75, 2001.

[22] O. R. Myhr, Ø. Grong, and K. O. Pedersen. A Combined Precipitation, Yield Strength, and Work Hardening Model for Al–Mg–Si Alloys. *Metallurgical and Materials Transactions A*, pages 2276–2289, 2010.

[23] S. Esmaeili, D. J. Lloyd, and W. J. Poole. A yield strength model for the Al–Mg–Si–Cu alloy AA6111. *Acta Materialia*, 51(8):2243 – 2257, 2003.

[24] A. Bahrami, A. Miroux, and J. Sietsma. An Age-Hardening Model for Al-Mg-Si Alloys Considering Needle-Shaped Precipitates. *Metallurgical and Materials Transactions A*, 43(11):4445–4453, 2012.

[25] B. Holmedal. Strength contributions from precipitates. *Philosophical Magazine Letters*, 95(12):594–601, 2015.

[26] M. Yang, H. Chen, A. Orekhov, Q. Lu, X. Lan, K. Li, S. Zhang, M. Song, Y. Kong, D. Schryvers, and Y. Du. Quantified contribution of β'' and β' precipitates to the strengthening of an aged Al-Mg-Si alloy. *Materials Science and Engineering: A*, 774:138776, 2020.

[27] F. Lu, J. K. Sunde, C. D. Marioara, R. Holmestad, and B. Holmedal. Strength and work hardening behavior of AA6082 alloy. *Submitted*, X:Y–Z, 2020.

[28] N. Gromada, G. Mishuris, and A. Öchsner. *Correction Formulae for the Stress Distribution in Round Tensile Specimens at Neck Presence*. Springer, Berlin, Heidelberg, 2011.

[29] S. J. Andersen. Quantification of the Mg_2Si β'' and β' phases in AlMgSi alloys by transmission electron microscopy. *Metallurgical Materials Transaction A*, 26(8):1931–1937, 1995.

[30] M. Torsæter, W. Lefebvre, C. D. Marioara, S. J. Andersen, J. C. Walmsley, and R. Holmestad. Study of intergrown L and Q′precipitates in Al–Mg–Si–Cu alloys. *Scripta Materialia*, 64(9):817–820, 2011.

[31] C. D. Marioara, J. Friis, E. Hersent, and A. Oskarsson. A transmission electron microscopy study of precipitate phases that form during operation in a heat exchanger alloy. *Materials Characterization*, 149:218–225, 2019.

[32] J. K. Sunde, S. Wenner, and R. Holmestad. In situ heating TEM observations of evolving nanoscale Al-Mg-Si-Cu precipitates. *Journal of Microscopy*, doi:10.1111/jmi.12845, 2019.

[33] A.K. Vasudévan and R.D. Doherty. Grain boundary ductile fracture in precipitation hardened aluminum alloys. *Acta Metallurgica*, 35(6):1193 – 1219, 1987.

[34] K. Marthinsen O. S. Hopperstad E. Christiansen, C. D. Marioara and R. Holmestad. Lattice rotations in precipitate free zones in an Al-Mg-Si alloy. *Materials Characterization*, 144:522 – 531, 2018.

[35] B. H. Frodal, E. Christiansen, O. R. Myhr, , and O. S. Hopperstad. The role of quench rate on the plastic flow and fracture of three aluminium alloys with different grain structure and texture. *International Journal of Engineering Science*, 150:103257, 2020.

[36] F. R. N. Nabarro. *Theory of Crystal Dislocations*. Oxford University Press, Oxford, 1967.

[37] A. de Vaucorbeil, W. J. Poole, and C. W. Sinclair. The superposition of strengthening contributions in engineering alloys. *Materials Science and Engineering: A*, 582:147 – 154, 2013.

[38] A. de Vaucorbeil, W. J. Poole, and C. W. Sinclair. The effect of obstacle strength distribution on the critical resolved shear stress of engineering alloys. *Materials Science Forum*, 794-796:449–454, 2014.

[39] J. K. Sunde, C. D. Marioara, A. T. J. van Helvoort, and R. Holmestad. The evolution of precipitate crystal structures in an Al-Mg-Si(-Cu) alloy studied by a combined HAADF-STEM and SPED approach. *Materials Characterization*, 142:458–469, 2018.

[40] P. Van Houtte, S. Li, M. Seefeldt, and L. Delannay. Deformation texture prediction: from the taylor model to the advanced lamel model. *International Journal of Plasticity*, 21(3):589 – 624, 2005.

Paper VI – Supplementary Information

Jonas Kristoffer Sunde, Feng Lu, Calin Daniel Marioara
Bjørn Holmedal, Randi Holmestad

Linking mechanical properties to precipitate microstructure in three high strength Al-Mg-Si(-Cu) alloys

Supplementary Information

Linking mechanical properties to precipitate microstructure in three high strength Al-Mg-Si(-Cu) alloys

Jonas K. Sunde[a,*], Feng Lu[b,*], Calin D. Marioara[c], Bjørn Holmedal[b], Randi Holmestad[a]

[a] *Department of Physics, Norwegian University of Science and Technology (NTNU), N-7491 Trondheim, Norway*
[b] *Department of Materials Science and Engineering, NTNU, N-7491 Trondheim, Norway*
[c] *Materials and Nanotechnology, SINTEF Industry, N-7465 Trondheim, Norway*

Abstract

The mechanical properties of age hardenable Al alloys depend strongly on the precipitate microstructure. This work presents an investigation into the connection between material strength and ductility to precipitate statistics in three high strength Al-Mg-Si(-Cu) alloys (Cu$\lesssim$0.1 at.%). A range of ageing conditions were examined in order to understand the effect of an evolving precipitate microstructure, and the results were used as input for strengthening models. The mechanical properties were obtained by tensile test experiments and microstructure characterisation was attained by transmission electron microscopy. The results showed that minor changes to the Si, Mg, and Cu additions – the total addition (at.%) kept approximately equal – had a significant impact on measured material properties with corresponding changes in the precipitate microstructure. On the peak strength plateaus, differences as large as 35 MPa in yield strength were measured between the strongest and weakest alloy, obtained as 410 MPa and 375 MPa, respectively. Higher material yield strength correlated well with a refined precipitate microstructure comprising higher number densities of smaller precipitates. Differences with respect to material ductility first appeared after moderate overageing, showing negative correlation with material strength. At significantly overaged conditions the differences in strength exceeded 100 MPa, demonstrating large differences with respect to the thermomechanical stability of these materials, which has important consequences for alloys exposed to elevated temperatures under in-service conditions. The highly comprehensive body of data presented should serve as a valuable reference in the development of strengthening models for the Al-Mg-Si-Cu system, and will hopefully spark further investigations on the topics covered.

Keywords: 6xxx Al alloys, Precipitation, Yield strength, Transmission electron microscopy, Strengthening models, Microstructure-property relationships

Author Information

Jonas Kristoffer Sunde, MSc, E-mail: jonas.k.sunde@ntnu.no

Feng Lu, MSc, E-mail: feng.lu@ntnu.no

Calin Daniel Marioara, PhD, E-mail: calin.d.marioara@sintef.no

Bjørn Holmedal, PhD, E-mail: bjorn.holmedal@ntnu.no

Randi Holmestad, PhD, E-mail: randi.holmestad@ntnu.no

*Corresponding author(s)
Email addresses: jonas.k.sunde@ntnu.no (Jonas K. Sunde), feng.lu@ntnu.no (Feng Lu)

SI 1. Tensile test data

True stress-strain curves

Fig. SI 1, **Fig. SI 2**, and **Fig. SI 3** show true stress-strain curves until fracture (raw data) from all ageing conditions studied in alloys S, C, and M, respectively.

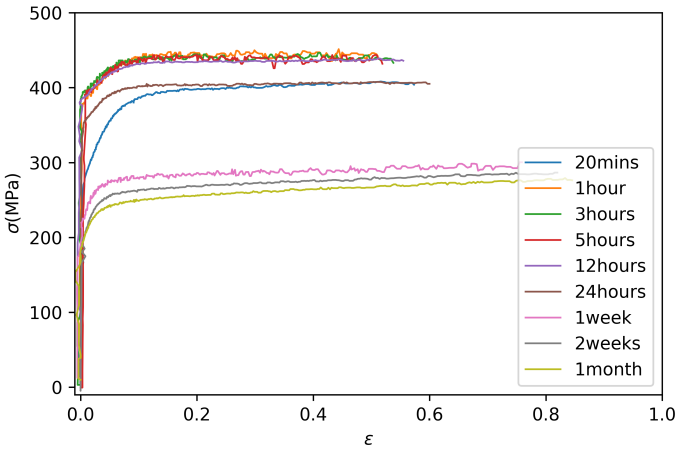

Fig. SI 1. True stress-strain curves for all ageing conditions studied in alloy S.

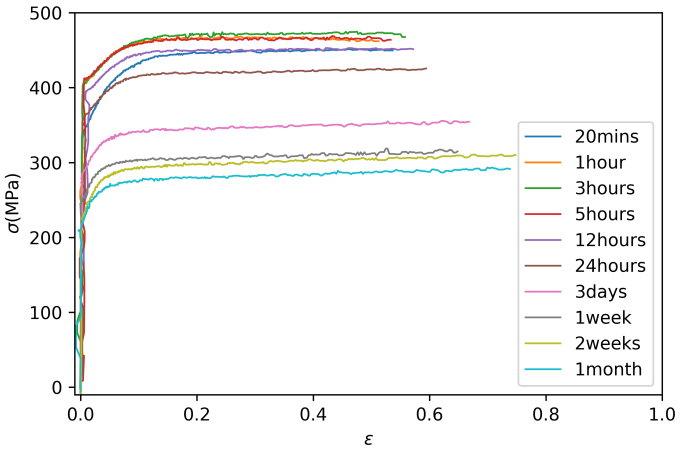

Fig. SI 2. True stress-strain curves for all ageing conditions studied in alloy C.

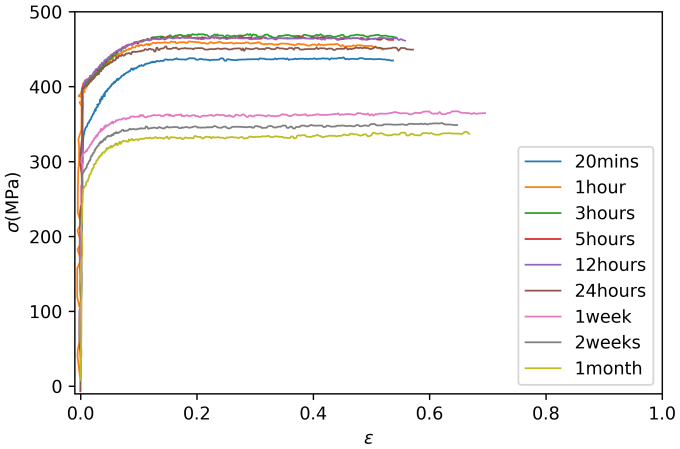

Fig. SI 3. True stress-strain curves for all ageing conditions studied in alloy M.

Voce fitting of flow stress-strain curves

Experimentally measured flow stress-strain curves until fracture for all conditions were fitted by a 4-term Voce equation, given as:

$$\sigma = \sigma_0 + \sum_{i=1}^{3} \sigma_i \left(1 - \exp\left(-\frac{\theta_i \epsilon}{\sigma_i}\right)\right). \quad (1)$$

The optimized parameters of Voce equation fitted curves, as well as the corresponding necking strain (ϵ_n) and fracture strain ϵ_f obtained from experiments are provided in **Table SI 1**, **Table SI 2**, and **Table SI 3** for alloys S, C, and M, respectively. This data can be directly used for numerical modelling of the work hardening behaviour analysis extended to large strains, in particular, after necking.

Table SI 1. Voce euqation parameter fitting of the flow stress-strain curves obtained for all ageing conditions tested for alloy S.

Condition	σ_0	σ_1	σ_2	σ_3	θ_1	θ_2	θ_3	ϵ_n	ϵ_f
20 min	284.92	7657.08	39.66	-7550.33	3.19E+05	48.76	-3.17E+05	0.08	0.55
20 min	296.45	2314.18	154.86	-2220.10	88966.54	36.20	-8.67E+04	0.08	0.55
20 min	289.01	183.98	36.38	-82.64	6450.12	44.24	-4427.84	0.09	0.58
1h	374.68	84.48	-9.89E+13	-6.85	2238.90	-9.81	-667.35	0.08	0.51
1h	378.79	83.09	-3.13E+12	-16.62	2305.95	-1.30	-1458.05	0.07	0.51
1h	383.16	111.76	-1.42E+04	-49.67	3406.65	-4.29	-3147.37	0.07	0.51
3h	391.21	133.91	132.85	-217.81	5610.50	5565.76	-1.10E+04	0.05	0.54
3h	387.69	64.54	-10.84	-8.61	1711.95	0.00	-851.74	0.06	0.55
3h	388.53	142.07	-1.05E+11	-91.64	5529.78	-0.45	-5252.46	0.06	0.55
5h	394.99	60.23	-1.00E+08	-14.42	1890.67	-8.06	-845.35	0.07	0.52
5h	395.04	111.82	-5343.24	-63.55	3796.20	-2.65	-3885.33	0.06	0.55
12h	382.43	8384.20	4912.88	-8333.37	3.62E+05	7.14	-3.61E+05	0.05	0.56
12h	382.63	62.96	-5.11	-15.03	1886.18	0.00	-1710.20	0.06	0.57
24h	352.93	8043.02	1.07E+04	-7992.17	4.04E+05	9.58	-4.04E+05	0.06	0.60
24h	357.99	2738.92	30.88	-2695.11	1.42E+05	10.26	-1.41E+05	0.06	0.60
24h	349.20	1398.53	7.12E+04	-1347.10	7.12E+04	9.23	-7.03E+04	0.05	0.58
1week	207.18	66.63	69.72	-34.23	3434.96	93.00	-45.65	0.06	0.77
1week	220.97	57.81	26.39	-1.97	3035.23	45.04	-2.88E+09	0.07	0.75
1week	219.63	64.75	32.79	-7.50	3216.12	37.16	-7.22E+04	0.05	0.76
1week	195.83	64.68	41.58	-1.60	3363.19	53.63	-4.08E+15	0.05	0.82
1week	198.45	64.20	43.16	-2.53	3299.30	49.45	-9085.00	0.05	0.79
1week	191.64	66.60	71.20	-35.56	3160.56	128.44	-64.14	0.06	0.84
1month	179.12	64.51	71.44	-23.99	3362.73	103.36	-34.71	0.05	0.85
1month	182.07	61.57	71.96	-31.43	3400.06	116.42	-50.84	0.05	0.85
1month	173.89	70.67	84.11	-41.76	3433.33	121.62	-60.38	0.06	0.86

Table SI 2. Voce euqation parameter fitting of the flow stress-strain curves obtained for all ageing conditions tested for alloy C.

Condition	σ_0	σ_1	σ_2	σ_3	θ_1	θ_2	θ_3	ϵ_n	ϵ_f
20 min	340.17	72.89	-1.01E+04	1387.34	1972.13	-120.52	129.43	0.08	0.51
20 min	345.42	9.39	92.18	-7.61	50.62	2691.87	-1532.58	0.07	0.53
20 min	343.89	167.95	3.48E+14	-66.97	4404.59	11.56	-2495.76	0.09	0.54
1h	405.22	79.55	-2.78E+04	-15.62	1887.10	-10.07	-1717.95	0.07	0.52
1h	407.34	72.69	-1.19E+04	-13.25	1853.24	-5.45	-1330.37	0.07	0.54
1h	406.14	49.23	47.89	-32.37	1308.34	1272.82	-2190.12	0.07	0.52
3h	414.91	263.57	243.58	-451.68	1.04E+04	9599.05	-1.98E+04	0.06	0.54
3h	410.39	1401.60	2.05E+04	-1340.05	5.06E+04	4.09	-5.02E+04	0.07	0.56
3h	409.58	87.10	5.93	-24.43	2069.46	0.00	-1836.28	0.08	0.56
5h	407.51	52.94	5.08	8.88	1222.70	117.31	-0.72	0.07	0.54
5h	409.06	4650.59	7801.40	-4592.33	1.76E+05	2.94	-1.75E+05	0.07	0.56
5h	410.79	926.36	-2.19E+04	-870.52	3.70E+04	-7.74	-3.66E+04	0.06	0.52
12h	395.26	836.29	1.68E+05	-782.57	3.38E+04	5.11	-3.32E+04	0.07	0.58
12h	398.84	230.61	1.18E+12	-181.61	9833.26	2.45	-9638.00	0.06	0.56
12h	396.68	1.34E+04	1689.19	-1.34E+04	5.89E+05	5.71	-5.89E+05	0.07	0.56
24h	366.29	73.52	-304.28	-21.09	2368.77	0.00	-1977.16	0.06	0.57
24h	364.30	1113.26	9.61E+04	-1060.45	5.05E+04	13.56	-5.00E+04	0.07	0.60
24h	370.88	2253.11	17.54	-2202.87	1.12E+05	16.96	-1.12E+05	0.06	0.60
3day	283.74	65.42	9.97E+04	-6.65	2451.69	20.27	-1517.65	0.06	0.67
3day	279.87	67.16	29.86	-7.66	2805.60	30.33	-1257.50	0.05	0.67
3day	285.90	63.68	166.94	-7.14	2572.72	19.34	-3329.44	0.06	0.67
1week	246.09	89.47	857.02	-32.65	3679.46	22.02	-1342.87	0.05	0.57
1week	245.72	67.99	52.85	-12.35	3278.66	24.12	-2482.23	0.05	0.65
1week	238.45	73.58	774.25	-12.23	3216.49	27.58	-4458.58	0.06	0.75
2weeks	235.08	97.18	36.48	-12.29	5191.20	48.13	-656.30	0.05	0.73
2weeks	225.41	70.84	34.73	-6.44	3135.07	36.75	-2586.67	0.06	0.75
2weeks	230.25	65.70	51.81	-4.86	2907.33	32.35	-1172.58	0.06	0.75
1month	213.88	2022.58	50.90	-1962.61	6.50E+04	30.61	-6.26E+04	0.05	0.74
1month	206.39	90.17	173.60	-21.78	4004.57	20.35	-967.28	0.06	0.73
1month	209.16	71.25	493.63	-473.67	2581.19	1811.79	-1838.60	0.06	0.74

Table SI 3. Voce euqation parameter fitting of the flow stress-strain curves obtained for all ageing conditions tested for alloy M.

Condition	σ_0	σ_1	σ_2	σ_3	θ_1	θ_2	θ_3	ϵ_n	ϵ_f
20 min	345.01	182.28	-5.98E+08	-85.25	5443.77	-17.93	-4017.13	0.08	0.49
20 min	346.38	104.97	-2.49E+13	-13.76	2660.56	-1.21	-1335.52	0.09	0.54
20 min	341.65	181.09	-4.08E+08	-76.06	4978.94	-23.34	-3066.25	0.08	0.51
20 min	348.59	4.08E+04	3.85E+04	-7.92E+04	3.48E+05	3.07E+05	-6.54E+05	0.09	0.55
1h	398.81	161.22	-1.32E+11	-81.74	4438.33	-7.87	-3574.61	0.08	0.55
1h	391.59	184.23	-4.46E+14	-112.66	5727.00	-18.15	-5071.73	0.07	0.52
1h	380.81	3726.15	-39.32	-3615.01	95212.10	-356.34	-9.36E+04	0.07	0.49
3h	400.60	132.92	-5.15	-63.97	3844.30	-31.20	-3256.29	0.06	0.56
3h	399.39	164.43	-49.52	-46.55	3475.94	-677.28	-2050.65	0.07	0.55
3h	402.88	104.53	-3.27E+04	-35.84	2668.14	-12.70	-2138.05	0.07	0.52
5h	398.95	148.81	-4.49E+12	-80.85	4299.96	-5.28	-3603.92	0.08	0.54
5h	397.56	279.13	-4.68E+09	-219.68	1.07E+04	-13.48	-1.04E+04	0.07	0.54
5h	409.77	128.41	-3.42E+13	-69.05	4461.58	-22.95	-3991.16	0.07	0.52
12h	406.39	3690.42	-1655.41	-1976.92	1.05E+05	-4.31E+04	-61203.61	0.07	0.56
12h	405.44	2.49E+04	-1.20E+04	-1.28E+04	7.20E+05	-3.36E+05	-3.84E+05	0.07	0.55
12h	404.15	2991.56	-1.98E+04	-2927.95	1.15E+05	-5.68	-1.14E+05	0.07	0.56
24h	409.85	217.62	-4.99E+04	-175.06	9832.49	-0.30	-9232.69	0.07	0.55
24h	374.14	103.36	-2.46E+14	-17.16	2350.94	-9.26	-928.55	0.08	0.55
24h	397.92	261.67	469.54	-678.39	1.16E+04	2.08E+04	-3.23E+04	0.06	0.58
1week	311.65	58.45	3080.63	-0.64	2188.76	7.08	-5.22E+04	0.06	0.61
1week	310.50	94.43	5.95E+04	-45.15	4660.75	7.82	-4489.94	0.06	0.70
1week	305.31	64.30	-12.37	-11.44	2309.32	0.00	-1714.86	0.05	0.69
2weeks	283.83	74.81	3.19E+04	-15.32	3412.09	10.86	-2322.33	0.06	0.65
2weeks	287.04	66.92	1.48E+04	-6.37	2446.66	5.82	-699.83	0.07	0.63
2weeks	285.92	683.81	3.48E+04	-627.49	4.14E+04	12.06	-4.01E+04	0.05	0.64
1month	266.35	71.19	2.68E+04	-11.51	2986.33	12.49	-2013.10	0.06	0.66
1month	264.21	81.27	6.19E+04	-15.98	3291.52	12.15	-1.19E+15	0.07	0.67
1month	260.75	1702.81	2.95E+04	-1636.15	1.01E+05	8.44	-99183.25	0.06	0.67

SI 2. Precipitate Statistics

The precipitate statistics were calculated for all alloys in the conditions selected for TEM studies, and the results for alloys S, C, and M are shown in **Table SI 4, Table SI 5**, and **Table SI 6**, respectively. The PFZ width at GBs were also measured in each condition studied. The distribution of precipitate phases in each alloy were presented in a related study by Sunde *et al.* [1]. As shown in this study, alloy M has a significant fraction of lath shaped (predominantly) L phases in addition to the rod-shaped phases such as β'', β', and Q′. Therefore, **Table SI 6** distinguishes between the two types which have different precipitate dimensions and distributions. Uncertainties list standard errors.

Table SI 4. Calculated precipitate statistics and PFZ widths at GBs for alloy S in all studied ageing conditions.

Ageing condition	Cross-section area [nm^2]	Precipitate length [nm]	Precipitate density [μm^{-3}]	Volume fraction [%]	PFZ width [nm]
20 min	11.6±0.6	8.7±0.2	73240±7354	0.74±0.04	65±3
3 h	12.5±0.7	14.3±0.3	67023±7106	1.20±0.07	75±3
12 h	15.2±0.6	19.4±0.4	49247±5207	1.45±0.06	87±14
24 h	15.8±0.6	19.5±0.7	46489±5231	1.43±0.08	94±5
1 week	45.1±2.3	241.6±6.8	1498±416	1.635±0.09	161±9
2 weeks	65.8±3.7	254.3±13.0	1130±290	1.89±0.14	235±17
1 month	78.0±4.9	269.9±8.5	1021±320	2.15±0.15	267±18

Table SI 5. Calculated precipitate statistics and PFZ widths at GBs for alloy C in all studied ageing conditions.

Ageing condition	Cross-section area [nm^2]	Precipitate length [nm]	Precipitate density [μm^{-3}]	Volume fraction [%]	PFZ width [nm]
20 min	9.2±0.3	8.1±0.2	113090±11370	0.84±0.03	56±3
3 h	10.1±0.4	12.6±0.3	92899±9401	1.19±0.06	76±3
12 h	14.5±0.7	15.2±0.4	57103±6315	1.27±0.07	84±6
24 h	15.3±0.7	19.4±1.1	47740±5344	1.42±0.11	102±7
3 days	50.1±2.7	100.9±6.1	3961±1402	2.02±0.16	130±8
1 week	55.3±3.0	180.9±5.8	2153±778	2.15±0.13	172±8

Table SI 6. Calculated precipitate statistics and PFZ widths at GBs for alloy M in all studied ageing conditions.

Ageing condition	Cross-section area [nm^2]	Length Rods / Laths [nm]	Precipitate density Rods / Laths [μm^{-3}]	Volume fraction Rods / Laths [%]	PFZ width [nm]
20 min*	8.4±0.3	6.9±0.1	141576±14231	0.82±0.04	53±4
3 h	10.3±0.3	10.7±0.3 / 25.3±1.7	98903±10723 / 9632±1211	1.09±0.05 / 0.25±0.02	68±3
24 h	12.7±0.4	11.9±0.6 / 38.5±2.2	81001±11544 / 8130±1430	1.22±0.07 / 0.40±0.03	70±4
1 month*	43.0±2.5	136±4	1479±244 / 2219±366	0.86±0.05 / 1.30±0.08	165±12

* UA and coarsened precipitates (OA) lying in-plane were not clearly separable as rods and laths and were assumed to be approximately equal in size.

SI 3. Fitting of precipitate length distributions

The distribution of precipitate lengths, ϕ_l , were found to be best fitted using a log-normal function. **Fig. SI 4** shows the results from fitting a log-normal function to the precipitate length distribution for the lengths measured in alloy S at (a) 20 min through (g) 1 month ageing, respectively.

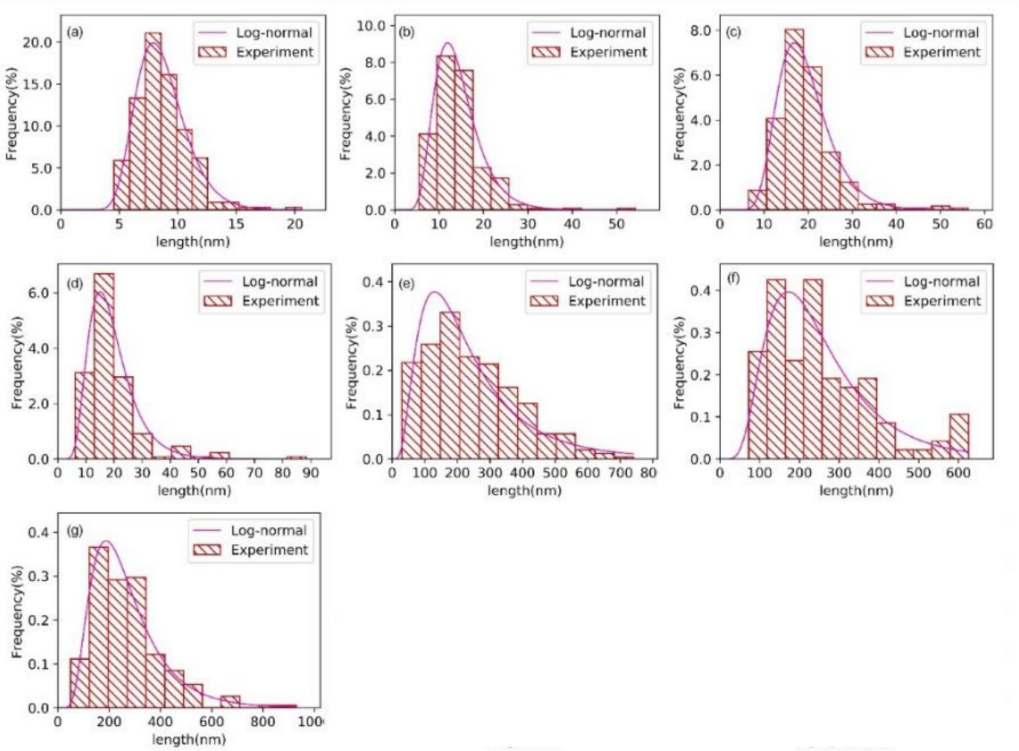

Fig. SI 4. Log-normal distribution fitting of precipitate length distributions measured at (a) 20 min through (g) 1 month ageing in alloy S.

Fig. SI 5 shows the fitting of the precipitate aspect ratios $\Omega(l)$ assuming a direct correlation between precipitate lengths, l, and cross-section areas, a.

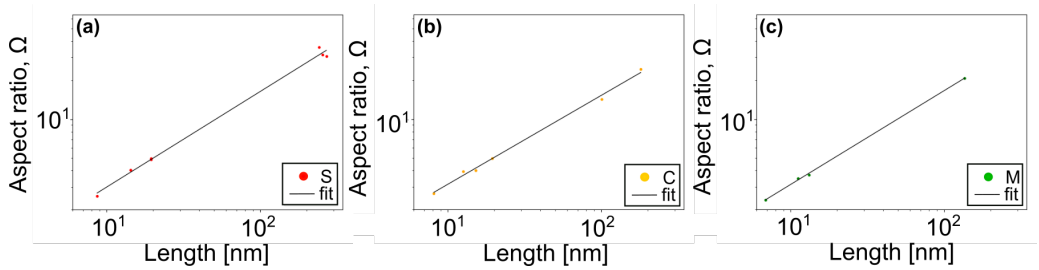

Fig. SI 5. Fitting of the precipitate aspect ratios $\Omega(l)$ for alloy (a) S, (b) C, and (c) M.

SI 4. Solute solution levels

The calculation of the solute solution strengthening contribution, σ_{ss}, requires as input the solid solution levels C_i (wt.%) for Mg, Si, and Cu as a function of ageing. This was approximated from measured precipitate volume fractions, precipitate phase fractions as obtained by scanning precession electron diffraction (SPED) experiments, and known precipitate phase chemical compositions. This methodology is elaborated in the related work by Sunde et al. [2]. The estimated values C_i for alloys S, C, and M in the conditions selected for TEM studies are shown in **Table SI 7, Table SI 8**, and **Table SI 9**, respectively.

Table SI 7. The amount of Si, Mg, and Cu (wt.%/at.%) locked in precipitates (p) and in solute solution (ss) for alloy S. ssss (supersaturated solid solution) indicates the as-quenched condition.

	Ageing time							
Element	ssss	20 min	3 h	12 h	24 h	1 week	2 weeks	1 month
Si (p)	0/0	0.29/0.28	0.48/0.46	0.55/0.53	0.53/0.51	0.47/0.45	0.60/0.58	0.69/0.66
Mg (p)	0/0	0.25/0.28	0.41/0.46	0.50/0.55	0.49/0.54	0.52/0.58	0.62/0.69	0.68/0.76
Cu (p)	0/0	0/0	0/0	0/0	0.02/0.01	0.028/0.012	0.028/0.012	0.03/0.013
Si (ss)[†]	0.69/0.67	0.4/0.39	0.21/0.21	0.14/0.14	0.16/0.16	0.22/0.22	0.09/0.09	0/0.01
Mg (ss)	0.72/0.80	0.47/0.52	0.31/0.34	0.22/0.25	0.23/0.26	0.2/0.22	0.1/0.11	0.04/0.04
Cu (ss)	0.03/0.013	0.03/0.013	0.03/0.013	0.03/0.013	0.01/0.003	0.002/0.001	0.002/0.001	0/0

[†] The incorporation of Si into dispersoids was taken into account using an estimate based on the thermal history of the material and the Alstruc microstructure solidification model [3].

Table SI 8. The amount of Si, Mg, and Cu (wt.%/at.%) locked in precipitates (p) and in solute solution (ss) for alloy C. ssss (supersaturated solid solution) indicates the as-quenched condition.

	Ageing time					
Element	ssss	20 min	3 h	12 h	24 h	1 week
Si (p)	0/0	0.34/0.33	0.46/0.44	0.49/0.47	0.54/0.52	0.69/0.67
Mg (p)	0/0	0.30/0.33	0.41/0.46	0.44/0.49	0.48/0.53	0.64/0.71
Cu (p)	0/0	0/0	0/0	0/0	0.02/0.01	0.09/0.04
Si (ss)[†]	0.69/0.67	0.35/0.34	0.23/0.23	0.2/0.2	0.15/0.15	0/0
Mg (ss)	0.64/0.71	0.34/0.38	0.23/0.25	0.2/0.22	0.16/0.18	0/0
Cu (ss)	0.09/0.04	0.09/0.04	0.09/0.04	0.09/0.04	0.07/0.03	0/0

[†] The incorporation of Si into dispersoids was taken into account using an estimate based on the thermal history of the material and the Alstruc microstructure solidification model [3].

Table SI 9. The amount of Si, Mg, and Cu (wt.%/at.%) locked in precipitates (p) and in solute solution (ss) for alloy M. ssss (supersaturated solid solution) indicates the as-quenched condition.

	Ageing time				
Element	ssss	20 min	3 h	24 h	1 month
Si (p)	0/0	0.28/0.3	0.45/0.48	0.48/0.52	0.48/0.52
Mg (p)	0/0	0.27/0.31	0.45/0.5	0.53/0.59	0.68/0.75
Cu (p)	0/0	0/0	0.02/0.01	0.07/0.03	0.23/0.1
Si (ss)[†]	0.48/0.51	0.19/0.21	0.03/0.03	0/0	0/0
Mg (ss)	0.77/0.86	0.48/0.55	0.31/0.36	0.23/0.27	0.09/0.11
Cu (ss)	0.23/0.1	0.23/0.1	0.21/0.09	0.16/0.07	0/0

[†] The incorporation of Si into dispersoids was taken into account using an estimate based on the thermal history of the material and the Alstruc microstructure solidification model [3].

References

[1] J. K. Sunde, C. D. Marioara, and R. Holmestad. The effect of low Cu additions on precipitate crystal structures in overaged Al-Mg-Si(-Cu) alloys. *Materials Characterization*, 110087, 2019.

[2] J. K. Sunde, C. D. Marioara, A. T. J. van Helvoort, and R. Holmestad. The evolution of precipitate crystal structures in an Al-Mg-Si(-Cu) alloy studied by a combined HAADF-STEM and SPED approach. *Materials Characterization*, 142:458–469, 2018.

[3] A. L. Dons, E. K. Jensen, Y. Langsrud, E. Tromborg, and S. Brusethaug. The Alstruc microstructure solidification model for industrial aluminum alloys. *Metallurgical and Materials Transaction A*, 30(8):2135–2146, 1999.

Paper VII

Jonas Kristoffer Sunde, Calin Daniel Marioara,
Randi Holmestad

On the microstructural origins of improvements in conductivity by heavy deformation and ageing of Al-Mg-Si alloy 6101

Manuscript in preparation.

On the microstructural origins of improvements in conductivity by heavy deformation and ageing of Al-Mg-Si alloy 6101

Jonas K. Sunde[a,*], Calin D. Marioara[b], Randi Holmestad[a]

[a] *Department of Physics, Norwegian University of Science and Technology (NTNU), N-7491 Trondheim, Norway*
[b] *Materials and Nanotechnology, SINTEF Industry, N-7465 Trondheim, Norway*

Abstract

The present work has examined an Al-0.54Mg-0.38Si (at.%) conductor alloy (6101) subjected to two different thermomechanical processing routes. Conventional solution treatment, quenching, and artificial ageing (170 °C) was compared to a process applying solution treatment, quenching, pre-ageing (7 h at 170 °C), 50% thickness reduction by cold-rolling, and re-ageing at 170 °C. Re-ageing after rolling resulted in a very rapid increase in conductivity. After 2 h re-ageing, the rate of change in conductivity had slowed to a comparable level as for the undeformed material at corresponding ageing times. From this point on, the deformed material maintained a 2 – 3%IACS gain in conductivity with further ageing. The improvement in conductivity was caused by an increased solute depletion of the Al matrix in the deformed material, which was quantified by atom probe tomography. The principal mechanism causing this depletion is proposed to be rapid dislocation mediated diffusion of solutes. By deforming a pre-aged microstructure, the introduced dislocations will become pinned at multiple points on precipitates and solute enriched regions. The resulting entangled dislocation microstructure will act as a network of fast diffusion pathways on subsequent re-ageing. Clear differences between the deformed and undeformed material were also seen in terms of the forming precipitate dispersions in the Al matrix, as shown by transmission electron microscopy results. The findings and the discussion presented are of importance to future alloy and process development for Al alloy conductor materials.

Keywords: 6xxx Al alloys, Precipitation, Electrical conductivity, Transmission electron microscopy, Atom probe tomography

1. Introduction

Al and its alloys are applied as conductor materials in land cables and overhead lines due to their high electrical conductivity-to-weight ratios and high specific strengths [1]. Al alloys are also under serious consideration for replacing Cu in subsea/offshore electrical cables. Here, the selection of an Al alloy will entail a trade-off between mechanical properties and conductivity. Strict demands are put on mechanical properties such as: tensile/yield strengths, creep, fatigue, welding properties, and thermal stability. The 6xxx series Al-Mg-Si alloys are good candidates for these applications, and are characterised by medium strengthening potential, good conductivity, and overall good forming and welding properties.

One of the key challenges with using 6xxx alloys in conductor applications, is to strike an ideal balance between high electrical conductivity and good mechanical performance. The problem is that all main factors that cause improvements in strength, including: solute strengthening, precipitate strengthening, and work hardening, will deteriorate electrical conductivity. The development of alloys and thermomechanical processing (TMP) routines that optimise for both properties are critically dependent on detailed knowledge of microstructure-property relationships [2, 3, 4].

For 6xxx alloys in conductor applications, the combined alloying addition of Mg and Si is typically less than 1.6 at.%, e.g. 6101 and 6201 type alloys. The low addition of solutes means that these alloys can reach relatively high conductivities, combined with a medium level of strength. The strengthening is primarily caused by nano-sized precipitate phases that form during thermal ageing. The precipitates are needle- or rod-shaped, with main growth axis in $\langle 100 \rangle_{\mathrm{Al}}$ directions. The types of precipitates that form, their sizes, and their dispersion in the Al matrix, all depend on alloy composition and TMP parameters. The precipitation sequence for the Al-Mg-Si system is normally stated as [5, 6]

$$\begin{aligned} \mathrm{SSSS} \rightarrow \text{solute clusters} \rightarrow \text{GP-zones (pre-}\beta'') \\ \rightarrow \beta'' \rightarrow \beta', \mathrm{U1}, \mathrm{U2}, \mathrm{B}' \rightarrow \beta, \mathrm{Si}. \end{aligned}$$

Here, SSSS denotes a supersaturated solid solution. For details on the different precipitate phase crystal structures, the following works should be consulted [7, 8, 9, 10, 11, 12].

Several previous studies have demonstrated how different TMP routes may yield good combinations of improved mechanical and electrical properties in 6xxx alloys, including: severe plastic deformation (SPD) [4, 13, 14], hydrostatic extrusion [15], drawing [16], and rolling [17, 18]. A TMP route applying cold-rolling has been used in this work. The focus of the present study has been to advance the understanding of the

*Corresponding author
Email address: jonas.k.sunde@ntnu.no (Jonas K. Sunde)

microstructural origins of improvements in conductivity. This has been done by studying a 6101 Al alloy subjected to two different TMP routes, with conductivity and hardness measured as a function of ageing time. Microstructure characterisation was obtained by transmission electron microscopy (TEM) and atom probe tomography (APT). This provided detailed information on precipitate sizes and distributions, in addition to quantifying the matrix solute levels at different ageing conditions. The characterisation results were used to explain the differences obtained in material properties after equal ageing times for the two TMP routes.

2. Methods

2.1. Material processing and property measurements

The studied 6101 alloy was manufactured by Hydro and was delivered as cast rods (Ø15 mm). The alloy composition was measured by inductively coupled plasma optical emission spectroscopy (ICP-OES), and is shown in **Table 1**. The material was solution heat treated (SHT) at 530 °C for 20 min and then water quenched to room temperature. It was kept at room temperature (RT) for 15 min before it was set to artificial ageing (AA) at 170 °C in an oil bath. In the following, this will be referred to as the undeformed material. In addition, another process was applied, comprising: solution treatment, quenching, pre-ageing (PA, 7 h at 170 °C), quenching, 50% thickness reduction by cold-rolling (50%CR), and subsequent re-ageing at 170 °C. This is denoted as the deformed material. A schematic of the two heat treatment procedures is provided in **Fig. 1**.

Table 1. Composition of alloy 6101 as measured by ICP-OES. All other element concentrations were < 0.005 at.%.

Alloy 6101	Al	Mg	Si	Fe
at./wt.%	bal.	0.54/0.50	0.38/0.41	0.05/0.10

Hardness and conductivity measurements were performed after a series of holding times from 30 min to 4 days ageing, which spanned underaged (UA) to overaged (OA) material conditions. Vickers hardness (VH1) tests were carried out on a Leica VMHT MOT hardness tester. 10 measurements were performed for each calculated average value. Conductivity was measured using a Foerster Sigmatester 2.069, and each value was determined as the average of 5 measurements.

2.2. TEM and APT experiments

Both TEM and APT specimens were prepared by standard electropolishing techniques. TEM specimens were obtained using a Struers Tenupol-5 twin-jet polishing unit with an electrolytic solution consisting of methanol (2/3) and nitric acid (1/3) held at −25 °C. APT specimens were obtained using three stages of thinning with gradually more reduced concentration of perchloric acid in the electrolyte mixture, see e.g [19].

A JEOL 2100 microscope operated at 200 kV and equipped with a Gatan Imaging Filter (GIF) was used for acquiring images for the calculation of precipitate statistics. The specimen

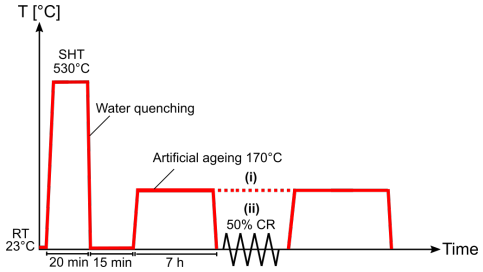

Fig. 1. The two heat treatment procedures applied for the studied Al-Mg-Si alloy. (i) Conventional SHT, water quenching, and AA. (ii) SHT, water quenching, PA (7 h at 170 °C), water quenching, 50%CR, and re-ageing at 170 °C.

thickness was measured by electron energy loss spectroscopy (EELS) using the t/λ (log-ratio) method. Precipitate number density, N, length, l, cross-section area, a, and volume fraction, V_f, were obtained using established methodologies in microstructure quantification of Al alloys by TEM [20]. The precipitate number density was calculated as $N = 3N_{\parallel}/(A(t + \bar{l}_m))$, where $N_{\parallel}$, is the number of precipitates oriented parallel to the beam direction, A is the area of the image, t is the thickness in the centre of the image, and $\bar{l}_m$ is the average measured precipitate length. The volume fraction of precipitates was calculated as $V_f = N \cdot l \cdot a$. Energy dispersive spectroscopy (EDS) was performed on a JEOL 2100F microscope operated at 200 kV. Atomic resolution high-angle annular dark-field scanning TEM (HAADF-STEM) images were obtained on a double corrected JEOL ARM 200F microscope operated at 200 kV using a detector collection angle of 42-178 mrad.

APT experiments were performed using a Cameca LEAP 5000XS system. One specimen condition was field evaporated using electric pulses with a 333 kHz pulse repetition rate and 20% pulse fraction, and a specimen temperature of 40 K. Laser mode was used for two material conditions, using a pulse energy of 40 pJ and a pulse frequency of 500 kHz, conducted at 40 K. After reconstructing the APT analysis volumes using the IVAS software, the precipitate phases were selected using Mg isosurfaces (normally 2 at.% Mg). Matrix Mg and Si solute levels were subsequently obtained using the proxigram method on obtained precipitate interfaces.

3. Results

3.1. Material properties

The obtained values for material material hardness and electrical conductivity as a function of ageing time are shown in **Fig. 2**. It is seen that the 7 h ageing condition, which was selected as the PA treatment, corresponded to an UA condition with a hardness of ≈ 74 HV1. After 50%CR reduction it is seen a significant increase (ΔHV1 ≈ 21) in material hardness, which reached about 95 HV1 in the as-deformed condition. This was higher than the maximum hardness obtained with conventional isothermal ageing at 170 °C, which reached 85 HV1 (24 h ageing). Shortly after re-ageing the as-deformed material, there

occurred large changes in the material hardness. At 10 h accumulated ageing, the hardness of the deformed material measured 90.0 ± 2.1 HV1, and beyond this point it gradually decreased with further ageing. At 15 h ageing the hardness of the deformed and undeformed materials were nearly equal at ≈ 80 HV1.

The conductivity of the as-deformed condition was unchanged relative to the 7 h undeformed ageing condition, both at 55.2%IACS (international annealed copper standard = 58 MS/m). Upon re-ageing the as-deformed material condition, there occurred a sharp increase in conductivity, from 7 h (deformation stage) to 9 h ageing. Here, the conductivity was increased from 55.2%IACS to 58.1%IACS. After the 9 h ageing condition, the slope of the conductivity curves were nearly equal for the deformed and undeformed materials, as seen from the fitted curves in **Fig. 2b**. After the stage of rapid conductivity increase, the conductivities of the deformed and undeformed materials maintained a difference of $\Delta\sigma \gtrapprox 2.1$%IACS, in favour of the former. Based on the obtained hardness and conductivity measurements, six conditions were selected for microstructure characterisation, see **Table 2**.

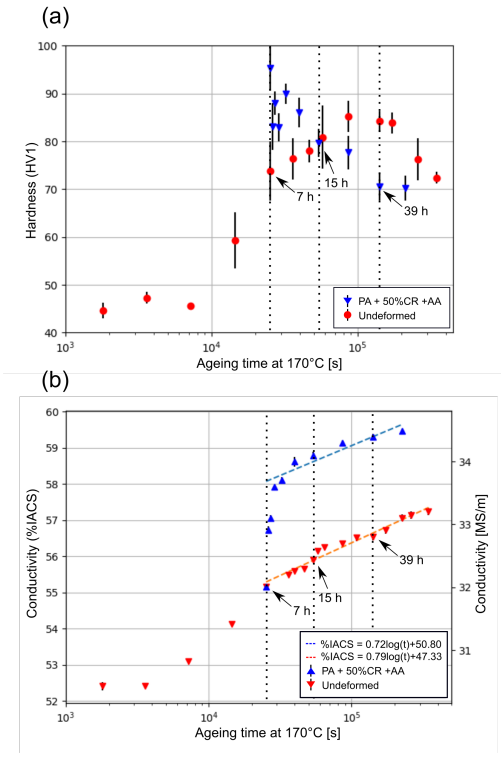

Fig. 2. (a) Vickers hardness and (b) electrical conductivity measured for the deformed and undeformed material as a function of ageing time at 170 °C. The conductivity data after 9 h ageing at 170 °C have been fitted using logarithmic functions of time, t.

Table 2. Ageing conditions selected for microstructure characterisation and the corresponding material properties.

Ageing condition	Hardness HV1	Conductivity MS/m / %IACS
7 h undef.	73.8 ± 6.2	32.0 ± 0.1 / 55.2 ± 0.2
15 h undef.	80.9 ± 6.5	32.4 ± 0.1 / 55.9 ± 0.2
39 h undef.	84.2 ± 2.2	32.8 ± 0.1 / 56.6 ± 0.2
7 h def.	95.4 ± 4.8	32.0 ± 0.1 / 55.2 ± 0.2
15 h def.	79.7 ± 2.9	34.1 ± 0.1 / 58.8 ± 0.2
39 h def.	70.6 ± 2.9	34.4 ± 0.1 / 59.3 ± 0.2

3.2. Microstructure observations by TEM

3.2.1. Undeformed material

From left to right, **Fig. 3** shows TEM images of alloy 6101 undeformed after 7 h, 15 h, and 39 h ageing at 170 °C, respectively. Based on a series of bright-field (BF) TEM images of precipitate length distributions (e.g. **Fig. 3a-c**) and cross-sections (e.g. **Fig. 3d-f**), the precipitate statistics in these conditions were calculated, see **Table 3**. At 7 h ageing it is seen a dense distribution of relatively short precipitates, most confined within the range 5 – 30 nm in length. From the HAADF-STEM lattice images (**Fig. 3g,h,m,n**) it is seen that the precipitates were predominantly β'' phase, albeit some with fragments from other Al-Mg-Si phases, such as B′ (**Fig. 3h**) and β' (**Fig. 3n**). At 15 h ageing it is seen from **Table 3** that there has occurred a significant drop in the precipitate number density, from 20 881 ± 2162 μm^{-3} to 13 861 ± 1499 μm^{-3}, obtained at 7 h and 15 h ageing, respectively. This is also qualitatively indicated from a comparison of images **Fig. 3a** and **Fig. 3b**, where the distribution in **Fig. 3b** seems less dense. HAADF-STEM lattice images (**Fig. 3i,j,o,p**) at 15 h ageing showed that β'' was still the dominant phase, and generally with larger cross-section area than for the 7 h condition. **Fig. 3j** shows an example of a near 50/50 β''/β' precipitate, with a sharp and well-defined interface between the two phases. As seen from the hardness plot in **Fig. 2a**, the hardness increases from the 7 h to the 15 h condition. The precipitates have increased in size, the number density has decreased, and the volume fraction of precipitates has increased, indicating coarsening of precipitates and a continued solute uptake in precipitate structures, see **Table 3**.

After 39 h ageing, it is seen from **Fig. 3c** that some precipitates had grown very long as compared to previous conditions, with several exceeding 100 nm in length. On closer observation, it is also seen that there existed a relatively high density of shorter precipitates, which is also seen from **Fig. 3f**. For the measured precipitate lengths at the 39 h ageing condition it was also seen a two-fold length distribution (not shown). HAADF-STEM lattice images (**Fig. 3k,l,q,r**) at 39 h ageing showed that large β'' phases were still present, but now pure post-β'' precipitates could also be seen, e.g. β' (**Fig. 3r**). **Fig. 3l** shows another example of a near 50/50 β''/β' precipitate. The calculated volume fraction was higher than for the 15 h condition, calculated as 0.82 ± 0.10% compared to 0.68 ± 0.09% for the 39 h and 15 h conditions, respectively. The 39 h condition is at

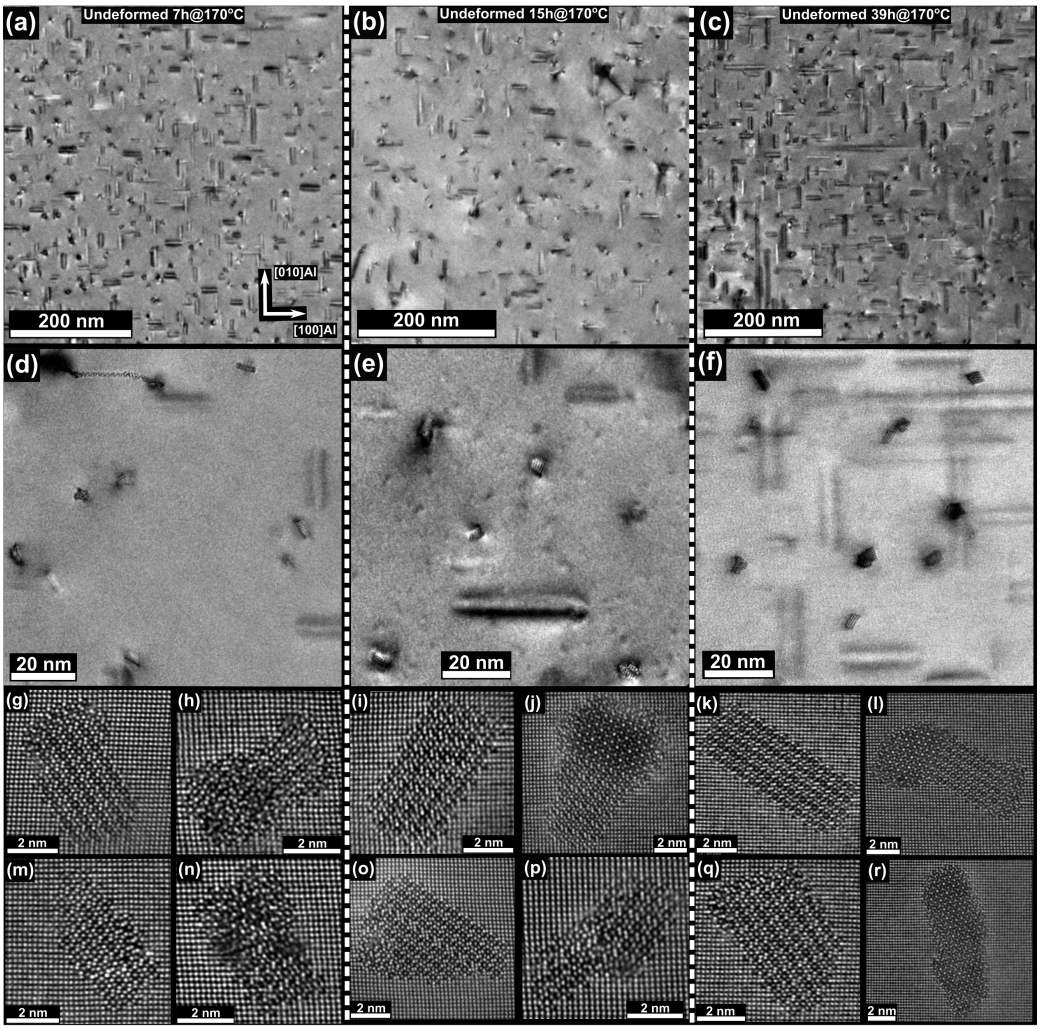

Fig. 3. Left to right: TEM images of alloy 6101 at indicated ageing conditions in the undeformed material. (a-f) BF TEM images and (g-r) HAADF-STEM lattice images showing representative precipitate structures from each ageing condition. All images are acquired near the $[001]_{Al}$ zone axis.

Table 3. Calculated precipitate statistics for alloy 6101 in the undeformed ageing conditions studied.

Ageing condition	Cross-section area [nm^2]	Precipitate length [nm]	Precipitate density [μm^{-3}]	Volume fraction [%]
7 h	12.5±0.5	20.6±0.4	20881±2162	0.54±0.06
15 h	14.5±0.4	33.8±1.0	13861±1499	0.68±0.09
39 h	14.0±0.4	29.3±0.8	20033±2093	0.82±0.10

the peak hardness plateau as seen from **Fig. 2a**, prior to the onset of overageing. More surprisingly, the calculated number density (20 033 ± 2093 μm^{-3}) is seen to be higher than the 15 h condition (see **Table 3**), and is similar to the 7 h condition. The measurements on this condition were repeated using a different specimen, which also gave a similar result. This indicated that there must be a re-precipitation occurring in-between the 15 h and 39 h ageing conditions.

3.2.2. Deformed material

Fig. 4 shows BF and dark-field (DF) TEM images of the deformed material (PA+50%CR+AA) in the three studied age-

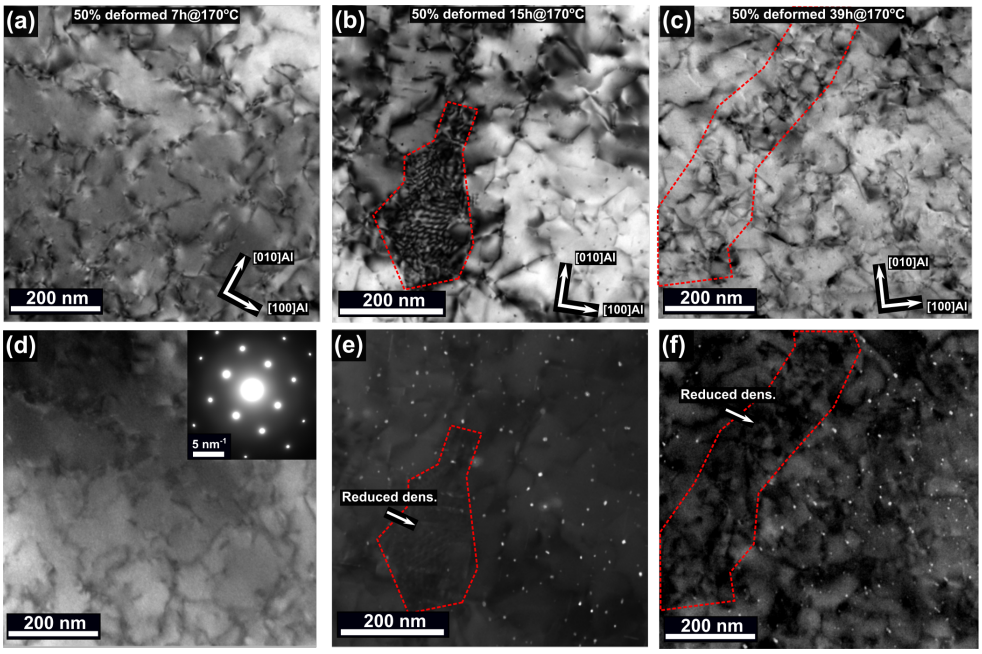

Fig. 4. BF (a-c) and corresponding DF (d-f) TEM images acquired in the deformed 6101 alloy after (a,d) 7 h (as-deformed), (b,e) 15 h, and (c,f) 39 h ageing at 170 °C, respectively. The insert of image (d) shows a selected area diffraction pattern acquired in the imaged region. Highlighted areas (red) indicate regions of reduced precipitate density. All images are acquired near the $[001]_{Al}$ zone axis.

ing conditions. The high degree of deformation introduced in the 50%CR stage is clearly visible in all images, showing a dense network of dislocations. In the as-deformed condition (**Fig. 4a,d**) it was difficult to discern any precipitates, in both BF and DF images. Nor did long exposure selected area diffraction patterns reveal their presence (**Fig. 4d**). This indicated that the precipitate crystal structures have been disrupted by the CR process, either partially or completely. Gradual disruption of β'' crystal structures has also been observed in pre-aged specimens compressed to different degrees [21], and is caused by precipitates being continuously sheared by moving dislocations. It has also been observed previously in the study of a 6101 Al alloy subjected to 70%CR [18].

After 15 h ageing (PA + 50%CR + 8 h ageing), there were clear observations of precipitates present, see **Fig. 4e**. From a series of corresponding BF/DF images as the ones shown in **Fig. 4**, there were indications of reduced precipitate density in regions that seemed particularly high in dislocation density, as exemplified by the highlighted region in **Fig. 4b,e**. This reduced precipitate density in regions of high dislocation density was also found for the 39 h deformed ageing condition, see **Fig. 4c,f**. Qualitatively, the overall precipitate density at the 39 h deformed condition seemed lower than the 15 h deformed condition.

Furthermore, the precipitate density seen from the 15 h and 39 h deformed conditions seemed to be lower than their respective undeformed conditions. Due to the heavy deformation, it was difficult to obtain any quantitative precipitate statistics at these conditions. Another difference observed between the deformed and undeformed material conditions was that the precipitate distribution in the deformed conditions was more inhomogeneous than the corresponding undeformed conditions. Larger bands of (seemingly) precipitate free regions were observed, usually corresponding with regions of increased dislocation density or dislocation bands, similar to the region highlighted in **Fig. 4c,f**.

Fig. 5 shows ADF-STEM images and EDS mapping results of the deformed alloy conditions. For the as-deformed condition shown in **Fig. 5a**, it is seen from the EDS maps that there were weak concentrations of Si and Mg at corresponding regions (highlighted). This indicates that GP-zones and/or precipitates are still present after deformation, although proving difficult to confirm with BF/DF imaging. In the Mg map there are also weak indications of elongated and narrow solute distributions. Some of these elongated, enriched regions are rather long as compared to precipitate sizes in the 7 h undeformed condition (see **Fig. 3a**), which suggests that solute interactions with dislocations have occurred, e.g. segregation.

As expected, in the 15 h deformed condition, see **Fig. 5b**, the EDS maps show that there were precipitates present, and the $\langle 001 \rangle_{Al}$ oriented needle morphology as observed near the $[001]_{Al}$ ZA is readily observed from the Si and Mg maps. Furthermore, it is also observed extented regions of solute enriched and depleted regions (highlighted), which correlate well with

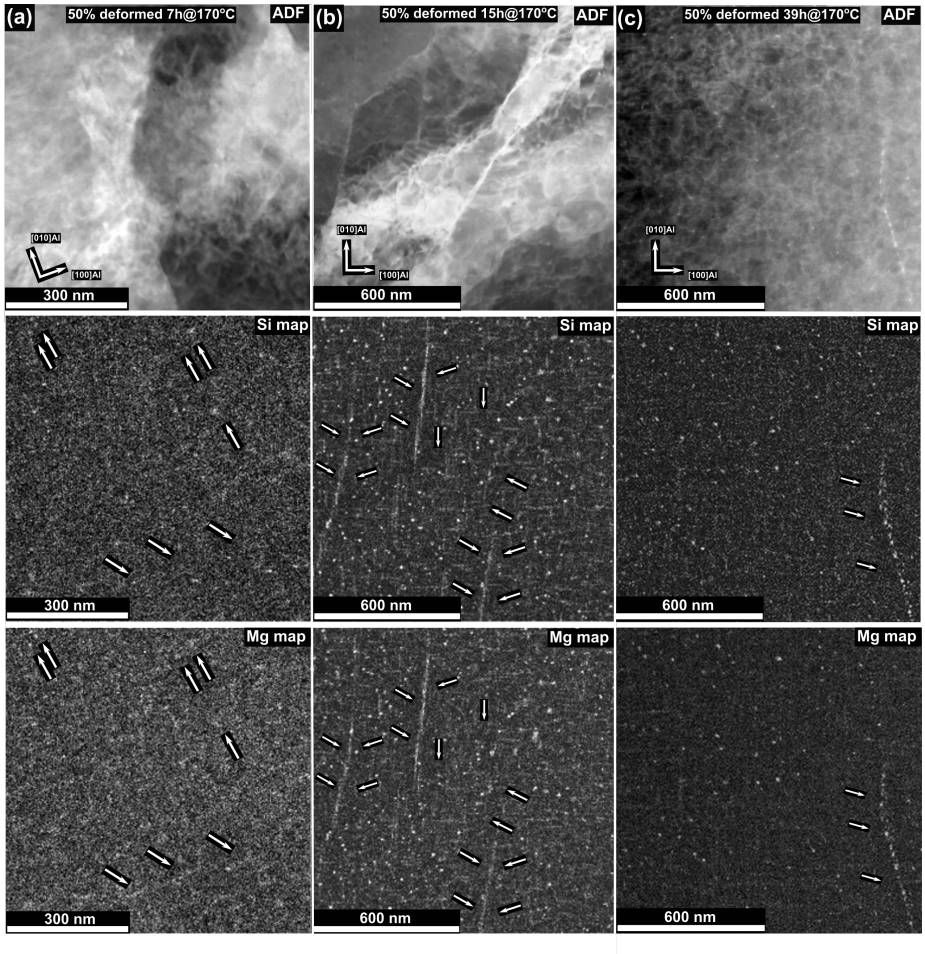

Fig. 5. Left to right: ADF-STEM images and EDS mapping results from the indicated material conditions of the deformed 6101 alloy. Arrows highlight regions rich in solutes and precipitates, surrounded by depleted regions. All images are acquired near the $[001]_{Al}$ zone axis.

some of the main dislocation features observed in the ADF-STEM image in **Fig. 5b**. This clearly demonstrated that the introduced dislocations have a significant impact on the re-distribution of solutes and the distribution of precipitates that form with re-ageing. These extended solute enriched regions indicate either a continuous precipitation along the dislocation lines, or a combined precipitation and solute segregation. It is also observed that these dislocation lines lie close to $[010]_{Al}$ orientation.

At the 39 h deformed condition (**Fig. 5c**) there were also similar observations of precipitate distributions having been affected by the dislocation microstructure. This is for instance seen from the highlighted line of continuous precipitation, with depleted regions on either side. The overall precipitate density seemed significantly lower than the 15 h deformed condition, and in addition much more inhomogeneous. This was also observed in additional EDS maps acquired (not shown).

3.3. Assessment of solute levels by APT

APT experiments were performed on the 7 h undeformed condition, as well as the 15 h undeformed and deformed alloy conditions. The reconstructed analysis volumes are shown in **Fig. 6**. By forming Mg and Si isosurfaces of varying at.% concentration, the precipitate phases could be isolated. It is seen that all volumes contain several precipitates. Having defined the precipitate volumes, the average precipitate composition was obtained, in addition to the matrix solute levels, which was obtained using the proxigram method. The results are presented in **Table 4**.

For the average precipitate compositions, it is seen that the Si and Mg content increases and the Al precipitate content decreases in the material condition ordering 7 h undeformed,

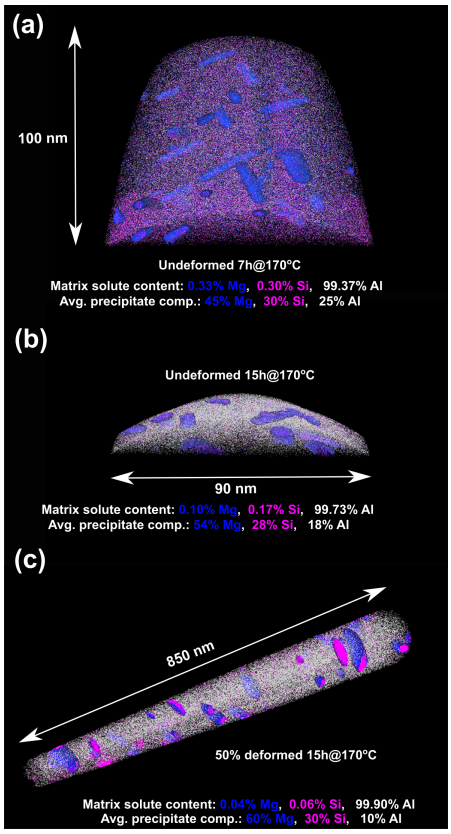

Fig. 6. Reconstructed APT volumes from indicated 6101 alloy conditions. Blue, pink, and white datapoints indicate respectively Mg, Si, and Al atoms. 2 at.% Mg isosurfaces (blue volumes) were used to isolate precipitate phases.

Table 4. Calculated average precipitate composition and the estimated solute content of the Al matrix by APT.

Ageing condition	Precipitate composition [%]	Matrix solute [at. %]
7 h undef.	46%Mg, 28%Al, 26%Si	0.33Mg, 0.30Si
15 h undef.	54%Mg, 18%Al, 28%Si	0.10Mg 0.17Si
15 h def.	60%Mg, 10%Al, 30%Si	0.04Mg, 0.06Si

15 h undeformed, and 15 h deformed. Also, the Mg content increases at a higher rate than Si. This is a generally expected development with increased ageing time in Al-Mg-Si alloys. When these alloys reach overageing conditions, post-β'' ($Mg_5Al_2Si_4$) precipitate phases such as β' ($Mg_6Si_{3.33}$) and eventually β (Mg_2Si) phase form, which are progressively more rich in Mg relative to Si [6]. In this sense, the precipitates of the 15 h deformed condition can be said to be effectively more aged as compared to the precipitates in the 15 h undeformed material.

The matrix solute levels also decrease in the same material condition ordering. At the 7 h undeformed ageing condition, which corresponds with an UA condition (see **Fig. 2a**), it is seen from **Table 4** that the matrix solute levels of Mg and Si are still over half the initial alloy composition (Al-0.54Mg-0.38Si at.%, **Table 1**). Particularly, most of the Si remains in solid solution. From the 7 h to the 15 h undeformed condition there has occurred a coarsening and dissolution of precipitates, seen from the drop in precipitate number density and the increase in average precipitate dimensions and volume fraction (see **Table 3**). In terms of material properties, there is a gain in alloy hardness of about 7 HV1 and 0.7%IACS in the 7 h to 15 h stage, see **Table 2**. The average precipitate composition shows increased Si and particularly Mg concentration, and the Al content has been reduced considerably. Therefore, as expected, the APT measurements of matrix solute levels have dropped notably, from 0.33 to 0.10 at.% Mg, and from 0.30 to 0.17 at.% Si, measured for the 7 h and the 15 h undeformed conditions, respectively.

For the 15 h deformed condition, there is a strikingly low matrix solute content, measuring 0.04 at.% Mg and 0.06 at.% Si. This is also significantly lower than the corresponding undeformed condition. These two conditions are at comparable hardness levels, 80.9 and 79.7 HV1 for the undeformed and deformed conditions, respectively (see **Table 2**). The conductivity of the deformed material is however significantly higher, at 58.8%IACS for the deformed condition compared to 55.9%IACS for the undeformed material. The difference of 2.9%IACS at similar hardness levels is an interesting finding. The APT data show support for the measured difference in electrical conductivity, due to the calculation of a significantly lower matrix solute content for the deformed material.

4. Discussion

4.1. Microstructural contributions to electrical resistivity

Matthiessen's rule is an empirical relation that expresses the total electrical resistivity of a material, ρ_{tot}, as a linear sum of the individual contributions from different microstructural features in the material. In Al alloys, there are several features in the microstructure that have an effect on the electrical resistivity. The total electrical resistivity, ρ_{tot}, as a function of temperature, T, and the matrix solute concentration of elements, c_{i}, may be stated as

$$\rho_{\text{tot}}(T, c_{\text{i}}) = \rho_0(T) + \sum_i \alpha_{\text{i}} c_{\text{i}} + \rho_{\text{disloc}} + \sum_j f_{\text{par, j}}\, \rho_{\text{par, j}} + \rho_{\text{GB}}. \quad (1)$$

Here, ρ_0 is the resistivity of pure aluminium. Among others, it contains the effect of phonons, and therefore has a strong temperature dependence. The conductivity measurements in this work were carried out at room temperature, where $\rho_0 = 2.655 \cdot 10^{-6}\Omega$cm. The factor $\rho_{\text{par, j}}$ accounts for the effect of precipitates (particles) in the microstructure, each with a volume fraction, $f_{\text{par, j}}$. ρ_{disloc}, ρ_{GB}, and α_{i} are constants accounting for the contribution of respectively dislocations, grain boundaries, and solute elements in the Al matrix of a concentration c_{i}. The element-specific coefficients α_{i} at 20 °C equal 0.6186 and 0.5745 μΩ·cm/wt.% for Si and Mg, respectively [22, 23]. This shows that the contributions to the electrical resistivity from the

precipitate forming elements Mg and Si left in solid solution are nearly equal. This also explains why conductivity curves obtained for Al-Mg-Si alloys as a function of ageing are generally continuously increasing. With ageing, progressively more solutes are locked inside precipitate phases, which increases the precipitate volume fraction, and leaves less solute left in the Al matrix. Furthermore, the sensitivity to either element in solid solution is similar, which means that despite changes in average precipitate composition, the overall conductivity should generally increase.

The mean free path of conducting electrons in Al is $\lambda_{\mathrm{Al}} = 14\,\mathrm{nm}$ at room temperature [23]. When both the average precipitate dimensions and interparticle spacing are larger than this value, the contribution to electrical resistivity is relatively small. As the grain size of typical Al alloys is also much larger than this length, the factor ρ_{GB} is also negligible. In alloys processed by severe plastic deformation, where average grain diameters can be on the order of 100 nm, the contribution can however be significant [4, 13, 14, 24]. In terms of the dislocation contribution, ρ_{disloc}, Miyajima et al. [25] have shown good agreement with experimental findings using $\rho_{\mathrm{disloc}} = 2.6{\cdot}10^{-16}\,\mu\Omega\mathrm{m}^2$. However, as seen from **Fig. 2a**, the conductivity of the studied material before and after 50%CR caused no measurable change in conductivity, and the dislocation contribution is therefore thought to be less important.

For the alloy conditions studied here, the main contribution to the electrical resistivity is hence due to solute solution contribution $\sum_i \alpha_i c_i$, with other terms in **Eq. 1** being relatively small in comparison. By comparing the 15 h deformed and undeformed ageing conditions, see **Table 4**, it was shown that the deformed material had a significantly lower matrix solute content of Si and Mg, which supports the measurement of a higher conductivity for this condition (see **Table 2**). The differences in matrix solute levels between the deformed and undeformed 15 h conditions are 0.06 at.% Mg and 0.11 at.% Si. Using the matrix solute levels measured by APT for the 15 h deformed and undeformed conditions given in **Table 4**, the calculated difference, and assuming all other contributions in **Eq. 1** are comparable for the two conditions, then the relative change in electrical conductivity is approximated as: $\Delta\sigma = 1/\rho_{\mathrm{7h,\,def}} - 1/\rho_{\mathrm{7h,\,undef}} \approx 1.4$ MS/m ≈ 2.4%IACS. This is to be compared with the 2.9%IACS difference in conductivity measured between the 15 h deformed and undeformed ageing conditions, see **Table 2**. This is a relatively good agreement considering the simplifications made in the calculations, and shows that the main cause of the difference in conductivity can be attributed to the change in matrix solute levels.

4.2. On the rapid increase in conductivity after deformation

Re-ageing following 50%CR caused a very sharp increase in conductivity, from 55.2%IACS to 58.1%IACS, in about 2 h ageing time at 170 °C, see **Fig. 2b**. In the 7 h undeformed ageing condition (= PA treatment), there existed a relatively dense microstructure of primarily pure β'' precipitates (**Fig. 3**), containing less than half of the total solute additions available in the alloy (**Table 4**). By subsequently deforming the material in this UA condition, strong precipitate-dislocation interactions will occur, causing a dense and evenly distributed network of dislocations. The solute atoms, atomic clusters/GP-zones, and precipitates present in the matrix, act as obstacles to the moving dislocations. The precipitates will be sheared multiple times due to the high degree of deformation introduced, which will cause partial or complete disruption of the preciptiate crystal structures [21].

Due to the high strain rates, $\dot{\gamma}$, involved in cold-rolling, and hence high dislocation velocities, solute segregation or formation of Cottrell atmospheres near moving dislocations will unlikely occur to a significant extent, since this is promoted at lower dislocation velocities [26]. Due to the large plastic deformation, the dislocation microstructure will develop into a highly complex and entangled network, where most dislocations will be pinned at multiple points on the different dislocation obstacles present in the 7 h condition. The disruption of precipitate crystal structures is rather clear from microstructure observations after 50%CR (**Fig. 4a,d**), where the precipitates proved difficult to observe based on TEM imaging techniques utilising diffraction contrast (BF/DF). Only EDS maps showed that Mg and Si rich regions were still present (**Fig. 5a**). Despite crystal structures being partially destroyed, the solutes are thought to remain relatively confined to their original positions. The high degree of deformation will also have increased the concentration of vacancies in the material considerably [27, 28].

In the next step, this highly entangled dislocation microstructure, pinned on partially/completely disrupted precipitate crystal structures and solute enriched regions, is subjected to re-ageing at 170 °C. In this stage, it is envisioned two different main mechanisms taking place: (i) conventional bulk diffusion and resulting nucleation and growth away from the dislocation network, and (ii) rapid pipe (/dislocation) diffusion of solutes causing re-growth of locally solute enriched regions pinning dislocations and new heterogeneous nucleation on dislocations. Both effects will be enhanced by the increase in vacancy levels introduced by the deformation stage. The dislocations will also be able to move and become unpinned, leading to dislocation recovery. The large changes in hardness seen from **Fig. 2a** immediately after deformation is a clear evidence of this. The balance between an increase in hardness from precipitation and a reduction due to dislocation recovery is shifting quickly at this stage.

Bulk solute diffusion around a static dislocation is well-established in continuum models [29, 30], which show that the Mg atoms will diffuse and bind to the tensile stress field of the dislocation due to its increased size misfit relative to Al atoms. This effect is well-known, particularly for Al-Mg alloys (5xxx), where it may manifests itself in the phenomena of dynamic strain ageing (DSA) and the Portevin-le Chatelier effect [29, 30]. Si on the other hand, will bind to the compressive field of the dislocation due to its negative size misfit [31].

Fast diffusion along dislocation cores for different types of dislocations in Al has been treated and demonstrated previously [26, 32, 33, 34, 35]. For Mg, this has been treated extensively, in studies of aspects related to DSA [30, 36]. For Si, the diffusion along a single dislocation line between silicon

nano-precipitates in an Al thin film was studied *in-situ* showing that dislocations accelerate the diffusion of impurities by almost three orders of magnitude as compared to bulk diffusion [37]. Similar results have also been demonstrated previously, by indirect assessments [38]. Calorimetric studies of the dynamics of solute clustering have also suggested that solute migration takes place by pipe diffusion at early times and by bulk diffusion at later times during the clustering process [39].

The increased diffusivity of solute elements as enhanced by the aforementioned effects will cause a more rapid depletion of the matrix solute levels in the deformed material as compared to the undeformed, and hence resulting in an increase in electrical conductivity. The improvement in conductivity is therefore seen as an effect of improved 'vacuuming' of the matrix solutes, leaving the conducting electrons with a path of least resistance through the matrix. **Fig. 7** presents a visualisation of the proposed evolution mechanisms for the two TMP routes applied in this work.

After the initial spike in conductivity increase, the slope of the conductivity plot is nearly equal for the deformed and undeformed materials, seen from fitted curves in **Fig. 2b**. Due to the similar increase in conductivity for the undeformed and deformed material after about 9 h, this is taken as an indication that the pipe diffusion of elements along dislocations has halted for the deformed material, and the subsequent microstructural changes proceed as conventional overageing, characterised by precipitate coarsening and dissolution of smaller precipitates.

This has important implications for the interest with retaining good material strength while optimising for high conductivity. The largest increase in conductivity occurs shortly after re-ageing the as-deformed material. Rapid precipitate regrowth/coarsening and dislocation recovery will occur concurrently, with an increasing conductivity and a gradually reduced material strength. Moderate ageing after deformation should therefore lead to an optimum combination of increase in conductivity while retaining material strength. Increasing the ageing temperature, and/or applying different durations of the PA treatment are also parameters that should be explored more carefully to design optimum processing routines for achieving good material property combinations.

5. Conclusions

This work has combined hardness and conductivity measurements, TEM observations, and APT experiments for studying a 6101 Al-0.54Mg-0.38Si (at.%) conductor alloy subjected to two different TMP routes. It was shown that a combination of PA, 50% thickness reduction by CR, and subsequent re-ageing caused a considerable improvement in conductivity (2 – 3%IACS) over conventional isothermal ageing at equal ageing times. APT experiments showed that the difference in conductivity could largely be explained based on the increased solute depletion of the Al matrix in the deformed and re-aged material, as compared to the undeformed material after similar ageing times. The electrical conductivity of the deformed material developed in two main stages. In the initial stage, at the beginning of re-ageing, there occurred a very rapid increase in

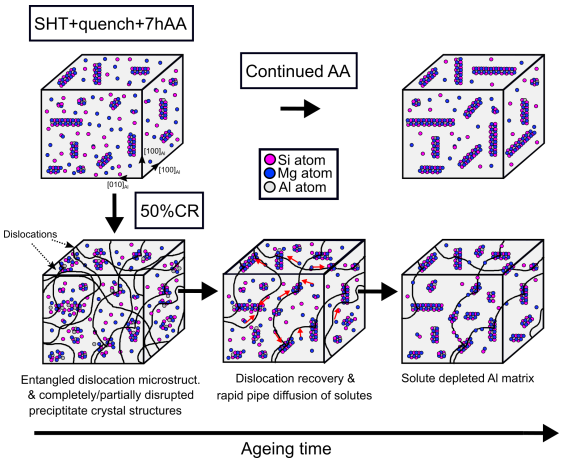

Fig. 7. Schematic representation of the microstructure evolution in the deformed and undeformed material with ageing.

conductivity, which is proposed to occur due to pipe diffusion of solutes along the entangled dislocation network, effectively 'vacuuming' the matrix of solutes. After 2 h re-ageing, the rate of change in conductivity was nearly equal in the deformed and underformed materials, and this subsequent stage is characterised by overageing behaviour, with precipitate coarsening and dissolution of smaller precipitates. TEM observations of the deformed and undeformed materials showed that there were several major differences with respect to the resulting distribution of precipitate phases that formed with ageing. Most strikingly, the precipitate distribution of the deformed material became progressively more inhomogeneous, and there were clear observations of precipitate-dislocation interactions.

From the obtained results it is suggested that for achieving a high conductivity and good strength, a relatively short ageing treatment should be applied after the deformation step. This is because the main increase in conductivity occurs shortly after re-ageing, with dislocation recovery occurring concurrently.

Acknowledgements

All authors acknowledge support from the AMPERE project (NFR 247783), a knowledge building project for industry, co-financed by The Research Council of Norway (NFR), and the industrial partners Hydro, Gränges, Neuman Aluminium Raufoss (Raufoss Technology), and Nexans. The (S)TEM work was carried out on the NORTEM infrastructure (NFR 197405) at the TEM Gemini Centre, Trondheim, Norway.

References

[1] F. Kiessling, P. Nefzger, J. F. Nolasco, and U. Kaintzyk. *Overhead Power Lines*. Springer-Verlag Berlin Heidelberg, 1st edition, 2003.

[2] S. Karabay. Modification of AA-6201 alloy for manufacturing of high conductivity and extra high conductivity wires with property of high tensile stress after artificial aging heat treatment for all-aluminium alloy conductors. *Materials & Design*, 27(10):821 – 832, 2006.

[3] S. Karabay. Influence of AlB2 compound on elimination of incoherent precipitation in artificial aging of wires drawn from redraw rod extruded from billets cast of alloy AA-6101 by vertical direct chill casting. *Materials & Design*, 29(7):1364 – 1375, 2008.

[4] X. Sauvage, E. V. Bobruk, M. Yu. Murashkin, Y. Nasedkina, N. A. Enikeev, and R. Z. Valiev. Optimization of electrical conductivity and strength combination by structure design at the nanoscale in Al-Mg-Si alloys. *Acta Materialia*, 98:355–366, 2015.

[5] G. A. Edwards, K. Stiller, G. L. Dunlop, and M. J. Couper. The precipitation sequence in Al–Mg–Si alloys. *Acta Materialia*, 46(11):3893–3904, 1998.

[6] C. D. Marioara, S. J. Andersen, H. W. Zandbergen, and R. Holmestad. The influence of alloy composition on precipitates of the Al-Mg-Si system. *Metallurgical and Materials Transactions A*, 36(13):691–702, 2005.

[7] H. S. Hasting, A. G. Frøseth, S. J. Andersen, R. Vissers, J. C. Walmsley, C. D. Marioara, F. Danoix, W. Lefebvre, and R. Holmestad. Composition of β'' precipitates in Al–Mg–Si alloys by atom probe tomography and first principles calculations. *Journal of Applied Physics*, 106(12), dec 2009.

[8] R. Vissers, M. A. van Huis, J. Jansen, H. W. Zandbergen, C. D. Marioara, and S. J. Andersen. The crystal structure of the β' phase in Al–Mg–Si alloys. *Acta Materialia*, 55(11):3815–3823, jun 2007.

[9] S. J. Andersen, C. D. Marioara, R. Vissers, A. Frø seth, and H. W. Zandbergen. The structural relation between precipitates in Al-Mg-Si alloys, the Al-matrix and diamond silicon, with emphasis on the trigonal phase U1-MgAl2Si2. *Materials Science and Engineering A*, 444(1-2):157–169, 2007.

[10] S. J. Andersen, C. D. Marioara, A. Frøseth, R. Vissers, and H. W. Zandbergen. Crystal structure of the orthorhombic U2-Al4Mg4Si4 precipitate in the Al–Mg–Si alloy system and its relation to the β' and β'' phases. *Materials Science and Engineering: A*, 390(1-2):127–138, jan 2005.

[11] S. D. Dumolt, D. E. Laughlin, and J. C. Williams. Formation of a modified β' phase in aluminum alloy 6061. *Scripta Metallurgica*, 18(12):1347 – 1350, 1984.

[12] A. H. Geisler and J. K. Hill. Analyses and interpretations of X-ray diffraction effects in patterns of aged alloys. *Acta Crystallographica*, 1(5):238–252, 1948.

[13] M. Yu Murashkin, I. Sabirov, V. U. Kazykhanov, E. V. Bobruk, A. A. Dubravina, and R. Z. Valiev. Enhanced mechanical properties and electrical conductivity in ultrafine-grained Al alloy processed via ECAP-PC. *Journal of Materials Science*, 48(13, SI):4501–4509, 2013.

[14] M. Murashkin, A. Medvedev, V. Kazykhanov, A. Krokhin, G. Raab, N. Enikeev, and R. Z. Valiev. Enhanced Mechanical Properties and Electrical Conductivity in Ultrafine-Grained Al 6101 Alloy Processed via ECAP-Conform. *Metals*, 5(4):2148–2164, 2015.

[15] K. Majchrowicz, Z. Pakiela, W. Chrominski, and M. Kulczyk. Enhanced strength and electrical conductivity of ultrafine-grained Al-Mg-Si alloy processed by hydrostatic extrusion. *Materials Characterization*, 135:104–114, 2018.

[16] J. P. Hou, Q. Wang, Z. J. Zhang, Y. Z. Tian, X. M. Wu, H. J. Yang, X. W. Li, and Z. F. Zhang. Nano-scale precipitates: The key to high strength and high conductivity in Al alloy wire. *Materials & Design*, 132:148–157, 2017.

[17] C. H. Liu, J. Chen, Y. X. Lai, D. H. Zhu, Y. Gu, and J. H. Chen. Enhancing electrical conductivity and strength in Al alloys by modification of conventional thermo-mechanical process. *Materials & Design*, 87:1–5, 2015.

[18] G. Lin, Z. Zhang, H. Wang, K. Zhou, and Y. Wei. Enhanced strength and electrical conductivity of Al-Mg-Si alloy by thermo-mechanical treatment. *Materials Science and Engineering A*, 650:210–217, 2016.

[19] D. J. Larson, T. J. Prosa, R. M. Ulfig, B. P. Geiser, and T. F. Kelly. *Local Electrode Atom Probe Tomography*. Springer, New York, 2013.

[20] S. J. Andersen. Quantification of the Mg2Si β'' and β' phases in AlMgSi alloys by transmission electron microscopy. *Metallurgical Material Transactions A*, 26(8):1931–1937, 1995.

[21] E. Christiansen, C. D. Marioara, B. Holmedal, O. S. Hopperstad, and R. Holmestad. Nano-scale characterisation of sheared β'' precipitates in a deformed aluminium alloy. *Scientific Reports*, 9(1):17446, 2019.

[22] M. H. Mulazimoglu, R. Drew, and J. E. Gruzelski. Electrical-conductivity of aluminum-rich Al-Si-Mg alloys. *Journal of Materials Science Letters*, 8(3):297–300, 1989.

[23] F. R. Fickett. Aluminum—1. A review of resistive mechanisms in aluminum. *Cryogenics*, 11(5):349 – 367, 1971.

[24] T. S. Orlova, A. M. Mavlyutov, A. S. Bondarenko, I. A. Kasatkin, M. Yu. Murashkin, and R. Z. Valiev. Influence of grain boundary state on electrical resistivity of ultrafine grained aluminium. *Philosophical Magazine*, 96(23):2429–2444, 2016.

[25] Y. Miyajima, S.-Y. Komatsu, M. Mitsuhara, S. Hata, H. Nakashima, and N. Tsuji. Change in electrical resistivity of commercial purity aluminium severely plastic deformed. *Philosophical Magazine*, 90(34):4475–4488, 2010.

[26] Y. Wang, D. J. Srolovitz, J. M. Rickman, and R. Lesar. Dislocation motion in the presence of diffusing solutes: A computer simulation study. *Acta Materialia*, 48(9):2163–2175, 2000.

[27] M. Militzer, W. P. Sun, and J. J. Jonas. Modelling the effect of deformation-induced vacancies on segregation and precipitation. *Acta Metallurgica et Materialia*, 42(1):133 – 141, 1994.

[28] M. J. Zehetbauer, G. Steiner, E. Schafler, A. Korznikov, and E. Korznikova. Deformation induced vacancies with severe plastic deformation: Measurements and modelling. In Z Horita, editor, *Nanomaterials by severe plastic deformation*, volume 503-504 of *Materials Science Forum*, pages 57–64, 2006.

[29] N. Louat. On The Theory of The Portevin-Le Chateriler Effect. *Scripta Metallurgica*, 15(11):1167–1170, 1981.

[30] W. A. Curtin, D. L. Olmsted, and L. G. Hector Jr. A predictive mechanism for dynamic strain ageing in aluminium-magnesium alloys. *Nature Materials*, 5(11):875–880, 2006.

[31] G. P. M. Leyson, W. A. Curtin, L. G. Hector Jr., and C. F. Woodward. Quantitative prediction of solute strengthening in aluminium alloys. *Nature Materials*, 9(9):750–755, 2010.

[32] G. R. Love. Dislocation Pipe Diffusion. *Acta Metallurgica*, 12(6):731–, 1964.

[33] J. Mimkes. Pipe Diffusion Along Isolated Dislocations. *Thin Solid Films*, 25(1):221–230, 1975.

[34] R. W. Balluffi. On measurements of self-diffusion rates along dislocations in f.c.c. metals. *Physica Status Solidi (b)*, 42(1):11–34, 1970.

[35] G. P. Purja Pun and Y. Mishin. A molecular dynamics study of self-diffusion in the cores of screw and edge dislocations in aluminum. *Acta Materialia*, 57(18):5531–5542, 2009.

[36] R. C. Picu and D. Zhang. Atomistic study of pipe diffusion in Al-Mg alloys. *Acta Materialia*, 52(1):161–171, 2004.

[37] M. Legros, G. Dehm, E. Arzt, and T. J. Balk. Observation of giant diffusivity along dislocation cores. *Science*, 319(5870):1646–1649, 2008.

[38] T. E. Volin, K. H. Lie, and R. W. Balluffi. Measurement of rapid mass transport along individual dislocations in aluminum. *Acta Metallurgica*, 19(4):263 – 274, 1971.

[39] A. Varschavsky and E. Donoso. A calorimetric investigation on the kinetics of solute segregation to partial dislocations in cu–3.34at%sn. *Materials Science and Engineering: A*, 251(1):208 – 215, 1998.